# Photosynthetic reaction center variants made via genetic code expansion show Tyr at M210 tunes the initial electron transfer mechanism

Jared Bryce Weaver<sup>a</sup>, Chi-Yun Lin<sup>a</sup>, Kaitlyn M. Faries<sup>b</sup>, Irimpan I. Mathews<sup>c</sup>, Silvia Russi<sup>c</sup>, Dewey Holten<sup>b</sup>, Christine Kirmaier<sup>b</sup>, and Steven G. Boxer<sup>a,1</sup>

<sup>a</sup>Department of Chemistry, Stanford University, Stanford, CA 94305; <sup>b</sup>Department of Chemistry, Washington University in St. Louis, St. Louis, MO 63130-4889; and <sup>c</sup>Structural Molecular Biology, Stanford Synchrotron Radiation Lightsource, SLAC National Accelerator Laboratory, Menlo Park, CA 94025

Edited by Donald Ort, Plant Biology, University of Illinois at Urbana-Champaign, Urbana, IL; received September 16, 2021; accepted November 2, 2021

Photosynthetic reaction centers (RCs) from Rhodobacter sphaeroides were engineered to vary the electronic properties of a key tyrosine (M210) close to an essential electron transfer component via its replacement with site-specific, genetically encoded noncanonical amino acid tyrosine analogs. High fidelity of noncanonical amino acid incorporation was verified with mass spectrometry and X-ray crystallography and demonstrated that RC variants exhibit no significant structural alterations relative to wild type (WT). Ultrafast transient absorption spectroscopy indicates the excited primary electron donor, P\*, decays via a ~4-ps and a ~20-ps population to produce the charge-separated state P<sup>+</sup>H<sub>A</sub><sup>-</sup> in all variants. Global analysis indicates that in the ~4-ps population, P+HAforms through a two-step process,  $P^* \rightarrow P^+B_A^- \rightarrow P^+H_A^-$ , while in the ~20-ps population, it forms via a one-step  $P^* \rightarrow P^+H_A^-$  superexchange mechanism. The percentage of the P\* population that decays via the superexchange route varies from ~25 to ~45% among variants, while in WT, this percentage is ~15%. Increases in the P\* population that decays via superexchange correlate with increases in the free energy of the  $P^+B_A^{\phantom{A}-}$  intermediate caused by a given M210 tyrosine analog. This was experimentally estimated through resonance Stark spectroscopy, redox titrations, and nearinfrared absorption measurements. As the most energetically perturbative variant, 3-nitrotyrosine at M210 creates an ~110-meV increase in the free energy of P+BA- along with a dramatic diminution of the 1,030-nm transient absorption band indicative of P+B<sub>A</sub>formation. Collectively, this work indicates the tyrosine at M210 tunes the mechanism of primary electron transfer in the RC.

reaction center | noncanonical amino acid | ultrafast transient absorption spectroscopy | Stark spectroscopy | superexchange

hotosynthetic reaction centers (RCs) are the integral membrane protein assemblies responsible for nearly all the solar energy conversion maintaining our biosphere. In this study, we focus on the initial electron transfer (ET) steps in bacterial RCs from Rhodobacter sphaeroides, a three-subunit (H, L, and M)  $\sim$ 100-kDa integral membrane protein complex. RCs in R. sphaeroides possess two branches of chromophores, the A and B (or L and M) branches (Fig. 1A), and each possesses nearly identical chromophore composition, orientation, and distances. The protein secondary structure is pseudo-C2 symmetric, and the symmetry-related amino acids that differ are often structurally similar (Fig. 1A) (1). Despite this high structural symmetry, ET proceeds rapidly down only the A branch of chromophores with near-unity quantum yield (2, 3). Additionally, RC ET is remarkably robust, as few structurally verified single mutations that maintain RC chromophore composition and positioning significantly impact ET kinetics or yield (1, 4–11).

To understand RC ET asymmetry or unidirectionality and factors underlying its robust nature, a thorough understanding of the mechanism of ET is required. In the model largely accepted in the current literature (1, 12–14), ET is initiated by

excitation of the excitonically coupled bacteriochlorophyll pair P. The lowest singlet excited state P\* transfers an electron to the bacteriochlorophyll B<sub>A</sub> with a time constant of ~3 ps to form P<sup>+</sup>B<sub>A</sub><sup>-</sup>. B<sub>A</sub><sup>-</sup> subsequently transfers an electron to the bacteriopheophytin H<sub>A</sub> with a time constant of 1 ps, thus forming  $P^{+}H_{A}^{-}$  in a two-step primary ET process,  $P^{*} \rightarrow P^{+}B_{A}^{-}$ P<sup>+</sup>H<sub>A</sub><sup>-</sup> (1, 12, 13). An alternative model for ET has been proposed in which P\* transfers an electron to H<sub>A</sub> directly through a superexchange mechanism, as defined by Parson et al. (1). Here, the B<sub>A</sub> chromophore mediates the electronic coupling between P\* and HA, and experimental evidence for superexchange ET must be inferred spectroscopically from the absence of P<sup>+</sup>B<sub>A</sub><sup>-</sup> formation during transient absorption (TA) measurements and generally slower ET. In wild-type (WT) RCs, evidence favors two-step ET at room temperature (1, 12, 13, 15, 16). It has been previously proposed that minor degrees of superexchange occur in WT RCs, likely arising from or enhanced by the inherent distribution in the energies of P\*, P+B<sub>A</sub>-, and P+H<sub>A</sub>- caused by protein populations with slight variations in amino acid nuclear coordinates around

#### **Significance**

Reaction centers (RCs) are critical to photosynthetic energy conversion. RCs in all characterized photosynthetic organisms contain two symmetrically arranged branches of chromophores and enable light-induced electron transfer with high yield. We fine-tune the properties of a key bacterial RC symmetry-breaking tyrosine via its replacement with noncanonical tyrosine analogs and determine kinetic outcomes. Results are interpreted through energetic characterization made possible by resonance Stark spectroscopy. Analysis indicates this tyrosine modulates the mechanism of the initial light-induced electron transfer, affording an alternative functional pathway that maintains the RC's robust electron transfer. Modern molecular biology, ultrafast spectroscopy, crystallography, and energetic characterization enable the mechanistic model we describe. Our results deepen understanding of RC function and may have implications for other photocatalysts and enzymes.

Author contributions: J.B.W., C.-Y.L., K.M.F., I.I.M., D.H., C.K., and S.G.B. designed research; J.B.W., C.-Y.L., K.M.F., I.I.M., S.R., D.H., and C.K. performed research; S.R. contributed new reagents/analytic tools; J.B.W., C.-Y.L., K.M.F., I.I.M., D.H., and C.K. analyzed data; and J.B.W., C.-Y.L., K.M.F., D.H., C.K., and S.G.B. wrote the paper.

The authors declare no competing interest.

This article is a PNAS Direct Submission.

Published under the PNAS license.

<sup>1</sup>To whom correspondence may be addressed. Email: sboxer@stanford.edu.

This article contains supporting information online at http://www.pnas.org/lookup/suppl/doi:10.1073/pnas.2116439118/-/DCSupplemental.

Published December 14, 2021.

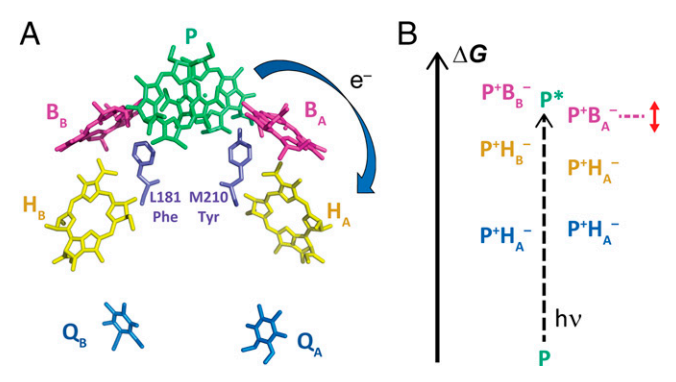


**Fig. 1.** RC chromophore arrangement and energetics. (*A*) Chromophore arrangement in WT RCs (PDB ID: 2J8C; accessory carotenoid, chromophore phytyl tails, and quinone isoprenoid tails are removed here for clarity). Tyr at M210, the target in this work, and its symmetry-related residue Phe at L181 are shown in purple. The blue arrow indicates unidirectionality of ET down the A branch. (*B*) Schematic free-energy diagram of different charge-separated states in WT RCs, where P\* is 1.40 eV above ground state and P<sup>+</sup>H<sub>A</sub><sup>-</sup> is 0.25 eV below P\*. The dashed magenta line and double-headed arrow next to P<sup>+</sup>B<sub>A</sub><sup>-</sup> indicates the expected major effect of ncAA incorporation at M210 on the free energy of this state.

chromophores (5, 17-19), but this has been difficult to study experimentally (1, 12).

The ET mechanisms in RCs likely have their origins in the different energies of the various charge-separated states for the two branches relative to P\* and each other (Fig. 1B) (20-22), but it is difficult to determine these energetics either experimentally or theoretically (1, 23). Contributions of individual symmetry-breaking amino acid have been thoroughly studied (1, 15, 24–28), and while the importance of certain amino acids has been ascertained, the roles of local protein-chromophore interactions are not always fully understood (8, 24, 25). One highly examined residue has been the tyrosine at site M210 (RC residue numbers are preceded by the protein subunit designation: H, L, or M) because it is a clear deviation in symmetry between A and B branches (Fig. 1A), it is close to B<sub>A</sub>, and it is the only one of 27 tyrosines that lacks a hydrogen bond acceptor. Theoretical studies indicate that the magnitude and orientation of the hydroxyl dipole of tyrosine M210 may play an important role in energetically stabilizing P<sup>+</sup>B<sub>A</sub><sup>-</sup> (29, 30). Indeed, previous efforts to change the orientation of this tyrosine's hydroxyl dipole significantly slowed ET (31). It is difficult, however, to subtly vary the electrostatic nature of this tyrosine using canonical mutagenesis without entirely removing the phenolic hydroxyl.

To perturb the effects of the tyrosine at M210 in WT protein, we used amber stop codon suppression (32–34) to site-specifically replace it with five noncanonical amino acids (ncAAs), each a tyrosine with a single electron-donating or electron-withdrawing *meta*-substituent (at the 3 position). We will refer to RC protein variants by acronyms for the amino acid incorporated at M210: 3-methyltyrosine (MeY), 3-nitrotyrosine (NO<sub>2</sub>Y), 3-chlorotyrosine (CIY), 3-bromotyrosine (BrY), and 3-iodotyrosine (IY) (Fig. 2 and *SI Appendix*, Fig. S1 and Table S1). In this way, we engineered a series of RC variants with more systematic electrostatic ET perturbation at this important tyrosine while minimally affecting other RC features.

#### **Results**

#### Verification of ncAA Incorporation and Minimal Structural Perturbation. In previous work, we took an amber suppression system devel-

In previous work, we took an amber suppression system developed for halotyrosine (CIY, BrY, and IY) incorporation in *Escherichia coli* (35) and transferred this system from *E. coli* to *R. sphaeroides* gene control, optimizing it for RC expression

(36). Here, incorporation of MeY (37) is also performed using this previously created system (SI Appendix, sections S1.1 and S1.3–S1.4). We apply the same strategy used earlier (36) to a recently created amber suppression system (38) and genetically encode NO<sub>2</sub>Y incorporation in R. sphaeroides (SI Appendix, sections S1.1–S1.4). Liquid chromatography—mass spectrometry (LC–MS) was used to verify ncAA incorporation for NO<sub>2</sub>Y and MeY RCs (SI Appendix, Figs. S2 and S3). The mass shifts of the M-subunit peak correspond to the respective mass of the incorporated ncAAs (within a mass accuracy of  $\pm 1$  Da for a 30-kDa subunit) (SI Appendix, Fig. S2), while the H and L subunits remained identical to their WT mass as shown in previous work (36). This shows the general adaptability of our previous methods for genetic code expansion in R. sphaeroides.

X-ray crystal structures of all variants were obtained at room temperature with resolutions comparable to those from previous room-temperature structures (39). These X-ray crystal structures (Fig. 2 and SI Appendix, Figs. S4-S6 and Table S2) also verify ncAA incorporation at only site M210. All crystal structures possess additional electron density in the M210 tyrosine meta-position (Fig. 2), which corresponds to the relevant ncAA incorporated with a phenolic position for the tyrosine side chain similar to WT (SI Appendix, Fig. S5). MeY and NO<sub>2</sub>Y RCs have respective methyl- and nitro-substituents solely oriented toward PA, while halotyrosine RCs display electron density (i.e., occupancy) that required modeling of two different halogen conformations, one oriented toward PA and the other toward the Mg<sup>2+</sup> of B<sub>A</sub> (Fig. 2). While the halogensubstituted tyrosines likely have comparable electrostatic properties given their similar Hammett parameters (40), pK<sub>a</sub> values (41), and because they have been noted to affect processes involving charge transfer similarly (42), differences in their size may have led to the change in population oriented toward PA as opposed to BA, since larger substituents are poorly accommodated by the smaller cavity next to  $B_A$  (Fig. 2). For the  $B_A$ -oriented substituent, this leads to halogen– $Mg^{2+}$  distances of 3.4 Å (CIY), 3.4 Å (BrY), and 2.9 Å (IY). Dual halogen conformations for halotyrosine-containing proteins have been noted previously (37, 42, 43). Importantly, incorporation of all ncAAs at M210 in this study also proved to be minimally perturbative with respect to the remaining protein structure and chromophore positions and orientations; we found nearly identical interchromophoric distances and relative orientations to those present in the WT structure (Protein Data Bank [PDB] entry numbers: 2J8C and 1K6L; SI Appendix, Figs. S4-S6 and Table S3). Rmsd is 0.229 to 0.261 Å for alignments to a roomtemperature WT structure (1K6L) and is 0.333 to 0.367 Å for alignment to a 77-K WT structure (2J8C).

ET Kinetics. ET dynamics of the M210 variants were determined by TA through a combination of 1) the assessment of raw real-time spectra (SI Appendix, Figs. S13-S18) and singlewavelength kinetic fits (SI Appendix, Figs. S7-S38), 2) modelindependent global analysis (Fig. 3 and SI Appendix, Figs. S39-S55), and 3) model-dependent global analysis (Fig. 4 and SI Appendix, Figs. S56-S73). Results are summarized in SI Appendix, Tables S4 and S5. TA kinetics at 924 nm and at 542 nm demonstrate that there is biexponential P\* decay and P+H<sub>A</sub>- formation for all variants (SI Appendix, Figs. S19 and S20). The biexponential P\* stimulated emission decay at 924 nm for WT and all variants reflects one  $P^*$  population that decays with a lifetime of  $\sim 3$  ps and a second  $P^*$  population that decays with a lifetime of ~20 ps (SI Appendix, Fig. S19 and Table S4). P<sup>+</sup>H<sub>A</sub><sup>-</sup> formation detected at 542 nm has similar kinetics (SI Appendix, Fig. S20 and Table S4). This biexponential P\* decay and P+H<sub>A</sub>- formation has been noted previously in the literature for WT RCs (6, 10, 15, 18, 19, 44, 45).

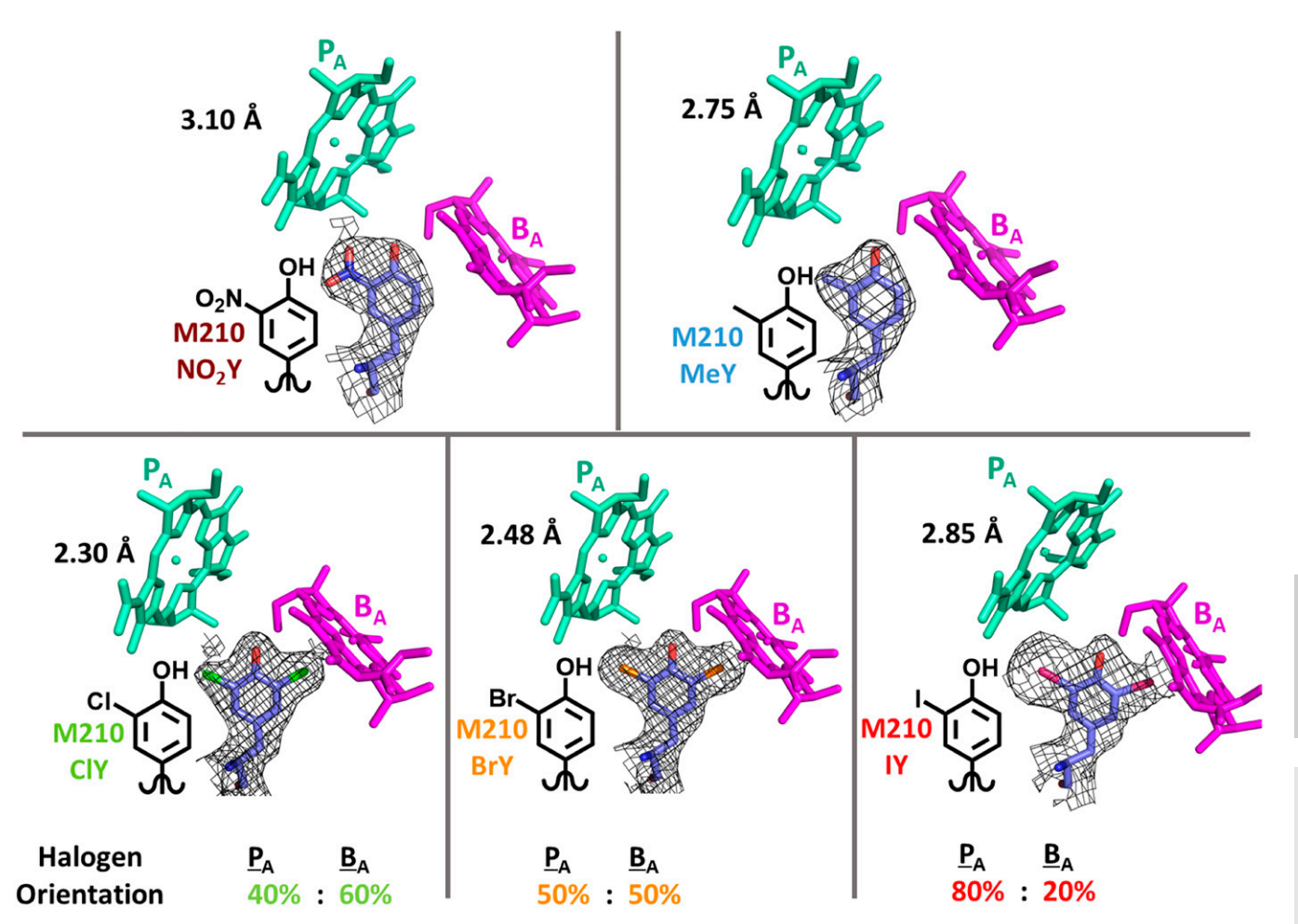


Fig. 2. RC variants made and structurally characterized in this study, in which truncated PA and BA chromophores are depicted for each variant (in teal and magenta, respectively) and electron density maps from solved X-ray structures are shown (2F<sub>o</sub>-F<sub>c</sub> contoured at 1 σ) for tyrosine analogs at M210. Halogen variants required two different tyrosine ring conformers to model halogen substituent orientations with the contribution of each indicated, one with the halogen oriented toward P (only PA depicted above) and the other with halogen toward BA. The resolution for each crystal structure is denoted in black next to the PA of each RC variant (PDB IDs for NO<sub>2</sub>Y, MeY, CIY, BrY, and IY RCs are 7MH9, 7MH8, 7MH4, and 7MH5, respectively; SI Appendix, Table S2).

Global analysis of the TA data also supports biexponential P\* decay and P+H<sub>A</sub>- formation (Fig. 3 and SI Appendix, Table S4). A model-independent global fit returns decay-associated difference spectra (DADS), which are spectra composed of the preexponential coefficients at every wavelength for a given lifetime component in the fit. A DADS reflects the change in absorbance associated with a given lifetime (46, 47). While no DADS corresponds directly to one ET intermediate, it contains features indicative of the associated ET species. DADS spectral features and lifetimes guide a target model for global analysis that returns species-associated decay spectra (SADS) (refer to SI Appendix, section S3.2 for further discussion of SADS and DADS). DADS for all variants are remarkably similar; the same number of lifetimes are required to fit every variant except for NO<sub>2</sub>Y (Fig. 3), which did not require a ~1-ps component for a global fit. Spectral features for each time component were also very similar among variants. The  $\sim$ 4-ps and  $\sim$ 1-ps DADS (for all variants but NO<sub>2</sub>Y) show features consistent with a two-step ET model for  $P^* \xrightarrow{} P^+ B_A^- \rightarrow P^+ H_A^-.$  These features include those for  $P^+$  (1,250 nm),  $B_A^-$  (1,030 nm),  $B_A$  and P bleaching (600 nm), and H<sub>A</sub> bleaching (542 nm), all appropriately signed. In comparison, the 12- to 20-ps DADS showed features consistent with a super-exchange ET model ( $P^* \rightarrow P^+H_A^-$ ), where  $P^+$  and  $H_A^-$  features are present but the 1,030-nm feature (associated with the B<sub>A</sub> anion absorption) is absent or significantly diminished, as noted previously (15). A greater proportion of the P\* population that

decays with the ~20-ps lifetime is present in all the variants than in WT (Fig. 3 and SI Appendix, Table S4). The ~4-ps DADS for the NO<sub>2</sub>Y variant does not possess a clear 1,030-nm feature that would indicate B<sub>A</sub> production. Further DADS comparisons are given in SI Appendix, Figs. S39–S55.

Based on the DADS features and single-wavelength kinetics discussed in the previous two paragraphs, two P\* populations are present, which give rise to P+H<sub>A</sub>- via different mechanisms as opposed to simply reflecting the same process with differing rates (refer to SI Appendix, section \$3.2 for details). For all the variants, except NO<sub>2</sub>Y, data were fit globally using a minimal target analysis model with one P\* population decaying via a two-step ET process and the other via one-step superexchange ET (Fig. 4A and SI Appendix, Fig. S56A). Using this target model, we can reproduce differences in kinetics for each variant primarily by varying the relative amounts of the two P\* populations. As was seen from the DADS, the SADS also show a larger portion of the ~20-ps P\* population in the variants relative to WT (Fig. 4B and SI Appendix, Table S4). Additional effects include relatively small increases in P+HA- lifetimes, similar to the effects of other mutations, which are closer to BA than  $H_A$  and also assumed nonperturbative on  $H_A$  (Fig. 4B and SI Appendix, Table S4) (48). Not needed in our target analysis (SI Appendix, Fig. S56) is a 100- to 200-ps component for P\* internal conversion to the ground state (27, 49), consistent with all variants having a high quantum yield of P+HA- formation

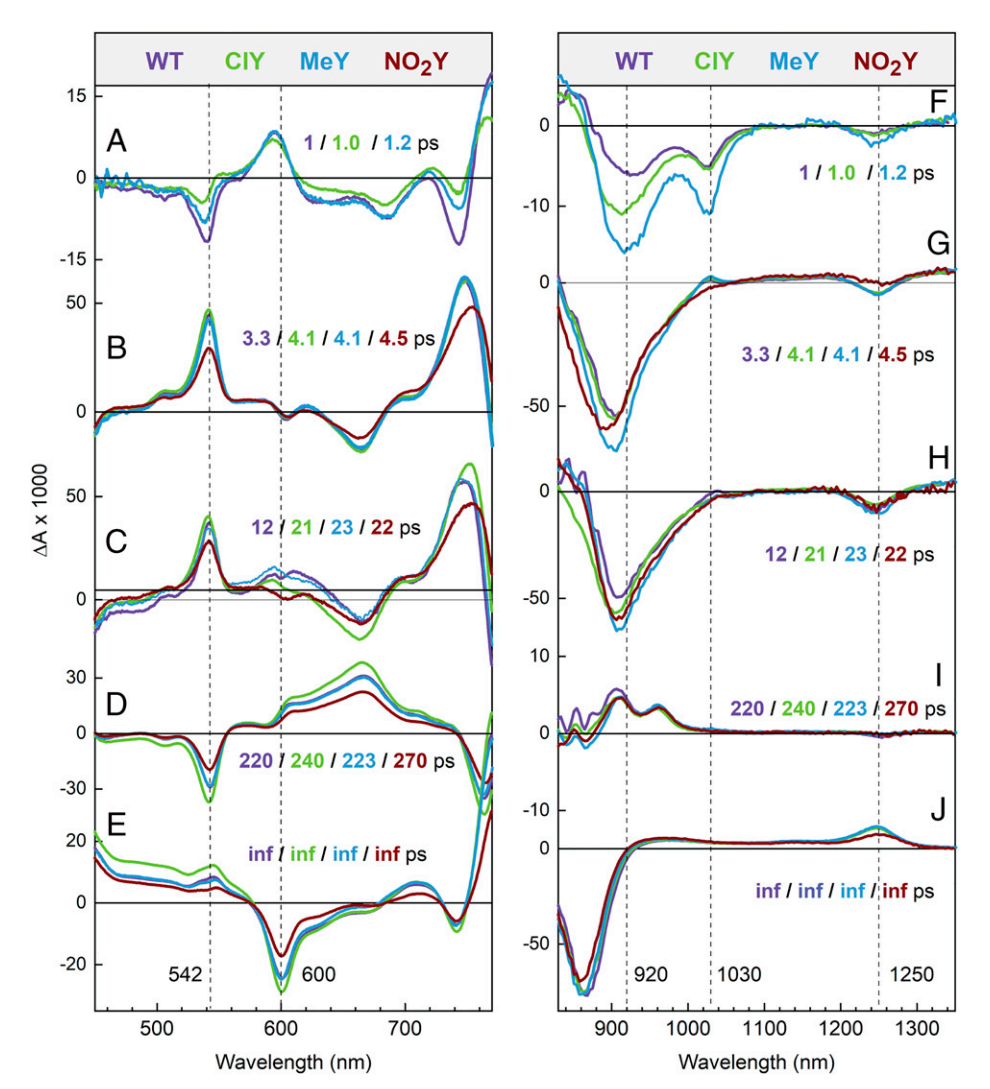
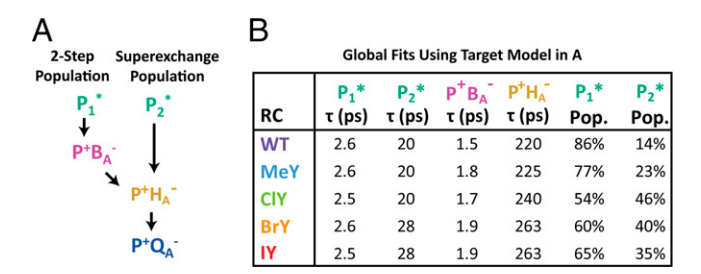


Fig. 3. Comparison of visible (A-E) and near-infrared (F-J) DADS for WT, CIY, MeY, and NO<sub>2</sub>Y. DADS for BrY and IY are very similar to that of CIY and are given in SI Appendix, Figs. S39–S43. Here "inf" refers to a component with an effectively infinite lifetime ( $\sim 10^8$  ps) to model charge-transfer states that do not decay over the duration of the experiment ( $10^4$  ps).

similar to WT. Raw TA spectra also support this high quantum yield. At probe times at which  $P^+H_A^-$  is the dominant species present (~25 ps) (*SI Appendix*, Figs. S63, S65, S67, S69, S71, and S73) and in the  $P^+H_A^-$  SADS (*SI Appendix*, Fig. S60), the bleaching magnitudes at 542 nm ( $H_A^-$ ) and 600 nm ( $P^*/P^+$ ) are



**Fig. 4.** Target analysis model and fits. (A) Kinetic model implemented for target analysis for WT and all variants except NO<sub>2</sub>Y (*SI Appendix*, Fig. 556). (*B*) Species decay lifetimes and RC population (Pop.) decaying through a two-step (P<sub>1</sub>\*) or superexchange (P<sub>2</sub>\*) ET pathway. While slight differences exist among RC variants for P<sub>1</sub>\* and P<sub>2</sub>\* decay time constants, data fit with a target analysis model with the same P\* decay lifetimes for all RC variants result in similar satisfactory SADS.

roughly equal, consistent with the similar extinction coefficients of these two  $H_A$  and P features in the chromophore basis spectra (50, 51). The 600-nm bleach at ~25 ps is also similar in magnitude to the 600 nm bleach for  $P^*$  at 0.5 ps (*SI Appendix*, Figs. S13A–S18A), again indicating high (essentially unity) conversion of  $P^* \to P^+H_A^-$  in both populations.

Except for the NO<sub>2</sub>Y variant, the TA data clearly support a model in which two-step and one-step superexchange ET both occur. This is less certain in the NO<sub>2</sub>Y variant, for which the 1,030-nm B<sub>A</sub> anion feature in the raw TA spectra (Fig. 3 and SI Appendix, Figs. S18, S36-S38) and in DADS/SADS (SI Appendix, Figs. S39, S54, S55, S57, and S72) is absent or substantially diminished. In the time evolution of the raw TA spectra in the 930- to 1,100-nm window (Fig. 5 and SI Appendix, Figs. S21–S38), WT and ClY/BrY/IY/MeY variants display B<sub>A</sub> anion band formation centered at 1,030 nm. NO<sub>2</sub>Y RCs, however, show little to no integrated area for the 1,030-nm transient feature above the baseline, which changes due to the background of  $P^*$  decay and growth of the  $H_A^-$  band at ~960 nm (Fig. 5). In overlays for NO<sub>2</sub>Y RCs in which baselining has not been performed (SI Appendix, Fig. S36), it is difficult to distinguish any 1,030-nm feature visually. It must also be noted that NO<sub>2</sub>Y RCs have 90% fidelity for replacement of tyrosine



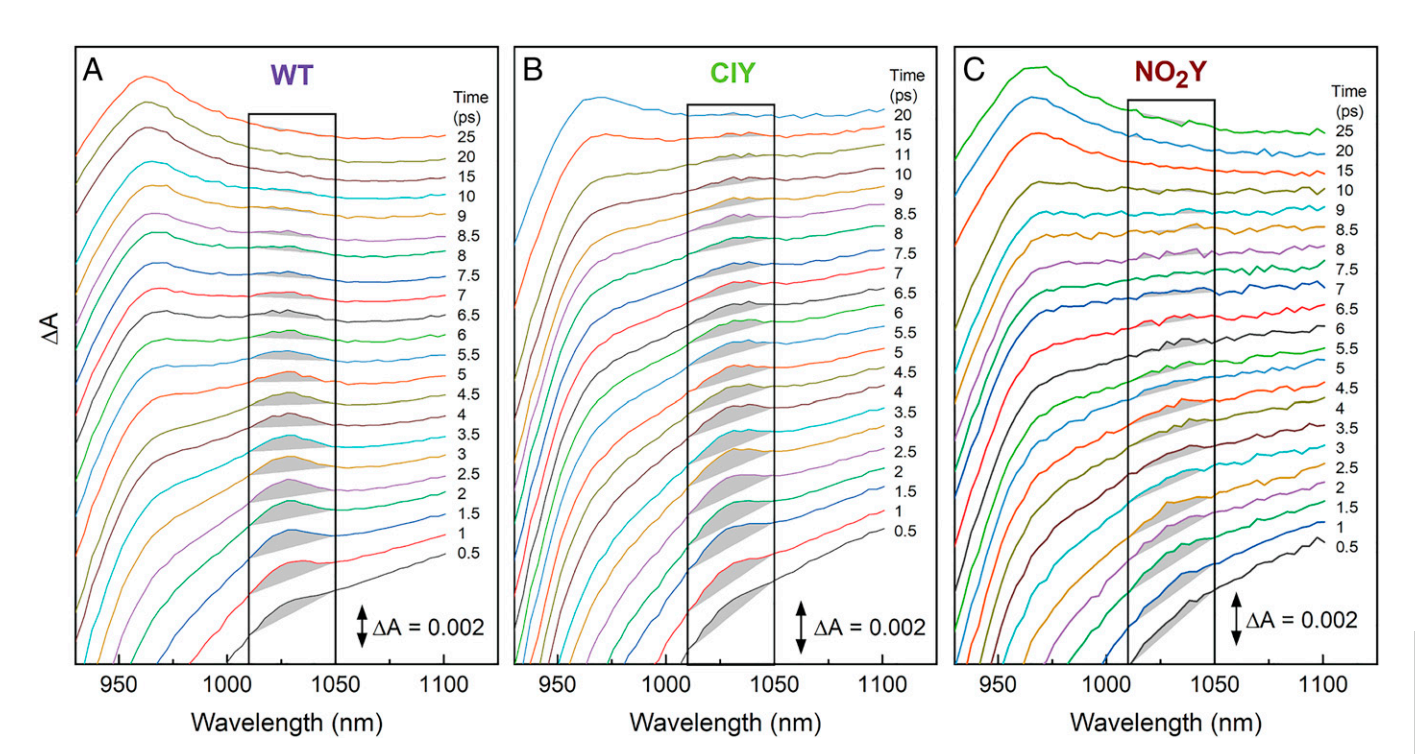


Fig. 5. Spectral evolution of the 930- to 1,130-nm TA spectrum at early times for (A) WT, (B) CIY, and (C) NO<sub>2</sub>Y RCs (BrY/IY/MeY variants shown in SI Appendix, Figs. S29, S32, and S35). The spectra are vertically offset from one another to best display the integrated area highlighted in gray (1,010 to 1,050 nm) of the 1,030-nm band of  $P^+B_A^-$  (SI Appendix, section S3.6). The gray integrated area for the 1,030-nm feature was separated from  $P^*$  and  $P^+H_A^-$  background via an applied linear baseline.

with NO<sub>2</sub>Y (SI Appendix, Fig. S2), and the 10% WT present would contribute a signal at 1,030 nm, further diminishing any 1,030-nm feature that might be attributed to NO<sub>2</sub>Y B<sub>A</sub><sup>-</sup>. The simplest explanation for the absent or significantly diminished 1,030-nm band in the NO<sub>2</sub>Y variant is that P\* decays directly to  $P^+H_A^-$  via one-step superexchange, without formation of  $P^+B_A^-$  as a discrete intermediate, in both  $P^*$  populations. Though the presence of a P\* population that undergoes fast ~5-ps superexchange ET alongside the previously identified ~12- to 20-ps superexchange population (15, 19, 52), has not been reported, we know of no reliable estimates that limit the rate of  $\hat{P}^* \to P^+ H_A^-$  superexchange ET in RCs. Alternatively, it is possible that P+B<sub>A</sub>- builds up to a much lesser extent in NO<sub>2</sub>Y RCs (compared to WT and the other variants) because the P<sup>+</sup>B<sub>A</sub><sup>-</sup> lifetime is much shorter. To account for the two possibilities, we modeled both scenarios for the NO<sub>2</sub>Y variant (SI Appendix, Figs. S54, S56, S72, and S73). Whichever model of ET is used, it is clear that primary ET in the NO<sub>2</sub>Y variant is affected more than primary ET in any other variant. Further mechanistic insight into ET in NO2Y and other RCs' ET requires information on how these RC variants change the free energy of P+BA-, as described in the following section (Energetic Characterization).

To be rigorous, it is important to note that superexchange ET involves a small degree of mixing of the  $P^+B_A^-$  virtual intermediate with the  $P^*$  reactant and  $P^+H_A^-$  product states when treated with first-order perturbation theory (53). This mixing would imply that some minor degree of  $B_A^-$  character could be manifest in spectral features, though significantly less than if  $P^+B_A^-$  were an actual intermediate. Computational insights into spectral contributions (e.g., at 1,030 nm) of a  $P^+B_A^-$  virtual intermediate in superexchange ET would be desirable.

As suggested by Niedringhaus et al. and others (14, 54), it is possible that the two-step versus superexchange mechanism dichotomy is too simplistic (55, 56). The difference in rates in the two  $P^*$  populations in  $NO_2Y$ , which may both involve some

form of superexchange ET, also suggests that the usual formulation of the superexchange mechanism itself may be too simplistic. Electronic interactions exist not just between the pair of bacteriochlorophylls in P but also involve the other RC chromophores. Thus, the true mechanism may be an admixture of two-step (i.e., sequential) ET and superexchange ET mechanisms, with the initial charge delocalized to varying extents over the  $B_{\rm A}$  and  $H_{\rm A}$  chromophores in the first ET intermediate depending on their relative energetics as discussed by Sumi et al. (55, 56). While we use limiting two-step versus superexchange models for tractability, further computational characterization of these more complex scenarios (55) and the limiting rates of superexchange ET in RCs are required to refine our analysis.

Energetic Characterization. To characterize the energetic perturbation of the tyrosine variants, we estimated the shift in  $P^*/P^+$ potential using P near-infrared absorption and P/P+ redox titrations and estimated the energetics of charge-separated intermediates using resonance Stark spectroscopy (Fig. 6). The room-temperature NIR Q<sub>y</sub> absorbance maxima of P shifted, at most, 15 nm (IY, 179 cm<sup>-1</sup> or 22 meV) compared to WT (*SI* Appendix, Figs. S74 and S76). Redox titrations show P redox potentials shift by, at most, 26 mV (IY, SI Appendix, Figs. S75 and S76). When changes in both P absorption and P redox potential are combined as performed previously (10) (SI Appendix, Fig. S76), RC variants at most disfavor P\* oxidation by  $18 \pm 5$  meV (MeY) relative to WT (Fig. 7 and SI Appendix, Fig. S76B). These P\* oxidation energetic changes are minimal when compared to the ~100- to 300-meV free-energy changes seen in certain mutants, which target P directly (10) and, given the proximity of residue M210 to P, are a surprising result, especially in the case of the NO<sub>2</sub>Y RC (Fig. 2).

There is no direct way to obtain information on the  $B_A/B_A^-$  reduction potential in situ. It is, however, possible to obtain information on the relative oxidation potentials of  $B_A$  in these

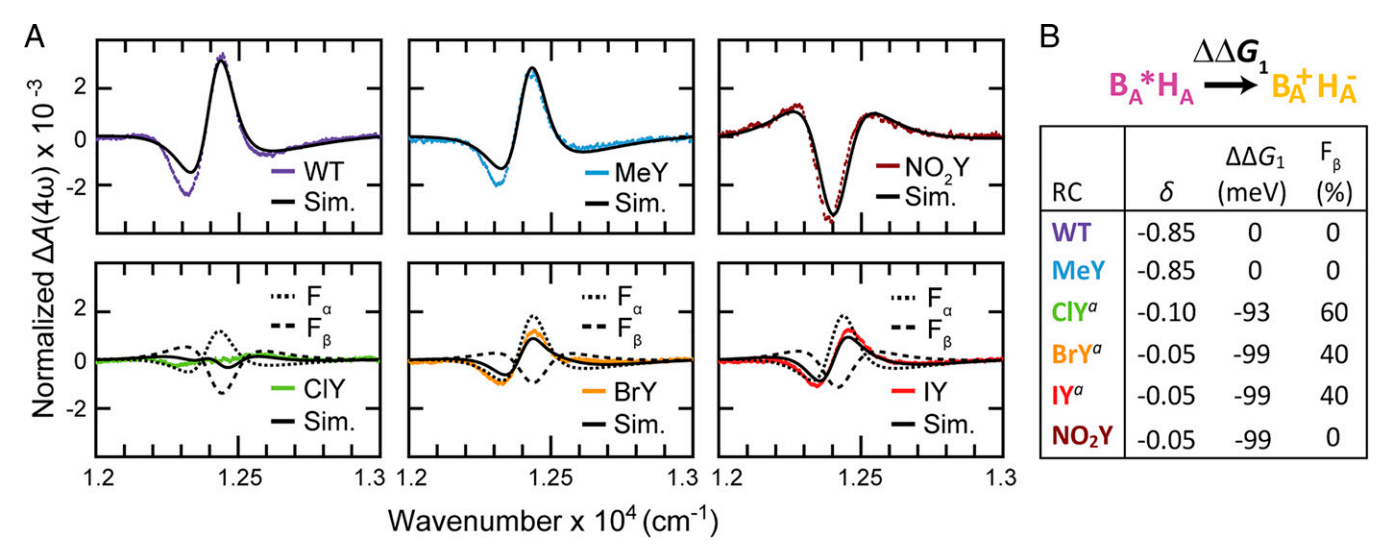


Fig. 6. Resonance Stark spectra for  $B_A$  and extracted energetics. (A) Resonance Stark spectra  $\Delta A$  determined for RC variants at the fourth harmonic (4ω) of the external electric field modulation frequency  $\omega$  (refer to *SI Appendix*, sections 55.1–55.4 for description and the corresponding  $6\omega$  spectra). Stark spectra are normalized to a field of 1 MV/cm (*SI Appendix*, section 55.3). (B) The values for the parameter,  $\delta$ , are extracted from the  $\Delta A(4\omega)$  and  $\Delta A(6\omega)$  Stark spectra in A and *SI Appendix*, section 55.4, respectively, and the change in  $\Delta G_1$  relative to WT ( $\Delta \Delta G_1$ ) is determined from  $\delta$  for the various RCs. Error in  $\Delta G_1$  is  $\sim$ 2 meV and is due to fitting error. The energetic process associated with  $\Delta \Delta G_1$  is depicted and labeled above the extracted Stark parameters. The superscript a next to CIY, BrY, and IY is used to note that halotyrosine Stark spectral fits require two fractions, which sum to 1; only  $\Delta \Delta G_1$  for the  $\beta$ -fraction ( $F_0$ ) is shown for halotyrosine RCs. The  $\alpha$ -fraction ( $F_0$ ) for halotyrosine RCs is comparable to WT in energetics.

variants using resonance Stark effect (RSE) spectroscopy. B<sub>A</sub>\* is coupled to B<sub>A</sub><sup>+</sup>H<sub>A</sub><sup>-</sup> whose energy is very sensitive to an applied electric field. We have described the RSE in detail in a series of papers (57-60) (SI Appendix, sections S5.1-S5.3 and Figs. \$78–\$80), discovered over the course of measurements of higherorder Stark effects for the RC and related pigments (61). Electronic Stark spectra ( $\Delta A$ ; field-on minus field-off absorbance) are typically obtained using lock-in detection at the second harmonic of the applied electric field modulation frequency, ω, giving  $\Delta A(2\omega)$ . For an isotropic immobilized sample,  $\Delta A(2\omega)$  is typically the second derivative of the absorption spectrum when the change in dipole moment between the ground and electronically excited states dominates the electrooptic parameters, as is the case for all the photosynthetic pigments in isolation (61). Data can also be extracted at higher even harmonics of the field modulation frequency (i.e.,  $4\omega$ ,  $6\omega$ , etc.);  $\Delta A(4\omega)$  is typically the fourth derivative of the absorption [or second derivative of  $\Delta A(2\omega)$ ],  $\Delta A(6\omega)$  is the sixth derivative, and so on. Surprisingly, when this experiment is performed for B<sub>A</sub>\* in the RC (but not for an isolated bacteriochlorophyll), a very different line shape dominates the higherorder spectra (57, 62), as the conventional derivatives become very small. Through a series of experiments, this effect has been linked to the driving force for the  $B_A^*H_A \rightarrow B_A^+H_A^-$  reaction  $(\Delta G_1)$ , and a comprehensive theory describing the unusual but expected line shapes of these RSEs has been developed (57-60). Since the Y(M210)F mutation dramatically affects the observed line shape and amplitude (60), we expected other changes in the vicinity of BA could affect the RSE spectra and provide information on the energetics of this process. We then use information on changes in the  $B_A/B_A^+$  potential to estimate effects on  $B_A/B_A^-$ , as described in detail in the following two paragraphs.

As shown in Fig. 64, it is immediately evident from the Stark spectra detected at the fourth harmonic of the modulation frequency,  $\Delta A(4\omega)$ , that MeY is quite similar to WT, that the halotyrosines show significantly reduced intensities compared to WT but are similar to each other, and that NO<sub>2</sub>Y has a very different line shape [refer to *SI Appendix*, Figs. S83–S89 for the sixth harmonic counterparts,  $\Delta A(6\omega)$ ]. We seek to extract the change in driving force of an RC variant relative to WT,  $\Delta \Delta G_1$ , encoded in the change in  $\delta$  (refer to Eq. S22 in *SI Appendix*,

section S5.3 for definition), from these line shapes (Fig. 6B). As performed previously (60), this energetic determination assumes that WT and all RC variants have the same homogeneous and inhomogeneous line widths for BA (and for BB) and identical reorganization energies for the pertinent chargetransfer process (SI Appendix, section S5.3). This is based on previous work showing that the choice of homogeneous and inhomogeneous line width does not appreciably affect fitting and derived parameters (59, 60); the combined effects from these parameters simply recapitulate the line shape of B without an applied external field. Only one set of physically reasonable ET parameters (i.e., single fractional component fits) is required to reproduce the line shapes and magnitudes of the Stark spectra for WT, MeY, and NO<sub>2</sub>Y. As expected, the introduction of the weakly electron-donating methyl group barely perturbs  $\Delta G_1$ , while the strongly electron-withdrawing nitro group lowers the energetics of  $B_A^*H_A \rightarrow B_A^+H_A^-$  by  $\sim 100$  meV (Fig. 6B). The halotyrosine variants fail to conform to the one-fraction fit strategy; they give rise to unsatisfactory fits and/or require unphysically small charge-transfer distances\* inferred from the diminished magnitude in Stark spectra (Fig. 6A and SI Appendix, Figs. S86-S89) and inconsistent with the invariant interchromophoric distances between BA and HA observed in the X-ray structures across all variants (SI Appendix, Table S3). Instead, a second fraction with a second set of ET parameters is required. One reasonable origin for these two fractions in halotyrosine RCs is the two halogen orientations modeled in the crystal structures (Fig. 2); only one orientation is observed for WT, MeY, and NO2Y, and a singlefraction fit to Stark spectra is sufficient for these samples. To deconvolve the underlying two fractions from the Stark spectra of halogenated RCs, we assume that the fraction that corresponds to the crystallographic population with the halogen

<sup>\*</sup>Short distances ranged from 7.0 Å/f to 8.2 Å/f as opposed to the 9.5-Å/f to 13.1-Å/f distances determined for RCs previously. Here, f is a local field factor, which arises because the applied electric field is different from the field experienced by the chromophore, and distances that are determined via resonance Stark spectroscopy contain this factor. The factor f is greater than 1 and considered constant for different RCs (refer to S/Appendix, sections 55.2–55.4 for further discussion).

atom pointing away from BA possesses WT-like energetics ( $\alpha$ -fraction). This is justified by the fact that halogens typically do not substantially perturb the electronic properties of aromatic rings even when directly attached to the  $\pi$ -system being spectroscopically probed (37, 42) and because MeY, which is similarly weakly perturbative, leaves  $\Delta G_1$  intact (Fig. 6B). By initializing fits with relative fractions from halogen occupancies in crystal structures, we reveal another fraction ( $\beta$  fraction;  $F_{\beta}$ in Fig. 6B) that showed energetics more similar to those in the  $NO_2Y$  counterpart ( $\Delta\Delta G_1 \sim -100$  meV; Fig. 6A and SI Appendix, Figs. S83–S89). The Stark features of the underlying populations (see WT and NO<sub>2</sub>Y as the limiting cases) tend to cancel, leading to diminished magnitudes in  $\Delta A(4\omega)$  for halogenated species. In ClY, a larger β-fraction contribution leads to near-complete Stark feature cancellation (Fig. 6A, green), while BrY and IY have a smaller contribution from the β-fraction and, consequently, less cancellation between Stark features from these two underlying fractions (Fig. 6A, orange and red). This degree of cancellation is largely consistent with the relative contributions of the two tyrosine rotamers as determined from crystal structures (Fig. 2). Refer to SI Appendix, section S5.4 for a detailed analysis of the modeling of these spectra.

The resonance Stark data indicate tyrosine perturbation has a significant impact on  $\Delta\Delta G_1$ . Since tyrosine modification is significantly farther from the  $H_A$  chromophore than it is to  $B_A$  or P (Fig. 1A and SI Appendix, Fig. S6A) and no structural changes are observed around  $H_A$  (SI Appendix, Fig. S6), we approximate the magnitude of  $\Delta\Delta G_1$  to be due primarily to an impact on the energetics of  $B_A$  oxidation. To better understand the origin of the observed TA kinetics, we require information on  $B_A$  reduction. We argue that  $\Delta\Delta G_1$  should be roughly equal to the  $-\Delta\Delta G$  for  $B_A \to B_A^-$  ( $\Delta\Delta G_3$ ) under the two following approximations: 1) The  $B_A^*$  energy,  $H_A$  reduction potential, and interchromophore coulombic interactions are not affected by tyrosine variant incorporation, as evidenced by the absence of structural changes and the insignificant energetic shifts in  $B_A$  absorbance maxima (SI Appendix, Figs. S74 and S76). 2) A general environmental effect of the mutations on the electronic structure of  $B_A$  would impact the propensities for  $B_A^+$  and  $B_A^-$ 

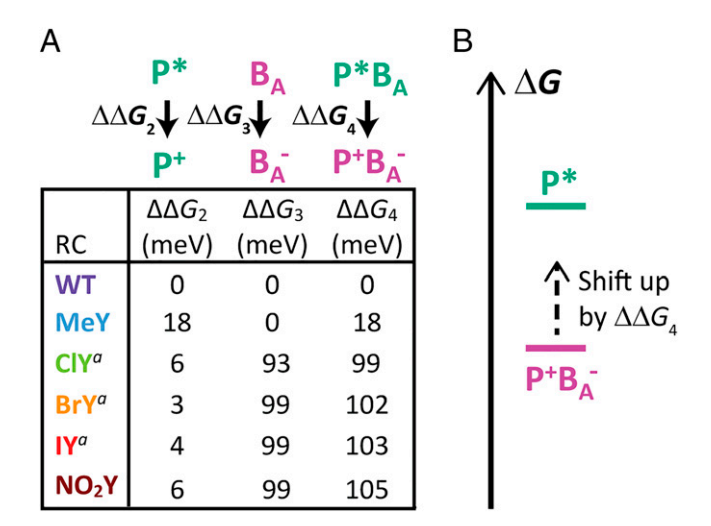


**Fig. 7.** (*A*) Relative change in energetics from WT for P\* oxidation ( $\Delta\Delta G_2$ ) and B<sub>A</sub> reduction ( $\Delta\Delta G_3$ ) from WT (refer to *SI Appendix*, Fig. S76 for  $\Delta\Delta G_2$  determination from NIR absorption and redox titration). We take  $\Delta\Delta G_2 + \Delta\Delta G_3 = \Delta\Delta G_4$  (where positive  $\Delta\Delta G_4$  values are destabilizing). Energetic processes are depicted and labeled above each column. The superscript a next to CIY, BrY, and IY is used to note that energetics for halotyrosine variants are shown only for the resonance Stark population (β-fraction) with non-WT B<sub>A</sub> redox energetics. (*B*) Diagram depicting the impact of  $\Delta\Delta G_4$ , where the free energy of P<sup>+</sup>B<sub>A</sub><sup>-</sup> is raised by  $\Delta\Delta G_4$ .

formation in an equal and opposite fashion (i.e., any electronic polarization effect can be neglected). In this regard, since the  $Q_y$  band of bacteriochlorins is dominated by the highest occupied molecular orbital (HOMO) to lowest unoccupied molecular orbital (LUMO) free energy gap (63), the HOMO and LUMO of  $B_A$  appear to be shifted similarly by the tyrosine variants because the  $Q_y$  band of  $B_A$  (and  $B_B$ ) at 800 nm is shifted at most  $\sim$ 3 nm ( $\sim$ 4 meV) among the RC variants (SI Appendix, Fig. S74). While these approximations may not be appropriate to characterize absolute energetics, they are reasonable to estimate changes in energetics relative to WT (refer to SI Appendix, section S4.4 for further discussion of these approximations).

When we combine the changes in energetics of P\* oxidation and  $B_A$  reduction, it is clear that the energetics of  $P^* \to P^+B_A^$ are significantly impacted in NO<sub>2</sub>Y and in one fraction (F<sub>6</sub>) of the halotyrosine variants, increasing the energetics of P+B<sub>A</sub>formation by over 100 meV relative to WT ( $\Delta\Delta G_4$  in Fig. 7). This is a significant change when considering P+BA- is estimated to be  $\sim$ 70 meV below P\* in energy in WT (Fig. 1B) (15, 19, 64, 65). In fact, in a recently published study performed at a high level of theory, Tamura et al. (22) indicate that P<sup>+</sup>B<sub>A</sub><sup>-</sup> is above P\* in energy in WT RCs, which, if correct, would mean 1) that the  $P^* \to P^+ B_A^- \to P^+ H_A^-$  two-step process would not occur, and 2) that an ~100-meV energetic increase would be even more significant. Comparing WT  $\rightarrow$  MeY  $\rightarrow$  halotyrosine RCs, as the energetics of  $P^+B_A^-$  formation ( $\Delta\Delta G_4$ ) increases (Fig. 7), so too does the amount of ~20-ps superexchange population observed in TA global analysis (Fig. 4B and SI Appendix, Table S4). This would match the smaller energetic dependence of the rate constant for P+BA- formation in the superexchange mechanism compared to the rate constant in the two-step pathway (53), as the former mechanism is less disfavored than the latter by the increased P+BA- energy. For both models used for NO<sub>2</sub>Y ET (SI Appendix, Fig. S56), there is also an increase in the ~20-ps P<sub>2</sub>\* population relative to WT (SI Appendix, Fig. S72 and Tables S4 and S5), similar to the other RC variants (*SI Appendix*, Table S4).

As stated earlier, the 1,030-nm B<sub>A</sub><sup>-</sup> feature is absent or significantly diminished for NO<sub>2</sub>Y RCs (Fig. 5). In the following, we reevaluate whether two-step or superexchange ET is occurring in the context of resonance Stark spectroscopy data and other kinetic and structural characterization. The NO<sub>2</sub>Y X-ray structure shows that the nitro group is significantly closer to P and B<sub>A</sub>, so it is unlikely that the H<sub>A</sub>/H<sub>A</sub><sup>-</sup> reduction potential is significantly affected (Figs. 1A and 2 and SI Appendix, Fig. S64). Past studies indicate P<sup>+</sup>B<sub>A</sub><sup>-</sup> decay is already energetically barrierless in WT (5, 66), so raising the free energy of P<sup>+</sup>B<sub>A</sub><sup>-</sup> while minimally affecting P+H<sub>A</sub>- free energy would decrease the rate of P<sup>+</sup>B<sub>A</sub><sup>-</sup> decay in a two-step mechanism. NO<sub>2</sub>Y RCs are like WT and other variants with regard to interchromophoric distances and other environmental features (SI Appendix, Table S3), but resonance Stark spectroscopy on B<sub>A</sub> indicates that the coupling between B<sub>A</sub>\* and B<sub>A</sub>+H<sub>A</sub> is smaller for NO<sub>2</sub>Y RCs (and every RC variant) relative to WT (SI Appendix, Table S7). This would suggest that if electronic coupling between P<sup>+</sup>B<sub>A</sub><sup>-</sup> and P<sup>+</sup>H<sub>A</sub><sup>-</sup> is changing, it also decreases (the electron transfers between the same set of molecular orbitals), which would further decrease the rate of P<sup>+</sup>B<sub>A</sub><sup>-</sup> decay. Because the P\* decay rate (i.e., P+B<sub>A</sub><sup>-</sup> formation rate) is unambiguous at 924 nm and only decreases modestly from a 3-ps lifetime in WT to 4.5 ps in NO<sub>2</sub>Y RCs (SI Appendix, Table S5), a decrease in P<sup>+</sup>B<sub>A</sub><sup>-</sup> decay rate would lead to increased P<sup>+</sup>B<sub>A</sub><sup>-</sup> buildup at 1,030 nm as opposed to the absent/diminished signal we observe (Fig. 5). Given the large increase in the free energy of P+B<sub>A</sub>- in NO<sub>2</sub>Y RCs, in the context of barrierless ET, decreased electronic coupling, and the absent/diminished 1,030-nm feature (made smaller by the 10% WT contribution, which must be discounted), it does not appear that two-step ET

is occurring in NO2Y RCs, and, instead, the population normally undergoing two-step ET is more likely a superexchange pathway. The P\* population with a ~5-ps superexchange ET alongside the ~20-ps population more commonly identified as a superexchange population may reflect the relative energy denominators for electronic mixing in superexchange that depend on the relative energies for P+B<sub>A</sub>-, P+H<sub>A</sub>- and P\*. The absence of this change in mechanism (the predominant loss of a two-step process) in halotyrosine RCs may be due to either or both of the following two effects: 1) only one fraction of halotyrosine RCs experience this large increase in energetics as evidenced by the two fractions observed from Stark spectroscopy; and 2) the RC fraction in which energetics are perturbed (Figs. 6 and 7) appears correlated with the fraction with the halogen <3.5 Å from the Mg<sup>2+</sup> (Fig. 2). Resonance Stark data for B<sub>A</sub> indicates that, as in NO<sub>2</sub>Y RCs, the coupling between P<sup>+</sup>B<sub>A</sub><sup>-</sup> and P+HA has likely decreased in halotyrosine RCs (SI Appendix, Table S7), and it is possible that other interchromophoric interactions in halotyrosine RCs are changing that we cannot experimentally assess. It is important to note that while we attempt to rationalize all experimental observations, ultimately, our models (and models of others in the field) are likely incomplete. For this reason, we have presented extensive documentation for all aspects of the data to encourage more sophisticated analyses.

#### Discussion

In this study, we have made a series of membrane protein complexes with site-specifically incorporated ncAAs. Within this series of pseudo-C2 symmetric proteins, we systematically vary one structural feature of an important symmetry-breaking amino acid, Tyr M210. In each tyrosine analog, the tyrosine's electrostatic nature is altered with different electron-donating and electron-withdrawing substituents at the *meta*-position, which modulates the tyrosine hydroxyl's interaction (29, 30, 67) with the B<sub>A</sub> chromophore via induction. We then utilize three distinct techniques, X-ray crystallography, TA spectroscopy, and resonance Stark spectroscopy, to determine structural information, ET kinetics, and the energetics relevant to primary ET. The collective information from these three distinct techniques helps to rationalize the consequences of our tyrosine analog incorporation.

Structural analysis indicates none of these tyrosine variants caused measurable structural perturbation (i.e., nuclear displacement) of other protein residues, cofactors, or electron donors and acceptors (*SI Appendix*, Figs. S4–S6 and Table S3). Consequently, interchromophoric interactions and chromophore molecular orbital overlap(s) should be relatively unaffected by tyrosine perturbation. This said, resonance Stark spectroscopy suggests electronic coupling(s) at least between P<sup>+</sup>B<sub>A</sub><sup>-</sup> and P<sup>+</sup>H<sub>A</sub><sup>-</sup> decreases for all RC variants, perhaps highlighting the importance of local interactions and small distance changes, which we cannot experimentally resolve.

Stark spectroscopy indicates the energetics of ET involving  $B_A$  are impacted significantly in halotyrosine ( $\beta$ -fraction) and  $NO_2Y$  RCs ( $\sim$ 100 meV, Figs. 6 and 7), while redox titrations and absorbance spectra indicate the effects on P\* oxidation are relatively minor ( $\leq$ 18 meV, Fig. 7). Only halotyrosine RCs require two conformers in crystallography and two energetic fractions for resonance Stark spectroscopy, but all RCs require two P\* populations to fit kinetic data; because of this observation, we only directly relate the resonance Stark fractions and the crystallographic conformations of halotyrosine RCs. Unlike in past studies (4, 10, 19, 48, 68), our energetic approach is a purely experimental estimate for the environmentally tuned energetics of  $P^+B_A^-$  formation. These estimations are at least

qualitative and are treated in this study as semiquantitative values. For discussion regarding potential structural origins of  $P^+B_A^-$  destabilization in MeY, NO<sub>2</sub>Y, and halotyrosine RCs, refer to *SI Appendix*, section S4.5.

As these RC variants exhibit increasingly disfavored  $P^+B_A^-$  formation energetically (Fig. 7), an increased proportion of the  $P^*$  population appears to decay by ET directly to  $H_A$  via a ~20-ps superexchange mechanism (e.g., no  $P^+B_A^-$  intermediate) (Fig. 4) based on DADS/SADS and an ET competition model proposed previously (19). With our introduction of amber suppression into *R. sphaeroides*, we hope to site-specifically introduce ncAAs containing nitrile vibrational probes (36, 69–71), which can act as true ET spectators whose response will not be obfuscated by interchromophoric electronic coupling or electronic absorption shifts from the formation and decay of charged intermediates.

Despite the significant energetic impact of some ncAAs and the impact on electronic coupling, no tyrosine modification made an order of magnitude impact on the overall rate (5, 10, 31, 72) or yield (27) of ET, highlighting the robust nature of the RC's protein design (1, 4-11). This small overall effect may be a consequence of this dual-mechanism model, in which the superexchange mechanism is acting as an alternative functional pathway for ET as previously proposed in the literature (19) through a lowered sensitivity to energetic changes of the P<sup>+</sup>B<sub>A</sub><sup>-</sup> intermediate. Without this additional pathway for ET, ET yield would likely decrease significantly following NO<sub>2</sub>Y introduction at M210 due to the increased amount of RC population possessing a P+BA- state higher in free energy than P\* and due to the decreased electronic coupling between P+BA- and P+HA-. Clearly, the tyrosine at M210 is not the only stabilizing factor for A branch ET. Multiple protein features contribute to overall RC function (20) and disfavor B-branch ET (15, 26, 27, 73). That said, the tyrosine at M210 is important for tuning the mechanism to be one of two-step ET in WT. This is highlighted by the NO<sub>2</sub>Y RC, in which the increase in a slow P\* population relative to WT is accompanied by the (near) absence of a 1,030-nm feature associated with B<sub>A</sub> anion formation (Fig. 5 and SI Appendix, Figs. S21-S38) indicating a change in ET mechanism. Given the specificity and efficiency of two-step ET in bacterial RCs, a tyrosine or phenol, which interacts with an electron donor and acceptor, as does the tyrosine at M210, may be helpful to encourage charge transfer and develop or improve other synthetic catalysts (74-76) and enzymes (77, 78). Further research on this model for photoinduced charge transfer with tools such as amber stop codon suppression will likely continue to enhance our understanding of how specific protein interactions are relevant to obtaining specific ET products, a key tenet of any catalysis and crucial to understanding ultrafast ET in the RC.

#### **Materials and Methods**

For a full description of methods utilized in this work, refer to SI Appendix. Briefly, RC variants were prepared via introduction of amber suppression machinery (with modifications) into R. sphaeroides (35, 36, 38), and protein expression was performed as described previously (SI Appendix, sections \$1. 1-S1.4) (36, 79). Fidelity of ncAA incorporation was assessed via LC-MS (36) (S/ Appendix, section S2.1). RC crystals were obtained via the hanging drop method, and room-temperature crystal structures were obtained using the Russi et al. procedure (SI Appendix, sections \$2.1-\$2.3) (80). TA measurements were acquired with a 1-KHz amplified Ti:Sapphire laser (Spectra Physics) coupled to Helios and EOS detection spectrometers (Ultrafast Systems) following previous methodology (15) (SI Appendix, section S3.1). Single-wavelength fits were performed using OriginLab, and global analysis was performed with CarpetView (Light Conversion) or SurfaceXplorer (Ultrafast Systems) (S/ Appendix, sections \$3.2-\$3.11). Redox titrations were done utilizing a potassium ferrocyanide/ferricyanide redox couple (SI Appendix, sections S4.2) (31). All resonance Stark spectroscopy was performed at 77K (37, 60) with the Stark

signal  $\Delta I$  (4 $\omega$ ) and  $\Delta I$  (6 $\omega$ ) detected at the fourth (4 $\omega$ ) and sixth harmonic (6 $\omega$ ), respectively, of the applied alternating current (AC) field (SI Appendix, sections S5.2), and the analysis was discussed extensively throughout SI Appendix, sections \$5.1-\$5.5.

Data Availability. X-ray crystal structures have been deposited in the PDB [7MH9 (81), 7MH8 (82), 7MH3 (83), 7MH4 (84), and 7MH5 (85)]. All other study data are included in the article and/or SI Appendix.

ACKNOWLEDGMENTS. J.B.W. was supported by a Stanford Center for Molecular Analysis and Design Fellowship. C.-Y.L. was supported by a Kenneth and Nina Tai Stanford Graduate Fellowship and the Taiwanese Ministry of

- 1. W. Parson, A. Warshel, "Mechanism of charge separation in purple bacterial reaction centers" in The Purple Phototrophic Bacteria, C. N. Hunter, F. Daldal, M. C. Thurnauer, J. T. Beatty, Eds. (Springer, 2009), pp. 356-377.
- 2. C. A. Wraight, R. K. Clayton, The absolute quantum efficiency of bacteriochlorophyll photooxidation in reaction centres of Rhodopseudomonas spheroides. Biochim. Biophys. Acta 333, 246-260 (1974).
- 3. R. K. Clayton, T. Yamamoto, Photochemical quantum efficiency and absorption spectra of reaction centers from Rhodopseudomonas sphaeroides at low temperature. Photochem. Photobiol. 24, 67-70 (1976).
- 4. L. M. P. Beekman et al., Primary electron transfer in membrane-bound reaction centers with mutations at the M210 position. J. Phys. Chem. 100, 7256-7268
- 5. V. Nagarajan, W. W. Parson, D. Davis, C. C. Schenck, Kinetics and free energy gaps of electron-transfer reactions in Rhodobacter sphaeroides reaction centers. Biochemistry 32, 12324-12336 (1993).
- 6. U. Finkele, C. Lauterwasser, W. Zinth, K. A. Gray, D. Oesterhelt, Role of tyrosine M210 in the initial charge separation of reaction centers of Rhodobacter sphaeroides. Biochemistry 29, 8517-8521 (1990).
- 7. V. Nagarajan, W. W. Parson, D. Gaul, C. Schenck, Effect of specific mutations of tyrosine-(M)210 on the primary photosynthetic electron-transfer process in Rhodobacter sphaeroides. Proc. Natl. Acad. Sci. U.S.A. 87, 7888-7892 (1990).
- 8. E. T. Johnson et al., Effects of ionizable residues on the absorption spectrum and initial electron-transfer kinetics in the photosynthetic reaction center of Rhodobacter sphaeroides. Biochemistry 42, 13673-13683 (2003).
- 9. J. C. Williams et al., Effects of mutations near the bacteriochlorophylls in reaction centers from Rhodobacter sphaeroides, Biochemistry 31, 11029-11037 (1992).
- 10. A. L. M. Haffa et al.. The dependence of the initial electron-transfer rate on driving force in Rhodobacter sphaeroides reaction centers. J. Phys. Chem. B 106, 7376-7384 (2002).
- 11. S. Schenkl et al., Selective perturbation of the second electron transfer step in mutant bacterial reaction centers. Biochim. Biophys. Acta 1554, 36-47 (2002).
- 12. W. Zinth, J. Wachtveitl, The first picoseconds in bacterial photosynthesis-Ultrafast electron transfer for the efficient conversion of light energy. ChemPhysChem 6, 871-880 (2005).
- 13. Y. Kakitani, A. Hou, Y. Miyasako, Y. Koyama, H. Nagae, Rates of the initial two steps of electron transfer in reaction centers from Rhodobacter sphaeroides as determined by singular-value decomposition followed by global fitting. Chem. Phys. Lett. 492,
- 14. A. Niedringhaus et al., Primary processes in the bacterial reaction center probed by twodimensional electronic spectroscopy. Proc. Natl. Acad. Sci. U.S.A. 115, 3563-3568 (2018).
- 15. P. D. Laible et al., Switching sides-reengineered primary charge separation in the bacterial photosynthetic reaction center. Proc. Natl. Acad. Sci. U.S.A. 117, 865-871 (2020).
- 16. A. G. Yakovlev, A. Y. Shkuropatov, V. A. Shuvalov, Nuclear wave packet motion between P\* and P+BA- potential surfaces with a subsequent electron transfer to H(A) in bacterial reaction centers at 90 K. Electron transfer pathway. Biochemistry 41, 14019-14027 (2002).
- 17. C. Kirmaier, D. Holten, Evidence that a distribution of bacterial reaction centers underlies the temperature and detection-wavelength dependence of the rates of the primary electron-transfer reactions. Proc. Natl. Acad. Sci. U.S.A. 87, 3552-3556 (1990)
- 18. Y. Jia et al., Primary charge separation in mutant reaction centers of Rhodobacter capsulatus. J. Phys. Chem. 97, 13180-13191 (1993).
- 19. M. Bixon, J. Jortner, M. E. Michel-Beverle, A kinetic analysis of the primary charge separation in bacterial photosynthesis. Energy gaps and static heterogeneity. Chem. Phys. 197, 389-404 (1995).
- 20. M. R. Gunner, A. Nicholls, B. Honig, Electrostatic potentials in Rhodopseudomonas viridis reaction centers: Implications for the driving force and directionality of electron transfer. J. Phys. Chem. 100, 4277-4291 (1996).
- 21. W. W. Parson, Z. T. Chu, A. Warshel, Electrostatic control of charge separation in bacterial photosynthesis. Biochim. Biophys. Acta 1017, 251-272 (1990).
- 22. H. Tamura, K. Saito, H. Ishikita, Acquirement of water-splitting ability and alteration of the charge-separation mechanism in photosynthetic reaction centers. Proc. Natl. Acad. Sci. U.S.A. 117, 16373-16382 (2020).
- 23. M. Richter, B. P. Fingerhut, Coupled excitation energy and charge transfer dynamics in reaction centre inspired model systems. Faraday Discuss. 216, 72-93 (2019).
- 24. M. Saggu, S. D. Fried, S. G. Boxer, Local and global electric field asymmetry in photosynthetic reaction centers. J. Phys. Chem. B 123, 1527-1536 (2019).

Education. This work was supported by a grant from the NSF Biophysics Program to S.G.B. (MCB-1915727). K.M.F, D.H., and C.K. were supported by a grant from the US Department of Energy, Office of Basic Energy Sciences (DE-CD0002036). We thank Prof. Thomas Beatty and Dr. Daniel Jun at the University of British Columbia for their generous contribution of the RC plasmid vector (pIND4-RC) and sequence information. We thank Prof. Ryan Mehl and Dr. Joseph Porter for providing amber suppression (F4 and A7) gene sequences (SI Appendix, sections S1.1 and S1.2) as well as helpful discussion regarding NO<sub>2</sub>Y incorporation in a new bacterial host. We thank the Vincent Coates Foundation Mass Spectrometry Laboratory, Stanford University Mass Spectrometry, and particularly Theresa Laughlin for their support in performing the LC-MS in this study. We also thank Tom Carver of the Stanford Nano Shared Facilities for depositing nickel on Stark windows.

- 25. S. J. Robles, J. Breton, D. C. Youvan, Partial symmetrization of the photosynthetic reaction center. Science 248, 1402-1405 (1990).
- 26. N. P. Dylla et al., Species differences in unlocking B-side electron transfer in bacterial reaction centers. FEBS Lett. 590, 2515-2526 (2016).
- 27. J. I. Chuang, S. G. Boxer, D. Holten, C. Kirmaier, High yield of M-side electron transfer in mutants of Rhodobacter capsulatus reaction centers lacking the L-side bacteriopheophytin. Biochemistry 45, 3845-3851 (2006).
- 28. E. J. Bylina, C. Kirmaier, L. McDowell, D. Holten, D. C. Youvan, Influence of an aminoacid residue on the optical properties and electron transfer dynamics of a photosynthetic reaction centre complex, Nature 336, 182-184 (1988).
- 29. R. Alden, W. Parson, Z. Chu, A. Warshel, Orientation of the OH dipole of tyrosine (M)210 and its effect on electrostatic energies in photosynthetic bacterial reaction centers. J. Phys. Chem. 100, 16761-16770 (1996).
- 30. K. Kawashima, H. Ishikita, Energetic insights into two electron transfer pathways in light-driven energy-converting enzymes. Chem. Sci. (Camb.) 9, 4083-4092 (2018).
- 31. M. Saggu et al., Putative hydrogen bond to tyrosine M208 in photosynthetic reaction centers from Rhodobacter capsulatus significantly slows primary charge separation. J. Phys. Chem. B 118, 6721-6732 (2014).
- 32. A. Dumas, L. Lercher, C. D. Spicer, B. G. Davis, Designing logical codon reassignment -Expanding the chemistry in biology. Chem. Sci. (Camb.) 6, 50-69 (2015).
- 33. I. Drienovská, G. Roelfes, Expanding the enzyme universe with genetically encoded unnatural amino acids. Nat. Catal. 3, 193-202 (2020).
- 34. D. D. Young, P. G. Schultz, Playing with the molecules of life. ACS Chem. Biol. 13, 854-870 (2018).
- 35. H. S. Jang et al., Efficient site-specific prokaryotic and eukaryotic incorporation of halotyrosine amino acids into proteins, ACS Chem. Biol. 15, 562-574 (2020).
- 36. J. B. Weaver, S. G. Boxer, Genetic code expansion in rhodobacter sphaeroides to incorporate noncanonical amino acids into photosynthetic reaction centers. ACS Synth. Biol. 7, 1618-1628 (2018).
- 37. C.-Y. Lin, M. G. Romei, L. M. Oltrogge, I. I. Mathews, S. G. Boxer, Unified model for photophysical and electro-optical properties of green fluorescent proteins. J. Am. Chem. Soc. 141, 15250-15265 (2019).
- 38. J. J. Porter et al., Genetically encoded protein tyrosine nitration in mammalian cells. ACS Chem. Biol. 14, 1328-1336 (2019).
- 39. P. R. Pokkuluri et al., The structure of a mutant photosynthetic reaction center shows unexpected changes in main chain orientations and quinone position. Biochemistry 41, 5998-6007 (2002).
- 40. L. P. Hammett, The effect of structure upon the reactions of organic compounds. Benzene derivatives. J. Am. Chem. Soc. 59, 96-103 (1937).
- 41. J. Jover, R. Bosque, J. Sales, Neural network based QSPR study for predicting pKa of phenols in different solvents. QSAR Comb. Sci. 26, 385-397 (2007)
- 42. M. G. Romei, C.-Y. Lin, I. I. Mathews, S. G. Boxer, Electrostatic control of photoisomerization pathways in proteins, Science 367, 76-79 (2020).
- 43. Y. Wu, S. D. Fried, S. G. Boxer, Dissecting proton delocalization in an enzyme's hydrogen bond network with unnatural amino acids. Biochemistry 54, 7110-7119 (2015).
- 44. P. Hamm et al., Subpicosecond emission studies of bacterial reaction centers. Biochim. Biophys. Acta Bioenerg. 1142, 99-105 (1993).
- 45. J. Zhu, I. H. M. van Stokkum, L. Paparelli, M. R. Jones, M. L. Groot, Early bacteriopheophytin reduction in charge separation in reaction centers of Rhodobacter sphaeroides. Biophys. J. 104, 2493-2502 (2013).
- 46. I. H. M. van Stokkum, D. S. Larsen, R. van Grondelle, Global and target analysis of time-resolved spectra. Biochim. Biophys. Acta Bioenerg. 1657, 82-104 (2004).
- 47. K. M. Faries et al., Manipulating the energetics and rates of electron transfer in Rhodobacter capsulatus reaction centers with asymmetric pigment content. J. Phys. Chem. B 121, 6989-7004 (2017).
- 48. P. Huppman et al., Kinetics, energetics, and electronic coupling of the primary electron transfer reactions in mutated reaction centers of Blastochloris viridis. Biophys. J. 82. 3186-3197 (2002).
- 49. C. Kirmaier et al., Comparison of M-side electron transfer in Rb. sphaeroides and Rb. capsulatus reaction centers. J. Phys. Chem. B 106, 1799-1808 (2002).
- 50. J. Fajer, D. C. Borg, A. Forman, D. Dolphin, R. H. Felton, Anion radical of bacteriochlorophyll. J. Am. Chem. Soc. 95, 2739-2741 (1973).
- 51. J. Fajer, D. C. Brune, M. S. Davis, A. Forman, L. D. Spaulding, Primary charge separation in bacterial photosynthesis: Oxidized chlorophylls and reduced pheophytin. Proc. Natl. Acad. Sci. U.S.A. 72, 4956-4960 (1975).

- 52. A. A. Zabelin, A. M. Khristin, V. A. Shkuropatova, R. A. Khatypov, A. Y. Shkuropatov, Primary electron transfer in Rhodobacter sphaeroides R-26 reaction centers under dehydration conditions. Biochim. Biophys. Acta Bioenerg. 1861, 148238 (2020).
- 53. B. P. Paulson, J. R. Miller, W.-X. Gan, G. Closs, Superexchange and sequential mechanisms in charge transfer with a mediating state between the donor and acceptor. J. Am. Chem. Soc. 127, 4860-4868 (2005).
- 54. T. Kondo et al., Cryogenic single-molecule spectroscopy of the primary electron acceptor in the photosynthetic reaction center, J. Phys. Chem. Lett. 11, 3980-3986 (2020).
- 55. H. Sumi, T. Kakitani, Unified theory on rates for electron transfer mediated by a midway molecule, bridging between superexchange and sequential processes. J. Phys. Chem. B 105, 9603-9622 (2001).
- 56. K. Saito, H. Sumi, Unified expression for the rate constant of the bridged electron transfer derived by renormalization. J. Chem. Phys. 131, 134101 (2009).
- 57. H. Zhou, S. G. Boxer, Probing excited-state electron transfer by resonance stark spectroscopy. 1. Experimental results for photosynthetic reaction centers. J. Phys. Chem. B 102. 9139-9147 (1998).
- 58. H. Zhou, S. G. Boxer, Probing excited-state electron transfer by resonance stark spectroscopy. 2. Theory and application. J. Phys. Chem. B 102, 9148-9160 (1998).
- 59. T. P. Treynor, S. G. Boxer, Probing excited-state electron transfer by resonance stark spectroscopy: 3. Theoretical foundations and practical applications, J. Phys. Chem. B 108, 13513-13522 (2004).
- 60. T. P. Treynor, C. Yoshina-Ishii, S. G. Boxer, Probing excited-state electron transfer by resonance stark spectroscopy: 4. Mutations near B<sub>L</sub> in photosynthetic reaction centers perturb multiple factors that affect B<sub>1</sub>\*  $\rightarrow$  B<sub>1</sub>+H<sub>1</sub>-. J. Phys. Chem. B 108, 13523-13535 (2004).
- 61. K. Lao, L. J. Moore, H. Zhou, S. G. Boxer, Higher-order stark spectroscopy: Polarizability of photosynthetic pigments. J. Phys. Chem. 99, 496-500 (1995).
- 62. S. G. Boxer, Stark realities. J. Phys. Chem. B 113, 2972-2983 (2009).
- 63. M. Gouterman, "Optical spectra and electronic structure of porphyrins and related rings" in The Porphyrins, D. Dolphin, Ed. (Academic Press, 1978), pp. 1–165.
- 64. A. Warshel, P. Sharma, M. Kato, W. Parson, Modeling electrostatic effects in proteins. Biochim. Biophys. Acta Proteins Proteom. 1764, 1647-1676 (2006).
- 65. S. Schmidt et al., Primary electron-transfer dynamics in modified bacterial reaction centers containing pheophytin-a instead of bacteriopheophytin-a. Spectrochim. Acta A Mol. Biomol. Spectrosc. 51, 1565-1578 (1995).
- 66. C. Lauterwasser, U. Finkele, H. Scheer, W. Zinth, Temperature dependence of the primary electron transfer in photosynthetic reaction centers from Rhodobacter sphaeroides. Chem. Phys. Lett. 183, 471-477 (1991).
- 67. M. Saggu, N. M. Levinson, S. G. Boxer, Experimental quantification of electrostatics in X-H···π hydrogen bonds. J. Am. Chem. Soc. 134, 18986–18997 (2012).
- 68. J. M. Hughes, M. C. Hutter, J. R. Reimers, N. S. Hush, Modeling the bacterial photosynthetic reaction center. 4. The structural, electrochemical, and hydrogen-bonding properties of 22 mutants of Rhodobacter sphaeroides. J. Am. Chem. Soc. 123, 8550-8563 (2001).
- 69. J. M. Tharp, Y. S. Wang, Y. J. Lee, Y. Yang, W. R. Liu, Genetic incorporation of seven ortho-substituted phenylalanine derivatives. ACS Chem. Biol. 9, 884-890 (2014).

- 70. S. K. Jha, M. Ji, K. J. Gaffney, S. G. Boxer, Direct measurement of the protein response to an electrostatic perturbation that mimics the catalytic cycle in ketosteroid isomerase. Proc. Natl. Acad. Sci. U.S.A. 108, 16612-16617 (2011).
- 71. L. Blankenburg et al., Following local light-induced structure changes and dynamics of the photoreceptor PYP with the thiocyanate IR label. Phys. Chem. Chem. Phys. 21, 6622-6634 (2019).
- 72. J. P. Allen, J. C. Williams, Relationship between the oxidation potential of the bacteriochlorophyll dimer and electron transfer in photosynthetic reaction centers. J. Bioenerg. Biomembr. 27, 275-283 (1995).
- 73. W. J. Coleman, E. J. Bylina, D. C. Youvan, "Reconstitution of photochemical activity in Rhodobacter capsulatus reaction centers containing mutations at tryptophan M-250 in the primary guinone binding site" in Current Research in Photosynthesis: Proceedings of the VIIIth International Conference on Photosynthesis, Stockholm, Sweden, August 6-11, 1989, M. Baltscheffsky, Ed. (Springer Netherlands, 1990), pp. 149-152.
- 74. J. Wang, T. Ding, K. Wu, Coulomb barrier for sequential two-electron transfer in a nano-engineered photocatalyst. J. Am. Chem. Soc. 142, 13934-13940 (2020).
- 75. G. E. M. Crisenza, D. Mazzarella, P. Melchiorre, Synthetic methods driven by the photoactivity of electron donor-acceptor complexes. J. Am. Chem. Soc. 142, 5461-5476
- 76. A. H. Proppe et al., Bioinspiration in light harvesting and catalysis, Nat. Rev. Mater. 5. 828-846 (2020)
- 77. K. F. Biegasiewicz et al., Photoexcitation of flavoenzymes enables a stereoselective radical cyclization. Science 364, 1166-1169 (2019).
- 78. D. J. Heyes et al., Photochemical mechanism of light-driven fatty acid photodecarboxylase. ACS Catal. 10, 6691-6696 (2020).
- 79. D. Jun, R. G. Saer, J. D. Madden, J. T. Beatty, Use of new strains of Rhodobacter sphaeroides and a modified simple culture medium to increase yield and facilitate purification of the reaction centre. Photosynth. Res. 120, 197-205 (2014).
- 80. S. Russi et al., Inducing phase changes in crystals of macromolecules: Status and perspectives for controlled crystal dehydration. J. Struct. Biol. 175, 236-243 (2011).
- 81. I. I. Mathews, J. Weaver, S. G. Boxer, Crystal structure of R. sphaeroides Photosynthetic Reaction Center variant; Y(M210)3-nitrotyrosine. The Protein Data Bank. https:// www.rcsb.org/structure/7MH9. Deposited 14 April 2021.
- 82. I. I. Mathews, J. Weaver, S. G. Boxer, Crystal structure of R. sphaeroides Photosynthetic Reaction Center variant; Y(M210)3-methyltyrosine. The Protein Data Bank. https:// www.rcsb.org/structure/7MH8. Deposited 14 April 2021.
- 83. I. I. Mathews, J. Weaver, S. G. Boxer, Crystal structure of R. sphaeroides Photosynthetic Reaction Center variant; Y(M210)3-chlorotyrosine. The Protein Data Bank. https:// www.rcsb.org/structure/7MH3. Deposited 14 April 2021.
- 84. I. I. Mathews, J. Weaver, S. G. Boxer, Crystal structure of R. sphaeroides Photosynthetic Reaction Center variant; Y(M210)3-bromotyrosine. The Protein Data Bank. https:// www.rcsb.org/structure/7MH4. Deposited 14 April 2021.
- 85. I. I. Mathews, J. Weaver, S. G. Boxer, Crystal structure of R. sphaeroides Photosynthetic Reaction Center variant; Y(M210)3-iodotyrosine. The Protein Data Bank. https://www.rcsb.org/structure/7MH5. Deposited 14 April 2021.

# **Supporting Information for**

# "Photosynthetic reaction center variants made via genetic code expansion show Tyr at M210 tunes the initial electron transfer mechanism"

Jared Bryce Weaver, <sup>1</sup> Chi-Yun Lin, <sup>1</sup> Kaitlyn M. Faries, <sup>2</sup> Irimpan I. Mathews, <sup>3</sup> Silvia Russi, <sup>3</sup> Dewey Holten, <sup>2</sup>

Christine Kirmaier,<sup>2</sup> Steven G. Boxer<sup>1,\*</sup>

# **Table of Contents**

S1	Sa	imple Preparation	S3
	S1.1	Plasmid Construction	S3
	S1.2	Prior Attempts at 3-Nitrotyrosine Incorporation	S9
	S1.3	Bacterial Growth and Protein Expression	. S10
	S1.4	Protein Purification	. S11
S2		Structural Characterization	. S14
	S2.1	Liquid chromatography–Mass Spectrometry (LC–MS)	. S14
	S2.2	Protein Crystallization	. S16
	S2.3	X-ray Data Collection and Structure Determination	. S17
	S2.4	Crystal Structure Overlays	. S19
S3		Transient Absorption (TA) Spectroscopy	. S25
	S3.1	Experimental Methods	. S25
	S3.2	Overview of TA Data and Analysis	. S26
	S3.3	Contour Profile Maps of Raw TA Data	. S31
	S3.4	Representative TA Spectra and Kinetic Profiles for Each Sample	. S38
	S3.5	Comparison of representative kinetic profiles/fits with mono- vs bi-exponential $P^*$ decay	. S46
	S3.6	Evolution of the NIR TA specta at early times for each sample	. S50
	S3.7	Comparison of DADS with specific time constants	. S76

<sup>&</sup>lt;sup>1</sup>Department of Chemistry, Stanford University, Stanford, California 94305, USA

<sup>&</sup>lt;sup>2</sup>Department of Chemistry, Washington University, St. Louis, MO 63130-4889, USA

<sup>&</sup>lt;sup>3</sup>Structural Molecular Biology, Stanford Synchrotron Radiation Lightsource, SLAC National Accelerator Laboratory, 2575 Sand Hill Road, Menlo Park, California 94025, USA

<sup>\*</sup>Correspondence to sboxer@stanford.edu

	S3.8	DADS summaries for each sample	S82
	S3.9	Comparison of SADS with specific time constants	S96
	S3.10	SADS summary for each sample	S104
	S3.11	Kinetic Analysis Summary Tables	S118
S4	Spe	ctroscopy and P/P <sup>+</sup> Redox Potential Determination	S121
	S4.1	298 K UV-vis-NIR Absorption and Data Analysis	S121
	S4.2	Redox Titration	S122
	S4.3	Redox Titration Data Analysis	S123
	S4.4	Energetic Approximations	S125
	S4.5	Characterization of Phenolic Dipoles	S126
S5	Reson	ance Stark Effect Spectroscopy	S128
	S5.1	Conceptual and Theoretical Framework for Resonance Stark Effect	S128
	S5.2	77K Electronic Stark Spectroscopy Experimental Procedure	S140
	S5.3	Stark Spectroscopy Data Analysis	S141
	S5.4	Stark Spectra and Simulated Fits of B	S154
	S5.5	Stark Spectra of P	S167
SA	Refe	prences	\$170

# S1 Sample Preparation

#### S1.1 Plasmid Construction

To genetically encode the ncAAs described in this manuscript in *R. sphaeroides* cells (Fig. S1), plasmids containing genes for the appropriate aaRS and tRNA were inserted into the plND4-RC vector inside gene cassettes which contained the proper *R. sphaeroides* transcriptional and translational control. As such, the plasmid plND4-RC-M210TAG-A7 was made where the tRNA and aaRS were placed in the same cassettes as the plasmid plND4-RC-M210TAG-HaloY1 whose construction has been previously described (1) but will be repeated here for clarity and comparison with the synthesis of plND4-RC-M210TAG-A7. These cassettes were inserted into the linearized vector plND4-RC using NEB-Hifi Assembly Master Mix where plND4-RC was linearized with restriction enzyme FastDigest Kpn2l from ThermoFisher.

#### Construction of pIND4-RC-M210TAG-HaloY1

 ${\tt CCCGCCTGATGAATGCTCATGCTAGCGAGCTCGCCGCTCATGGCGTTCTGTTGCCCGTCTCACTGGTGAAAAGAAA}$ 

Gene cassette inserts: PrrnB-HaloY-Tomega and PrrnB-tRNA (E.coli TrrnC)

PrrnB-HaloY1-Tomega: Promoter (PrrnB), RBS, HaloY aaRS, terminator (Tomega)

Vector: pIND4-RC-M210TAG

CTATCGCAAAGAAAGCGATGGCAAAGAACACCTGGAAGAATTCACCATGGTTGGCTTTAACCAAATGGGCAGCGG

#### P<sub>rrnB</sub>-tRNA (*E.coli* T<sub>rrnC</sub>): Promoter (P<sub>rrnB</sub>), tRNA, terminator (*E. coli* T<sub>rrnC</sub>)

#### pIND4-RC-M210TAG: H-Subunit, L-subunit, M-subunit

The pIND4-RC-M210TAG DNA sequence that follows is data provided by Professor Thomas Beatty and Dr. Daniel Jun at the University of British Columbia. The TAC (Tyr)  $\rightarrow$  TAG (Amber Stop) codon mutation at M210 is highlighted in turquoise.

GGCCGCGCAATTCGAGCTCGGTACCGACGTAGCCCAGCGCCGCCAGCTTGCAATTCGCGCTAACTTACATT AATTGCGTTGCGCTCACTGCCCGCTTTCCAGTCGGGAAACCTGTCGTGCCAGCTGCATTAATGAATCGGCCAACGC GCGGGGAGAGGCGGTTTGCGTATTGGGCGCCAGGGTGGTTTTTCTTTTCACCAGTGAGACGGGCAACAGCTGATT GCCCTTCACCGCCTGGCCCTGAGAGAGTTGCAGCAAGCGGTCCACGCTGGTTTGCCCCAGCAGCAGACAAATCCTG TTTGATGGTGGTTAACGGCGGGATATAACATGAGCTGTCTTCGGTATCGTCGTATCCCACTACCGAGATATCCGCA CCAACGCGCAGCCCGGACTCGGTAATGGCGCGCATTGCGCCCAGCGCCATCTGATCGTTGGCAACCAGCATCGCA GTGGGAACGATGCCCTCATTCAGCATTTGCATGGTTTGTTGAAAACCGGACATGGCACTCCAGTCGCCTTCCCGTT TTAATGGGCCCGCTAACAGCGCGATTTGCTGGTGACCCAATGCGACCAGATGCTCCACGCCCAGTCGCGTACCGTC TTCATGGGAGAAAATAATACTGTTGATGGGTGTCTGGTCAGAGACATCAAGAAATAACGCCGGAACATTAGTGCA GGCAGCTTCCACAGCAATGGCATCCTGGTCATCCAGCGGATAGTTAATGATCAGCCCACTGACGCGTTGCGCGAG AAGATTGTGCACCGCCGCTTTACAGGCTTCGACGCCGCTTCGTTCTACCATCGACACCACCACGCTGGCACCCAGTT GATCGGCGCGAGATTTAATCGCCGCGACAATTTGCGACGGCGCGTGCAGGGCCAGACTGGAGGTGGCAACGCCA ATCAGCAACGACTGTTTGCCCGCCAGTTGTTGTGCCACGCGGTTGGGAATGTAATTCAGCTCCGCCATCGCCGCTT CCACTTTTTCCCGCGTTTTCGCAGAAACGTGGCTGGCCTGGTTCACCACGCGGGAAACGGTCTGATAAGAGACACC GGCATACTCTGCGACATCGTATAACGTTACTGGTTTCACATTCACCACCCTGAATTGACTCTCTTCCGGGCGCTATC GGGGTTCCGCGCACATTTCCCCGAAAAGTGCCACCTGACGTCTAAGAAACCATTATTATCATGACATTAACCTATAA AAATAGGCGTATCACGAGGCCCTTTCGTCTTCACCTCGAGAAAATTTATCAAAAAGAGTGTTGACTTGTGAGCGGA TAACAATGATACTTAGATTCAATTGTGAGCGGATAACAATTTCACACATCTAGAATTAAAGAGGAGAAATTAACCA TGGTTGGTGTGACTGCTTTTGGAAACTTCGATCTGGCGTCGCTGGCGATCTATAGCTTCTGGATCTTCCTCGCGGG CCTGATCTACCTCCAGACCGAGACATGCGCGAGGGCTATCCGCTGGAGAACGAGGACGGCACCCCGGCCGC GAACCAGGGCCCGTTCCCGCTGCCGAAGCCCAAGACCTTCATCCTGCCCCACGGCCGCGCACGCTGACCGTACC

CGGCCCGGAAAGCGAAGACCGCCCGATCGCGCGCGCGGACGGCCGTCTCGGAAGGCTTCCCGCATGCGCCCA CGGGCGACCCGATGAAGGACGGCGTCGGCCCGGCCTCGTGGGTTGCCCGTGACCTGCCCGAACTCGACGGG CTGCCCGTCCGCGGCTGCGATCTCGAGATCGCGGGCAAGGTCGTGGACATCTCGGGTCGACATCCCCGAGCAGATG GCCCGCTTCCTCGAGGTCGAACTCAAGGACGGCTCGACCCGCCTCCTGCCGATGCAGATGGTCAAGGTCCAGTCG CGCTCCTCGAAGAGGACAAGATCTGCGGCTACGTCGCCGGCGGCCTGATGTATGCCGCCGCCGAAGCGCAAGTCG GTCGTGGCGGCGATGCTGGCCGAATACGTGCACCACCACCACCACTGAGGATCCGTTGGGCCGACTGCAAGC GGAGAGGGAAGCATGGCACTGCTCAGCTTCGAGCGAAAATATCGCGTGCCGGGGGGCACGCTGGTCGGCGGAA ACCTGTTCGACTTCTGGGTCGGCCCTTTCTATGTCGGCTTCTTCGGGGGTTGCGACGTTTTTCTTCGCGGCCCTGGGT ATCATTCTGATTGCCTGGAGTGCCGTACTCCAGGGTACCTGGAACCCCCAACTCATCTCTGTCTACCCGCCGGCCCT TGAATATGGCCTGGGAGGTGCACCCCTCGCAAAAGGCGGGCTGTGGCAGATCATCACGATCTGCGCCACTGGTGC  $\underline{CTTCGTCAGCTGGGCGCTGCGCGAAGTCGAAATCTGCCGTAAGCTGGGCATCGGGTACCACATCCC}GTTCGCCTTC$ GCGTTCGCCATCCTGGCCTACCTGACGCTGGTGCTGTTCCGCCCGGTGATGATGGGCGCCTGGGGCTATGCCTTCC CCTACGGGATCTGGACGCACCTCGACTGGGTGTCGAACACGGGCTACACCTACGGCAACTTCCACTACAACCCTGC CCACATGATCGCCATCTCGTTCTTCACGAACGCGCTGGCTCTGGCGCTGCACGGCGCCCTTGTGCTCTCCGCGG CCAACCCCGAGAAGGGCAAGGAAATGCGGACGCCGGATCACGAGGATACGTTCTTCCGCGATCTGGTCGGCTACT CGATCGGGACGCTCGGCATCCACCGCCTCGGCCTGCTGCTCTCGCTGAGCGCCGTCTTCTTCAGCGCCCTCTGCAT GAACATCCCGGGAGGCATCAATGGCTGAGTATCAGAACATCTTCTCCCAGGTCCAGGTCCGCGGACCGGCCGACC GCAACGCCCAGCTCGGCCCGATCTATCTCGGCTCGCCTCGGCGTCCTGTCCCTCTTCTCGGGCCTGATGTGGTTCTTC ACCATCGGGATCTGGTATCAGGCGGGCTGGAACCCGGCCGTCTTCCTGCGCGACCTGTTCTTCTCTCGC CGTTCTTCATGTTCGTCGCGGTCTGGTCCTGGTGGGGCCGCACCTATCTCCGCGCTCAGGCGCTGGGCATGGGCAA ACCTGTTCTACAACCCCTTCCACGGTCTCTCGATCGCCTTCCTCTAGGGGTCGGCCCTGCTCTTCGCGATGCACGGT GCGACCATCCTCGCGGTCTCCGGCTTCGGCGGCGAGCGGAGCTGGAGCAGATCGCCGACCGCGGGACGGCAGC GGAGCGGCCCCCTCTTCTGGCGCTGGACCATGGGTTTCAACGCCACGATGGAAGGCATCCACCGCTGGGCCAT CTGGATGGCGGTCCTCGTGACCCTCACCGGCGCATCGGCATCCTGCTCTCGGGCACGGTCGTGGACAACTGGTA CGTCTGGGGCCAGAACCACGGCATGGCGCCGCTGAACTGAAAGCTTAATTAGCTGAGCTTGGACTCCTGTTGATA GATCCAGTAATGACCTCAGAACTCCATCTGGATTTGTTCAGAACGCTCGGTTGCCGCCGGGCGTTTTTTATTGGTG AGAATCCAAGCTAGCTTGGCGAGATTTTCAGGAGCTAAGGAAGCTAAAATGGAGAAAAAAATCACTGGATATACC GACCGTTCAGCTGGATATTACGGCCTTTTTAAAGACCGTAAAGAAAAATAAGCACAAGTTTTATCCGGCCTTTATTC ACATTCTTGCCCGCCTGATGAATGCTCATCCGGAATTTCGTATGGCAATGAAAGACGGTGAGCTGGTGATATGGG ATAGTGTTCACCCTTGTTACACCGTTTTCCATGAGCAAACTGAAACGTTTTCATCGCTCTGGAGTGAATACCACGAC GATTTCCGGCAGTTTCTACACATATATTCGCAAGATGTGGCGTGTTACGGTGAAAACCTGGCCTATTTCCCTAAAG GGTTTATTGAGAATATGTTTTTCGTCTCAGCCAATCCCTGGGTGAGTTTCACCAGTTTTGATTTAAACGTGGCCAAT ATGGACAACTTCTTCGCCCCCGTTTTCACCATGCATGGGCAAATATTATACGCAAGGCGACAAGGTGCTGATGCCG CTGGCGATTCAGGTTCATCATGCCGTTTGTGATGGCTTCCATGTCGGCAGAATGCTTAATGAATTACAACAGTACT GCGATGAGTGGCAGGGCGGGCGTAATTTTTTTAAGGCAGTTATTGGTGCCCTTAAACGCCTGGGGTAATGACTC TCTAGCTTGAGGCATCAAATAAAACGAAAGGCTCAGTCGAAAGACTGGGCCTTTCGTTTTATCTGTTGTTGTCGG TGAACGCTCTCCTGAGTAGGACAAATCCGCCGCTAGGAGCTTGCGGCCCTGGCGTAATAGCGAAGAGGCCCGCAC CGATCGCCCTTCCCAACAGTTGCGCAGCCTGAATGGCGAATGCGATTTATTCAACAAAGCCGCCGTCCCGTCAAGT CAGCGTAATGCTCTGCCAGTGTTACAACCAATTAACCAATTCTGATTAGAAAAACTCATCGAGCATCAAATGAAAC TGCAATTTATTCATATCAGGATTATCAATACCATATTTTTGAAAAAGCCGTTTCTGTAATGAAGGAGAAAACTCACC

GAGGCAGTTCCATAGGATGGCAAGATCCTGGTATCGGTCTGCGATTCCGACTCGTCCAACATCAATACAACCTATT AATTTCCCCTCGTCAAAAATAAGGTTATCAAGTGAGAAATCACCATGAGTGACGACTGAATCCGGTGAGAATGGC CAAACCGTTATTCATTCGTGATTGCGCCTGAGCGAGACGAAATACGCGATCGCTGTTAAAAGGACAATTACAAACA GGAATCGAATGCAACCGGCGCAGGAACACTGCCAGCGCATCAACAATATTTTCACCTGAATCAGGATATTCTTCTA ATACCTGGAATGCTGTTTTCCCGGGGATCGCAGTGGTGAGTAACCATGCATCAGGAGTACGGATAAAATGCT TGATGGTCGGAAGAGGCATAAATTCCGTCAGCCAGTTTAGTCTGACCATCTCATCTGTAACATCATTGGCAACGCT ACCTTTGCCATGTTTCAGAAACAACTCTGGCGCATCGGGCTTCCCATACAATCGATAGATTGTCGCACCTGATTGCC CGACATTATCGCGAGCCCATTTATACCCATATAAATCAGCATCCATGTTGGAATTTAATCGCGGCTTCGAGCAAGA CGTTTCCCGTTGAATATGGCTCATAACACCCCTTGTATTACTGTTTATGTAAGCAGACAGTTTTATTGTTCATGATGA TATATTTTTATCTTGTGCAATGTAACATCAGAGATTTTGAGACACAACGTGGCTTTGTTGAATAAATCGAACTTTTG CTGAGTTGAAGGATCAGATCACGCATCTTCCCGACAACGCAGACCGTTCCGTGGCAAAGCAAAAGTTCAAAATCA CCAACTGGTCCACCTACAACAAAGCTCTCATCAACCGTGGCTCCCTCGAGGCTCCGCGCCCTCGATCCGACCGCCC AGAGTTTGCATAGTGTGCGCCATTCAGATACCTTCATGGCAGGCCCCACCGTGGATTTTGCTGTCATGGTTCGATTC ATCACGACGCCCGCAACGCCGACTGCACAGCGGCCCGCACCACGAACGCCTGCGCAGCAGGAAGCTGCGGCTGA ACTGAAGGCTGCGCGAACTGCCGAAGCAGCCCGCCTCGACACCCGGCGCAAGGTGGTGCTCGGGGGCGCGC TCCTGGCACTGGCAGAACGTGATGCAGCAGCAGCCGCGATGCTGGCCCGGCTGAAGCAGATGCTGACCCGCCCA GCAGATCGGAAGCTGTTCGCGGATCTACCCGATGGCTGACGGTGCAATCTTCCACCTCGATGTGCGCACGGTCAG CCTGACCCACGACTTCGCGCGCAAGCGGGGCGTCTTGACAACCTTCATCGCCGCCCCGGACGGCTGCGACTGGAT CACAGACAGGGACACGCTCTGGAACGCGGCTGAGGCGGCAGAGAAGCGCAAGAACAGCACCGTGGCCCGTGAG GGCGCAGCGGTTCGGGGTGGCCGTGGATGTGGCAATCCACGCAGCTTCGGGCGAGGGCGACCAGCGGAACCAT CACGCGCATTTGCTGACCACGACGCGCACGCACGGCCCGGACGGGCTGGGCGACAAGACCCGCGTTCTGGATGC GCCGCACAAAGCTCGGCCCGCGTCGATCACCGCCGCATAGCCGTGATCGCCGCCGATGCGCGGGCCGAGGCCGA GGCGCTGGAGAAACAGGCCAAAGCCGTCGAAACCCTGAACGCCAAGCCCGCCGACGCCGGGGGGGCTGTGGAAG GGCCTTGGCAGCGCCGCCCGCGCAATATGGGAAGGCGGCATGACCGCCCTCAAATCGACCGCCGAGACAGCCAA CGAGCTGCGGGAGAGGCCAACGAGCTGCGACAGAAGGCAGCCCGCTACACCCGCGCCACCGAACCTCACCACG GCCCCGTCCTGACGGCCTTCTTGCGGCGCATGGCTCCCGTCTGGGCGGAGCAGGCCAAGGCCGAGGAAGCCCGG AGAGCCGCGCAGGAGGCCGCACAGCGCGCACTGATGGCCGAGAGGGCTGAACAGGCCCGGAAGGCCAAGGAA GCCTCTGAGGCCGCTCGCCGGGCCGCTACGGCAGCGCGAGGAGGCCGAGGAAGCCCGCGAACGCTGCGCCCGCG AGGTGTTGCCGCTCATCCGCCGCCCGGCACGACCCGATCACCGCCGAAGTGATCAAGCGGGAGGGCATCGAC CTCGACCGCCCGACCAACAGGTGGCCCGCGACCCGATCTGGCTCATGGCCGGACGCCAAGATCAGGCGCACCCG GTCTGGCTGATCGTCCACGCCTACACCGCCGCGCGCGACAGGCACGCGAACCTGCTGGCGAGAATCGAAGCCAAA GATCCAGACCCACCGCCCGGCGGGATTGGGGCCGGCCGTCTGGACCCTGATCCACCCCCCATTCTCAGCAACTCC GAGCCAGCCAGAGGCGCTGGCTCGGGGCATCTGGACCCCCTTCCTCACCCCAAATTTTCACGAAAAAGGGGCCCCA GCCCTTCTTGTTCAATAAGTTCTATAAGTTCAGGCGAAAATCGCCTTTCATTTTCAATGGCTTGCGCGCCTATCGGG GAGAAATGGGGCCGCAAAAGGGAGAAATGGGGCCGCAAAAGGGAGAAATGGGGCCGATAGCGGCTGTTGACA GGGGGATATTTTGCCCCCTACATTTCTCCCCATGACAAAGACCACGCAAATCGCCGCTGATCGAGCCTATGACGAG GCCAAAACCGTGCTGCCGCAGAGGTGGCGCGGGGGGTCTACATGCGCAACGCCCCAGCCTCGCCGCCCTCAA GCTGATGCACCTGCTGATCGGTAAGGCGGGCGGGCGTATGGCCGAACCCATTCGGCACGAAATCCGCCTCTCAGA CATCCGCAAGATCGACGGGATGAAGAACCATGACAGGGCCAGCCTCACCCCCTTTTCGCGGAATTGTCGGCGGC TGTCCTGACCCATGATGACCCCGAAAAAATGGTCGTGACCATTGGCGGCTTGCTGGACTTCGCCCGCATCGACTAC CGCCACGAAGTCAGCAACGATCTGCTGGTGTCGTGGTATTTTGGCGGGGGCCTTCCGCGAGATGGCCGAGAAGTCC TGCCACTGGGCGATCCTCGACCGGCAGACCGTTTTTGCCCTGTCCAGCAAGTATTCGATCCTGCTGTTCCAGCACAT CGCCAGCCTCGTGAACCTCGATCACGTCGCCAGCAAGACCTTCACCGTGGCCGAACTGCGGGCCGTGCTAGGGGT GCCGCACGGAAAGATGGAGCGGTGGAACGACGTGAACCGCTTTGCGCTGACGCCCGCGATTGCCGAGATCAACC AGACCTCGCGCCTGATCCTGACCGCGACCCCGAACAAGATCGGGCGGACGGTCGCCAGCGTGACAATCACGTGG GCGGAGAAGCCTCCCGAGGGCAAGCAGGAAGCCAAGCGCGAACTGGACCGCCCCAAGGTGGGCCGAGAGGCGC GGCGCAACGGCTCAGCCGAGACCGTGGCGCGGGCCTTCCCGAGCTCGGGCAGCATCGAGTTCGATGACCACTGG AAGGCCCTCAAGCGGCGGCGGGCTGCAACATGGACAACACCATGATTGCCGAGAAGTTCCGGGCGTGGTGCGC CAGCAAGGGGCTTTCCCTCGACGGCCGAAACATCGAGCAGGCGTTCAGCAACTTCTGCGCCACAGTGGGCAAGGT CTGAGGCCGCCGCTGCCAGTGACCCGCCGCCGCCGACCGTGAGCGGGCCGCAGCCCTTCCAGCGCCGCCAA GAGGGCGGCAAGCCCCGGTCTGCCCCCTCGTCGCCCGCAAAGCGGGCAGGGGGCAGACCGGGGCGCTGGAACC ATGGTAAAGCATGTGGGGGCAGTCCAGCCGTCAATCCGCGCTCCGCACCACGGCGCCTCGAGCAACACCTTCTTC ACGAGGCAGACCTCTCGACGGAGTTCCACTGAGCGTCAGACCCCGTAGAAAAGATCAAAGGATCTTCTTGAGATC GAGCTACCAACTCTTTTTCCGAAGGTAACTGGCTTCAGCAGAGCGCAGATACCAAATACTGTTCTTCTAGTGTAGC CGTAGTTAGGCCACCACTTCAAGAACTCTGTAGCACCGCCTACATACCTCGCTCTGCTAATCCTGTTACCAGTGGCT GCTGCCAGTGGCGATAAGTCGTGTCTTACCGGGTTGGACTCAAGACGATAGTTACCGGATAAGGCGCAGCGGTCG GGCTGAACGGGGGGTTCGTGCACACAGCCCAGCTTGGAGCGAACGACCTACACCGAACTGAGATACCTACAGCG TGAGCTATGAGAAAGCGCCACGCTTCCCGAAGGGAGAAAGGCGGACAGGTATCCGGTAAGCGGCAGGGTCGGA ACAGGAGAGCGCACGAGGGAGCTTCCAGGGGGAAACGCCTGGTATCTTTATAGTCCTGTCGGGTTTCGCCACCTC TTACGGTTCCTGGCCTTTTGCTGGCCTTTTGCTCACATGTTCTTTCCTGCGTTATCCCCTGATTCTGTGGATAACCGT ATTACCGCCTTTGAGTGAGCTGATACCGCTCGCCGCAGCCGAACGACCGAGCGCAGCCGAGTCAGTGAGCGAGGA AGCGGAAGAAGCTCGCACATTCAGCAGCGTTTTTCAGCGCGTTTTCGATCAACGTTTCAATGTTGGTATCAACACC AGGTTTAACTTTGAACTTATCGGCACTGACGGTTACTGATTTTGAACTTTTGCTTTGCCACGGAACGGTCTGCGTTG TCGGGAAGATGCGTGATCTGATCCTTCAACTCAGCAAAAGTTCGCCAATACGCAAACCGCCTCTCCCCGCGCGTTG GCCGATTCATTAATGCAG

Protocol: The gene cassette inserts were ordered as IDT gBlocks Gene Fragments and were processed (1) such that the aaRS (HaloY) and tRNA gene cassettes had homologous overlap regions for each other and for the vector at the appropriate 5' and 3' end of the cassette. Then through linearizing the pIND4-RC vector with restriction enzyme Kpn2I (Thermo-Fisher), the vector and the aaRS and tRNA gene casesttes were ligated together with the NEBuilder® HiFi DNA Assembly Cloning Kit. In constructed plasmids, the orientation of the tRNA gene cassette is reversed with respect to the orientation of the aaRS gene cassette orientation as depicted in Fig. S1 Weaver *et al.* (1). Professor Ryan Mehl generously provided the plasmid pDule-haloTyrRS and plasmid sequence information, whose aaRS (C6) and tRNA sequence were implemented in pIND4-RC-M210TAG-HaloY1. Note that the aaRS used in pIND4-RC-M210TAG-HaloY1 has two additional mutations beyond those published by Jang *et al* (2): the threonine

at site 13 is mutated to alanine and the phenylalanine at site 82 is mutated to a leucine. While the effects of these two additional mutations are unclear, some sources indicate that T13A is detrimental to amber suppression efficiency (3, 4). Regardless, pIND4-RC-M210TAG-HaloY1 has been shown to produce experimentally tractable levels of amber suppression efficiency to spectroscopically characterize RC variants (1), so off-target mutations in this aaRS do not appear to be overly detrimental.

#### Construction of pIND4-RC-M210TAG-A7

Gene cassette inserts: PrrnB-A7-Tomega and PrrnB-tRNA (E.coli TrrnC)

Vector: pIND4-RC-M210TAG

PrrnB-A7-Tomega: Promoter (PrrnB), RBS, A7 NO<sub>2</sub>Y aaRS, terminator (Tomega)

CCCGCCTGATGAATGCTCATGCTAGCGAGCTCGCCGCTCATGGCGTTCTGTTGCCCGTCTCACTGGTGAAAAGAAA AACAACCCTGGCGCCGCTTCTTTGAGCGAACGATCAAAAATAAGTGGCGCCCCATCAAATTGTTACGGAGCCCAAA AAATCCGCTTGCGCCCGGGGCCGTCTGCTCCTAGAAACCGCTTCACCGAGACGAAGACCGGCAGCGCCGGACGG AGACGAGGGAGCGGATGACAGAAACGTCGGCCGCGACAATTGAAGATGAGGCGGACGGGATCGCTGGTTGTCT GCATCAACGGAGGTCCCCCATGATGGATAAAAAACCGCTGGATGTGCTGATTAGCGCGACCGGCCTGTGGATGA GCCGTACCGGCACCCTGCATAAAATCAAACATCATGAAGTGAGCCGCAGCAAAATCTATATTGAAATGGCGTGCG CTGCAAACGTTGCCGTGTGAGCGATGAAGATATCAACAACTTTCTGACCCGTAGCACCGAAAGCAAAAACAGCGT GAAAGTGCGTGTGGTGAGCGCCGAAAGTGAAAAAAGCGATGCCGAAAAGCGTGAGCCGTGCGCCGAAACCG CTGGAAAATAGCGTGAGCGCGAAAGCGAGCACCAACACCAGCCGTAGCGTTCCGAGCCCGGCGAAAAGCACCCC TGTCTCCGGAAGATAAAATTAGCCTGAACATGGCGAAACCGTTTCGTGAACTGGAAACGGAACTGGTGACCCGTC GTAAAAACGATTTTCAGCGCCTGTATACCAACGATCGTGAAGATTATCTGGGCAAACTGGAACGTGATATCACCAA ATTTTTTGTGGATCGCGGCTTTCTGGAAATTAAAAGCCCGATTCTGATTCCGGCGGAATATGTGGAACGTATGGGC ATTAACAACGACACCGAACTGAGCAAACAATTTTCCGCGTGGATAAAAAACCTGTGCCTGCGTCCGATGCTGGCCC CGACCCTGTATAACTATAGGCGTAAACTGGATCGTATTCTGCCGGGTCCGATCAAAATTTTTGAAGTGGGCCCGTG CTATCGCAAAGAAAGCGATGGCAAAGAACACCTGGAAGAATTCACCATGGTTGGCTTTAACCAAATGGGCAGCGG CTGCACCCGTGAAAACCTGGAAGCGCTGATCAAAGAATTCCTGGATTATCTGGAAATCGACTTCGAAATTGTGGG CGATAGCTGCATGGTGTATGGCGATACCCTGGATATTATGCATGGCGATCTGGAACTGAGCAGCGCGGTGGTGG GTCCGGTTAGCCTGGATCGTGAATGGGGCATTGATAAACCGTGGATTGGCCGGGGTTTTGGCCTGGAACGTCTGC TGAAAGTGATGCATGGCTTCAAAAACATTAAACGTGCGAGCCGTAGCGAAAGCTACTATAACGGCATTAGCACGA **ACCTGTAA**GATCCGGTGGATGACCTTTTGAATGACCTTTAATAGATTATTACTAATTAGTTAATTGGGGACCCTAGAG CCTGAGGTCGGGC

Prinb-trna (E. coli Trinc) - 2: Promoter (Prinb), trna, terminator (E. coli Trinc)

CGAAATAGTACTTCCGGACTCgAGAGTGAAAATTGTTACGGAGCCCAAAAAATCCGCTTGCGCCCGGGGCCGTCT
GCTCCTAGAAACCGCTTCACCGAGACGAAGACCGGCAGCGCCGGACGAGAGACGAGAGCGAGAGACAC
GTCGGCCGCGACAATTGAAGATGAGGCGGACGGACGGTTGTCTGTGTAACGTCGCGGCCGCGGAACCT
GATCATGTAGATCGAATGGACTCTAAATCCGTTCAGCCGGGTTAGATTCCCGGGGTTTCCGCCACTGCAGCCTTAG

CGAAAGCTAAGGATTTTTTTTAAGCTTGGCACTGGCCGTCGTTTTTACAACGTCGTGACTGGGAAAACCCTGGCGTT

pIND4-RC-M210TAG: See sequence information in "Construction of pIND4-RC-M210TAG-HaloY1".

Protocol: The gene cassette inserts were ordered as IDT gBlocks Gene Fragments such that the aaRS (A7 for NO<sub>2</sub>Y incorporation) (5) and tRNA gene cassettes had homologous overlap regions for each other and for the vector at the appropriate 5' and 3' end of the cassette. Then through linearizing the pIND4-RC vector with restriction enzyme Kpn2I (Thermo-Fisher), the vector and the aaRS and tRNA gene cassettes were ligated together with the NEBuilder® HiFi DNA Assembly Cloning Kit. In constructed plasmids, the orientation of the tRNA gene cassette is reversed with respect to the orientation of the aaRS gene cassette orientation as in Fig. S1 Weaver *et al* (1). Professor Ryan Mehl generously provided the sequence information for the A7 mutant of *Mb*. pyrrolysyl-tRNA synthetase (MbPylRS) which incorporates NO<sub>2</sub>Y along with its cognate tRNA (5).

# S1.2 Prior Attempts at 3-Nitrotyrosine Incorporation

Prior to using the A7 mutant, we attempted to use the F4 MbPyIRS mutant for 3-nitrotyrosine (Fig. S1) incorporation creating a plasmid identical to pIND4-RC-M210TAG-A7 but with the F4 MbPyIRS replacing A7. Like the amber suppression performed in mammalian cells by Porter *et al.* (5), plasmids containing the F4 mutant failed to produce RCs with 3-nitrotyrosine at M210 in our photosynthetic bacteria. In the study performed by Porter *et al.* they attributed the F4 mutant's inability to incorporate 3-nitrotyrosine in mammalian cells to the lower amber suppression efficiency of the F4 mutant when under low amino acid concentrations. This may also be the reason for the F4 mutant's inability to elicit 3-nitrotyosine incorporation in *R. sphaeroides*.

We also attempted to produce RCs with 3-nitrotyrosine at M210 through use of the aaRS found in the pIND4-RC-M210TAG-HaloY1 plasmid — Porter *et al.* has demonstrated low levels of 3-

nitrotyrosine incorporation at amber stop codons in *E. coli* (2). Despite using identical expression conditions for 3-nitrotyrosine incorporation as used with other halotyrosine ncAAs, which were incorporated successfully (see below), we saw no production of RCs with 3-nitrotyrosine incorporation. Note also, this was in the absence of any noticeable toxicity to cells of the ncAA since final cell pellet volumes following growth with 3-nitrotyrosine were similar to cell pellets from WT RC expression. The pIND4-RC-M210TAG-HaloY1 plasmid's inability to incorporate 3-nitrotyrosine could be due to the same aaRS attributes which allowed the F4 aaRS for 3-nitrotyrosine to function in *E. coli* to but not in mammalian cells (2).

**Fig. S1**. The ncAAs used during protein expression to create M210 protein variants from WT's tyrosine at M210: (A) 3-methyltyrosine, (B) 3-nitrotyrosine, (C) 3-chlorotyrosine, (D) 3-bromotyrosine, and (E) 3-iodotyrosine.

#### S1.3 Bacterial Growth and Protein Expression

All *E. coli* growth for plasmid amplification and screening and following NEB HiFi-assembly was performed in NEB's DH5-alpha cells. These cells were grown in LB supplemented with kanamycin (Kan) at 30  $\mu$ g/mL and shaken at 200 RPM and 37 °C. Likewise, all *E. coli* transformations were done following manufacturer protocol for NEB 5-alpha competent *E.* coli (High Efficiency) and plated on LB/Kan agar plates. The preparation of the cell growth media utilized here (LB) and below (RLB) is described previously in the literature (1, 6).

For all *R. sphaeroides* bacterial growth, cells were grown on media or agar plates supplemented with 25  $\mu$ g/mL Kanamycin (Kan) for antibiotic selection. *R. sphaeroides* strain RCx was transformed with

either pIND4-RC (for WT RC production), pIND4-RC-M210TAG-A7 (for NO₂Y RC production) or pIND4-RC-M210TAG-HaloY1 (for MeY and halotyrosine RC production) and plated on RLB/Kan as described previously. In this paper use of the plasmid pIND4-RC-M210TAG-HaloY1 to genetically encode 3-methyltyrosine (in addition to the three halotyrosine ncAAs already incorporated in *R. sphaeroides*) was performed due to reports in the literature of 3-methyltyrosine incorporation using the HaloY aaRS (7). Following 4 days incubation at 30-33 °C, colonies were picked and used to inoculate 3-4 mL of RLB in 14 mL Falcon Round Bottom culture tubes. After two days incubation at 30 °C and shaking at 200 RPM, the culture media, now at saturated growth, was used to inoculate 50 mL of RLB in 250 mL Erlenmeyer flasks which were grown overnight under the same conditions. The 50 mL overnight cultures were then added to 2.5 L baffled Tunair™ shake flasks containing 1 L RLB and shaken until an OD700 = 0.2 − 0.3 (scattering at 700 nm) was obtained. At this point protein expression was induced by adding 1 mL of 1 M IPTG and 10 mL of 100 mM of the appropriate ncAA to each liter of bacterial culture. Both 3-methyltyrosine and 3-nitrotyrosine required the addition of 160 µL of 8 M NaOH for every 10 mL of 100 mM stock solution followed by <1 hr of sonication at 35-50 °C to fully dissolve. Protein expression then continued for 32-36 hours at 30 °C and 200 RPM.

#### S1.4 Protein Purification

Protein purification was performed per literature procedure with minor modifications (1, 6, 8, 9). Cells were pelleted by centrifugation at 12,000 g for 6 minutes and resuspended in 2 mL Lysis Buffer per 1 gram (wet mass) of cell pellet, where Lysis Buffer is an aqueous buffer containing 10 mM Tris HCl (Fisher) and 150 mM NaCl (Fisher) at pH 8.0. Resuspended cells were then frozen in liquid nitrogen.

Frozen cells were thawed and minimal DNase was added (several crystals). For each gram of cell pellet, 1 µL of 1 M MgCl<sub>2</sub> (Sigma) was added. The cell slurry was lysed by 2 rounds of homogenization. In each round, the cell slurry was passed more than three times through an Avestin EmulsiFlex-C3 Homogenizer operating at 15,000 – 20,000 psi. Cell slurry volume was made low enough to make this less than 3

minutes of homogenization. Cell homogenization was performed the sample cylinder chilled with ice throughout and cells were placed on ice for 4 minutes between rounds to minimize heating of lysate. The cell lysate produced was centrifuged for 90 minutes at 4 °C and the insoluble phase, cell debris, was removed by decanting off the soluble cell lysate. The detergent, N,N-dimethyldodecylamine N-oxide (LDAO, Sigma-Aldrich), was added to the soluble phase from a 30% stock until the liquid lysate was at a final LDAO concentration of 1% to solubilize RC chromatophores (6, 8). Membrane debris was removed from this suspension by spinning solubilized chromatophores at 26,700 g at 4 °C for 90 minutes and the liquid phase carefully collected (via pipette if necessary) to not disturb any debris collected. Solubilized RCs were then passed through a 0.22  $\mu$ m PES or PVDF Stericup® Filter Unit (Millipore) to remove remaining cell debris.

Crude solubilized RCs were bound to a Ni-NTA (Qiagen) column, containing 5-10 mL of resin, by gravity passage of the solubilized RCs through the Ni-NTA resin. The column was washed with enough Wash Buffer (10 mM Tris HCl, 150 mM NaCl, 0.03% LDAO, pH 8.0) such that flow—through had an absorbance at 280 nm of less than 0.02. This took less than 6 column volumes. Protein was then eluted by addition of 3 column volumes of LDAO Dialysis Buffer (10 mM Tris HCl, 0.03% LDAO, pH 8.0 containing 100 mM Imidazole (Sigma)) and the colored fraction pooled and collected. Eluted RCs were purified with anion exchange chromatography on a GE ÄKTA Purifier 100. Protein was loaded onto 3 x 5 mL Q HP anion exchange columns connected in series and purified by running a gradient of 25–40% Buffer B (LDAO Dialysis Buffer containing 600 mM NaCl) at a flow rate of 5 mL/min. The remaining buffer (Buffer A) in the gradient was LDAO Dialysis Buffer + 30 mM NaCl. Protein eluted between 28% and 38% Buffer B and protein fractions which contained a 280/800 nm absorbance ratio less than 2.0 were collected and pooled. Pooled fractions were placed in 15 mL 50 kDa Centrifigual Filter Units (Millipore) and NaCl was removed through buffer exchange with LDAO Dialysis Buffer. The yields for purified protein samples were 0.14 mg/L and 0.17 mg/L for RCs with 3-methyltyrosine and 3-nitrotyrosine at

M210 respectively. To reiterate the labeling scheme used in the main text and throughout this document, protein samples in this study were labeled as depicted in Table S1. Mass spectrometry and crystallography required RCs to be purified using buffers which contained LDAO (out of necessity due to the requirements of the method). Transient absorption measurement required RCs be purified with Deriphat 160C using the same protocols as is listed above (See S3.1). The only difference was any buffer with 0.03% LDAO was replaced with 0.05% Deriphat and solubilization of chromatophores was performed with 1% Deriphat (10, 11) instead of 1% LDAO.

**Table S1**. Protein sample labeling scheme

Amino acid at residue M210	RC Protein Sample Label		
tyrosine	WT		
3-methyltyrosine	MeY		
3-nitrotyrosine	NO <sub>2</sub> Y		
3-chlorotyrosine	CIY		
3-bromotyrosine	BrY		
3-iodotyrosine	IY		

### **S2** Structural Characterization

# S2.1 Liquid chromatography–Mass Spectrometry (LC–MS)

LC-MS was performed with the help of Theresa Laughlin at the Stanford University Mass Spectrometry facility. LC-MS on MeY was performed as published previously. LC-MS on NO<sub>2</sub>Y was performed similarly with exception of the column used during chromatography. Here a BioResolve RP mAb Polyphenyl Column with 450 Å pore diameter, 2.7  $\mu$ m bead size, and 2.1 mm x 100 mm dimensions from Waters was used. A lower temperature of 50 °C was also employed during chromatography. The change in column did not influence mass spectra of proteins seen when run using previous columns but did, as would be expected, alter the LC elution profile. In this paper, only data for new variants which had not been previously genetically encoded in *R. sphaeroides* are displayed in Fig. S2, as data for halotyrosine variants were reported earlier (1). Mass spectra for the L- and H-subunits showed no change in mass for MeY and NO<sub>2</sub>Y and are not displayed as they are identical to WT mass spectra, which we have presented previously (1).

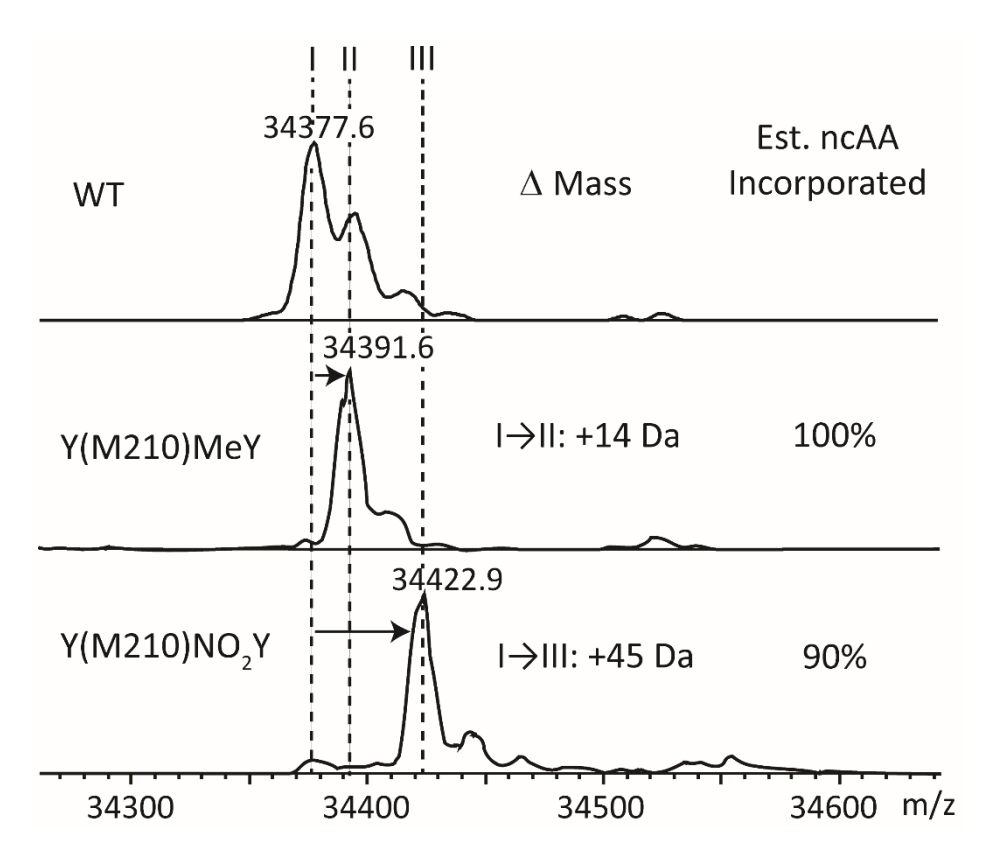


**Fig. S2.** Deconvoluted ESI-MS spectra of the RC M-subunit. Change in mass from WT to ncAA incorporated variants is indicated for each with the major low m/z peak used for mass change determination indicated with a dashed line. Change of mass from Peak I (WT) to each variant peak (II=MeY, III=NO<sub>2</sub>Y) is indicated for each along with the fidelity of ncAA incorporation (percent of protein with tyrosine variant present as opposed to tyrosine). Estimations of fidelity were determined via the ratio of intensity at the tyrosine variant peak (II or III) relative to any intensity at 34377.6 m/z (Peak I), indicative of residual WT peak. Less than 10% WT is present in NO<sub>2</sub>Y RCs and little to no WT is seen in MeY. Mass change for both MeY and NO<sub>2</sub>Y RCs matches the expected mass change for their respective ncAA incorporations due to substitution of a proton with a methyl or nitro group, respectively. Minor peaks of variable intensity are observed at +16-19 Da intervals from the major peak for all RC variants and are likely due to oxidative modifications (see also Fig. 5 in ref. (1)).

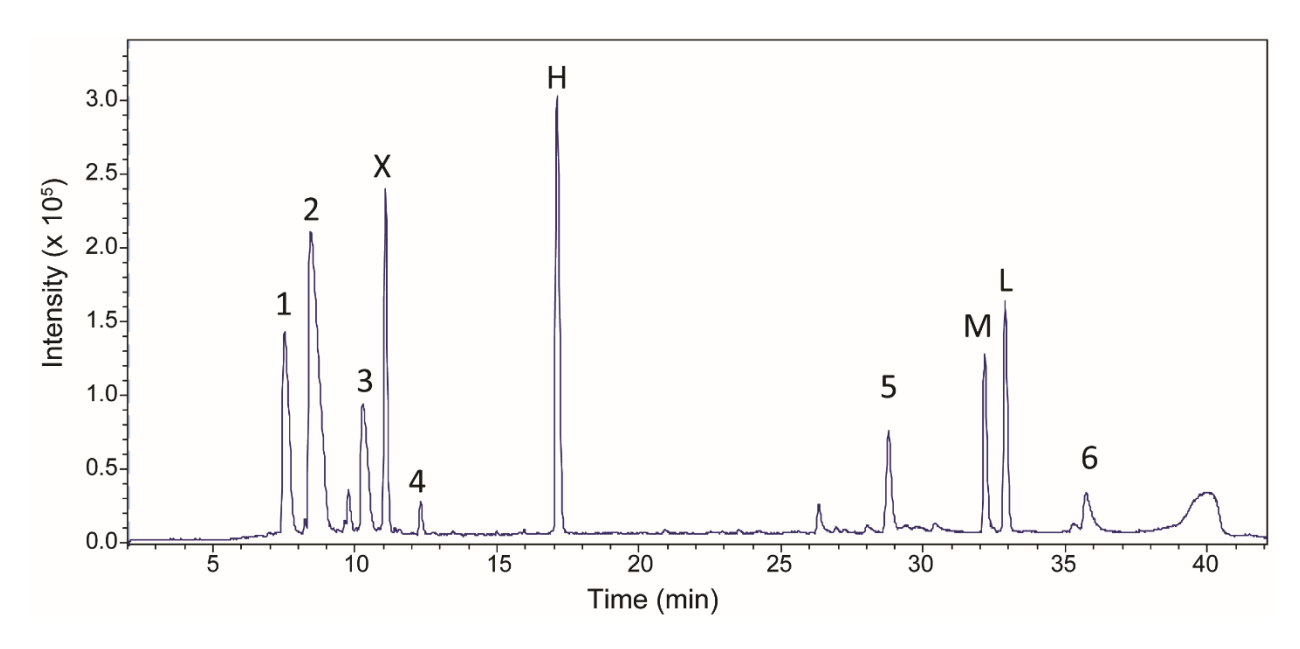


**Fig. S3.** BioResolve Polyphenyl column LC chromatogram for NO<sub>2</sub>Y RCs. As in previous work (1), peaks 1-6 are small molecules consisting of detergents and RC chromophores. RC subunit peaks H, M, and L are labeled above. Peak X is an impurity with a mass of 23,785 Da which also was found in CIY RCs. Given the mass and the hydrophilic nature of the peptide indicated by its early elution, it seems unlikely that it is RC-related. It is also unlikely that transient absorption kinetic results would be contaminated by this contaminant, since few proteins that size are photoactive (or have a bound photoactive cofactor) at 850 nm, the wavelength of excitation for transient absorption experiments. Additionally, NIR ground state absorbance spectra do not indicate an additional contaminant band when fitted (Fig. S74 and Fig. S90). Bands in the chromatogram obtained with the Polyphenol Bioresolve HPLC column were lower in signal than those from an Agilent Pursuit diphenyl 150 mm x 2.1 mm column despite the same quantity of sample injected as performed previously, 5 μL of 3.5 μM RCs (1). Bands were, however, better resolved than those obtained on previous chromatograms performed with the Agilent Pursuit diphenyl column.

#### S2.2 Protein Crystallization

All protein constructs were crystallized via the hanging drop method described by Saer *et al.* (8). Fresh preparations of purified RCs in LDAO Dialysis Buffer were concentrated with Amicon Ultra-0.5 mL 50 kDa Centrifugal Filters and stocks of 5 mg/mL, 7 mg/mL, and 9 mg/mL RC were prepared. RC concentration was assessed via the 288,000  $M^{-1}$ cm<sup>-1</sup> molar absorptivity at the  $B_A/B_B$   $Q_y$  band maximum (see band at  $\sim$ 12,400 cm<sup>-1</sup> in Fig. S74) (1, 12, 13). All stocks were centrifuged for 1 minute at 16,700 g to remove bubbles. Hanging drops were set manually using 24-well VDX plates with sealant (Hampton Research) and 22 mm siliconized glass (Hampton Research). Drops were set such that each drop contained 1  $\mu$ L of precipitant solution, and either 2 or 3  $\mu$ L of one of the protein stocks. These glass covers were then set

over wells with 0.5 mL potassium phosphate buffer whose concentration ranged from 1.4 M–1.7 M. Precipitant contained 1 M potassium phosphate, 3.5% 1,2,3-heptanetriol, and 0.1% LDAO and phosphate buffer was prepared from potassium phosphate monobasic (Sigma). Both solutions were minimally titrated with NaOH (Fisher) and HCl (Sigma) solutions until at pH 8. Crystal trays were covered with foil to protect from light and samples were minimally exposed to light following the placement of the hanging drops. Optimal crystallization conditions for all RC variants at M210 matched those of Saer *et al.* (8) with multiple wells displaying diffraction quality crystals at 1.4 M and/or 1.5 M potassium phosphate.

#### S2.3 X-ray Data Collection and Structure Determination

X-ray diffraction data for the samples described in this paper were collected at SSRL (Menlo Park, CA) (14). We tried various cryo-solutions and oils to cryo-cool these crystals and all approaches resulted in markedly poor diffraction or high mosaicity. We used the Arinax HC-Lab Humidity Controller to determine the optimum humidity level for good quality diffraction data for the room temperature data collection. All data sets were collected with 88% relative humidity at room temperature (289 K). The data sets for CIY, BrY, and IY RCs were collected at beamline 9-2 using the PILATUS 6M detector. The data sets for NO<sub>2</sub>Y and MeY RCs were collected at beamline 14-1 using the Eiger 16M detector. Crystals were mounted on mesh loops and placed in the humidified air stream as previously described (15, 16). Data were processed using XDS (17) using the autoxds script developed at SSRL. All proteins crystalized in the P3<sub>1</sub>21 space group with one RC per unit cell. Molecular replacement was performed in MOLREP (18) using the highest resolution RC structure (PDB code: 2J8C) as the search model for M210 RC variants. Iterative refinement was performed manually in Coot (19) and REFMAC (20). Details of the data collection and refinement parameters are provided below in Table S2.

**Table S2.** X-ray data collection and refinement characteristics for RC variants.

Crystallographic Parameters							
RC			BrY		IY	NO <sub>2</sub> Y	MeY
PDB Entry		7MH3	7MH4		7MH5	7MH9	7MH8
Space Group		P3 <sub>1</sub> 21	P3 <sub>1</sub> 21		P3 <sub>1</sub> 21	P3 <sub>1</sub> 21	P3 <sub>1</sub> 21
		141.67	14	1.34	141.41	141.21	140.96
Unit Ce Lengths (		141.67	14	1.34	141.41	141.21	140.96
Lenguis	Α)	186.87	18	6.87	186.50	187.59	187.01
		90		90	90	90	90
Unit Cell Ar	ngles	90	90		90	90	90
( )		120	120 120		120	120	120
			Data Colle	ction Stat	tistics		
RC		CIY	E	BrY	IY	NO <sub>2</sub> Y	MeY
Resolution   Resol		40 – 2.30	40 – 2.48		40 – 2.85	40 - 3.10	40-2.75
No: of obse		484297	388566		340963	661446	479326
No: of uni reflectio	-	91797	76551		50807	39799	56220
CC <sub>1/2</sub>		99.6(55.3)	99.6(58.8)		99.8(58.2)	99.4(70.6)	99.8(64.9)
Redunda	ncy	5.3	Ţ	5.1	6.7	16.6	8.5
Completeness Overall (outer shell)		94.8(95.8)	99.6(99.8)		99.9(100)	99.9(100)	99.7(100)
R <sub>sym</sub> <sup>a</sup> (%) Overall (outer shell)		12.7(131.7	") 12.1(115.4)		12.6(139.1)	35.8(158.0)	15.3(140.5)
I/σ Overall (outer shell)		9.8(1.6)	10.2(1.7) 12.		12.2(1.6)	7.2(1.6)	11.4(1.7)
			Refinem	ent Statis	stics		
	RC		CIY	BrY	IY	NO <sub>2</sub> Y	MeY
		n limits	40 – 2.3	40 – 2.4		40-3.10	40 - 2.75
% Comple			94.10	99.70	99.90	99.90	99.70
Number F	Reflect R <sub>free</sub>	ions used for	4508	3768	2495	1990	2811
R <sub>factor</sub> <sup>b</sup> (%)			15.7	16.8	18.0	16.9	17.9
R <sub>free</sub> (%)		%)	17.4	19.3	20.5	20.5	20.1
Number		Protein	6494/46.5	6462/50	.3 6472/73.3	6475/61.7	6459/63.8
atoms/B-		ctor/buffer/ion	628/63.6	628/64.	·	628/75.4	627/72.3
factors Wa (Ų)		ter Molecules	312/54.0	244/50.	0 184/61.8	136/51.3	132/55.9

RMS	Bond length (Å)	0.01	0.01	0.01	0.01	0.01
deviations	Bond angle (°)	2.17	2.22	2.21	2.22	2.14
Ramachandran favored (%)/outliers		97.8/1	97.1/1	96.5/1	96.0/1	96.7/2

# S2.4 Crystal Structure Overlays

In Figs. S4–S6, protein structural overlays are displayed from both a lateral perspective (as in Fig. 1 in the main text) and a vertical perspective (~90° rotation from that shown in the lateral perspective looking down from the P- or periplasmic-end of the protein). All overlays are created using the align command in Pymol. While all room-temperature variant crystal structures are being compared to the Protein Data Bank 77 K structure, 2J8C, comparisons with the room temperature WT structure, 1K6L, are nearly identical to the 77 K structure (Table S3). The cryo-structure was used for overlays because of its significantly higher resolution; 2J8C had a resolution of 1.87 Å while 1K67 had a resolution of 3.10 Å.

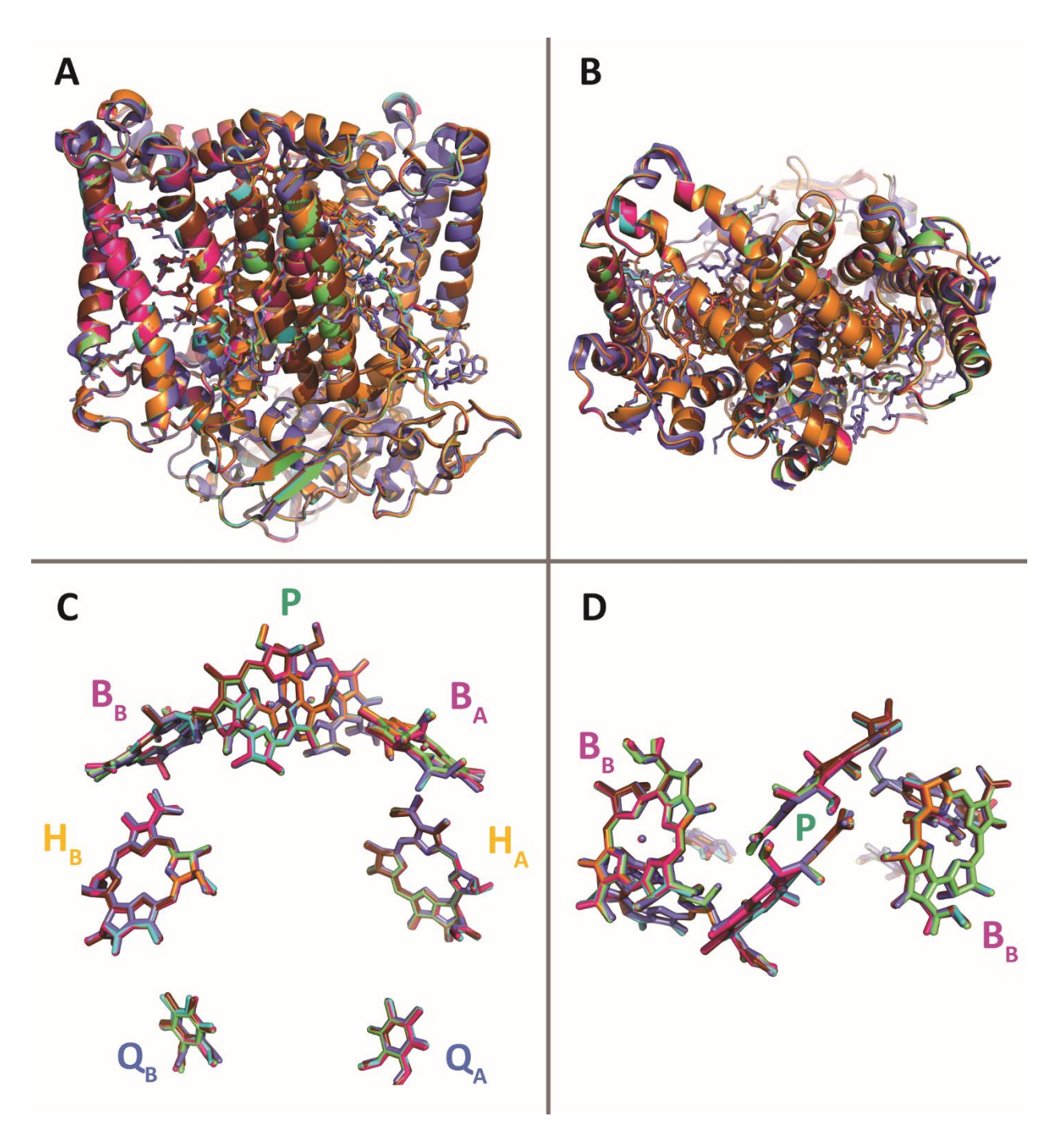


**Fig. S4.** (A) Protein overlay of WT and all RC variants from a lateral perspective. (B) Same protein overlay in (A) from a vertical perspective. (C) Overlay of just the A- and B-chromophore branches (phytl-chains are not shown for clarity) in comparing chromophore orientations and positioning. (D) Same overlay in (C) but from a vertical perspective. Due to the high level of structural similarity within the experimental error, individual protein color codes are not highlighted.

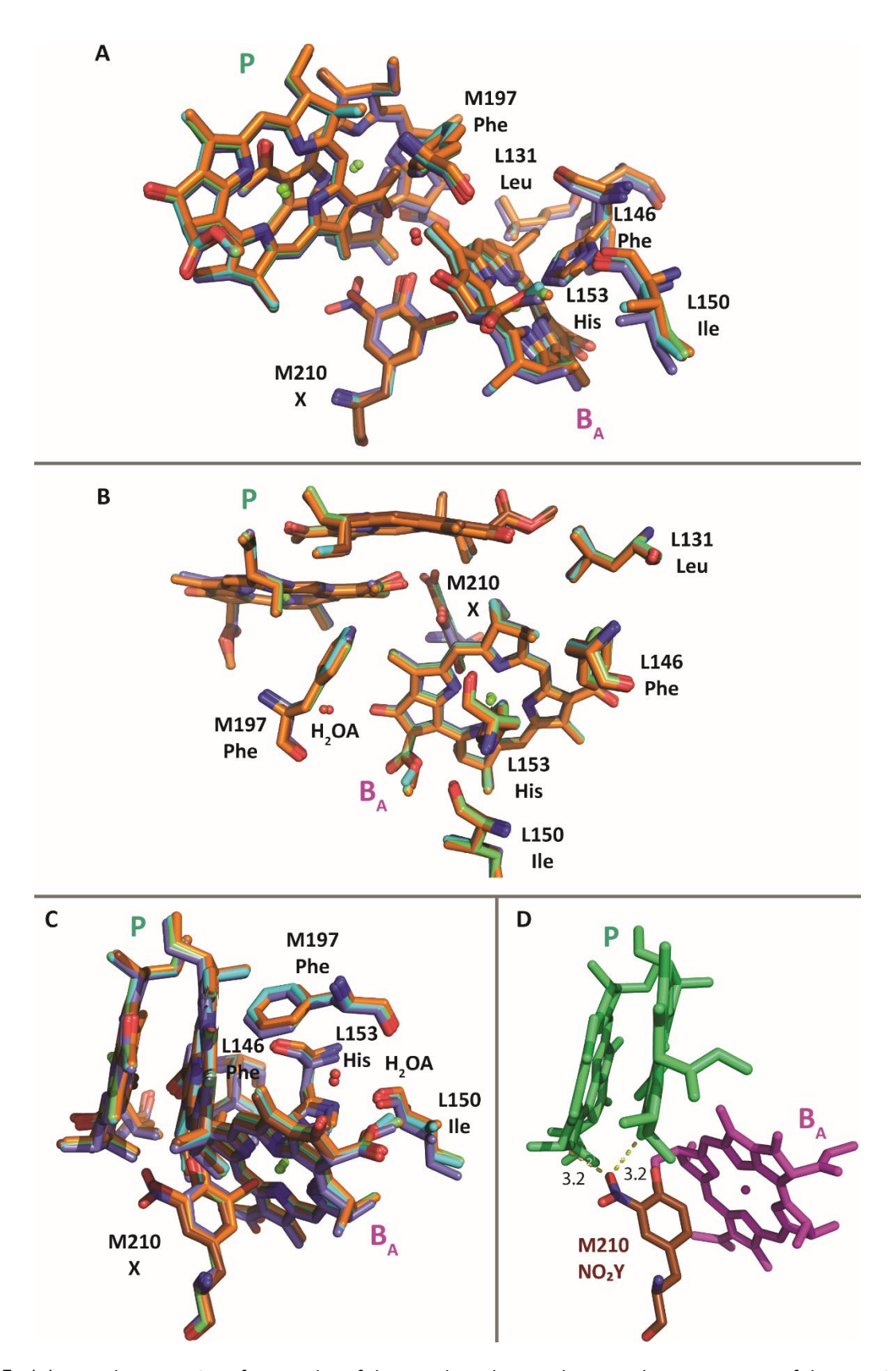


**Fig. S5.** (*A*) Lateral perspective of an overlay of the P and BA chromophores and an assortment of the protein residues near B<sub>A</sub> from WT (2J8C) and RC variant crystal structures. (*B*) Vertical perspective of the overlay. Due to

the high level of structural similarity within the experimental error, individual protein color codes are not highlighted. (C) Sideview of A. (D) A simplified sideview of just the NO<sub>2</sub>Y RC structure in (A), where only P, B<sub>A</sub>, and 3-nitrotyrosine at M210 are depicted and P and B<sub>A</sub> are colored green and magenta, respectively. Here, a dashed line is drawn between the nitro oxygen and the closest two atoms on the special pair, the C3A carbon of P<sub>A</sub> and the CMB carbon of P<sub>B</sub>, with the distance written by each respective line (for bacteriochlorophyll carbon labeling scheme, see ligand BCL in PDB entry 2J8C). Note that neither C3A nor CMB is part of the special pair  $\pi$ -system. This is done to help illustrate the orientation and distance of the substituent on M210 tyrosine analogs to P, where the NO<sub>2</sub>Y structure is shown as an example.

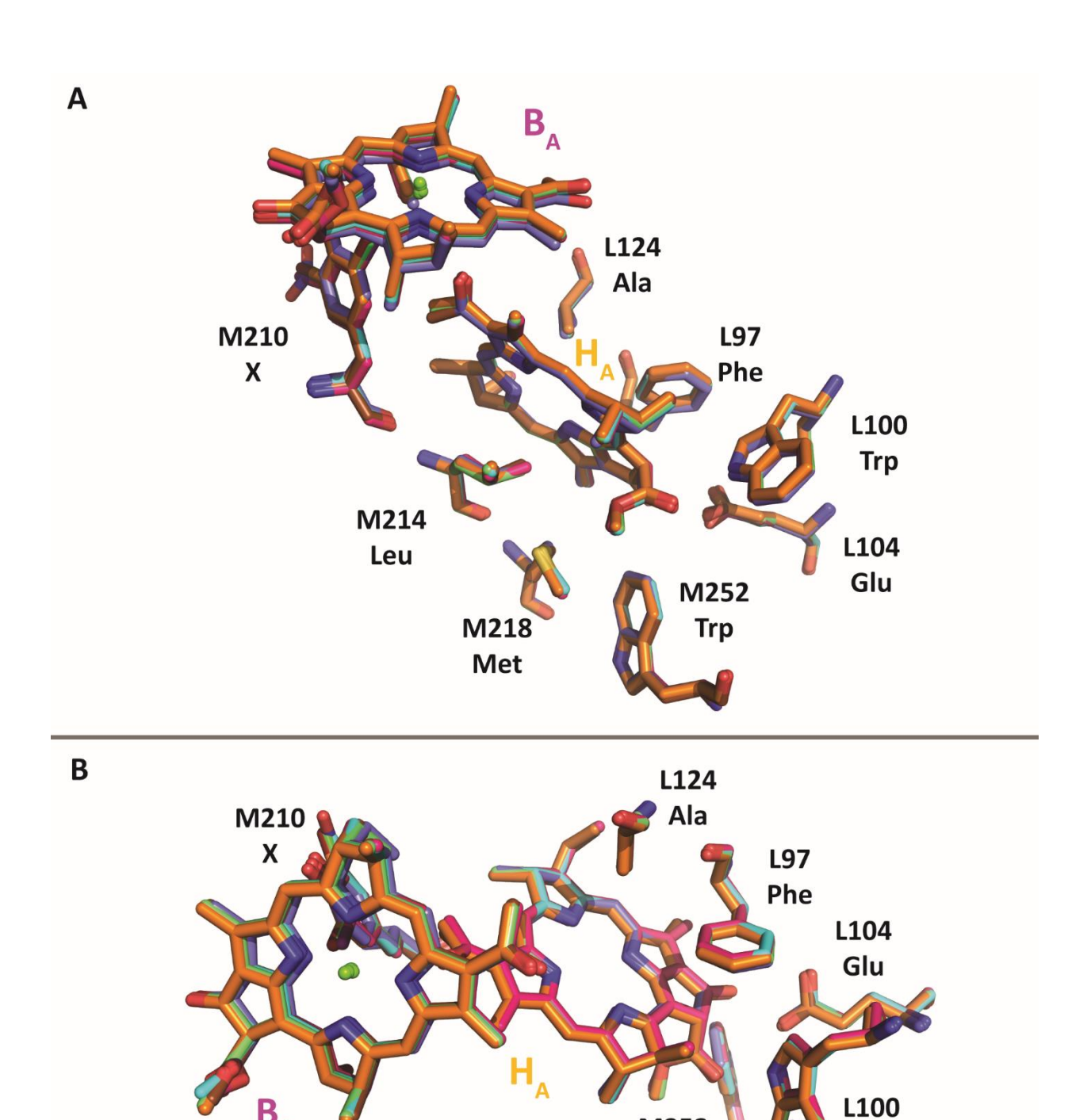


**Fig. S6.** (A) Lateral perspective of an overlay of the  $H_A$  and  $B_A$  chromophores and an assortment of protein residues near  $H_A$  from WT (2J8C) and RC variant crystal structures. (B) Vertical perspective of overlay. Due to the high level of structural similarity within the experimental error, individual protein color codes are not highlighted.

M252

Trp

Trp

**Table S3.** Representative interchromophoric distances.

RC	$P_A (Mg) - B_A (Mg)^1$	$P_B(Mg) - B_A(Mg)^1$	$P_B$ (CHB) $-B_A$ (CHD) <sup>2</sup>	$P_A$ (CHD) – $B_A$ (CHD) <sup>2</sup>
WT 77 K				
(2J8C)	11.1	12.8	8.7	8.1
WT RT				
(1K6L)	11.0	12.8	8.8	8.1
MeY	11.0	12.9	9.0	8.1
CIY	11.1	12.9	9.1	8.3
BrY	11.0	12.9	9.1	8.3
IY	11.1	12.9	9.1	8.2
NO <sub>2</sub> Y	11.1	12.9	8.9	8.0
RC	$P_B$ (CAB) $-B_A$ (C2D) <sup>2</sup>	$P_B$ (C3B) $- B_A$ (C2D) <sup>2</sup>	$B_A (Mg) - H_A (C3B)^3$	$B_A$ (CHB) – $H_A$ (C2B) <sup>2</sup>
WT 77 K				
(2J8C)	5.1	5.7	6.9	5.4
WT RT				
(1K6L)	5.1	5.6	6.9	5.4
MeY	5.0	5.5	6.9	5.6
CIY	5.0	5.5	7.1	5.7
BrY	5.0	5.5	7.1	5.7
IY	4.9	5.5	6.9	5.6
NO <sub>2</sub> Y	5.0	5.5	6.9	5.7

<sup>&</sup>lt;sup>1</sup>Center-to-center interchromophoric distance.

<sup>&</sup>lt;sup>2</sup>Edge-to-edge interchromophoric distance.

<sup>&</sup>lt;sup>3</sup>Center-to-edge interchromophoric distances. Atom labeling followed literature bacteriopheophytin and bacteriochlorophyll convention and are present in deposited PDB files. Atoms were picked for distance measurement to help create a picture of the relative similarity among chromophore distances. Those atoms chosen to represent "edge" atoms were the atoms participating in the chromophore pi-system which were the closest to the neighboring chromophore.

# S3 Transient Absorption (TA) Spectroscopy

# S3.1 Experimental Methods

Femtosecond to nanosecond TA measurements were acquired with a 1 KHz amplified Ti:Sapphire laser system (Spectra Physics) coupled to Helios and EOS detection spectrometers (Ultrafast Systems). These systems were described in previously (21). All samples were  $\sim$ 12  $\mu$ M with the exception of MeY and NO<sub>2</sub>Y which were 6  $\mu$ M and 9  $\mu$ M, respectively (MeY and NO<sub>2</sub>Y had low protein yields per liter bacterial culture grown and were difficult to produce). Samples were exchanged into a buffer containing 0.05% Deriphat 160 C (Cognis), 10 mM Tris, pH 8.0 for TA measurements. These measurements were performed on samples in a Deriphat 160 C buffer due to the formation of a Q<sub>A</sub>inactive population which accumulated in all samples as the experiment progressed when measurements were performed in LDAO-containing buffer. While it is unclear what caused this Q<sub>A</sub>inactive population, the kinetics for primary electron transfer (ET) is the focus of this paper and all kinetics for early ET are the same in both buffers regardless which buffer was used. This is consistent with the literature which shows similar kinetics for primary ET in R. sphaeroides RCs when comparing WT isolated in Deriphat 160 C or in LDAO detergents (22–24). Additionally, the Q<sub>A</sub>-inactive population formation seen in LDAO-solubilized RCs was reversible; following an overnight incubation at 4° C, samples did not initially display P<sup>+</sup>H<sub>A</sub><sup>-</sup> charge recombination features, indicating the Q<sub>A</sub> inactive population which had formed in previous TA experiments had reverted overnight.

A 100–fold molar excess of sodium ascorbate (Fisher) and a 25–fold molar excess of terbutryn (Fisher) were both added to each RC sample prior to measurements. Ascorbate was added to prevent oxidation of RC-samples and terbutryn was added to displace any  $Q_B$  quinone (eliminating the long-lived  $P^+Q_B^-$  state ( $\sim 1$  s)). Measurements were performed at room temperature and utilized a spinning sample cell with an  $\sim 2$  mm pathlength. Sample volume in the spinning cell was 3 mL and samples were spun at

~350 RPM. Samples were excited with ~1  $\mu$ J, ~100-fs pulses at 850 nm which directly excited the primary electron donor P. Pulses were focused to ~1 mm and had a 500 Hz repetition rate. The 3D TA data sets generated consist of absorbance changes ( $\Delta$ A) across the visible region (450–770 nm) and the near-infrared (NIR) region (830–1350 nm) encompassing pump-probe delay times before the excitation flash to ~7 ns.

# S3.2 Overview of TA Data and Analysis

This overview is intended to help orient the reader to the contents of the following extensive data analysis approaches performed on the TA data. Raw data and analysis results for all 6 RC samples (WT, MeY, CIY, BrY, IY, and NO<sub>2</sub>Y) are presented from different perspectives. This allows comparisons of a specific type of data among all six RCs in a given figure (Sections S3.5, S3.7, and S3.9) or comparison of different results for one RC in a given figure (Sections S3.3-S3.4, S3.6, S3.8, and S3.10).

The TA data were analyzed using functions that consist of the instrument response convolved with multiple exponentials (an amplitude and time constant) plus a constant (referred to as the infinity value). The data were analyzed globally using CarpetView (Light Conversion) or SurfaceXplorer (Ultrafast Systems). Fits at individual wavelengths utilized custom fitting routines in Origin (Origin Lab).

One type of global fitting utilized independent exponentials (which CarpetView terms a "parallel model"). This fitting is model independent, other than the number of exponentials chosen. This analysis returns decay-associated difference spectra (DADS). DADS are spectra of the pre-exponential factors (amplitudes) of the kinetic component and represent the spectral changes that occur with a particular time constant. As such, the DADS are not attributable to a specific state or intermediate, but represent spectral changes that accompany a process; in this study the process is typically an ET reaction in which one state decays to another state. An example is the ET process  $P^+H_A^- \rightarrow P^+Q_A^-$  that occurs with an average time constant of ~250 ps. Even though the ~250 ps DADS for a given sample represents this

process, for convenience that DADS may be referred to as the  $P^+H_A^-$  DADS.  $P^+H_A^-$  is the state that decays with a time constant of ~250 ps and that lifetime is also the time constant for formation of  $P^+Q_A^-$ .

The signs of the features in DADS carry useful information. A negative feature in a DADS reflects (1) decay of bleaching of a ground state absorption band (i.e., of  $H_A$  in the above example), (2) the decay of excited state stimulated emission (e.g, from  $P^*$ ), or (3) the formation of a transient absorption band associated with the product of the ET process. A positive feature in a DADS reflects (1) formation of a bleaching of a ground state absorption band or (2) the decay of a transient absorption band (i.e., of  $H_A^-$  in the example given above).

The second type of global fitting performed, often referred to as target analysis, depends on a particular kinetic model, which underpins the multi-exponential function used to fit the kinetic profiles at each wavelength in the global analysis. The analysis returns species-associated difference spectra (SADS). A SADS plots the change in extinction coefficient ( $\Delta \varepsilon$ ) as a function of wavelength for a particular transient state referenced to the ground state. The concentration of the particular state (species) as a function of time is also returned from the fit. If the model is appropriate, the magnitude of  $\Delta \varepsilon$  for key features in a SADS should match expectations based on known spectra for the participating species.

The analysis to obtain SADS uses the same number of exponential terms used to obtain DADS. However, the pre-exponential factor for a given exponential term for SADS is not just one parameter (as it is in DADS) but contains contributions of the pre-exponential factors (amplitudes) as well as time constants from the DADS components. In effect, each SADS is a complex combination of all the DADS. Thus, particularly if a given state can decay by more than one pathway in the kinetic model, SADS "fits" often do not converge to yield the correct time parameters (e.g. time constants of processes). Usually, for SADS one fixes one or more time constant (obtained from DADS and fitting at individual wavelengths), and may fix one or more initial component amplitudes consistent with independent information on the yields of processes or estimates of relative populations of species. As such, global

analysis to obtain SADS is best referred to as "simulating" the spectral evolution data rather than "fitting" it.

A great deal of previous work on WT RCs and many mutants show multi-exponential P\* decays, indicating that there exists a distribution of P\* populations (9, 11, 21, 23–39). All that is known from the TA experiments is what happens after excitation of P to P\*. Before excitation, thermal motions involving the amino acids and the cofactors lead to a distribution of cofactor-protein and cofactor-cofactor interactions. At the instant of excitation (laser pump pulses posesses a spectral bandwith of ~12 nm), this distribution will be mapped onto the excited-state potential energy surface and give rise to distributions in free energies of P\* and each of the subsequent charge separated states. The excitation process might contribute further to the distribution of free energies of the states, for example by causing a change in the distance between the two macrocycles of P (11, 40) or by changing the solvation environment of P\* due to its charge transfer character (41–43). The system then evolves due to protein and molecular relaxations, accompanied by relaxations in energy, and, of course, ET processes (33, 44–52).

In the present study, the influence of these P\* distributions is not discussed explicitly and the data are simplified to a model with two P\* populations, denoted  $P_1^*$  and  $P_2^*$ . In general,  $P_1^*$  produces  $P^*H_A^-$  via a two-step ET process  $P_1^* \to P^*B_A^- \to P^*H_A^-$ . Consistent with prior work on WT RCs and mutants (11, 24, 53–55), it is found here that the rate of the second step is greater than or comparable to that of the first step (e.g., 3.0 ps followed by 1.5 ps) with details depending on the sample. As such, the maximal population of  $P^*B_A^-$  during the time evolution does not represent the true yield of this state from  $P_1^*$ . In fact, the typical combination of rate/time constants lead to a low maximal transient population (e.g., ~20% of the initial  $P_1^*$ ). As will be seen,  $NO_2Y$  RCs appear to have little to none of the  $P^*B_A^-$  intermediate, which if present, is near the detectibility limit.

In the general model used here,  $P_2^*$  decays directly to  $P^*H_A^-$  via a slower (10-30 ps) one-step superexchange process  $P_2^* \to P^*H_A^-$  that is mediated by  $P^*B_A^-$  as a virtual intermediate. In effect,  $P^*B_A^-$  electronically mixes with both  $P_1^*$  and  $P^*H_A^-$ , and the extent of this mixing involves orbital overlap of  $P^*$ ,  $B_A$  and  $H_A$  and an energy denominator that depends on the vertical (energy) separation of the potential energy surfaces for the three states. That mixing underpins the effective electronic coupling for the superexchange ET process. As stated in the main text, the two  $P^*$  populations are treated here as being consequences of two different mechanisms as opposed to simply being evidence of two populations from a  $P^*$  distribution which decay with differing rates. This distincition is based on DADS features discussed in the main text.

Thus, in the analysis presented here, global fitting of the data (to obtain DADS or SADS) generally utilized a function consisting of five exponentials plus a constant (convolved with the instrument response). The function has one term each for  $P_1^*$  ( $\sim$ 3-5 ps),  $P_1^*$ B<sub>A</sub> ( $\sim$ 1-2 ps),  $P_2^*$   $\sim$ 10-20 ps), and  $P_1^*$ B<sub>A</sub> (220-270 ps). The constant (infinity value) accounts for  $P_1^*$ B<sub>A</sub>, which does not decay on the time scale of the measurements. For SADS, this model is shown in Fig. S56A. A fifth exponential was fixed at 0.1 ps component to account for flash artifacts from the laser pump pulse including Raman features at some wavelengths near t = 0 (pump-probe temporal overap). Incorporation of the 0.1 ps term avoids such features potentially contributing to the  $P_1^*$  spectrum. For the reasons noted above,  $P_1^*$ Bar and  $P_2^*$ Bar without formation of  $P_1^*$ Bar as a true intermediate. This model for  $P_2^*$ Bar and  $P_3^*$ Bar as a true intermediate. This model for  $P_2^*$ Bar and  $P_3^*$ Bar as a true intermediate. This model for  $P_3^*$ Bar and  $P_3^*$ Bar as a true intermediate. This model for  $P_3^*$ Bar as a true intermediate.

Fits at individual wavelengths (and some global analysis runs) used (1) three exponentials that models P\* decay as reflecting two populations (like in global analysis) or (2) two exponentials that models P\* decay as reflecting a single population. We display (1) and (2) below for 542 nm and 924 nm (Figs. S19-S20).

Table S4 summarizes results of the global analysis to obtain SADS and DADS along with the results of representative single-wavelength fits at 924 nm and 542 nm, the importance of which is described below. Table S5 gives the results of additional analysis for NO<sub>2</sub>Y RCs.

## S3.3 Contour Profile Maps of Raw TA Data

Section S3.3 (Figs. S7–S12) presents contour profile maps of the 3D data sets in the visible and NIR regions for each of the six samples.

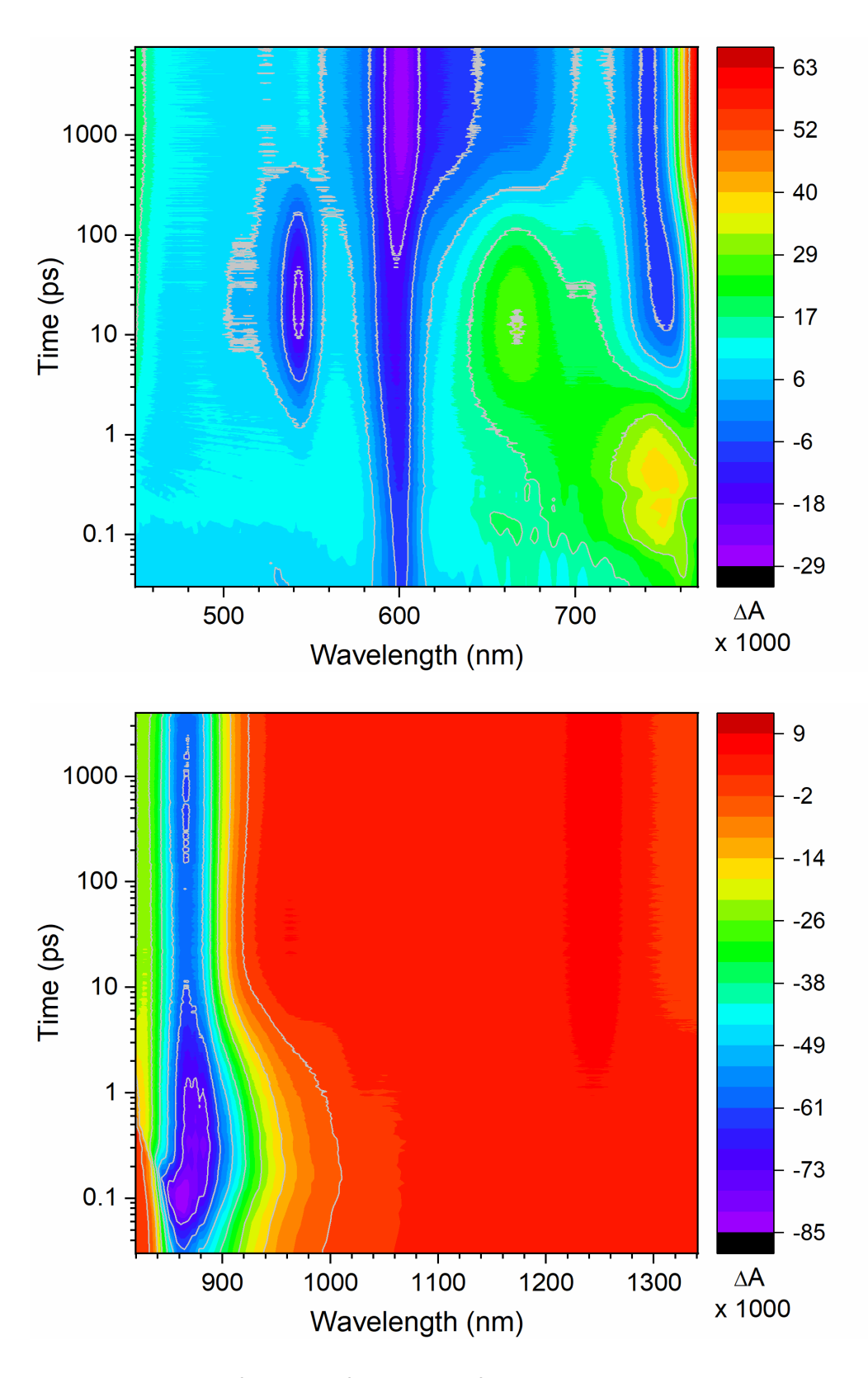


**Fig. S7.** Contour profile maps of the TA data for WT RCs. The color range versus  $\Delta A$  scale is different for the visible (top) and NIR (bottom) regions as shown at the right.

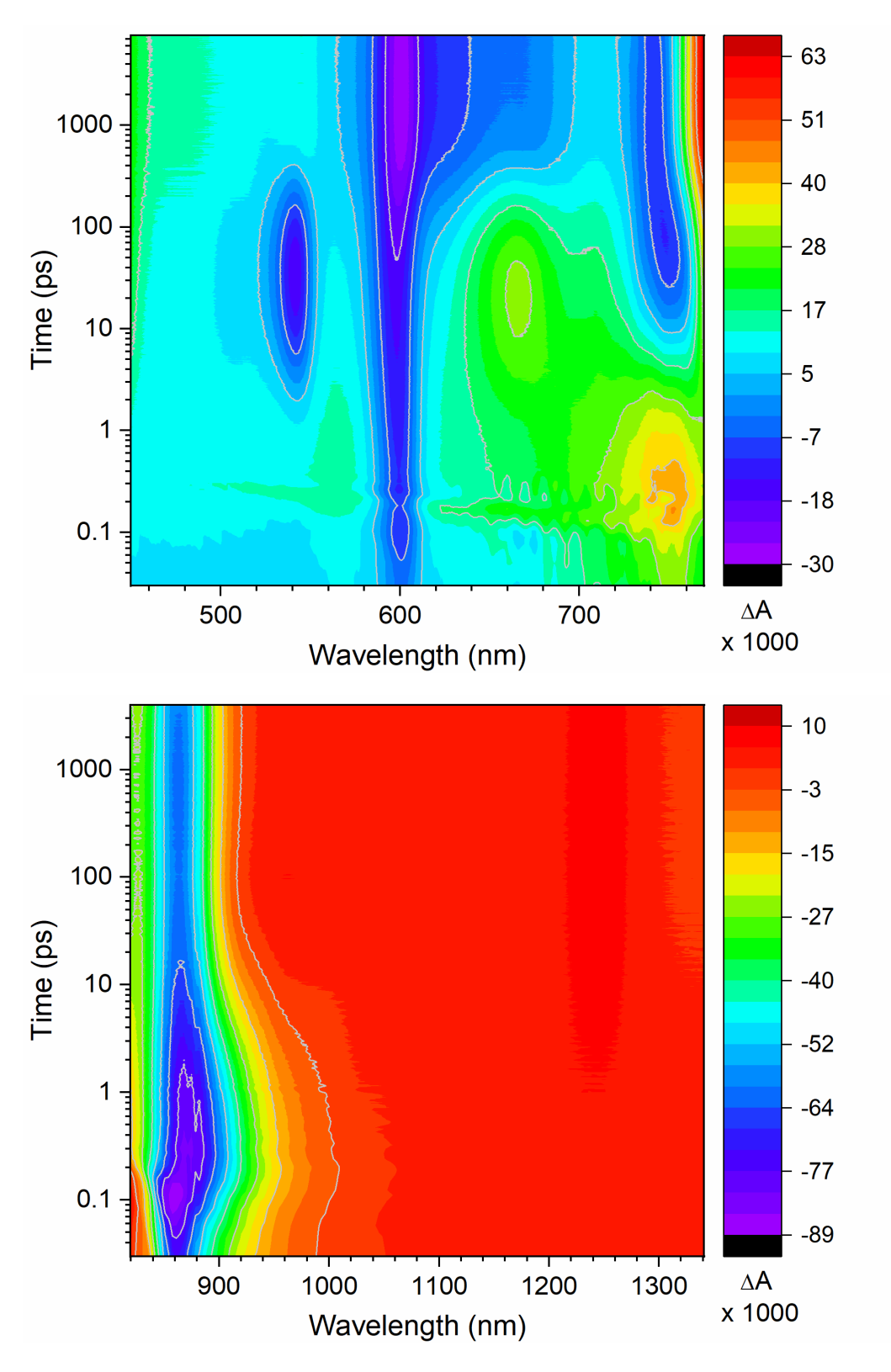


**Fig. S8.** Contour profile maps of the TA data for CIY RCs. The color range versus  $\Delta A$  scale is different for the visible (top) and NIR (bottom) regions as shown at the right.

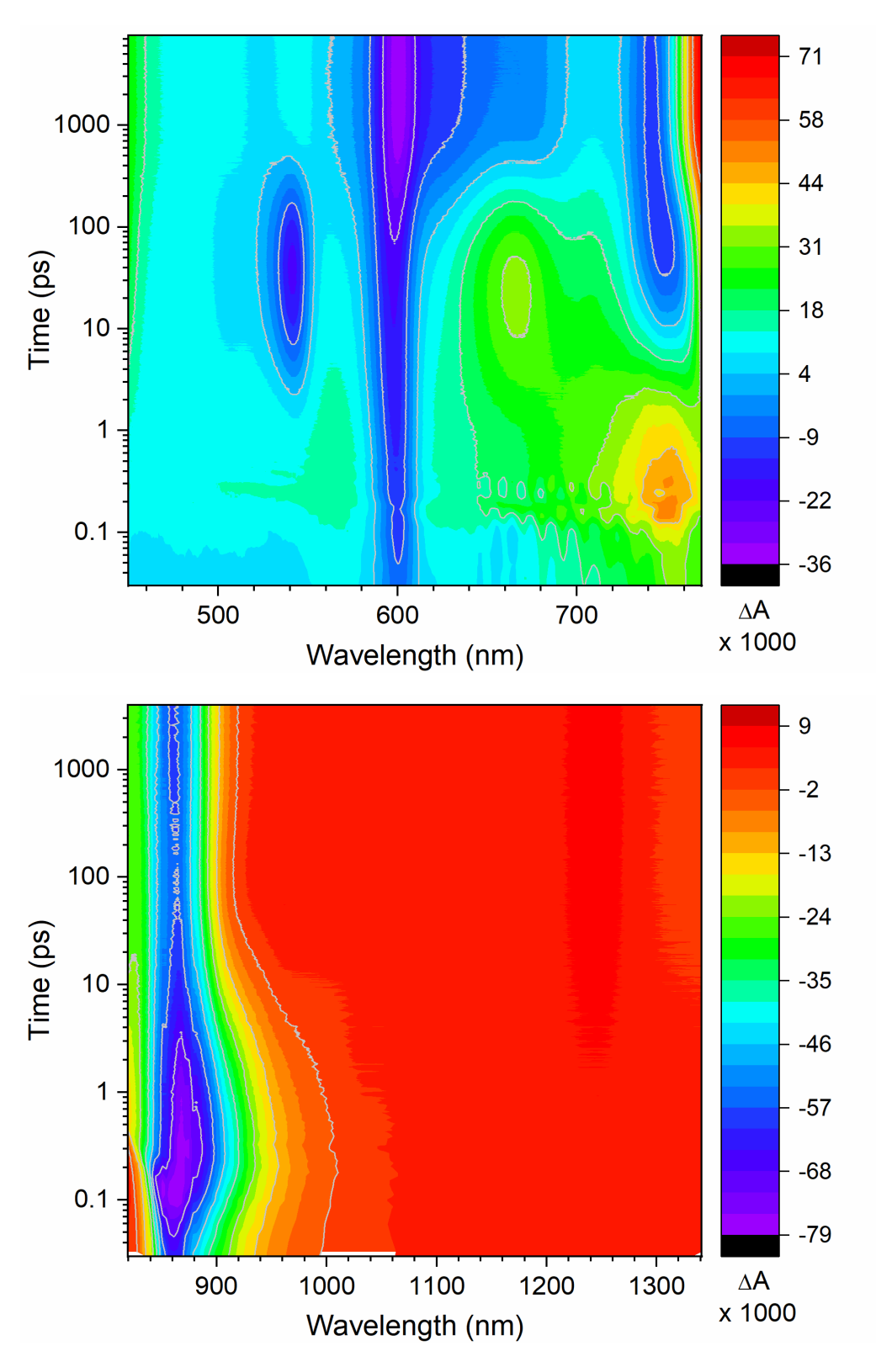


**Fig. S9.** Contour profile maps of the TA data for BrY RCs. The color range versus  $\Delta A$  scale is different for the visible (top) and NIR (bottom) regions as shown at the right.

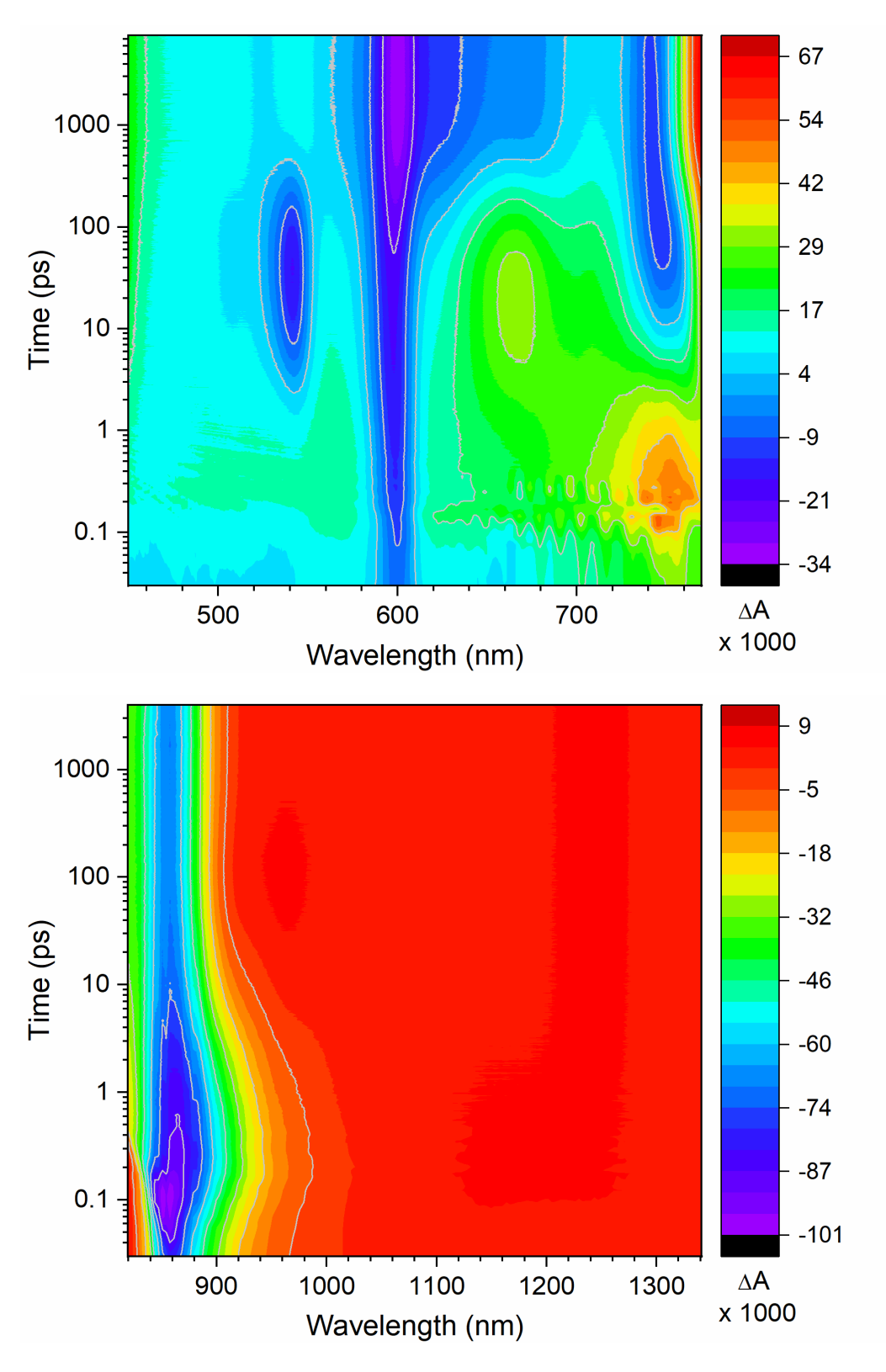


**Fig. S10**. Contour profile maps of the TA data for IY RCs. The color range versus  $\Delta A$  scale is different for the visible (top) and NIR (bottom) regions as shown at the right.

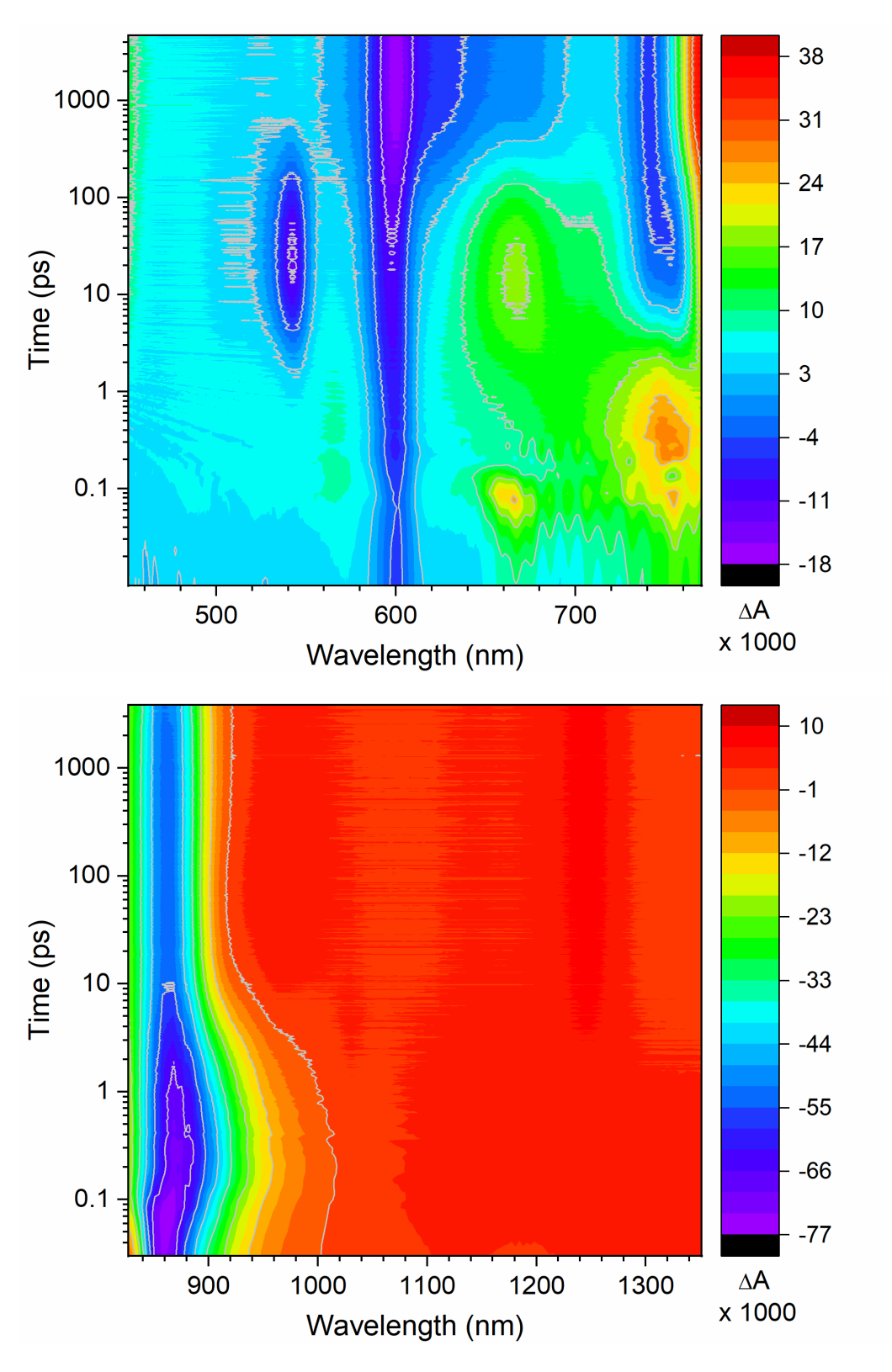


**Fig. S11.** Contour profile maps of the TA data for MeY RCs. The color range versus  $\Delta A$  scale is different for the visible (top) and NIR (bottom) regions as shown at the right.

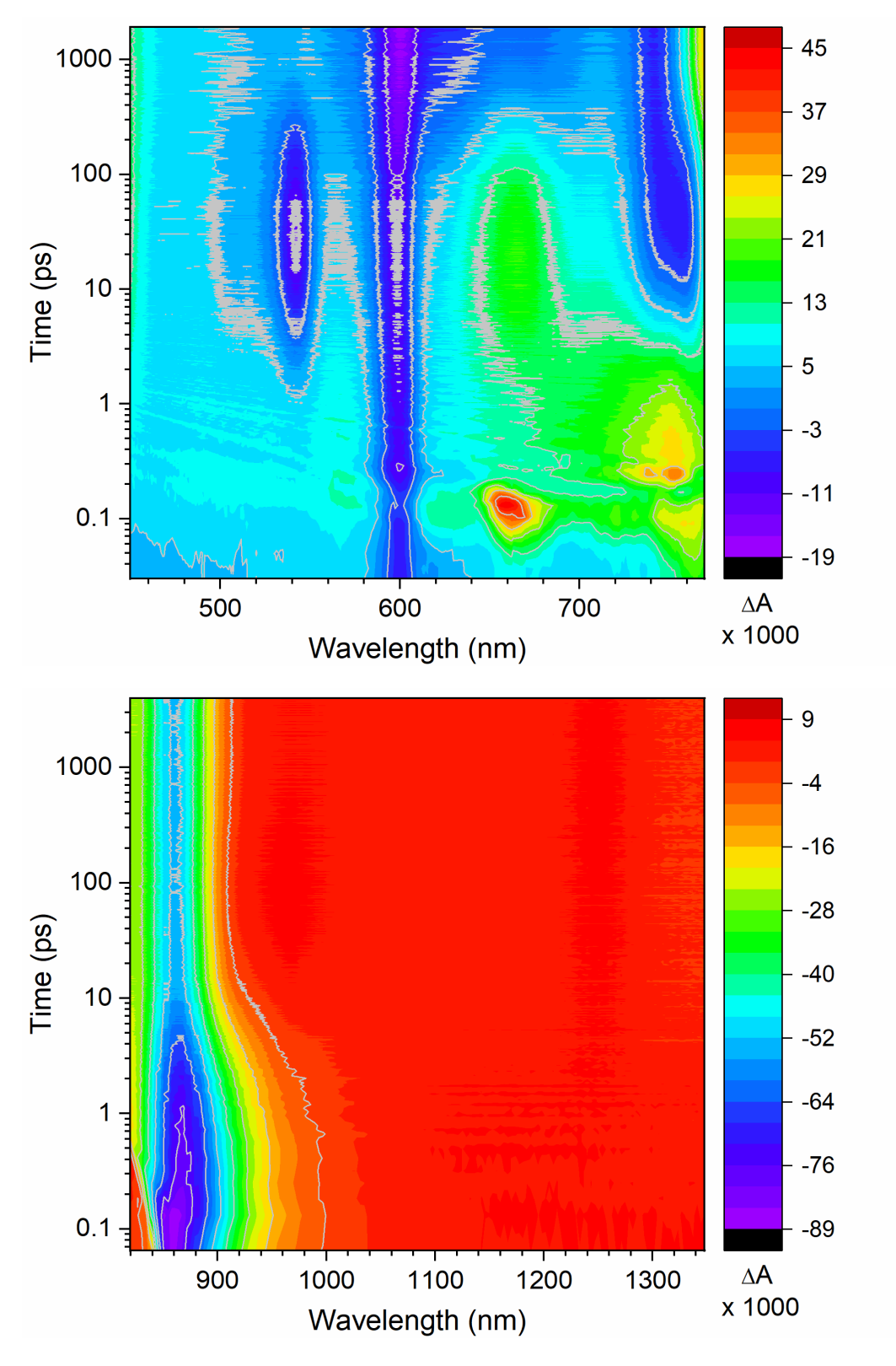


**Fig. S12.** Contour profile maps of the TA data for MeY RCs. The color range versus  $\Delta A$  scale is different for the visible (top) and NIR (bottom) regions as shown at the right.

## S3.4 Representative TA Spectra and Kinetic Profiles for Each Sample

Section S3.4 (Fig. S13–S18) gives, for each of the six samples, representative TA spectra at key times and representative kinetic profiles. The spectra at 0.5 ps, 5 ps, 25 ps and 2 ns show the expected characteristics for the states involved:  $P^*$ ,  $P^*$  and  $P^+H_A^-$  along with  $P^+B_A^-$ , primarily  $P^+H_A^-$ , and  $P^+Q_A^-$ , respectively. These spectra and assignments are fully consistent with prior studies on RC photochemistry and are summarized as follows.

For WT RCs (Fig. S13), the spectrum for P\* at 0.5 ps (gray) shows relatively featureless transient absorption across the visible and NIR broken by bleaching of the ground state absorption bands of P at  $\sim$ 600 nm (Q<sub>x</sub>) and  $\sim$ 865 nm (Q<sub>y</sub>). Stimulated emission from P\*, like bleaching, appears as a negative  $\Delta$ A, has its largest amplitude at  $\sim$ 920 nm and extends to past 1000 nm. At 5 ps (mauve spectrum) in the NIR, the P\* stimulated emission has significantly decayed and mainly only the Q<sub>y</sub> bleach centered at  $\sim$ 865 nm remains. In the visible region at 5 ps, bleaching of the Q<sub>x</sub> band of H<sub>A</sub> has appeared along with the broad absorption centered at 665 nm of the H<sub>A</sub> anion due to the presence of P\*H<sub>A</sub><sup>-</sup>. The 1250 nm absorption band of P\* can be seen at 5 ps. Close examination of the inset to Fig. S13B at 5 ps (mauve spectrum) shows the small absorption band assigned to the B<sub>A</sub> anion at 1030 nm due to the presence of P\*B<sub>A</sub><sup>-</sup>. The 1030 nm feature observed at 5 ps is not present at later times, but is present (with low amplitude) in the 0.5 ps spectrum and rests on the P\* stimulated emission (gray spectrum).

The spectrum for WT RCs at 25 ps (light blue line in Fig. S13) shows the characteristics of  $P^+H_A^-$  noted above for the 5 ps spectrum, but with larger amplitude. Additionally, in the inset to Fig. S7B, one can see the weak  $H_A$  anion absorption feature at ~950 nm that is the analog of the feature of the  $B_A$  anion at 1030 nm (56, 57). (Note that the true peak of the  $H_A$  anion band in the NIR is likely at a shorter wavelength than 950 nm, offset due to overlap with the P bleaching that has the opposite sign.) At 2 ns, the bleaching of the  $Q_X$  ground-state absorption of  $H_A$  has disappeared along with the  $H_A$  anion absorptions at 665 and ~950 nm. What remains are the spectral characteristics of  $P^+Q_A^-$ . These include

featureless absorption spanning the visible and NIR broken by bleaching of the  $Q_x$  band (600 nm) and  $Q_y$  band (865 nm) of P, along with P<sup>+</sup> absorption (1250 nm). All of these features are unchanged from those present at  $\sim$ 5 ps reflecting the near quantitative yield of P<sup>+</sup>H<sub>A</sub><sup>-</sup>  $\rightarrow$  P<sup>+</sup>Q<sub>A</sub><sup>-</sup> ET.

Examination of the analogous TA data for CIY RCs (Fig. S14) shows key differences from WT (Fig. S13). In short, for CIY RCs it takes longer for P\* stimulated emission to decay (panel D). It takes longer for P\*H<sub>A</sub><sup>-</sup> to form as evidenced by the 542 nm bleach (panel A), 665 nm anion absorption (panel A) the 960 nm anion (panel B and inset). Also, as will be seen below, because about half the P\* population for CIY RCs decays with a time constant of about 20 ps, substantially more stimulated emission is present at 5 ps relative to that for WT. Thus, for CIY RCs, the P\*B<sub>A</sub><sup>-</sup> anion feature at 1030 nm sits on top of a sloping P\* stimulated emission signal (B inset), whereas for WT the baseline for the 1030 nm feature is roughly flat (Fig. S13B inset). Finally, because about half the P\* population produces P\*H<sub>A</sub><sup>-</sup> by this slower process (assigned as due to superexchange) with a time constant of ~20 ps, it takes over 100 ps for P\*H<sub>A</sub><sup>-</sup> to fully form (five 1/e times). This can be seen in the spectra (panel A) and kinetics of the H<sub>B</sub> bleach formation (panel C) and 1250 nm P\* formation (panel D). This also means that since P\*H<sub>A</sub><sup>-</sup> decays with a ~250 ps lifetime, the maximal amount of P\*H<sub>A</sub><sup>-</sup> that is seen in the spectral time evolution is less for CIY RCs than for WT. This can be seen by the ratio of the 542 nm bleach relative to the 600 bleach at 100 ps in the spectra for CIY RCs compared to the 25 ps spectrum for WT. The same basic comparisons hold for BrY and IY RCs (Figs. S15-S16).

For MeY RCs (Fig. S17), the time evolution of the spectra (e.g., the time constants) is more like that of WT RCs than of the CIY, BrY and IY RCs. A key difference for the  $NO_2Y$  RCs (Fig. S18) is the  $B_A$  anion absorption at 1030 nm which is not readily distinguished or barely present (5 ps spectrum in Fig. S18B inset). The spectra at other times are similar to those of the other variants and WT, with differences in detail. The kinetic data for the six samples are examined in more detail below.

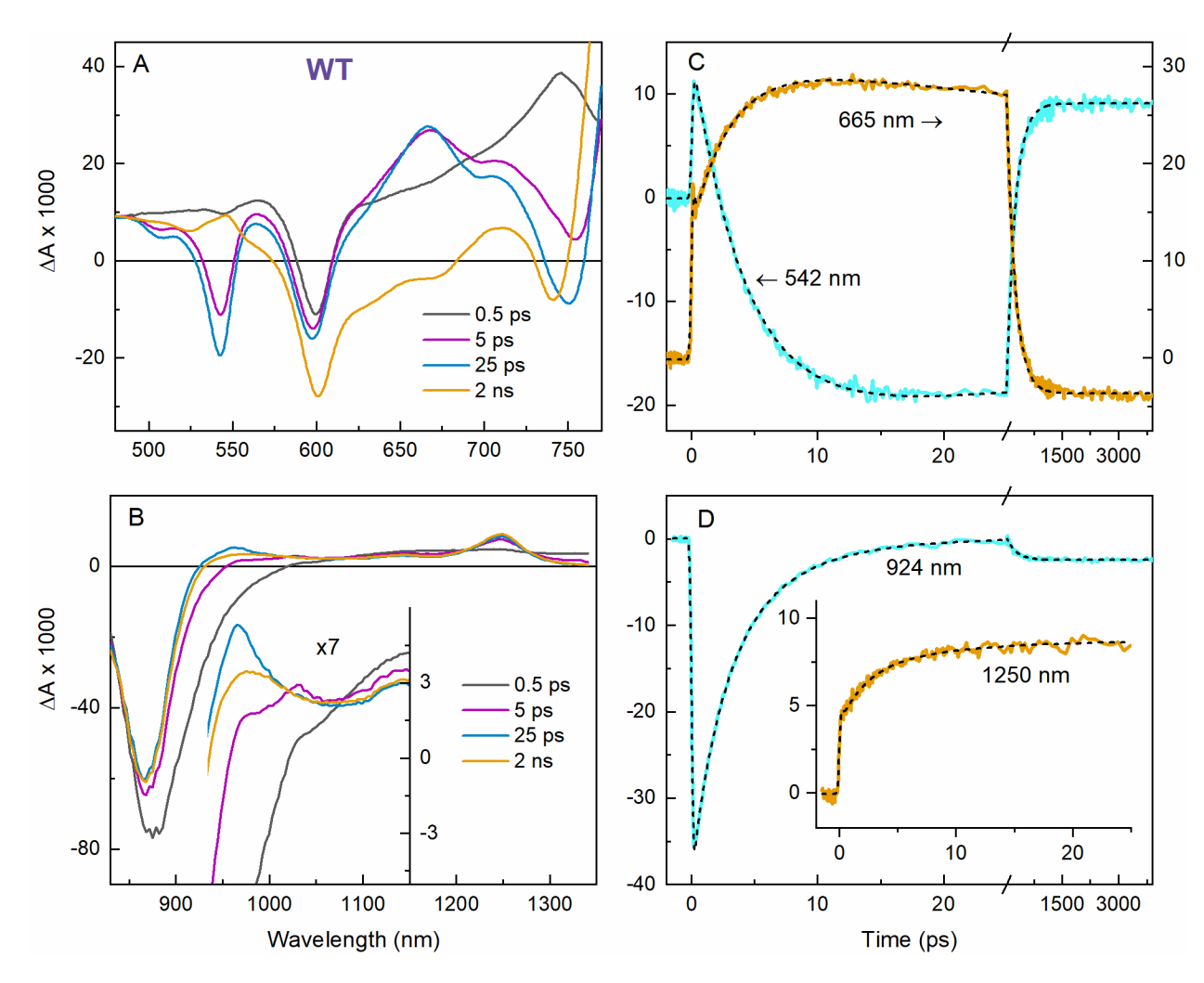


**Fig. S13.** TA summary for WT RCs showing TA data at select times in the visible region (A) and NIR region (B). The small absorption band for the  $B_A$  anion at  $\sim$ 1030 nm can be seen at 5 ps (mauve) in the inset for panel B. Time profiles (colored lines) and fits to a function consisting of three exponentials and a constant (dashed black lines) are shown for evolution of  $H_A$  bleaching (C, blue),  $H_A$  anion (C, gold),  $P^*$  stimulated emission (D, blue) and  $P^+$  absorption (D inset, gold). The time constants derived from the fits at these individual wavelengths are consistent with those derived from global analysis DADS and are given in Table S4. Note the break in the time axis scale in C and D at 25 ps.

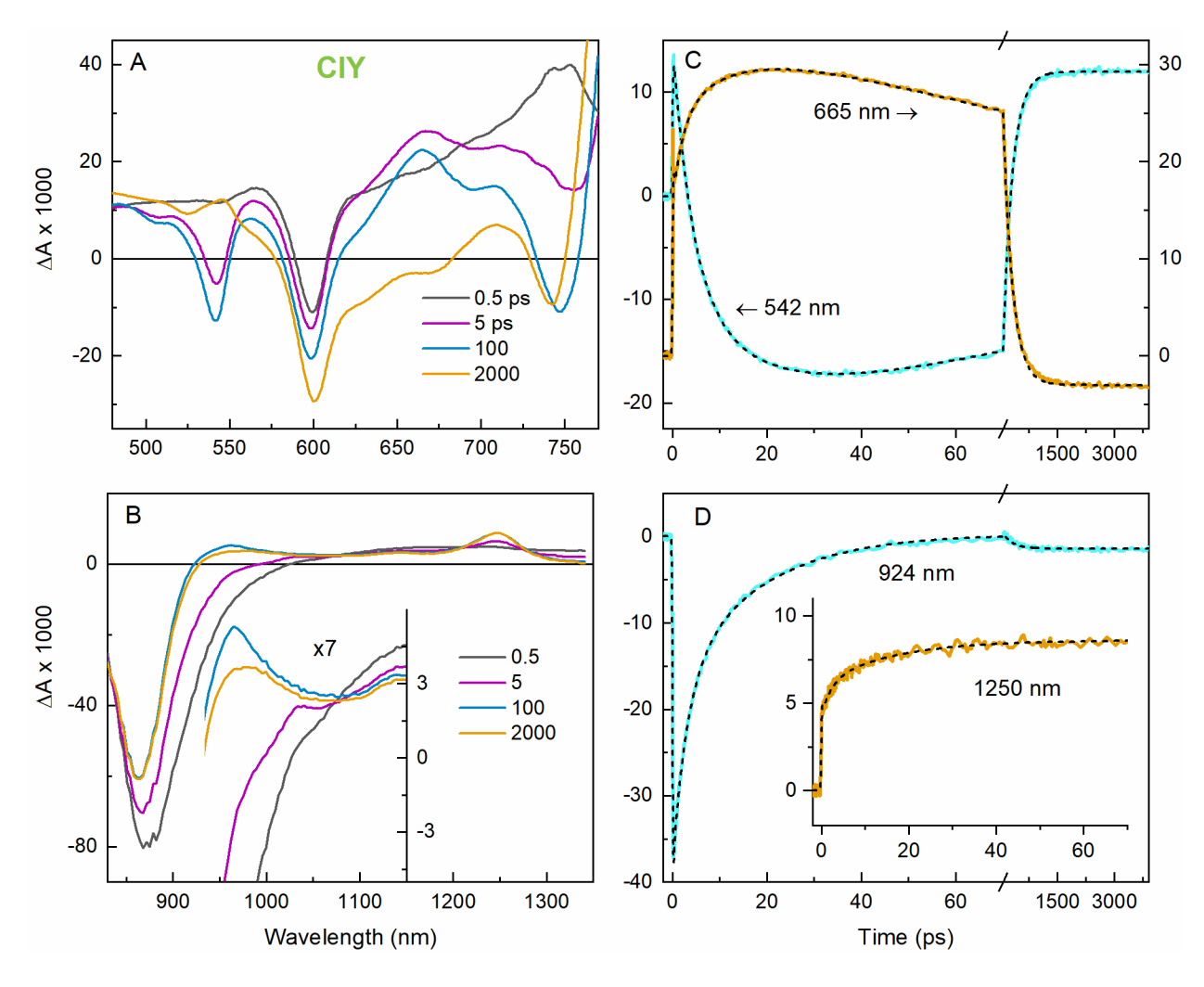


**Fig. S14.** TA summary for CIY RCs showing TA data at select times in the visible region (A) and NIR region (B). The small absorption band for the  $B_A$  anion at  $\sim$ 1030 nm can be seen at 5 ps (mauve) in the inset for panel B. Time profiles (colored lines) and fits to a function consisting of three exponentials and a constant (dashed black lines) are shown for evolution of  $H_A$  bleaching (C, blue),  $H_A$  anion (C, gold),  $P^*$  stimulated emission (D, blue) and  $P^+$  absorption (D inset, gold). The time constants derived from the fits at these individual wavelengths are consistent with those derived from global analysis DADS and are given in Table S4. Note the break in the time axis scale in C and D at 70 ps.

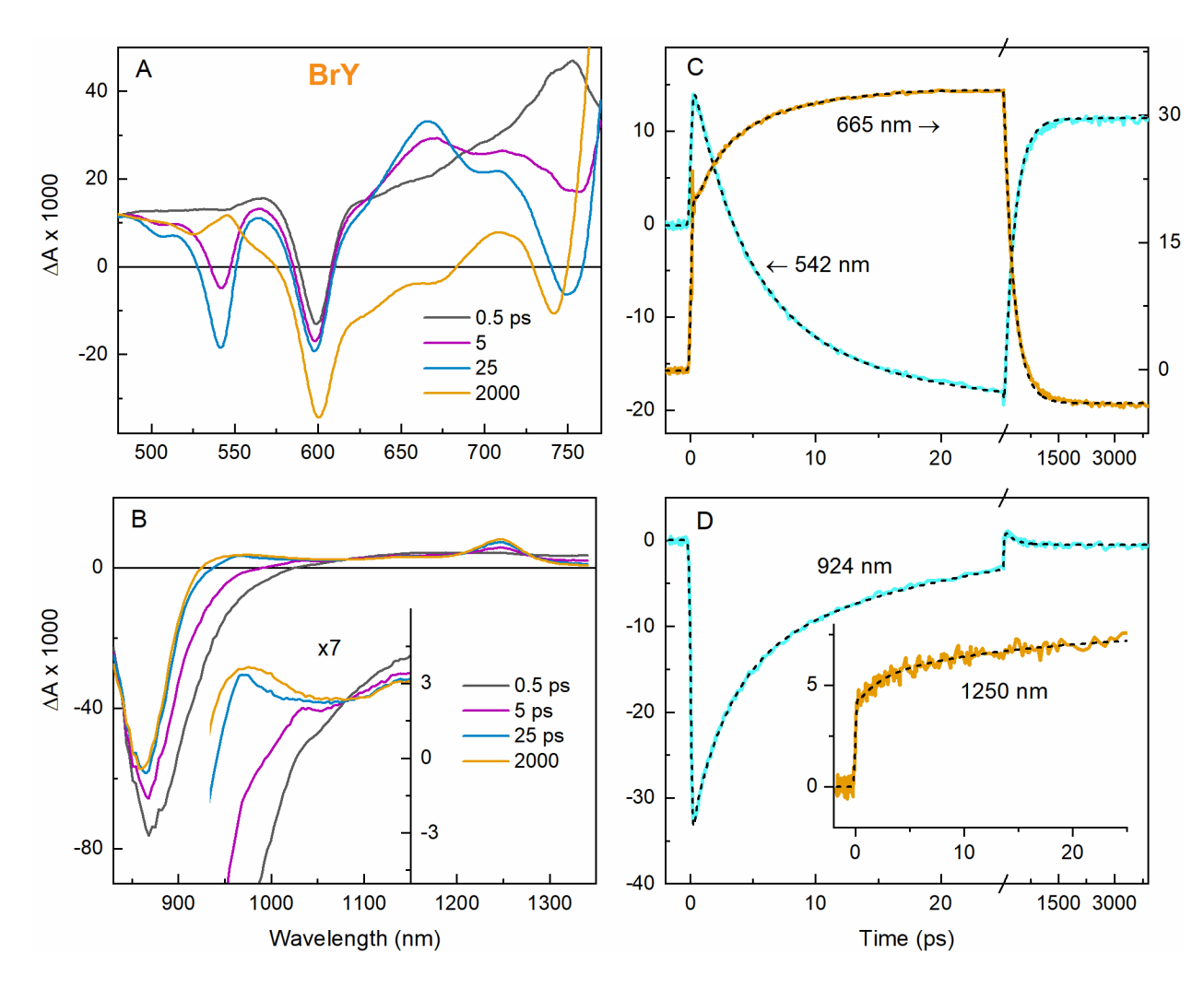


**Fig. S15.** TA summary for BrY RCs showing TA data at select times in the visible (A) and NIR (B) regions. The small absorption band for the  $B_A$  anion at  $\sim 1030$  nm can be seen at 5 ps (mauve) in the inset for panel B. Time profiles and fits to a function consisting of three exponentials and a constant are shown for evolution of  $H_A$  bleaching (C, blue),  $H_A$  anion (C, gold),  $P^*$  stimulated emission (D, blue) and  $P^*$  absorption (D inset, gold). The time constants derived from the fits at these individual wavelengths are consistent with those derived from global analysis DADS and are given in Table S4. Note the break in the time axis scale in C and D at 25 ps.

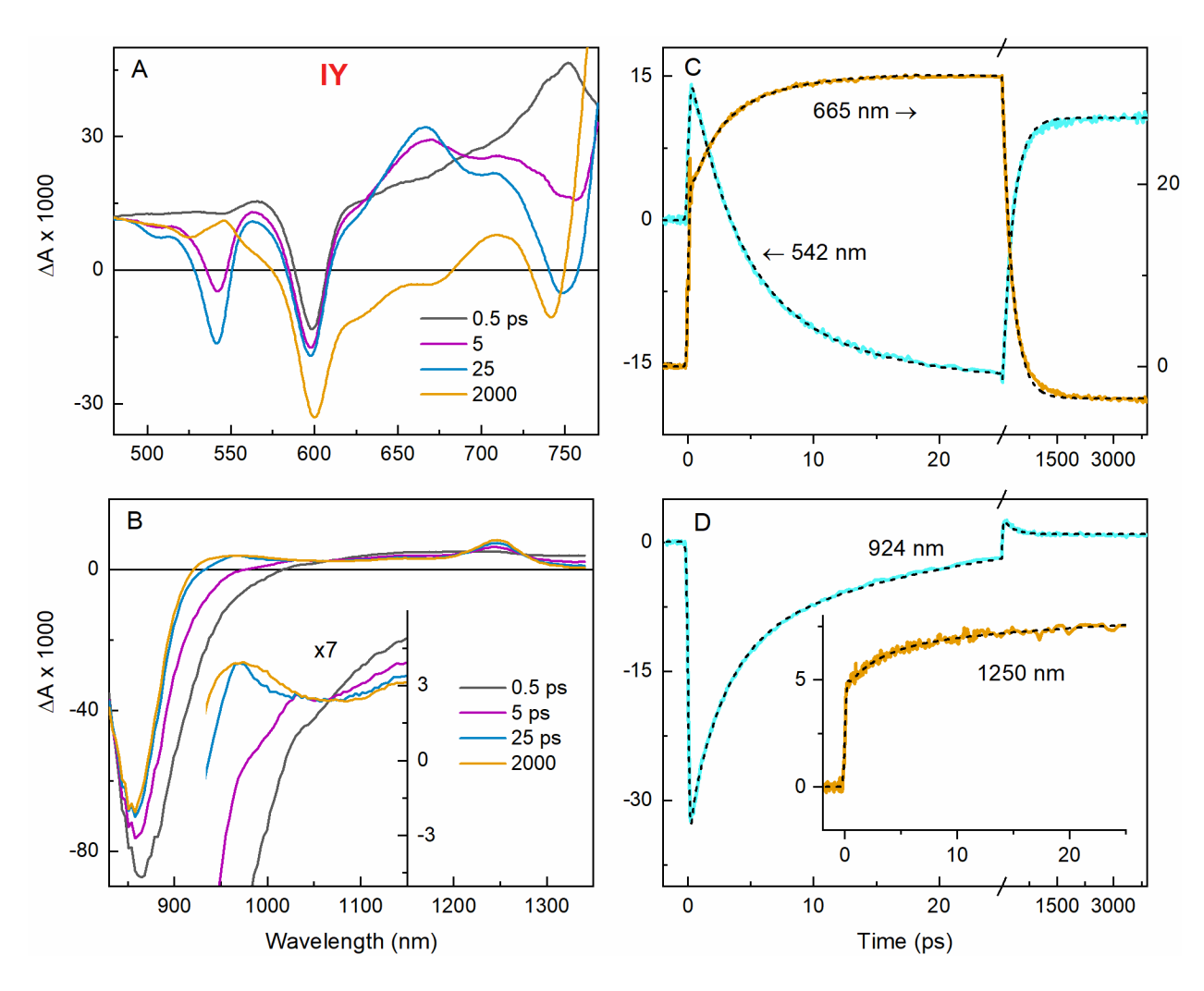


**Fig. S16.** TA summary for IY RCs showing TA data at select times in the visible (A) and NIR (B) regions. The small absorption band for the  $B_A$  anion at  $\sim$ 1030 nm can be seen at 5 ps (mauve) in the inset for panel B. Time profiles and fits to a function consisting of three exponentials and a constant are shown for evolution of  $H_A$  bleaching (C, blue),  $H_A$  anion (C, gold),  $P^*$  stimulated emission (D, blue) and  $P^*$  absorption (D inset, gold). The time constants derived from the fits at these individual wavelengths are consistent with those derived from global analysis DADS and are given in Table S4. Note the break in the time axis scale in C and D at 25 ps.

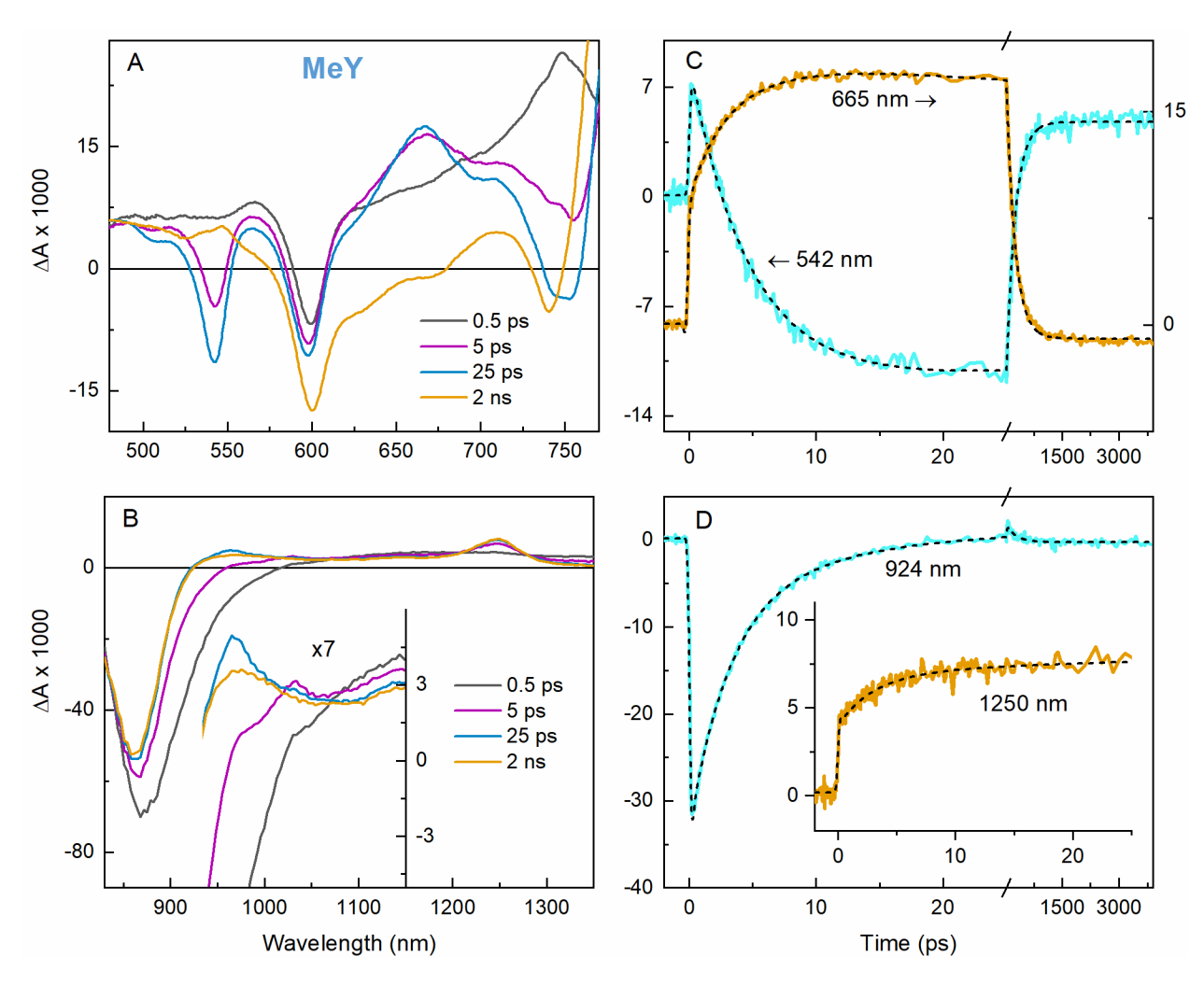


**Fig. S17.** TA summary for MeY RCs showing TA data at select times in the visible (A) and NIR (B) regions. The small absorption band for the  $B_A$  anion at  $\sim$ 1030 nm can be seen at 5 ps (mauve) in the inset for panel B. Time profiles and fits to a function consisting of three exponentials and a constant are shown for evolution of  $H_A$  bleaching (C, blue),  $H_A$  anion (C, gold),  $P^*$  stimulated emission (D, blue) and  $P^*$  absorption (D inset, gold). The time constants derived from the fits at these individual wavelengths are consistent with those derived from global analysis DADS and are given in Table S4. Note the break in the time axis scale in C and D at 25 ps.

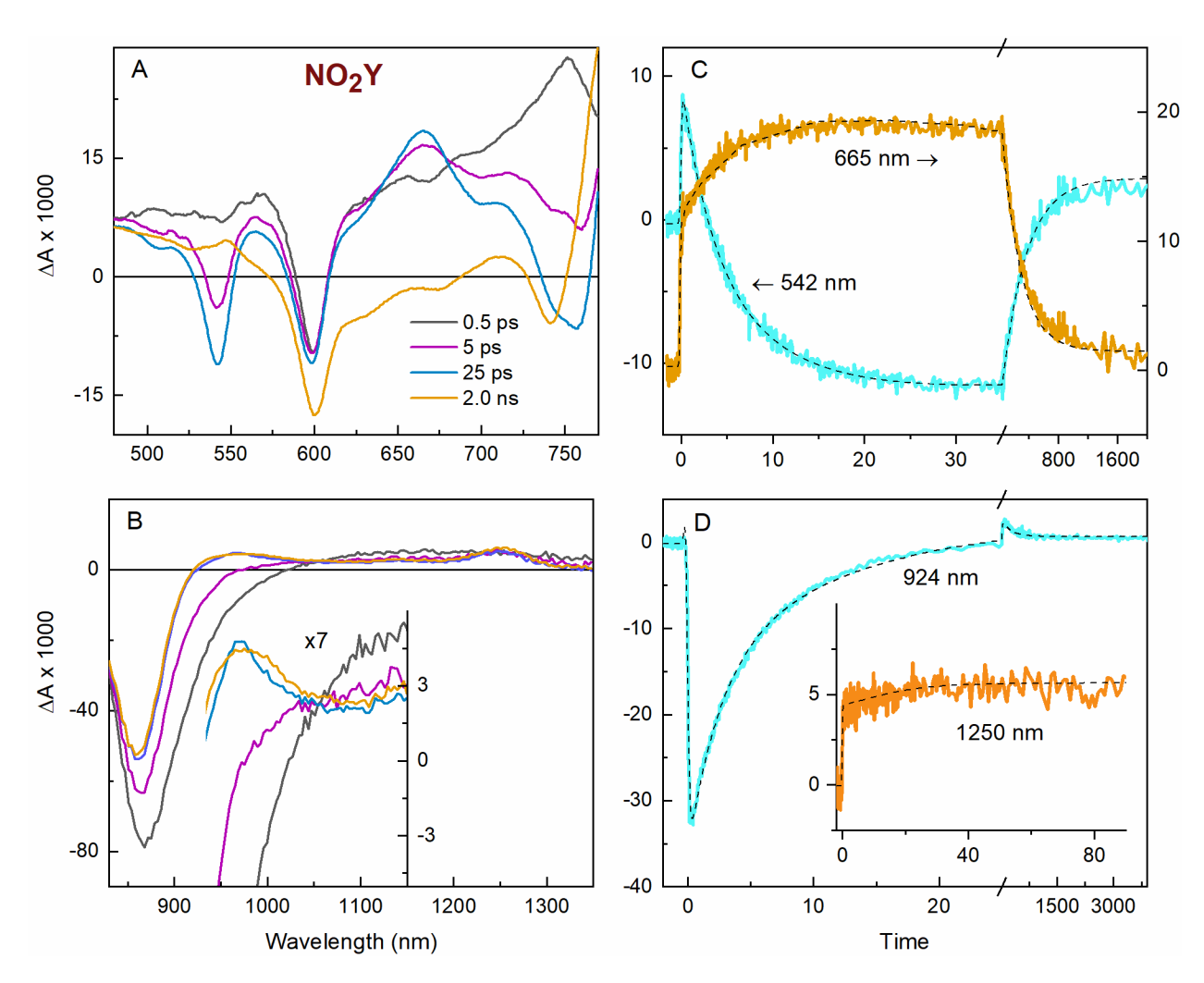


**Fig. S18.** TA summary for NO<sub>2</sub>Y RCs showing TA data at select times in the visible (A) and NIR (B) regions. Note the *lack* of the small absorption band for the B<sub>A</sub> anion at ~1030 nm at 5 ps (mauve) in the inset for panel B. Time profiles and fits to a function consisting of three exponentials and a constant are shown for evolution of H<sub>A</sub> bleaching (C, blue), H<sub>A</sub> anion (C, gold), P\* stimulated emission (D, blue) and P<sup>+</sup> absorption (D inset, gold). The time constants derived from the fits at these individual wavelengths are consistent with those derived from global analysis DADS and are given in Table S4. Note the break in the time axis scale in C and D at 25 ps.

S3.5 Comparison of representative kinetic profiles/fits with mono- vs bi-exponential P\* decay

Section S3.5 contains two figures — Fig. S19 shows kinetics at 924 nm, which is dominated by decay of P\* stimulated emission, and Fig. S20 shows kinetics at 542 nm, which is dominated by growth and decay of bleaching of the  $Q_x$  band of  $H_A$ . Both figures show a kinetic profile for all six samples along with (1) a 2-exponential fit composed of mono-exponential P\*decay plus the P\* $H_A$ <sup>-</sup> decay, and (2) a 3-exponential fit that reflects a bi-exponential P\*decay (i.e.,  $P_1$ \* and  $P_2$ \* decays) plus the P\* $H_A$ <sup>-</sup> decay. It is immediately seen that representing the decay of P\* by a single exponential is inadequate and that the dual-exponential P\* decay model leads to excellent agreement with the data. The P\* decay may reflect the evolution of more than two populations or a distribution of populations. That said, a model involving just two populations,  $P_1$ \* and  $P_2$ \*, appears to capture the main features of the data and differences among the six samples.

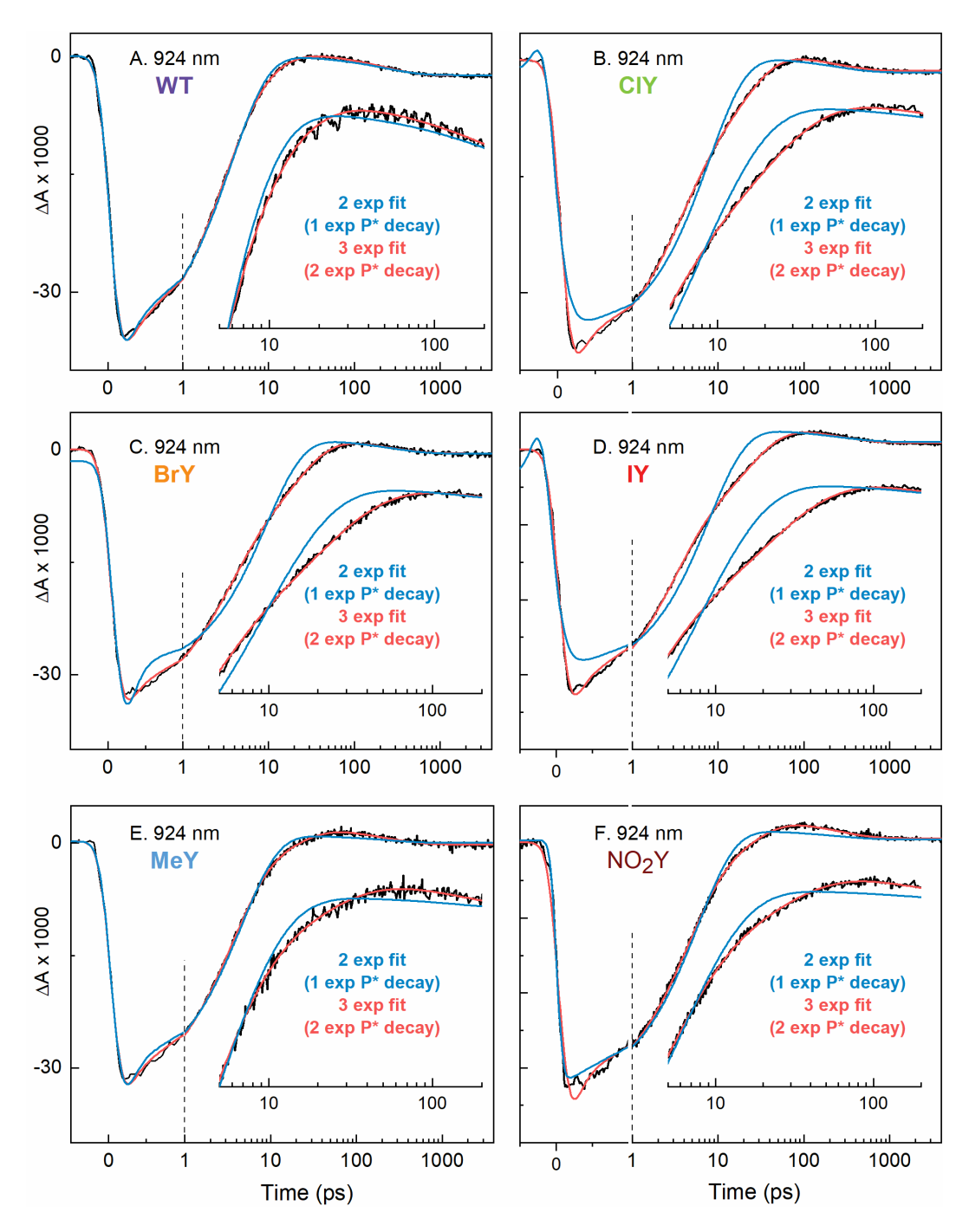


**Fig. S19.** Comparison of the kinetic profiles at 924 nm for WT (A), CIY (B), BrY (C), IY (D), MeY (E), and NO<sub>2</sub>Y (F) RCs. The time axis is linear below 1 ps and logarithmic above 1 ps. Fits to the data (black lines) with a function comprising the instrument response convoluted with two exponentials (blue lines) or three exponentials (red lines) plus a constant are shown. The longest-time exponential reflects a small signal with a downward trend with time due to decay of a small transient absorption at this wavelength by  $P^+H_A^-$ . The main signal is due primarily to decay of stimulated emission from  $P^*$ . Thus, the two-exponential fits assume a mono-exponential  $P^*$  decay (i.e., one  $P^*$  population) and the three-exponential fits assume a bi-exponential  $P^*$  decay (i.e., two  $P^*$  populations denoted  $P_1^*$  and  $P_2^*$ ).

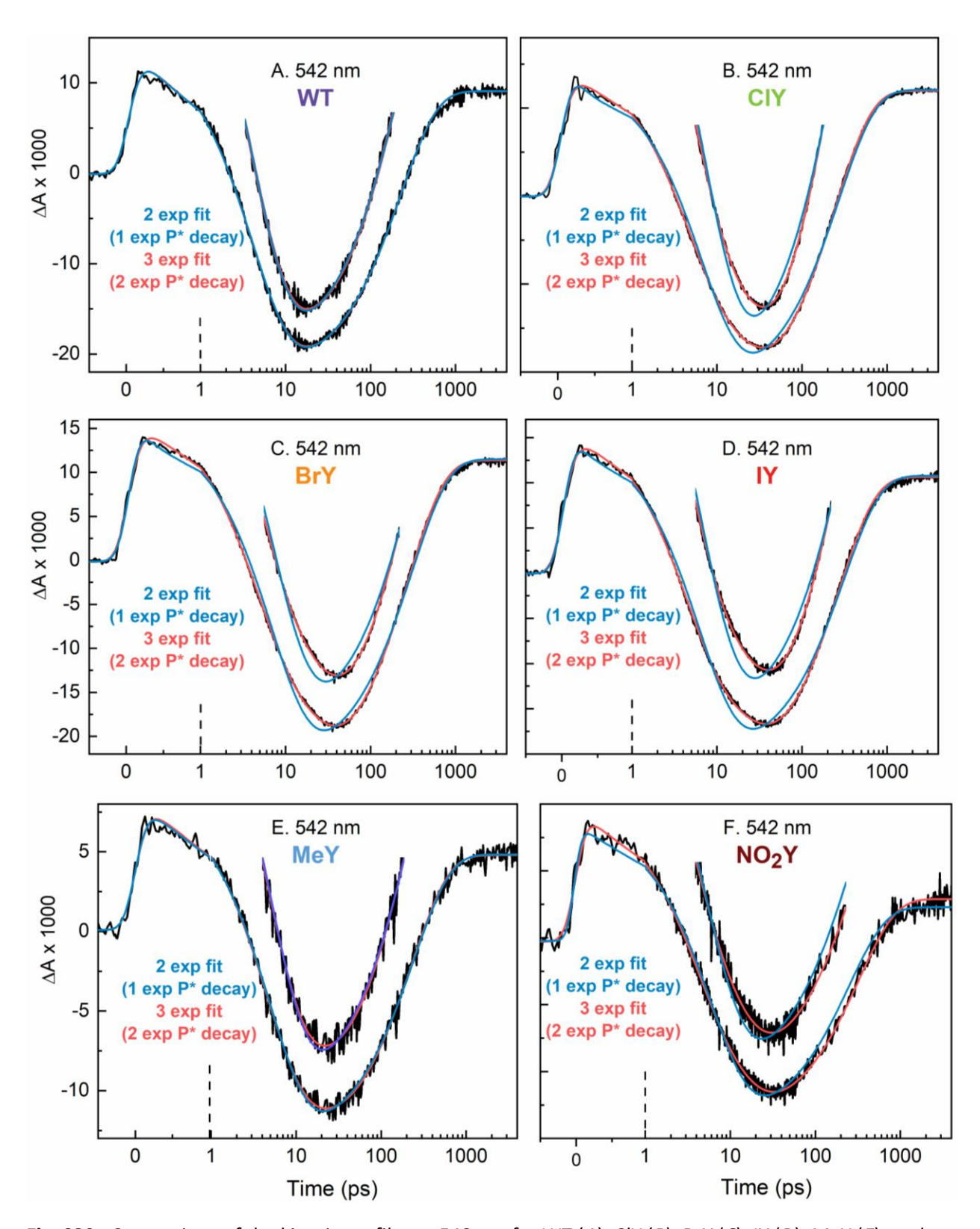


**Fig. S20.** Comparison of the kinetic profiles at 542 nm for WT (A), ClY (B), BrY (C), IY (D), MeY (E), and NO<sub>2</sub>Y (F) RCs. The time axis is linear below 1 ps and logarithmic above 1 ps. Fits to the data (black lines) with a function comprising the instrument response convoluted with two exponentials (blue lines) or

three exponentials (red lines) plus a constant are shown. The longest-time exponential reflects a large signal with an upward trend with time due to decay of the  $H_A$   $Q_x$  bleaching associated with state  $P^+H_A^-$ . The main signal is due primarily to formation of bleaching of the  $H_A$   $Q_x$  absorption associated with state  $P^+H_A^-$ , and reflects the lifetime of  $P^*$ , which produces  $P^+H_A^-$ . Thus, the two-exponential fits assume a mono-exponential  $P^*$  decay (i.e., one  $P^*$  population) and the three-exponential fits assume a bi-exponential  $P^*$  decay (i.e., two  $P^*$  populations denoted  $P_1^*$  and  $P_2^*$ ).

## S3.6 Evolution of the NIR TA specta at early times for each sample

Section S3.6 (Figs. S21–S38) contains three figures for each sample. These three spectra show, with different details of the presentation, the evolution of the NIR TA spectrum over the first ~25 ps after excitation. For each sample, the first figure in the trio (e.g., Fig. S21 for WT) shows the spectral evolution over a large NIR wavelength range (900-1350 nm) and marks the position of the weak ~1030 nm absorption feature for the  $B_A$  anion for state  $P^+B_A^-$ . This 1030 nm feature reaches its maximum amplitude at ~4 ps and is largely gone by ~10 ps. The more prominent feature at 1250 nm is an absorption band of the oxidized BChI dimer  $P^+$ . That feature is expected to form along with  $P^+B_A^-$  (in the population that undergoes  $P_1^* \to P^+B_A^- \to P^+H_A^-$  two-step ET) and form along with  $P^+H_A^-$  in the population that undergoes  $P_2^* \to P^+H_A^-$  one-step superexchange ET. The 1250 nm feature does not change in amplitude as  $P^+B_A^- \to P^+H_A^-$  and  $P^+H_A^- \to P^+Q_A^-$  ET occur because these processes have a near quantitative yield. Indeed, the 1250 nm band of  $P^+$  does not change amplitude significantly over the time course of the measurements. This can be seen in the representative TA data presented in Section S3.4.

It should be noted that spectra for the BChl anion in solution (56, 57), and prior work on spectra for trapped  $P^+B_A^-$  and analogous spectra for  $P^+\beta_A^-$  (where  $\beta_A$  is a BChl that replaces  $H_A$ ) (58), suggest that the extinction coefficient for the  $B_A$  anion band at 1030 nm is comparable to that of the  $P^+$  band at 1250 nm. Thus, the much smaller amplitude of the 1030 nm band of  $B_A^-$  compared to the 1250 nm band of  $P^+$  is an indicator that the maximum transient population of  $P^+B_A^-$  is small. This deduction is consistent with the global analysis and SADS described below.

For each sample, the top panel in the second of the trio in Section S3.6 (e.g, Fig. S22 for WT) is the same as the first (Fig. S21 for WT) but shades the area under the 1030 nm  $B_A$  anion band. Panel B of the second figure plots the integrated area under the 1030 band as a function of time over the entire time course of the data set. Also shown is a 3-exponenital fit to the 1030 nm band integrated area as a function of time, giving one rise component and two decay components. (Fits with one decay

component do not adequately describe the data.) Note that there may be a contribution of  $P^*$  (at early times) and  $P^*H_A^-$  (at longer times) to the integral because the contribution of these states to the baseline may not be precisely linear (as is assumed in performing the integrations) and evolve with time. Also, note that the rise component likely reflects the decay time of  $P^*B_A^-$  (rather than its formation time as  $P^*$  decays); the shortest time component in a set of events (even if it is the second step in a two-step process) will necessarily show up first in a time evolution. For  $NO_2Y$  RCs, the apparent rise of the integrated area under the 1030 nm band (i.e., the  $P^*B_A^-$  lifetime, Fig. S37) is instrument-response limited, again suggesting little (if any) transient population of this state for this sample. The third figure in the trio (e.g., Fig. S23 for WT) differs from the top panel in the second figure in showing a reduced wavelength range (930-1130 nm) so as to better focus on the area under the 1030 nm band and how this evolves as  $P^*B_A^-$  forms and decays.

Comparison of these figures in Section S3.6 for each sample, particularly the third figure in the set for each sample, shows that the basic description given above for WT RCs holds for the CIY, BrY, IY, and MeY variants. However, there is a significant difference for  $NO_2Y$  RCs. Comparing the reduced wavelength range in Fig. S23 for WT and in Fig. S38 for  $NO_2Y$  RCs shows that the 1030 nm band does not develop the same amplitude in  $NO_2Y$  RCs as in WT (and the other mutants). It is either not present or barely resolvable above the noise. Furthermore, for the  $NO_2Y$  mutant, the apparent 1030 nm band of  $P^+B_A^-$  appears to reach its maximum amplitude at shorter times (2.0-2.5 ps) and decay away more quickly compared to WT (and the other mutants). These observations suggest that for  $NO_2Y$  RCs, the state  $P^+B_A^-$  either (1) is not produced as in other variants, or (2) decays more rapidly (< 1 ps) than in the other variants (~1.5 ps), or (3) both of these scenarios contribute. Regardless of the exact details, there is no doubt that the formation/decay of  $P^+B_A^-$  is greatly perturbed in  $NO_2Y$  RCs compared to WT and to the CIY, BrY, IY, and MeY variants.

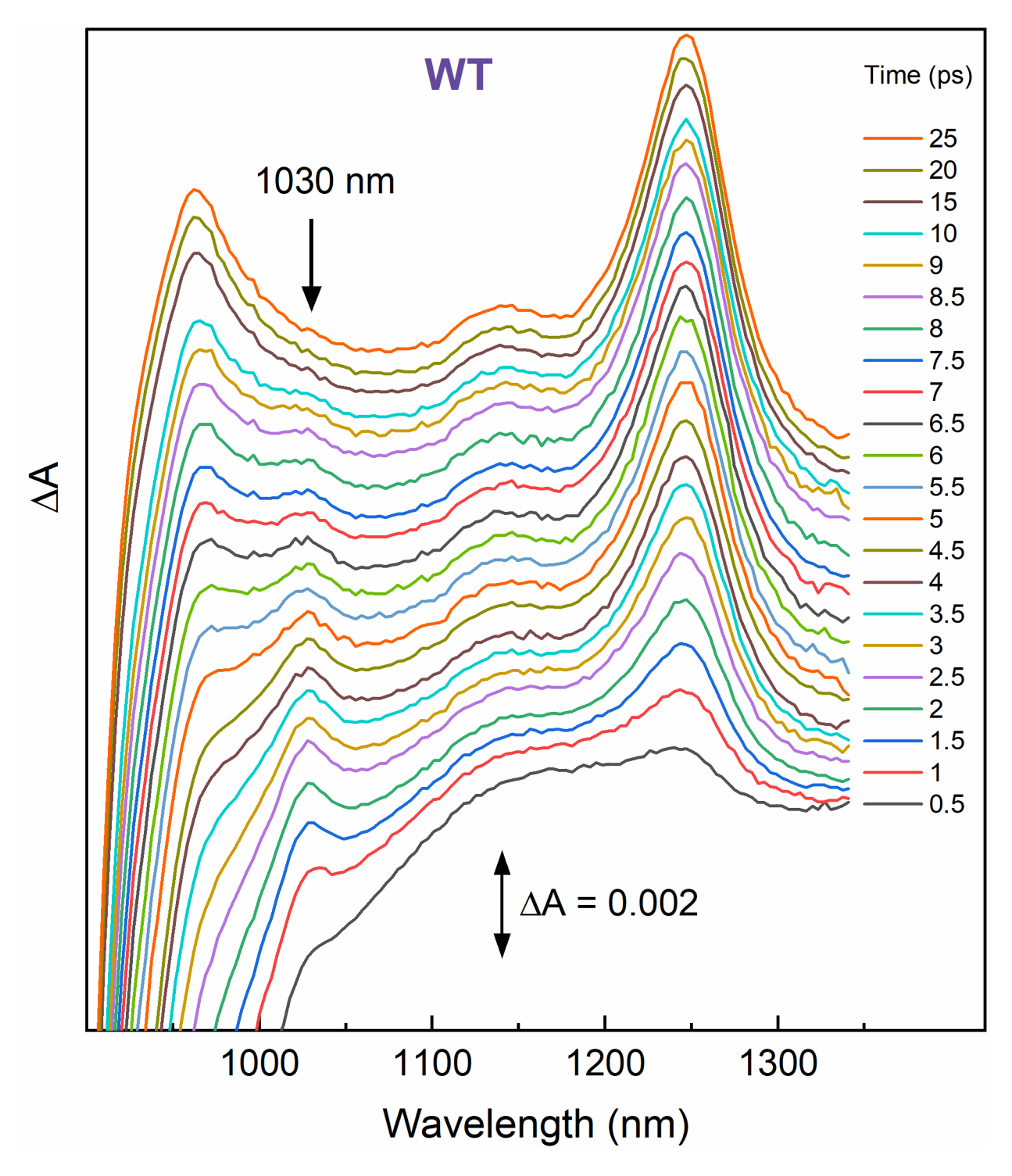
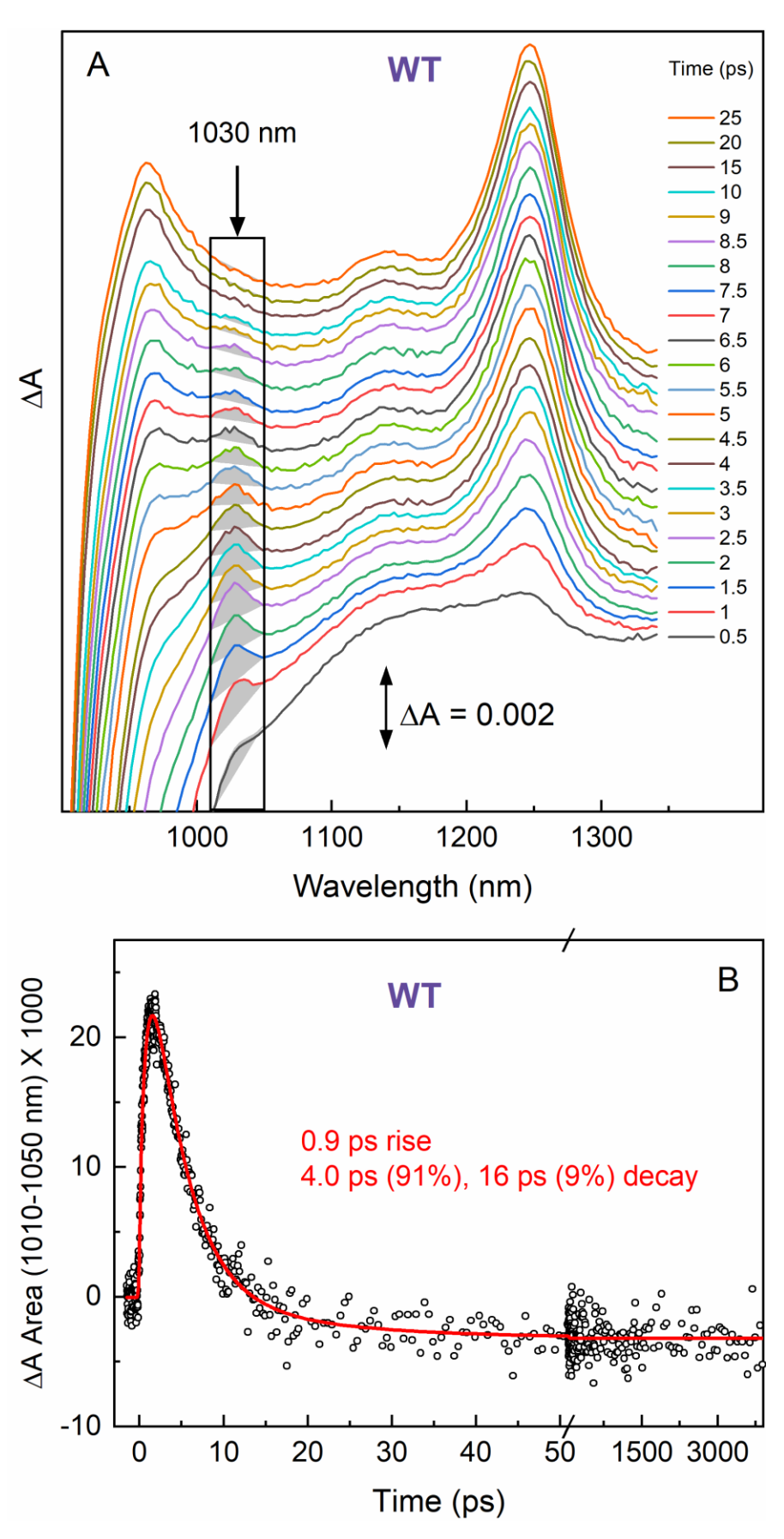
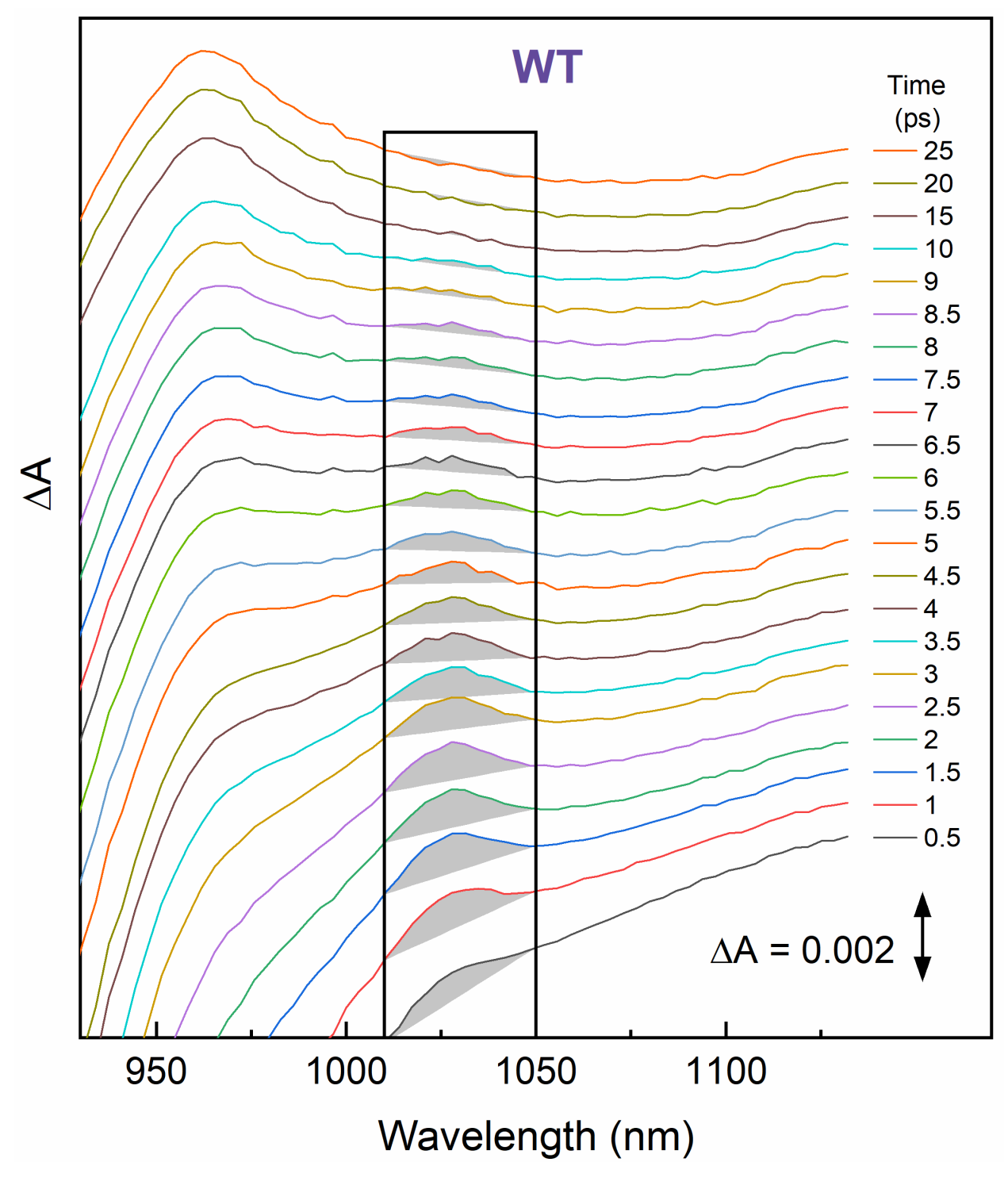


Fig. S21. Evolution of the NIR TA spectra at early times for WT RCs.



**Fig. S22.** (*A*) Evolution of the NIR TA spectra at early times for WT RCs. The spectra in this stack plot are vertically offset from one another to best display the integrated area (1010-1050 nm) of the 1030 nm band of  $P^+B_A^-$ . A plot with a reduced wavelength span (930-1170 nm) is shown in Fig. S23. (*B*) Evolution of the integrated area under the 1030 nm band using a straight-line baseline across the integration region (1010-1050). The red line is a 3-exponential fit giving one rise component and two decay components. Note that there may be a contribution of  $P^*$  (at early times) and  $P^+H_B^-$  (at longer times) to the integrated area because the contribution of these states to the baseline may not be precisely linear and will differ with time. Also, note that the 0.9 ps rise component reflects the *decay* time of  $P^+B_A^-$ ; the shortest time component in a set of events (regardless of its position in a sequence of events) will necessarily show up first in the time evolution data. Note the change in the time axis at 50 ps.



**Fig. S23.** Evolution of a portion (930-1170 nm) of the NIR TA spectra at early times for WT RCs. The spectra in this stack plot are vertically offset from one another to best display the integrated area (1010-1050 nm) of the 1030 nm band of  $P^+B_A^-$ .

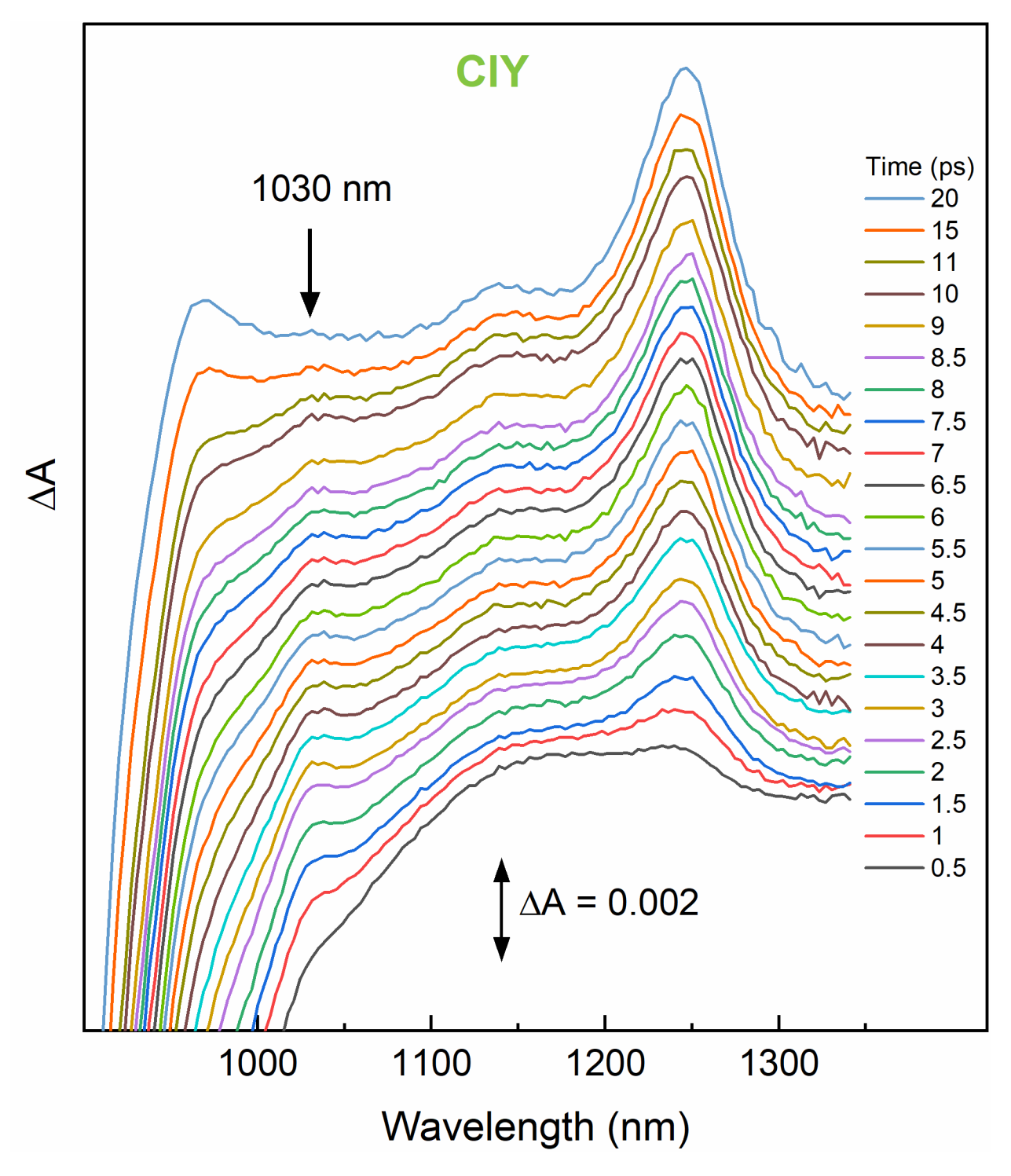
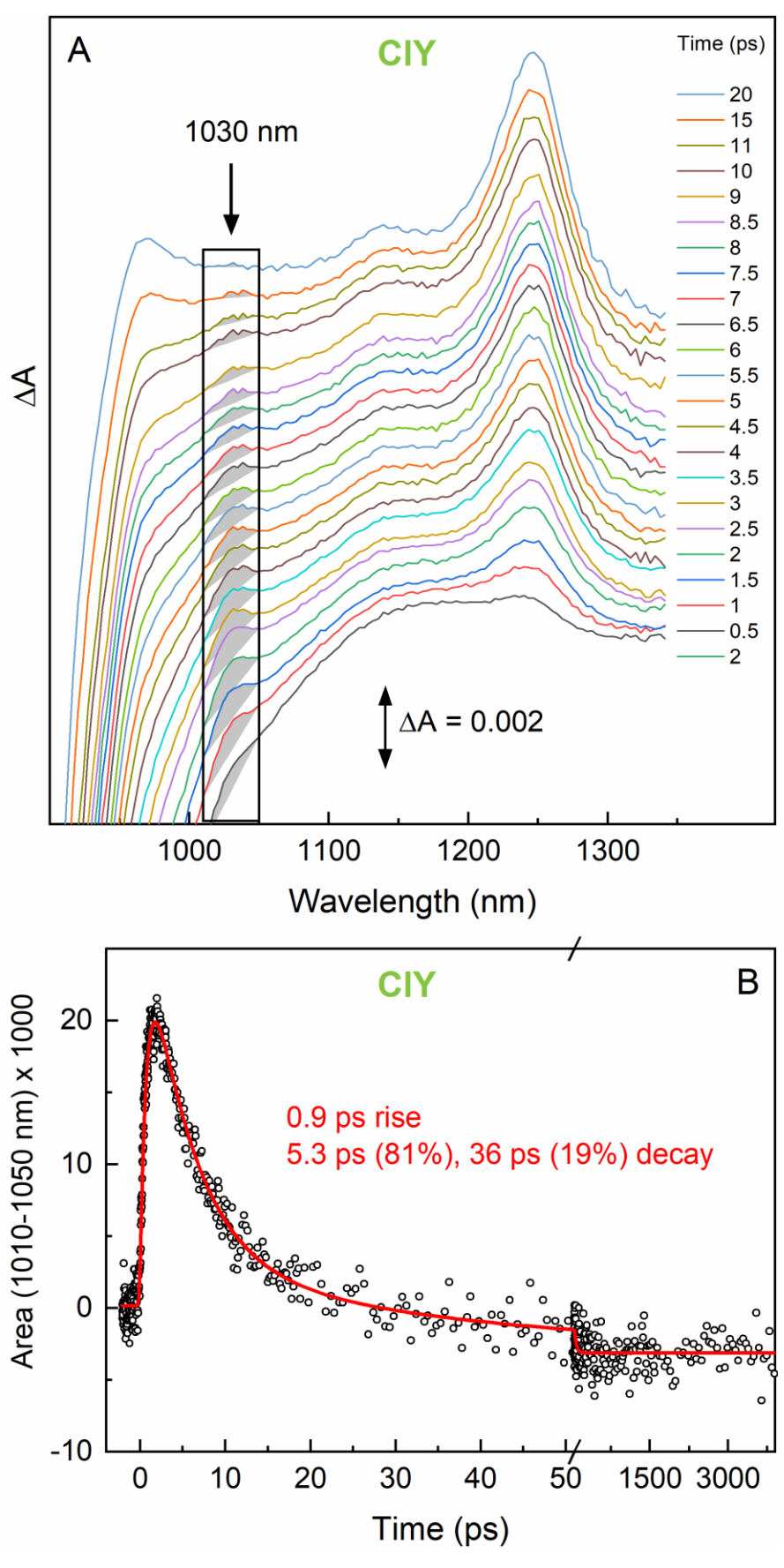
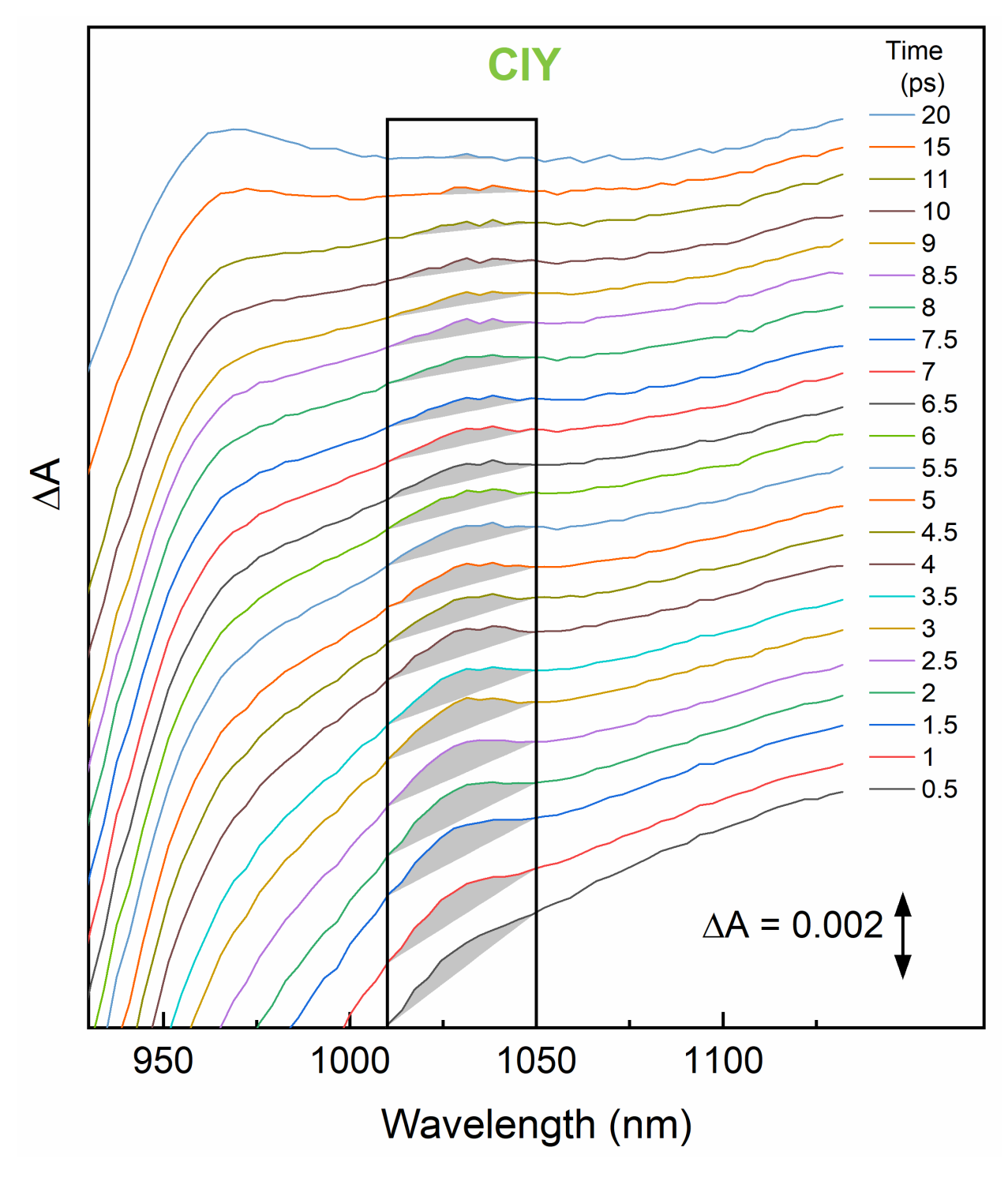


Fig. S24. Evolution of the NIR TA spectra at early times for CIY RCs.



**Fig. S25.** (*A*) Evolution of the NIR TA spectra at early times for CIY RCs. The spectra in this stack plot are vertically offset from one another to best display the integrated area (1010-1050 nm) of the 1030 nm band of  $P^+B_A^-$ . A plot with a reduced wavelength span (930-1170 nm) is shown in Fig. S26. (*B*) Evolution of the integrated area under the 1030 nm band using a straight-line baseline across the integration region (1010-1050). The red line is a 3-exponential fit giving one rise component and two decay components. Note that there may be a contribution of  $P^*$  (at early times) and  $P^+H_B^-$  (at longer times) to the integral because the contribution of these states to the baseline may not be precisely linear and will differ with time. Also, note that rise component likely reflects the *decay* time of  $P^+B_A^-$  (rather than its formation time as  $P^*$  decays); the shortest time component in a set of events (even if it is the second step in a two-step process) will necessarily show up first in a time evolution. Note the change in the time axis at 50 ps.



**Fig. S26.** Evolution of a portion (930-1170 nm) of the NIR TA spectra at early times for CIY RCs. The spectra in this stack plot are vertically offset from one another to best display the integrated area (1010-1050 nm) of the 1030 nm band of  $P^+B_A^-$ .

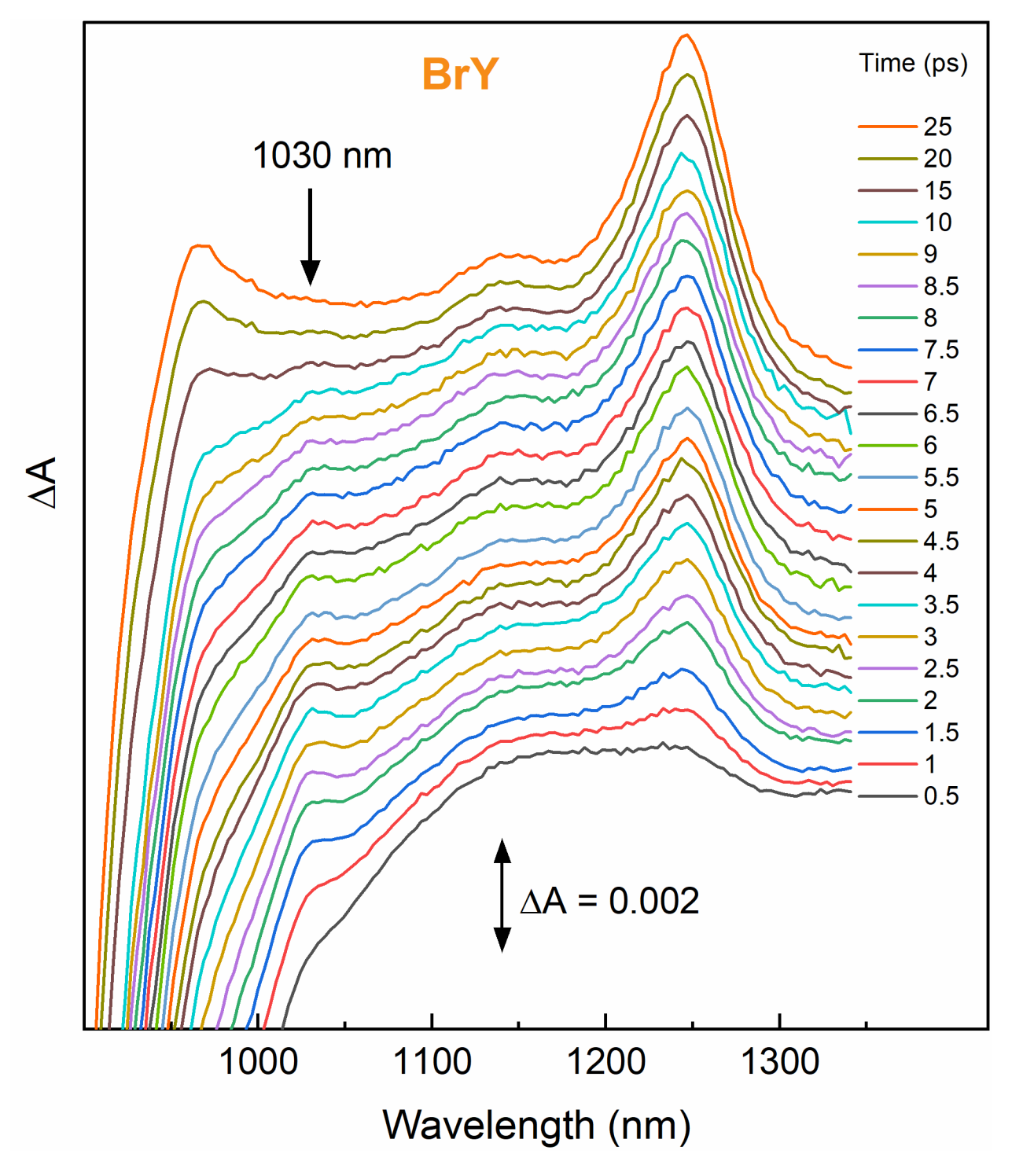
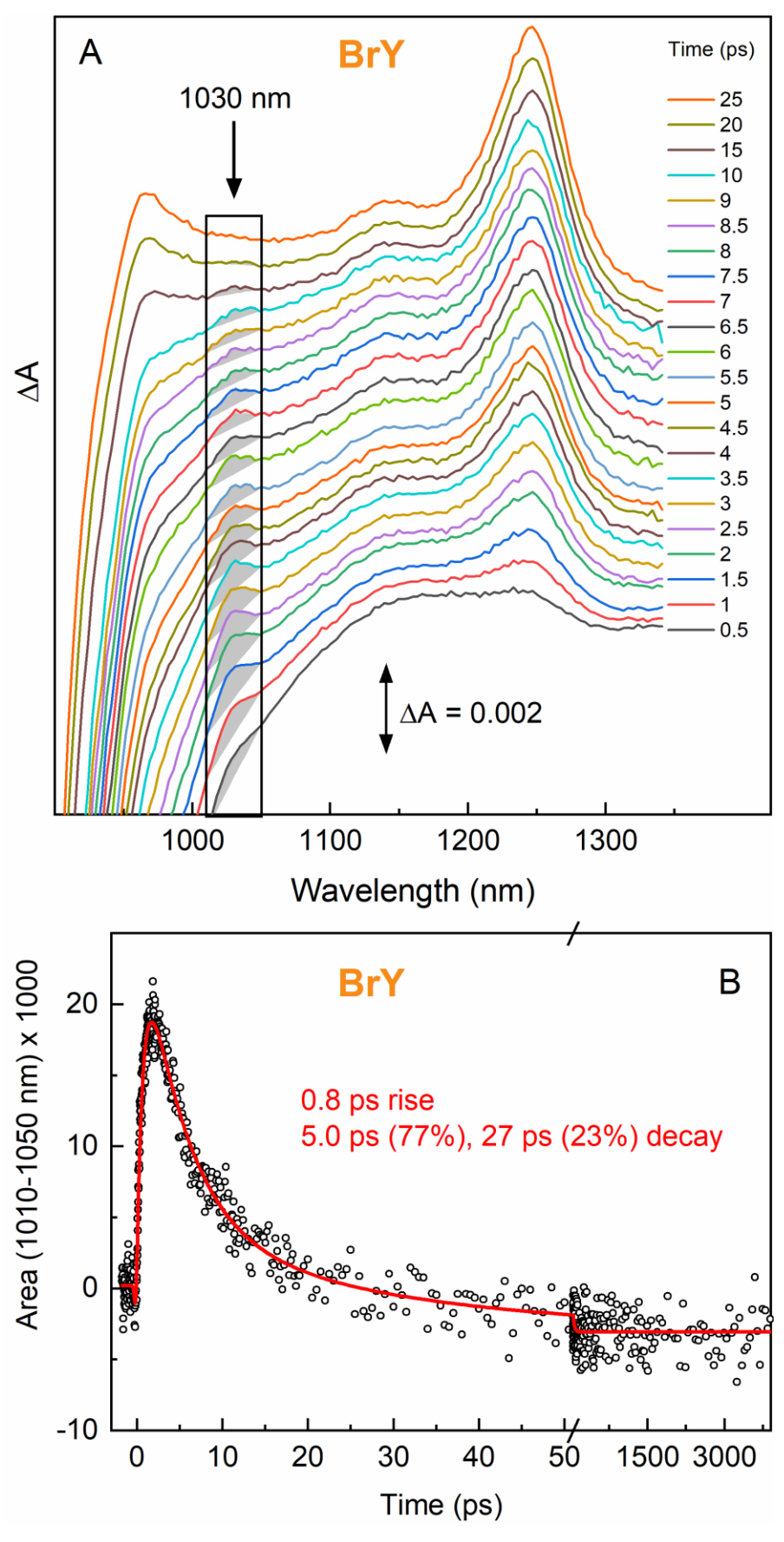
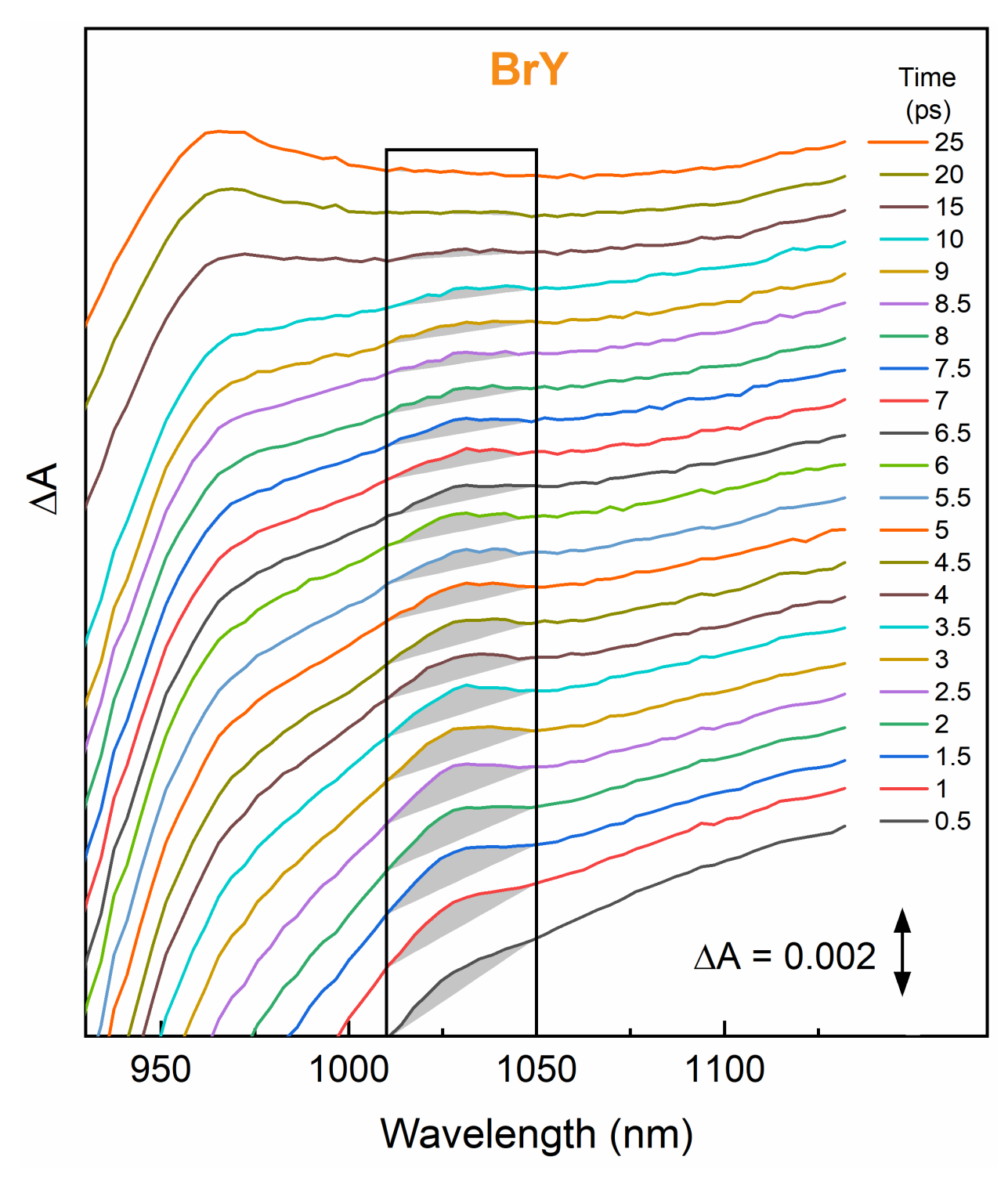


Fig. S27. Evolution of the NIR TA spectra at early times for BrY RCs.



**Fig. S28.** (*A*) Evolution of the NIR TA spectra at early times for BrY RCs. The spectra in this stack plot are vertically offset from one another to best display the integrated area (1010-1050 nm) of the 1030 nm band of  $P^+B_A^-$ . A plot with a reduced wavelength span (930-1170 nm) is shown in Fig. S29. (*B*) Evolution of the integrated area under the 1030 nm band using a straight-line baseline across the integration region (1010-1050). The red line is a 3-exponential fit giving one rise component and two decay components. Note that there may be a contribution of  $P^*$  (at early times) and  $P^+H_B^-$  (at longer times) to the integral because the contribution of these states to the baseline may not be precisely linear and will differ with time. Also, note that rise component likely reflects the *decay* time of  $P^+B_A^-$  (rather than its formation time as  $P^*$  decays); the shortest time component in a set of events (even if it is the second step in a two-step process) will necessarily show up first in a time evolution. Note the change in the time axis at 50 ps.



**Fig. S29.** Evolution of a portion (930-1170 nm) of the NIR TA spectra at early times for BrY RCs. The spectra in this stack plot are vertically offset from one another to best display the integrated area (1010-1050 nm) of the 1030 nm band of  $P^+B_A^-$ .

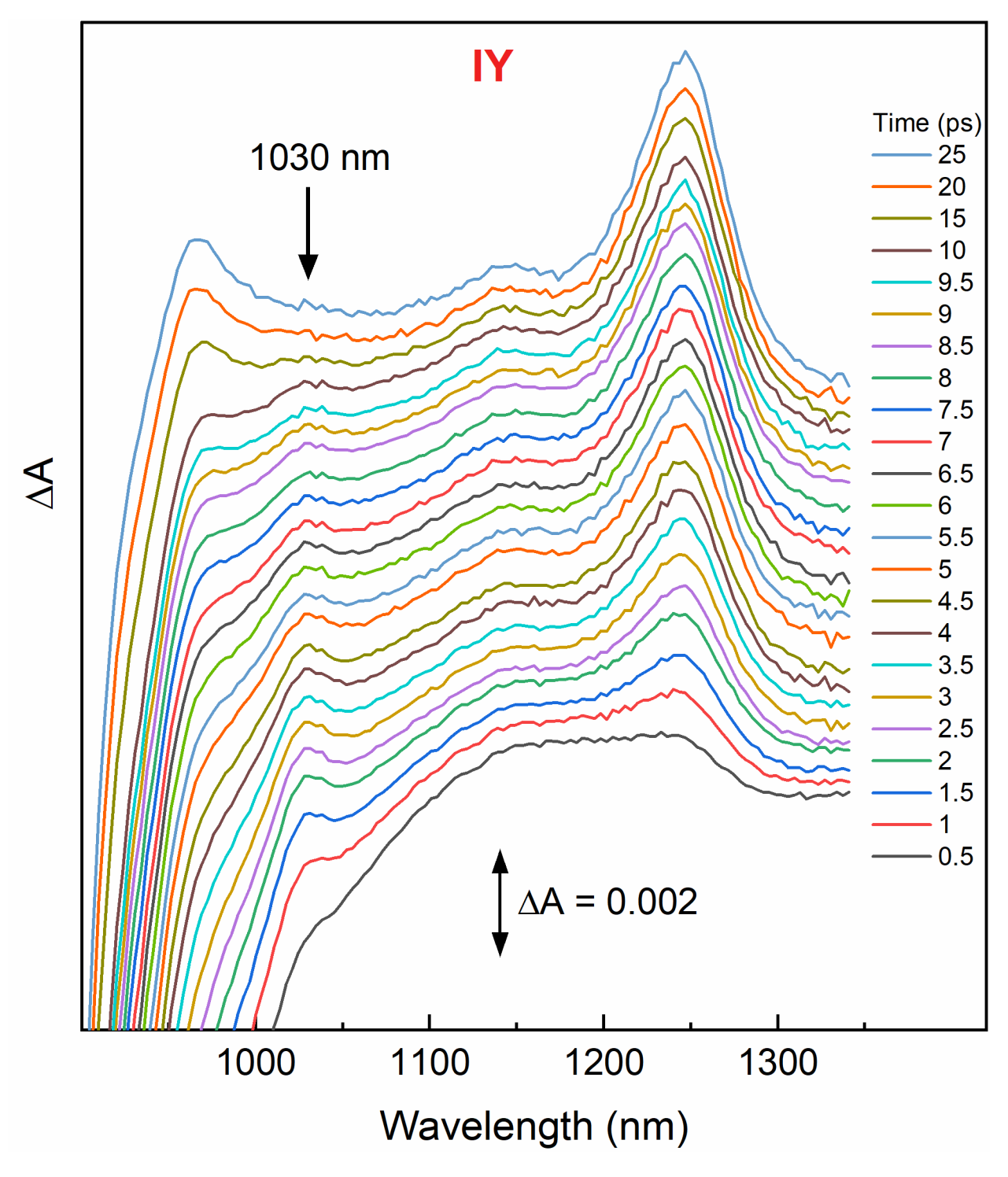
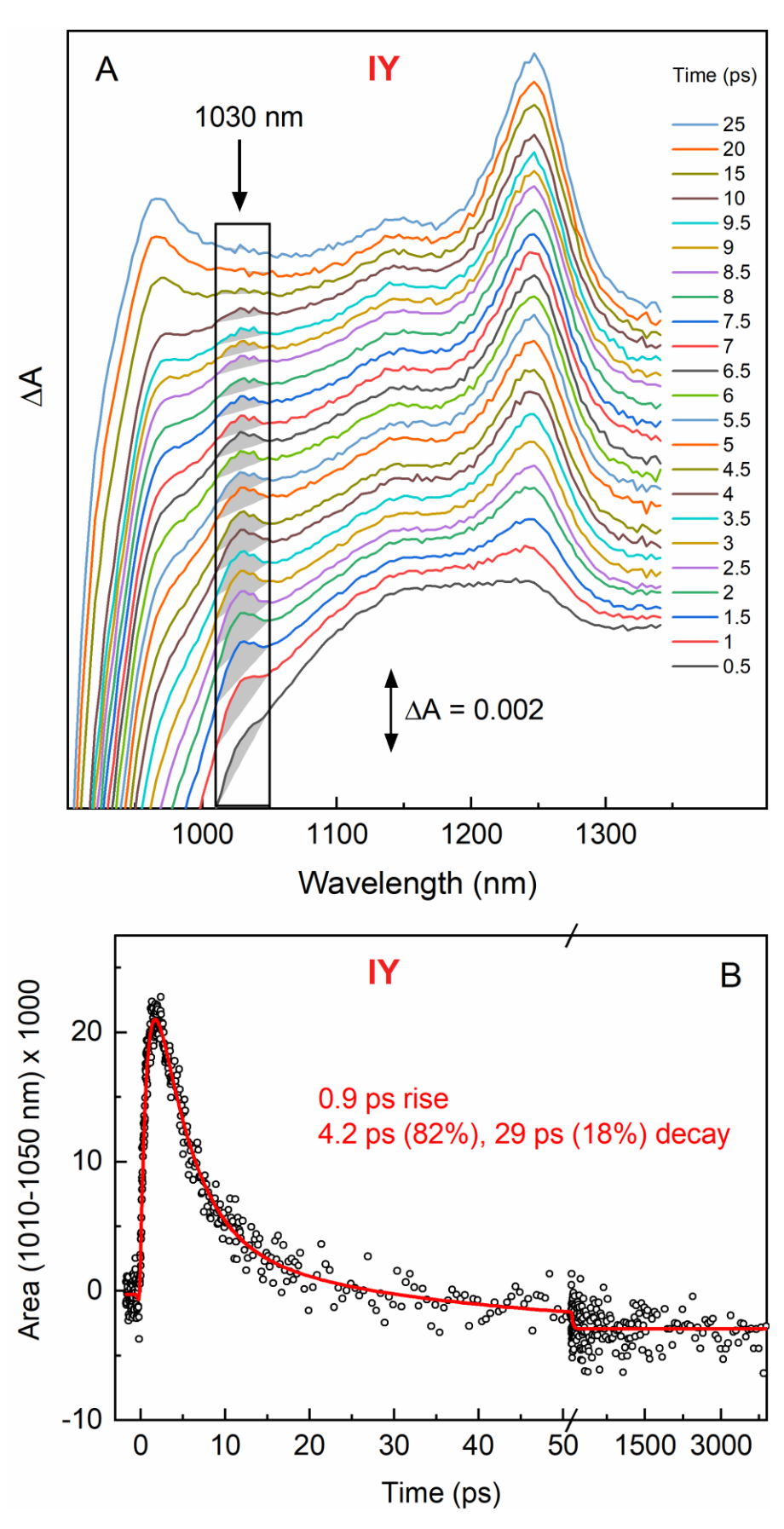
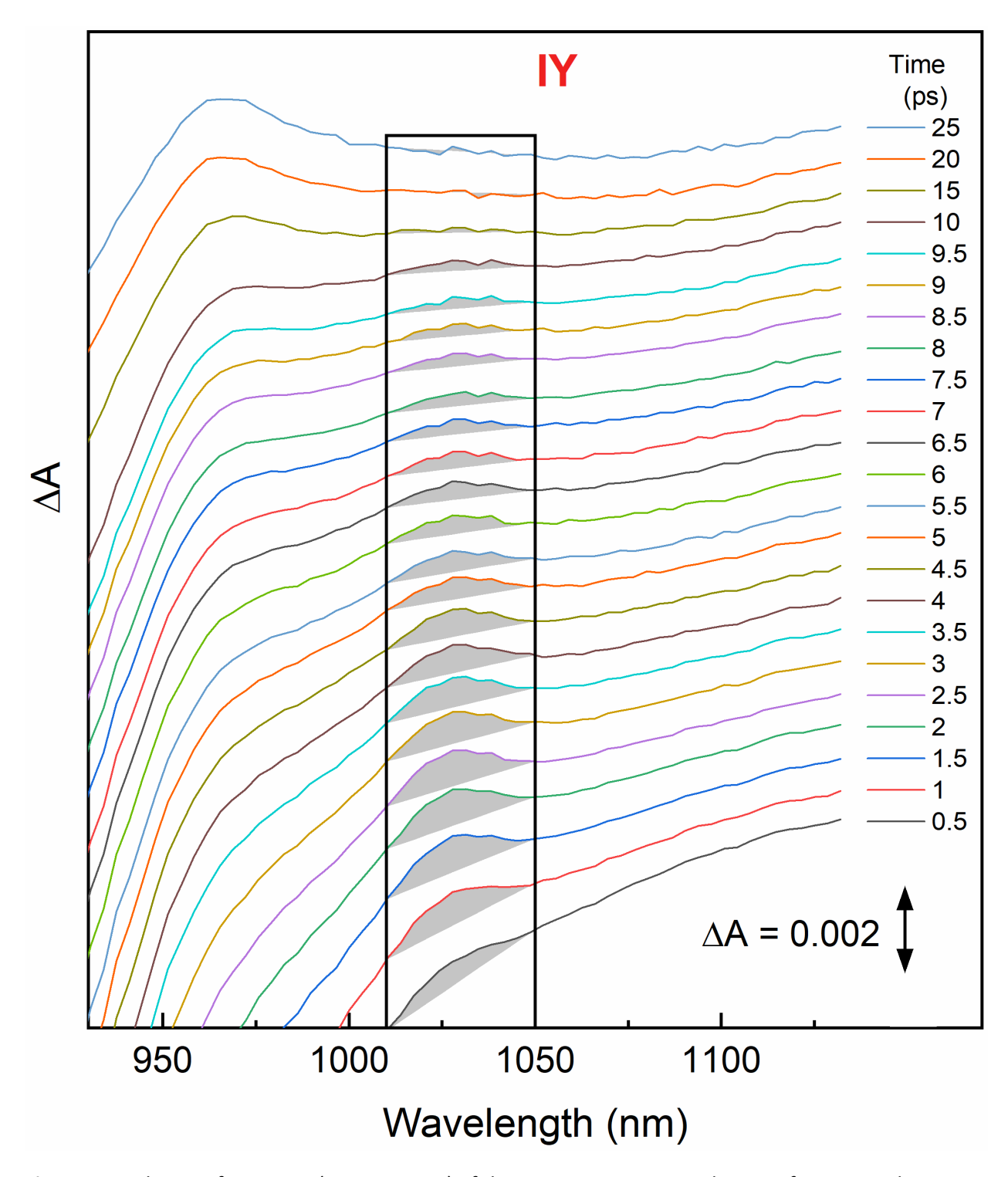


Fig. S30. Evolution of the NIR TA spectra at early times for IY RCs.



**Fig. S31.** (*A*) Evolution of the NIR TA spectra at early times for IY RCs. The spectra in this stack plot are vertically offset from one another to best display the integrated area (1010-1050 nm) of the 1030 nm band of  $P^+B_A^-$ . A plot with a reduced wavelength span (930-1170 m) is shown in Fig. S32. (*B*) Evolution of the integrated area under the 1030 nm band using a straight-line baseline across the integration region (1010-1050). The red line is a 3-exponential fit giving one rise component and two decay components. Note that there may be a contribution of  $P^*$  (at early times) and  $P^+H_B^-$  (at longer times) to the integral because the contribution of these states to the baseline may not be precisely linear and will differ with time. Also, note that rise component likely reflects the *decay* time of  $P^+B_A^-$  (rather than its formation time as  $P^*$  decays); the shortest time component in a set of events (even if it is the second step in a two-step process) will necessarily show up first in a time evolution. Note the change in the time axis at 50 ps.



**Fig. S32.** Evolution of a portion (930-1170 nm) of the NIR TA spectra at early times for IY RCs. The spectra in this stack plot are vertically offset from one another to best display the integrated area (1010-1050 nm) of the 1030 nm band of  $P^{+}B_{A}^{-}$ .

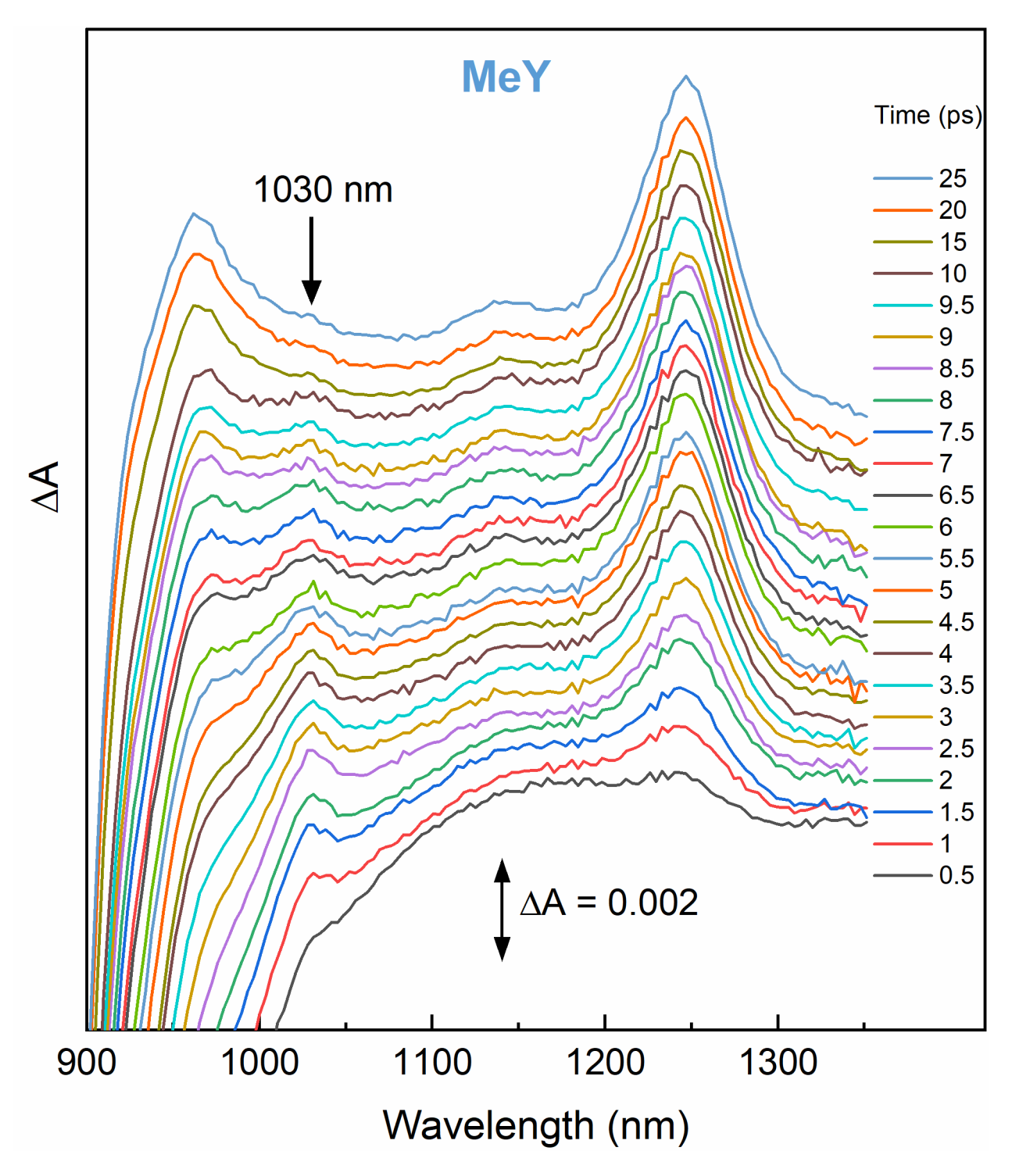
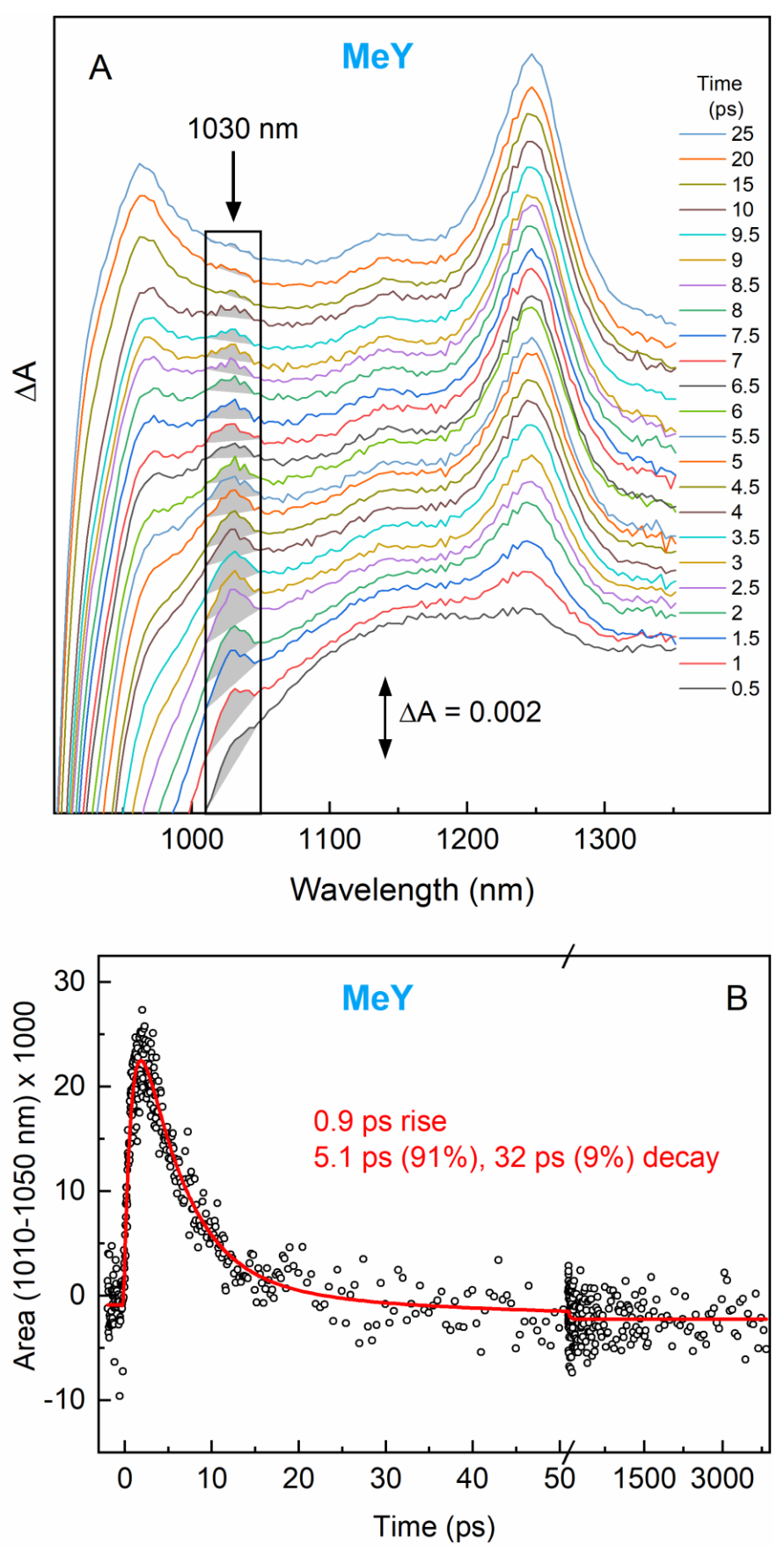
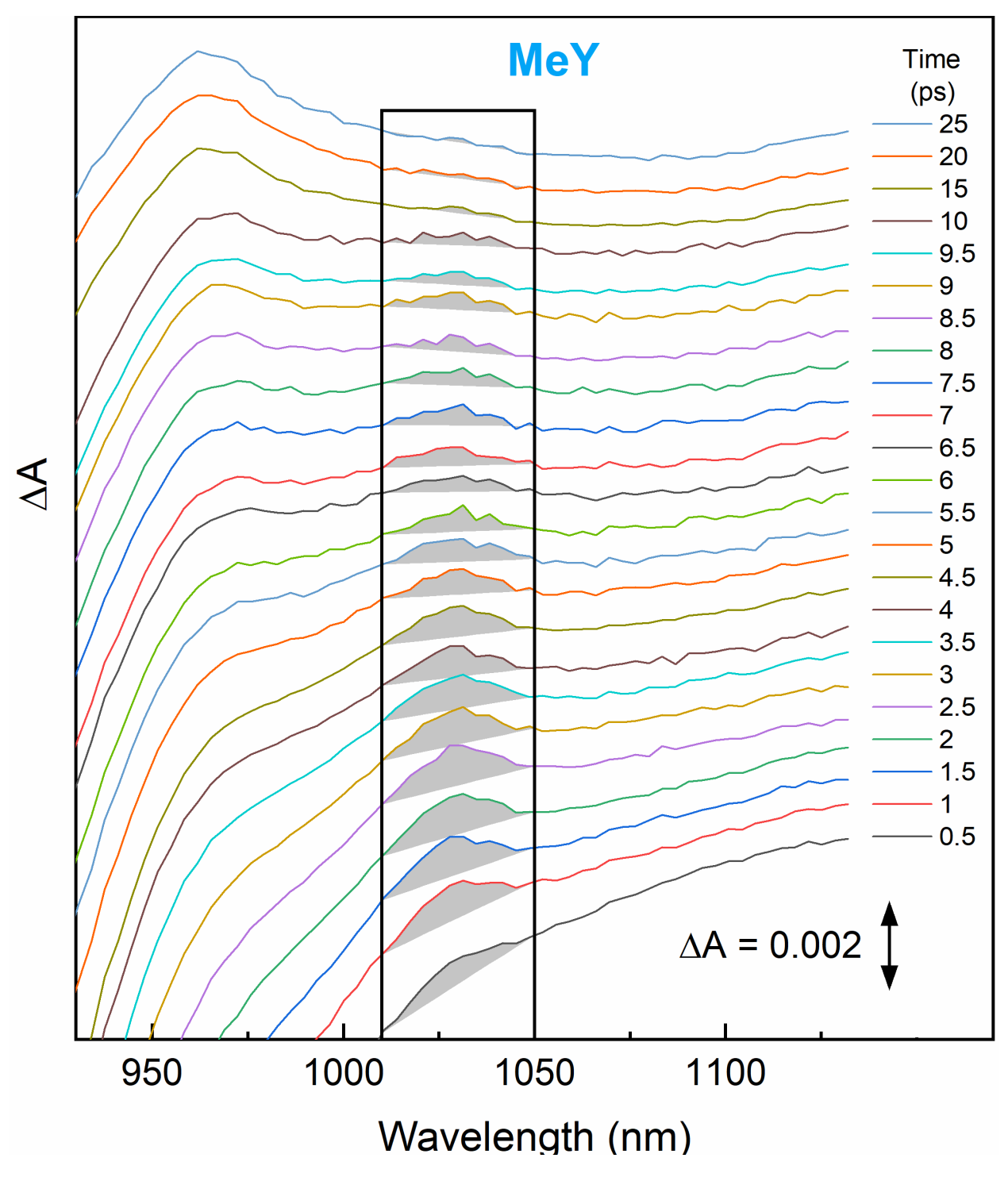


Fig. S33. Evolution of the NIR TA spectra at early times for MeY RCs.



**Fig. S34.** (*A*) Evolution of the NIR TA spectra at early times for MeY RCs. The spectra in this stack plot are vertically offset from one another to best display the integrated area (1010-1050 nm) of the 1030 nm band of  $P^+B_A^-$ . A plot with a reduced wavelength span (930-1170 nm) is shown in Fig. S35. (*B*) Evolution of the integrated area under the 1030 nm band using a straight-line baseline across the integration region (1010-1050). The red line is a 3-exponential fit giving one rise component and two decay components. Note that there may be a contribution of  $P^*$  (at early times) and  $P^+H_B^-$  (at longer times) to the integral because the contribution of these states to the baseline may not be precisely linear and will differ with time. Also, note that rise component likely reflects the *decay* time of  $P^+B_A^-$  (rather than its formation time as  $P^*$  decays); the shortest time component in a set of events (even if it is the second step in a two-step process) will necessarily show up first in a time evolution. Note the change in the time axis at 50 ps.



**Fig. S35.** Evolution of a portion (930-1170 nm) of the NIR TA spectra at early times for MeY RCs. The spectra in this stack plot are vertically offset from one another to best display the integrated area (1010-1050 nm) of the 1030 nm band of  $P^+B_A^-$ .

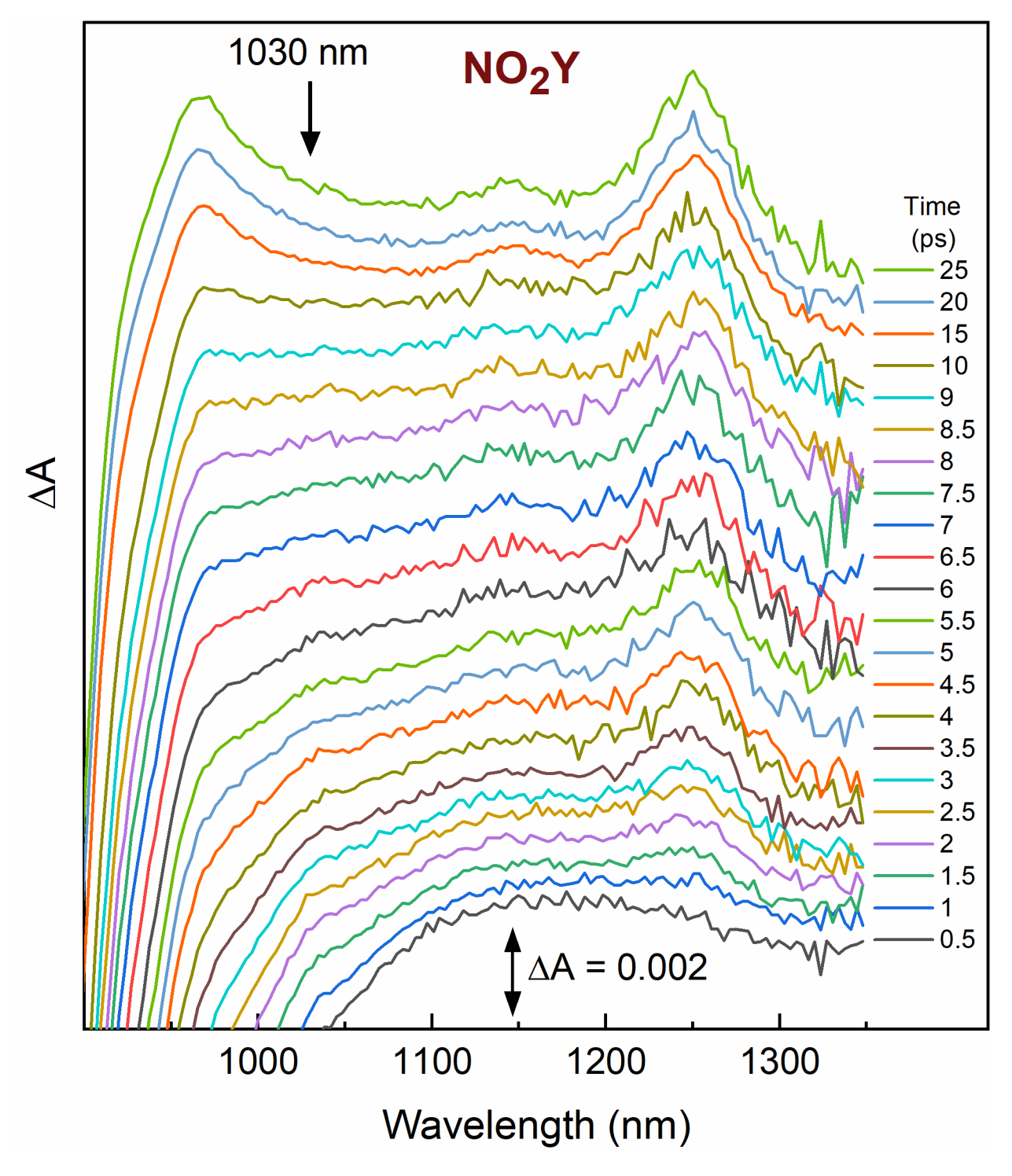
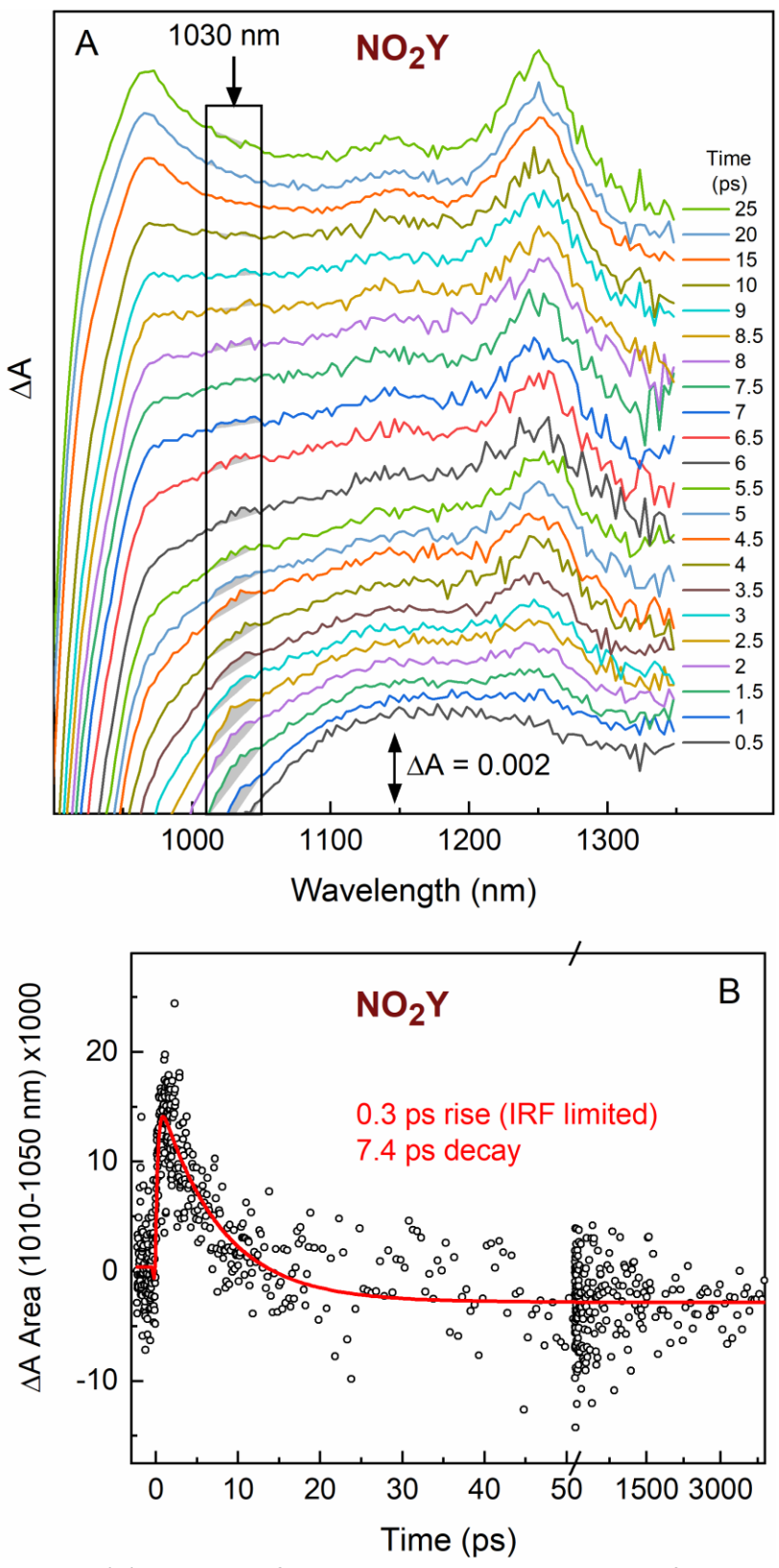
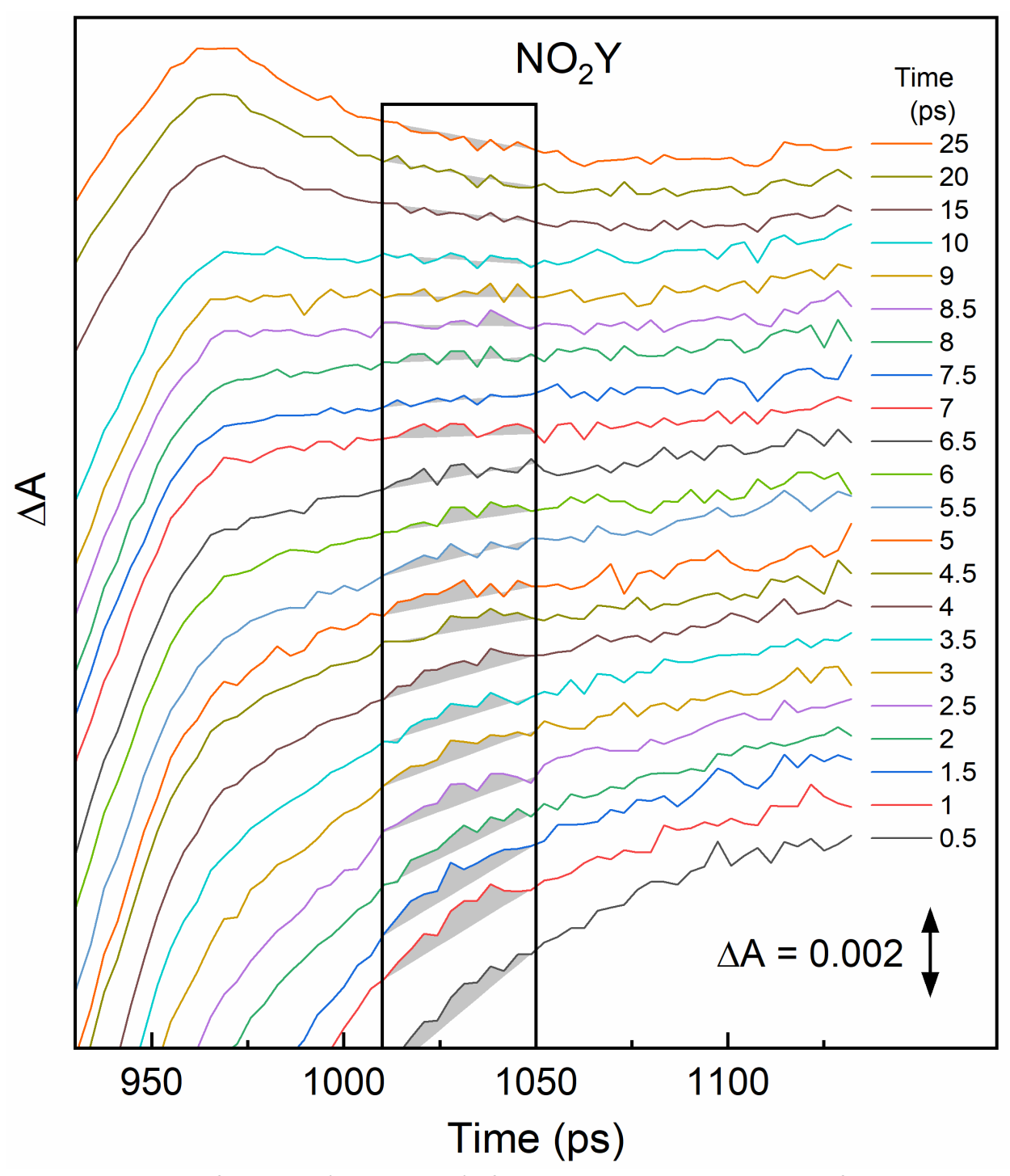


Fig. S36. Evolution of the NIR TA spectra at early times for NO<sub>2</sub>Y RCs.



**Fig. S37.** (*A*) Evolution of the NIR TA spectra at early times for  $NO_2Y$  RCs. The spectra are vertically offset from one another to best display the integrated area (1010-1050 nm) of the 1030 nm band of  $P^+B_A^-$ . A plot with a reduced wavelength span (930-1170 nm) is shown in Fig. S38. (*B*) Evolution of the integrated

area under the 1030 nm band using a straight-line baseline across the integration region (1010-1050). The red line is a 2-exponential fit giving one rise and one decay component. The 0.3 ps rise time matches the instrument response function (IRF). The absence of a clearly identifiable peak absent of drawn baselines (Fig. S36) may evidence that integrated area plotted could be an artifact of an imperfect baseline which errs the most at short times where P\* shows the most curvature. As with other variants, there may be a contribution of P\* (at early times) and P\*H<sub>A</sub><sup>-</sup> (at longer times) to the integral because the contribution of these states to the baseline may not be precisely linear and will differ with time. In the absence of a clearly identifiable 1030 nm feature and when the rise time of the feature is at or below the IRF, it is difficult to determine if this short rise time reflects an equally short *decay* time of P\*B<sub>A</sub><sup>-</sup> (the shortest time component in a set of events appears first in kinetics of a two-step process) or is an artifact. As the purpose of these fits is not meant to be highly quantitative and since for other RC variants the 1030 nm feature is both identifiable, has higher signal amplitude, and has a rise time significantly larger than the IRF, the potential error introduced by baselining is not as significant and the fits are more definitive of a contribution of a two-step ET mechanism. Note the change in the time axis at 50 ps.



**Fig. S38.** Evolution of a portion (930-1170 nm) of the NIR TA spectra at early times for  $NO_2Y$  RCs. The spectra in this stack plot are vertically offset from one another to best display the integrated area (1010-1050 nm) of the 1030 nm band of  $P^+B_A^-$ .

## S3.7 Comparison of DADS with specific time constants

The DADS are presented in different ways in Sections S3.7 and S3.8 to foster different types of comparisons. Each figure in Section S3.7 (Figs. S39–S43) compares DADS for each of the six samples for a given time component. In this DADS analysis, the amplitudes of the 3.3-4.7 ps component ( $P_1*$ ) and of the 12-20 ps component ( $P_2*$ ) are adjusted relative to one another (the amplitude sum is unity). The relative amplitudes were chosen so that the DADS for the two components would match each other in spectral amplitude to the extent possible over the visible and NIR regions. Similar time constants and spectral shapes are obtained from traditional DADS in which all amplitudes are set at 1 (see Section S3.8 for comparison and discussion). Relative amplitudes of  $P_1*$  and  $P_2*$  obtained in this way from the DADS analysis are similar to the ratio obtained from  $P^*$  stimulated emission decay (Table S4), showing consistency in the analysis. Recall the caveat given above that DADS truly reflect the spectral changes that occur with a particular time constant and thus a process that converts one state to another. However, to foster comparisons with other parts of the analysis, the DADS can be labeled to the state that appears to largely decay on a particular time scale. As such, the various DADS reflect the following (progressing from shorter to longer time components):  $P^+B_A^-$  ( $\sim 1$  ps; Fig. S39),  $P_1*$  (3.3-4.5 ps; Fig. S40),  $P_2*$  (12-27 ps; Fig. S41),  $P^+H_A^-$  (220-265 ps; Fig. S42), and  $P^+Q_A^-$  (infinity = no decay; Fig. S43).

Cursory inspection of each figure in Section S3.7 shows that the DADS on each time scale are are virtually the same for all six samples. The only deviation is that there is no short-lived ( $\sim$ 1 ps) DADS for NO<sub>2</sub>Y RCs (Fig. S39) because, as noted above, there is little to no formation of P<sup>+</sup>B<sub>A</sub><sup>-</sup> relative to the other five samples. The 0.7 ps component which was fixed for DADS for NO<sub>2</sub>Y RCs is noisy and not as readily assigned to formation/decay of P<sup>+</sup>B<sub>A</sub><sup>-</sup> as it is for the other samples. Overall, the excellent agreement in the DADS for a given kinetic component for the samples (Figs. S39–S43) reflects the overall similarity in the photochemistry among the samples (with important differences discussed in detail) and the consistency of the analysis.

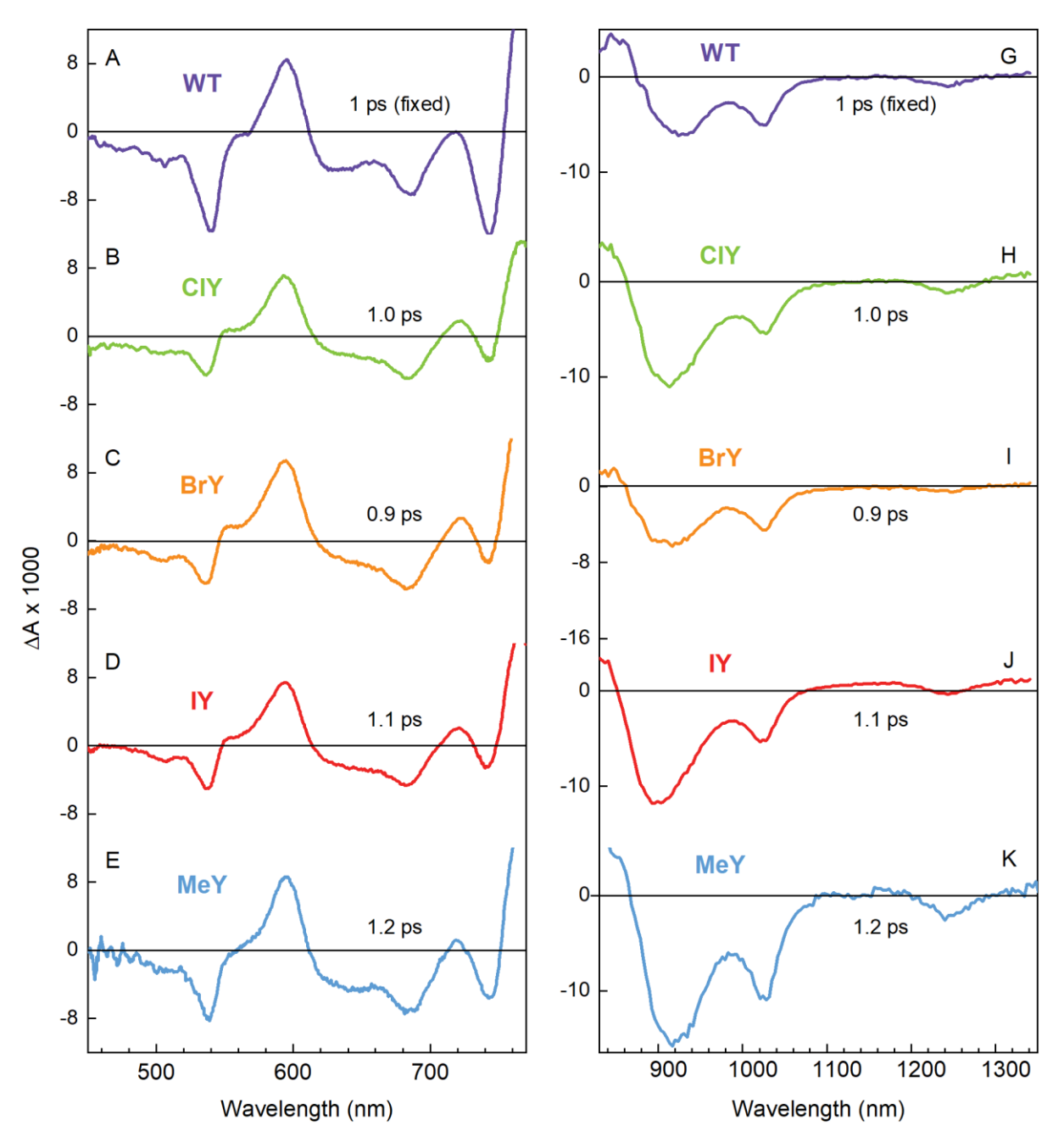


**Fig. S39.** Comparison of the ~1 ps DADS in the visible region (left) and NIR region (right) for WT (A,G), CIY (B, H), BrY (C, I), IY (D, I), and MeY (E, K). The spectra contain negative features at ~920 nm and 1030 nm that likely represent primarily decay of  $P_1^*$  stimulated emission and formation of the  $B_A$  anion absorption band. Note that for a two-step process  $P^* \to P^+B_A^- \to P^+H_A^-$ , if the rate of the second step is greater or comparable to that of the first process, absorption changes associated with both processes could contribute to the ~1 ps DADS. For  $NO_2Y$  RCs, an ~1 ps component is not included in the DADS analysis shown here and in Fig. S40–S43 for the longer-lived components. If a 0.7 ps component is fixed for  $NO_2Y$  RCs, the associated DADS (Fig. S54A&B or Fig. S55A&B) are noisy and less readily assigned, indicating either no  $P^+B_A^-$  formation or a much smaller transient population. The time constants of the longer-lived components are similar to those obtained if the 0.7 ps fixed component is not included (Fig. S54C&D or Fig. S55C&D).

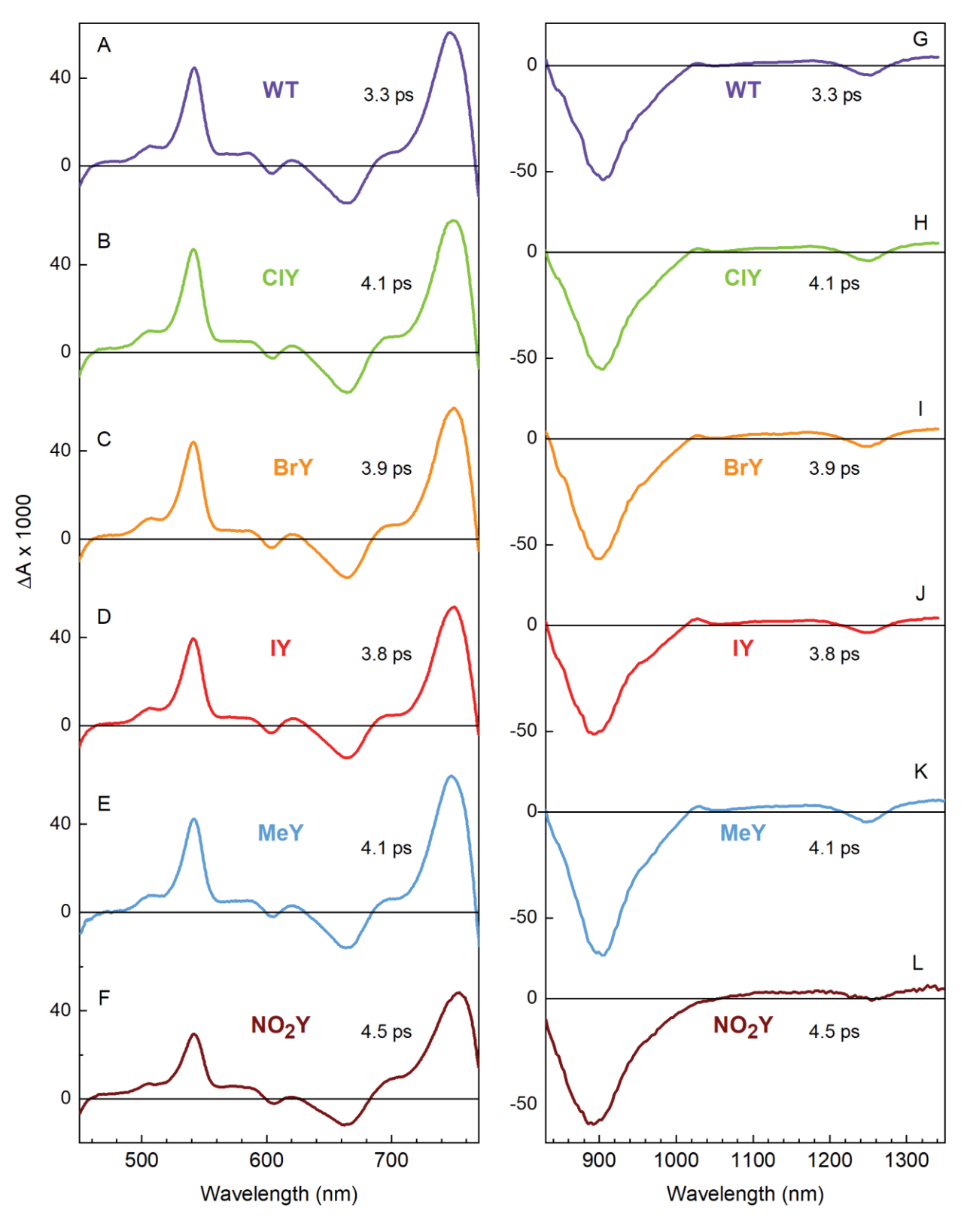


**Fig. S40.** Comparison of the  $\sim$ 4 ps DADS in the visible region (left) and NIR region (right) for WT (A,G), CIY (B, H), BrY (C, I), IY (D, I), MeY (E, K), and NO<sub>2</sub>Y (F, I) RCs. The DADS on this time scale are expected to reflect mainly decay of P<sub>1</sub>\* and formation of associated charge-separated products.

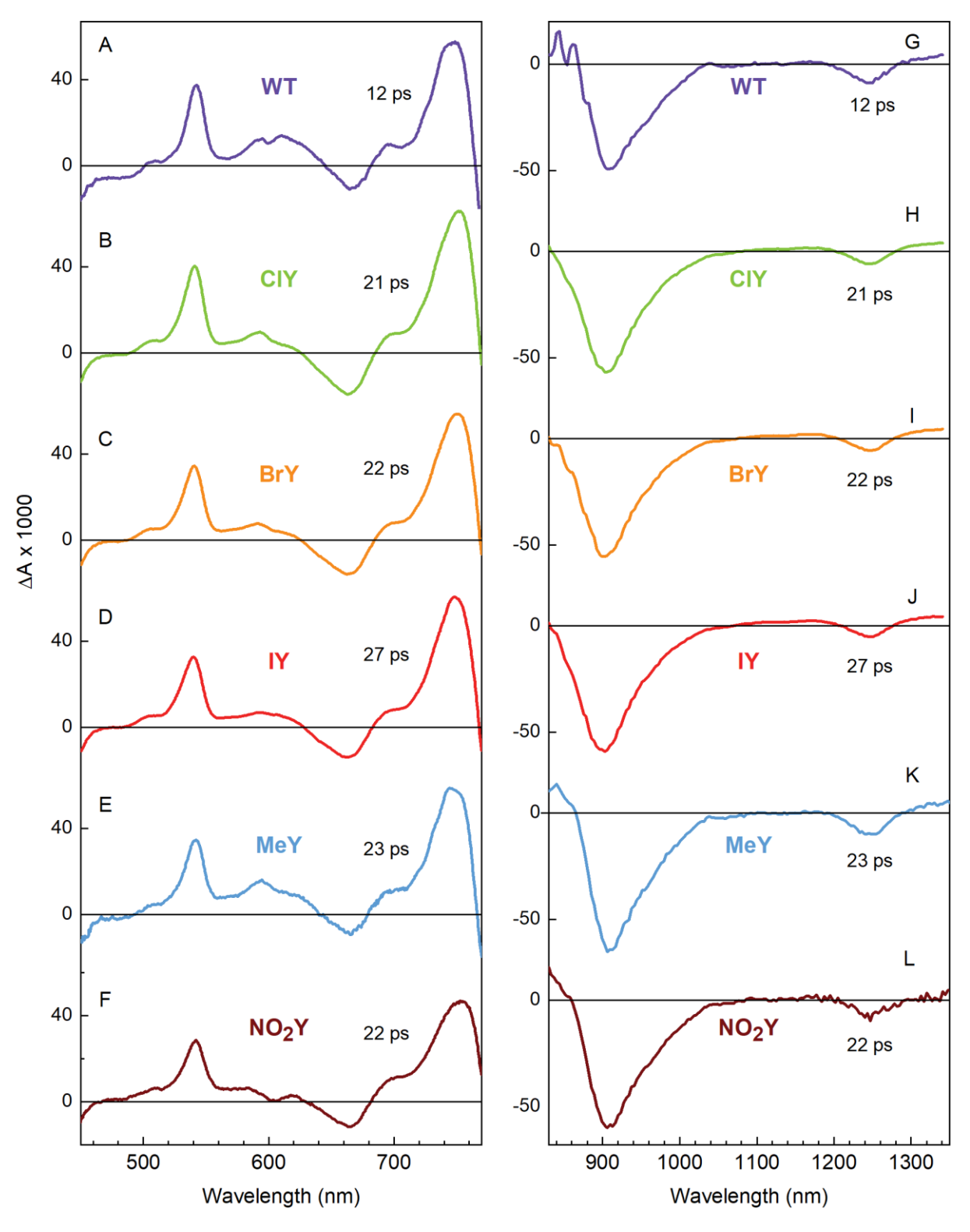


**Fig. S41.** Comparison of the ~20 ps DADS in the visible region (left) and NIR region (right) for WT (A,G), CIY (B, H), BrY (C, I), IY (D, I), MeY (E, K), and NO<sub>2</sub>Y (F, I) RCs. The DADS on this time scale are expected to reflect mainly decay of P<sub>2</sub>\* and formation of with P<sup>+</sup>H<sub>A</sub><sup>-</sup> via a one-step superexchange process P\*  $\rightarrow$  P<sup>+</sup>H<sub>A</sub><sup>-</sup>.

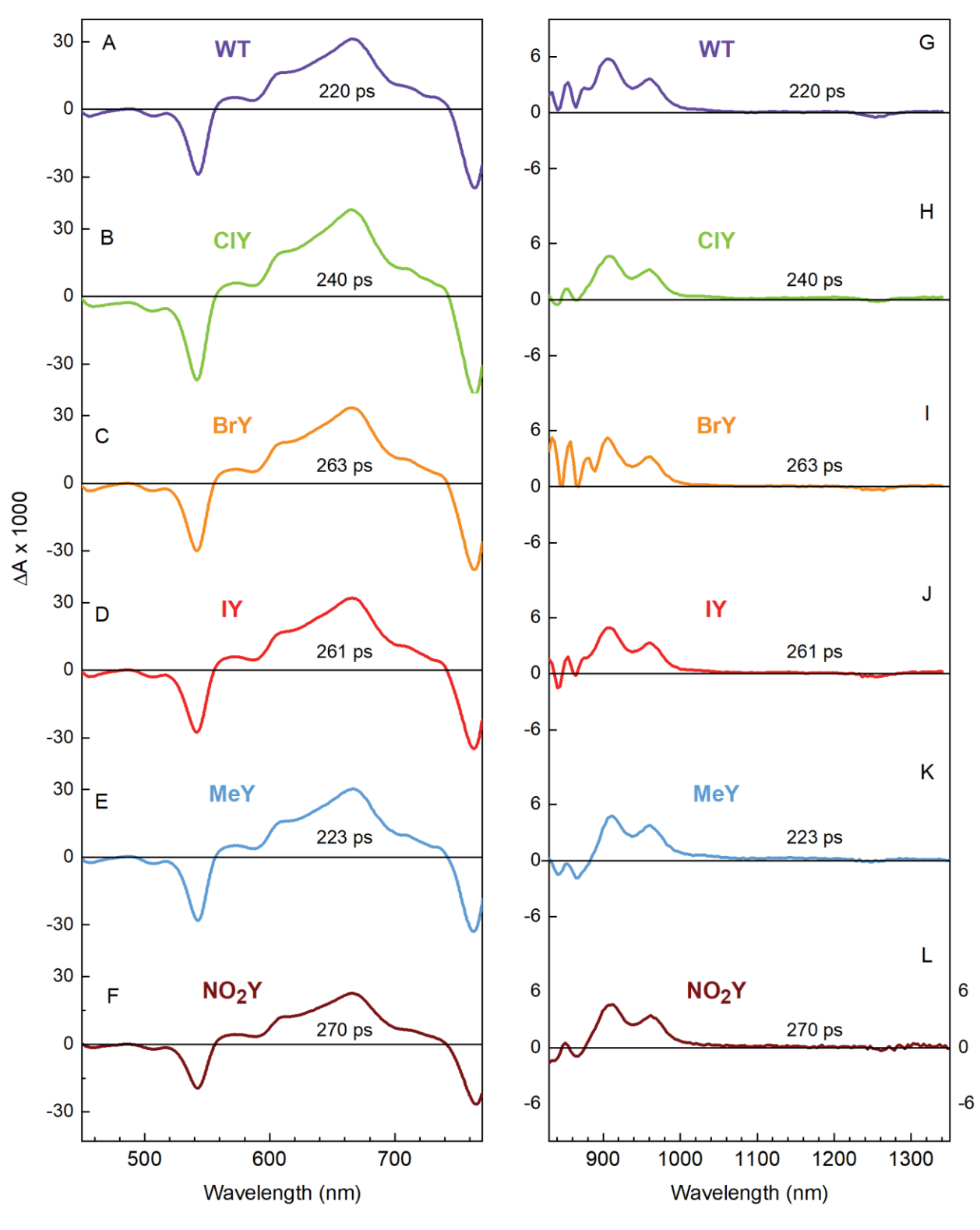


**Fig. S42.** Comparison of the ~250 ps DADS in the visible region (left) and NIR region (right) for WT (A,G), CIY (B, H), BrY (C, I), IY (D, J), MeY (E, K), and NO<sub>2</sub>Y (F, L) RCs. The DADS on this time scale are expected to reflect mainly decay of  $P^+H_A^-$  and formation of  $P^+Q_A^-$ .

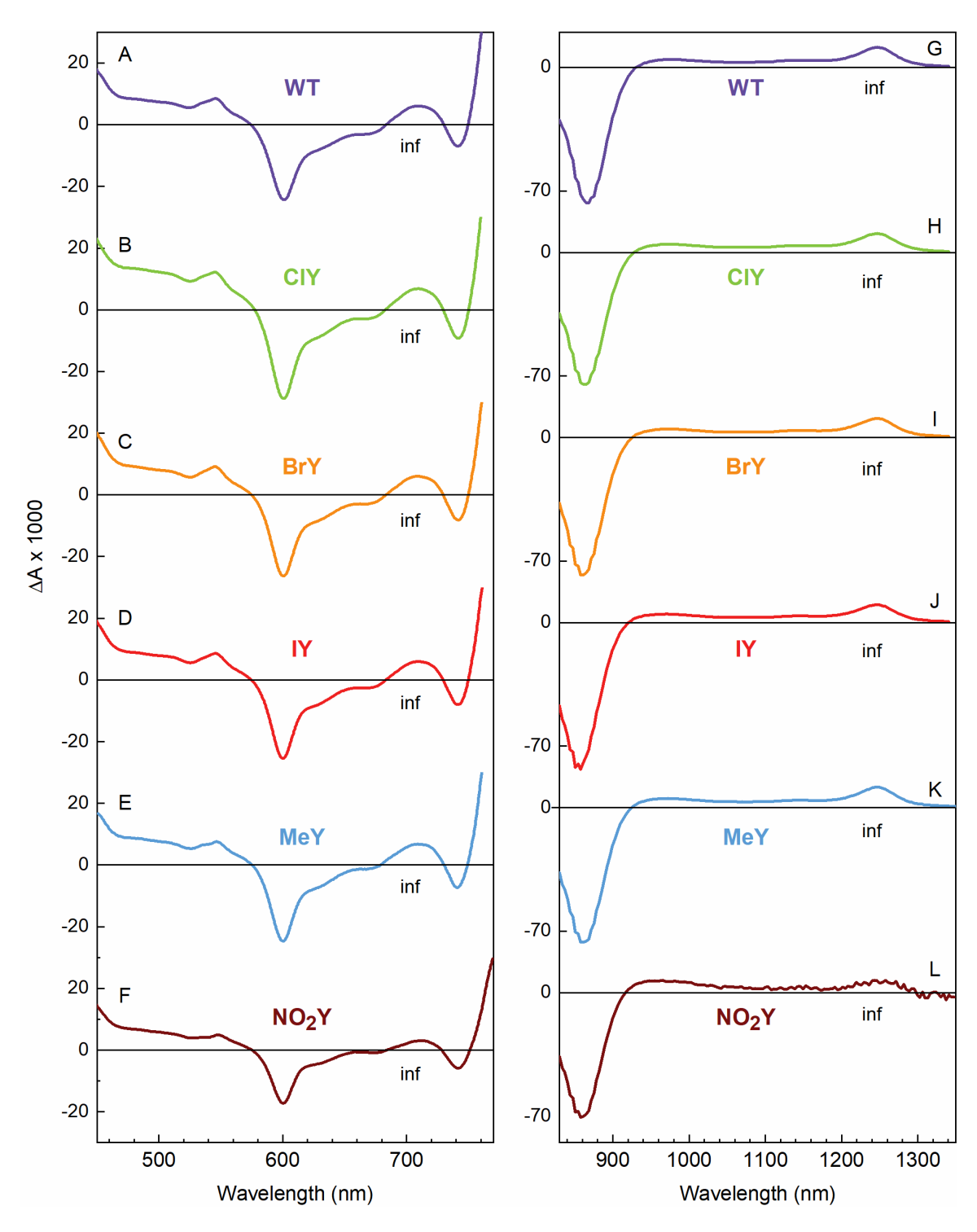


**Fig. S43.** Comparison of the "infinity" DADS in the visible region (left) and NIR region (right) for WT (A,G), CIY (B,H), BrY (C,I), IY (D,J), MeY (E,K), and NO<sub>2</sub>Y (F,L) RCs. These DADS reflect  $P^+Q_A^-$ , which does not decay on the time scale of the experiments.

## S3.8 DADS summaries for each sample

Section S3.8 (Figs. S44–S55) compares the DADS in a different way from Section S3.7. Section S3.8 also offers additional information pertinent to the relative  $P_1^*$  verus  $P_2^*$  populations among the six samples. Each figure in Section S3.8 shows the DADS for all the time components for a single sample so that changes in spectra with time (for each sample) can be compared. The features in the spectra can be assigned in analogy to the description of the features in the raw TA spectra given in Section S3.4.

Note that in this section there are two DADS summary figures for each sample (e.g. Fig. S44 and Fig. S45 for WT RCs). The first figure in each pair is the "traditional" DADS in which the amplitudes of all the kinetic components (the independent exponential terms) are set to unity. The second figure in each pair has the amplitudes of the 3.3-4.7 ps component ( $P_1$ \*) and of the 12-20 ps component ( $P_2$ \*) adjusted relative to one another (the sum is unity). The relative amplitudes were chosen so that the DADS for the two components would match each other in spectral amplitude to the extent possible over the visible and NIR regions. This scaling does not change the shapes of these two spectra, and in fact reveals that these DADS for  $P_1$ \* and  $P_2$ \* have the same characteristics, with some small differences in detail. This is true for all six samples.

Several points can be made concerning the scaling of the DADS components attributed to  $P_1^*$  and  $P_2^*$ :

- (1) The close similarity of the scaled 3.3-4.5 ps and the 12-27 ps DADS (for each sample) validates the assignment to populations of P\*.
- (2) The relative amplitudes by which the two DADS are scaled is one measure of the relative populations of  $P_1^*$  and  $P_2^*$  for each sample. These  $P_1^*/P_2^*$  relative fractions from this DADS analysis are as follows: WT (0.87/0.13), CIY (0.60/0.40), BrY( 0.55/0.45), IY (0.65/0.35), MeY (0.86/0.14), and NO<sub>2</sub>Y (0.76-0.79/0.21-0.24). These relative amounts of  $P_1^*$  and  $P_2^*$  are generally in good agreement with those obtained from analysis of kinetic profiles at key individual wavelengths (Section S3.5) and SADS

(Sections S3.9 and S3.10), as summarized in Table S4 (Section S3.11). Note that for NO<sub>2</sub>Y RCs, DADS and SADS were also generated under the assumption that  $P^+B_A^-$  is not produced (i.e. lack the  $\sim$ 1 ps component). The DADS and SADS for all the other components do not change appreciably for NO<sub>2</sub>Y RCs if the  $\sim$ 1 ps component for  $P^+B_A^-$  is included or not as can be seen in Fig. S54 and Fig. S55.

(3) The DADS for both components (3.3-4.5 ps and 12-27 ps) for each sample contains decay of  $P^*$  stimulated emission in the NIR, a pronounced positive feature at 542 nm due to formation of  $H_A$  bleaching (as  $P^*H_A^-$  forms), and a large broad negative feature at 665 nm due to the formation of the  $H_A$  anion (as  $P^*H_A^-$  forms). The main difference between the two DADS for a given sample is that the shorter component associated with  $P_1^*$  differs from the longer component associated with  $P_2^*$  mainly in the presence of additional small features near 600 and 1030 nm that can be associated with  $B_A$  and  $B_A^-$ , respectively. This difference is consistent with the notion that decay of  $P_1^*$  drives the two-step ET route  $P_1^* \to P^*B_A^- \to P^*H_A^-$  while  $P_2^*$  drives the one-step superexchange pathway  $P_2^* \to P^*H_A^-$ . The otherwise close similarity of the two DADS components is consistent with the small build up of  $P^*B_A^-$  and thus the idea that its rate of formation from  $P_1^*$  is comparable to and likely somewhat greater than its rate of decay to  $P^*H_A^-$ . This consideration is reflected in the SADS analysis described in Sections S3.9 – 3.10..

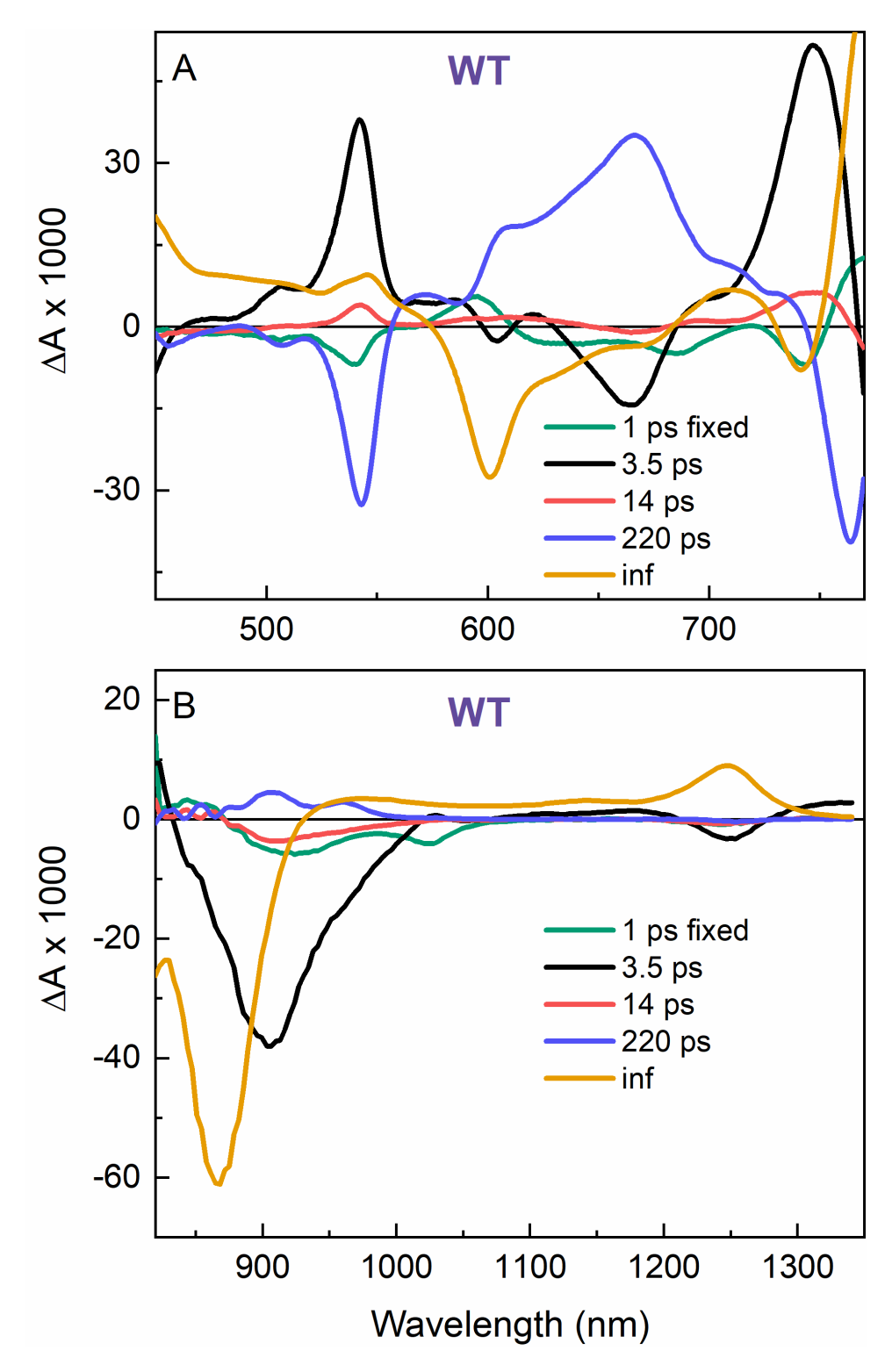
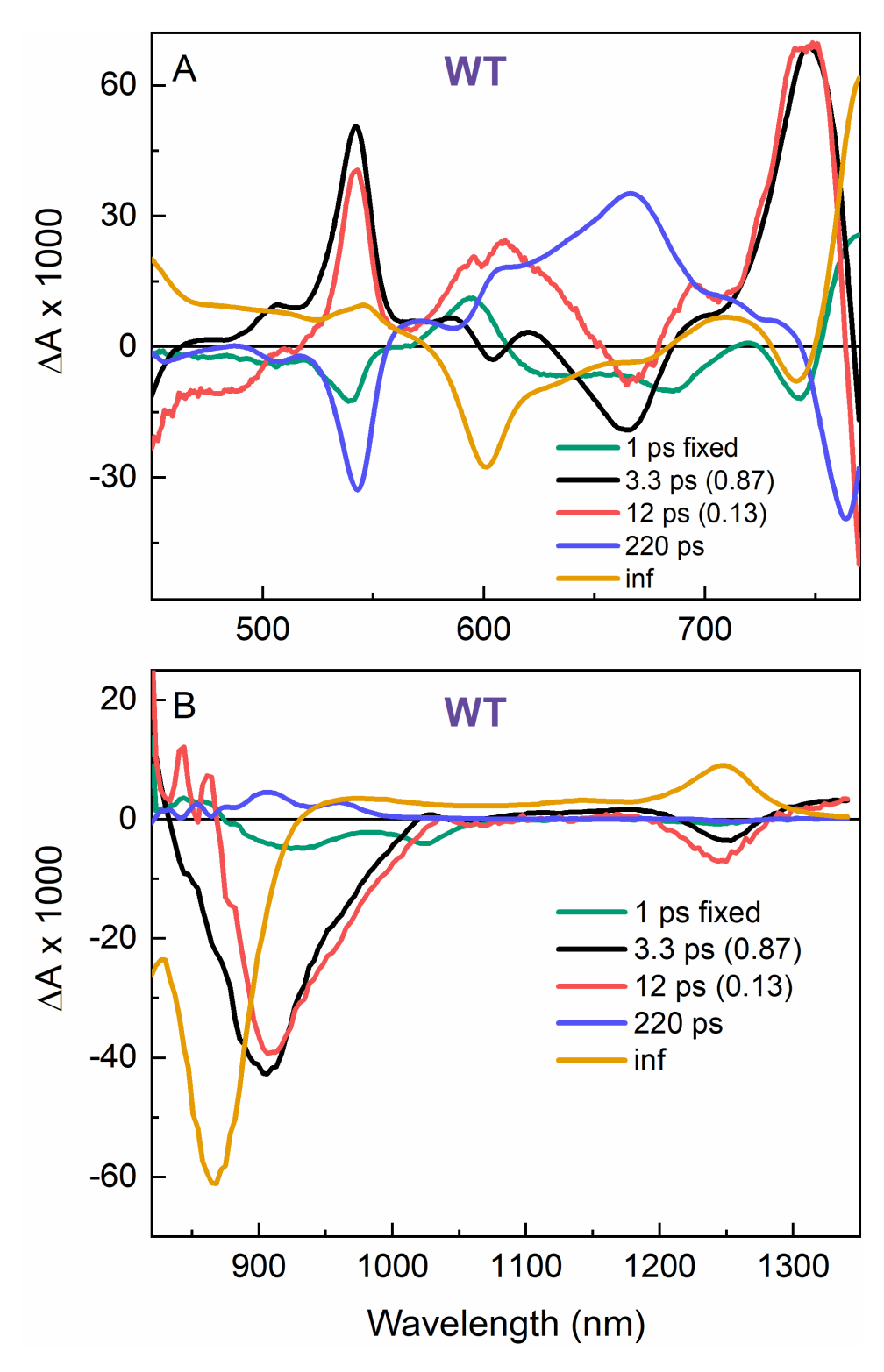


Fig. S44. Visible (A) and NIR (B) traditional DADS (all amplitudes = 1) for WT RCs.



**Fig. S45.** Visible (A) and NIR (B) DADS for WT RCs with amplitudes of the  $\sim$ 3 and  $\sim$ 12 ps components set (values in parenthesis) to obtain comparable amplitudes of the two DADS, which are expected to reflect decay of  $P_1^*$  and  $P_2^*$ , respectively. The time constants are similar (but not identical) to those obtained for traditional DADS in Fig. S44 and are the values listed in Table S4.

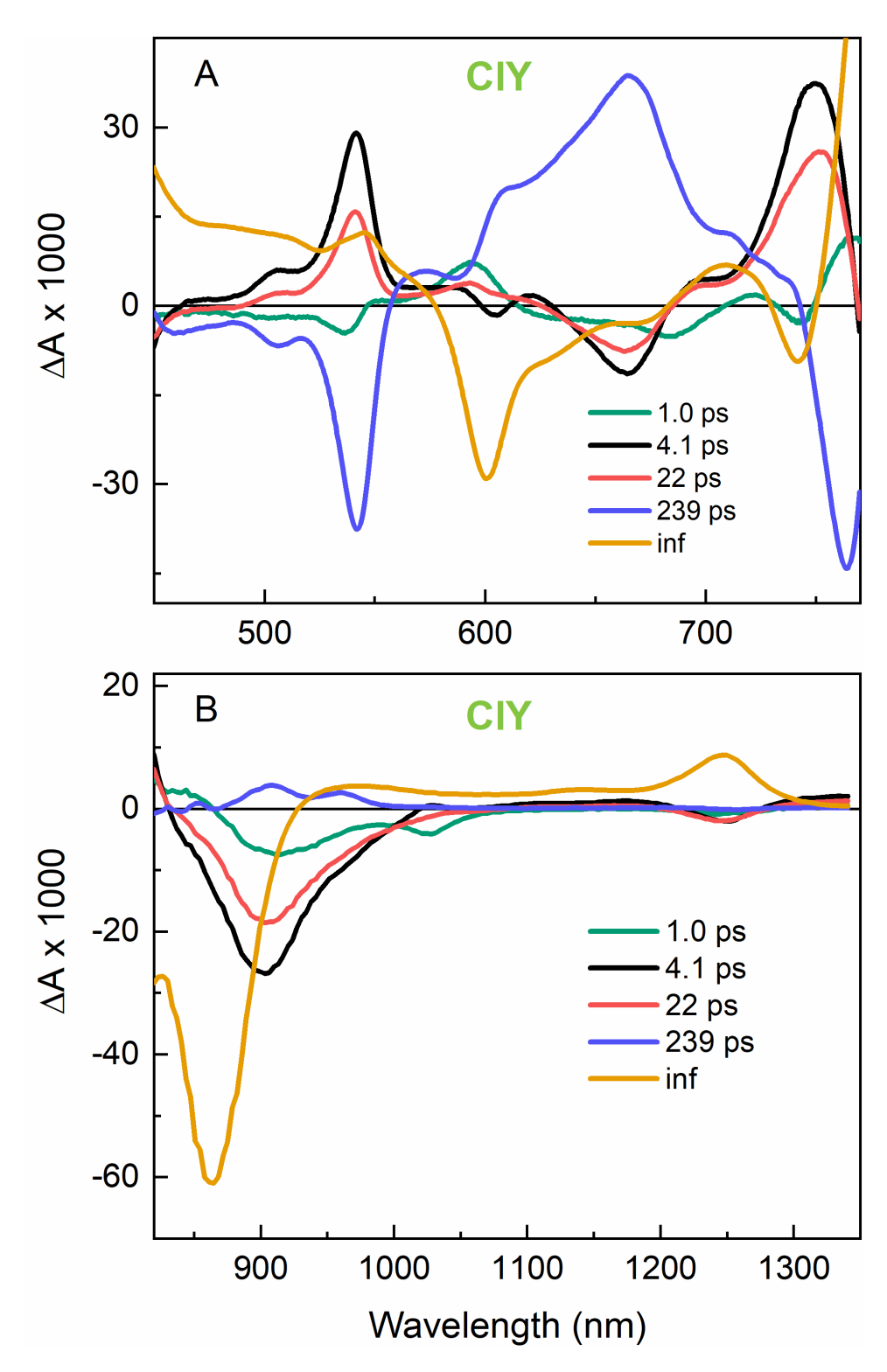
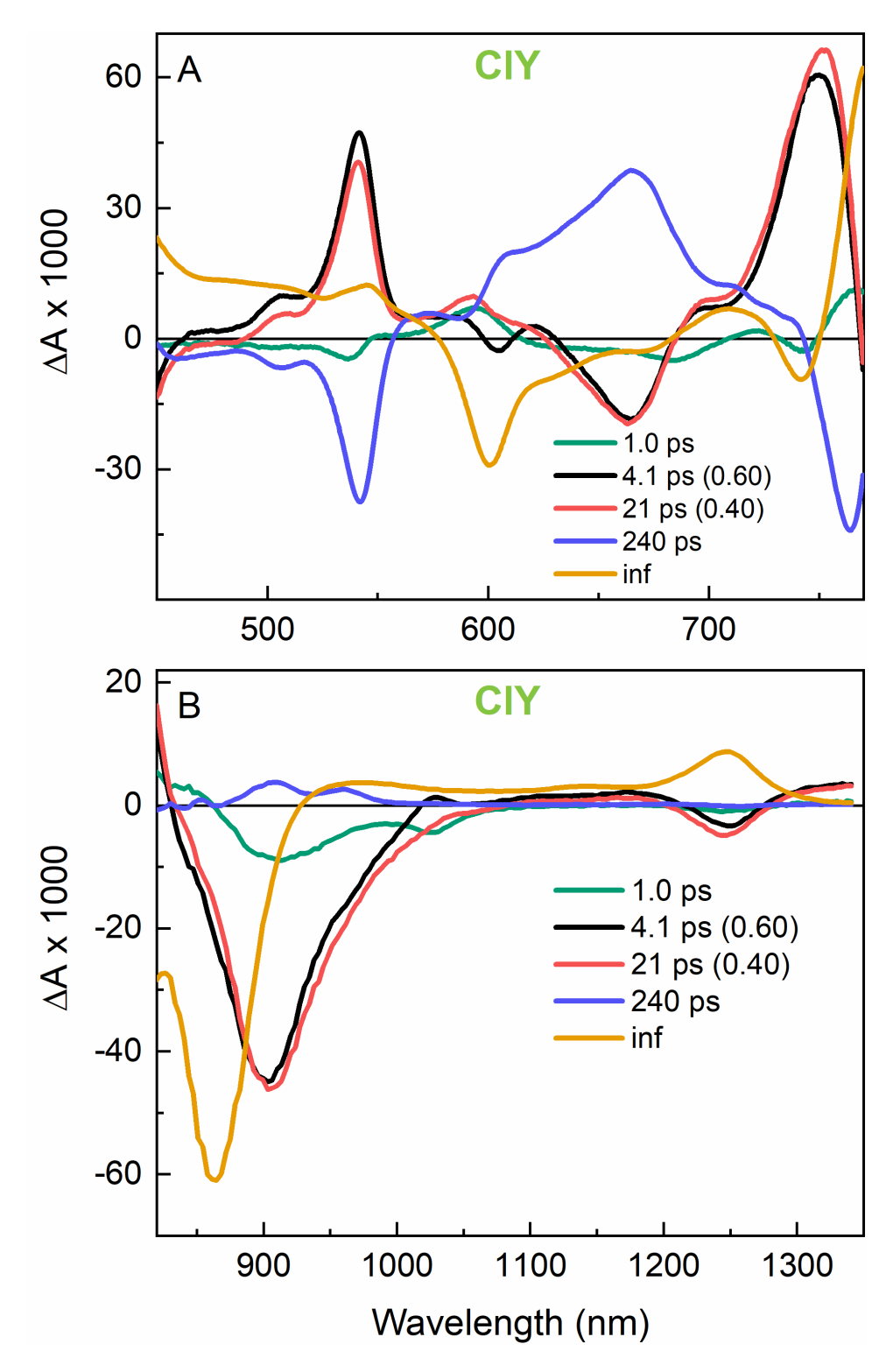


Fig. S46. Visible (A) and NIR (B) traditional DADS (all amplitudes = 1) for CIY RCs.



**Fig. S47.** Visible (A) and NIR (B) DADS for CIY RCs with amplitudes of the  $\sim$ 3 and  $\sim$ 12 ps components set (values in parenthesis) to obtain comparable amplitudes of the two DADS, which are expected to reflect decay of  $P_1^*$  and  $P_2^*$ , respectively. The time constants are similar (but not identical) to those obtained for traditional DADS in Fig. S46 and are the values listed in Table S4.

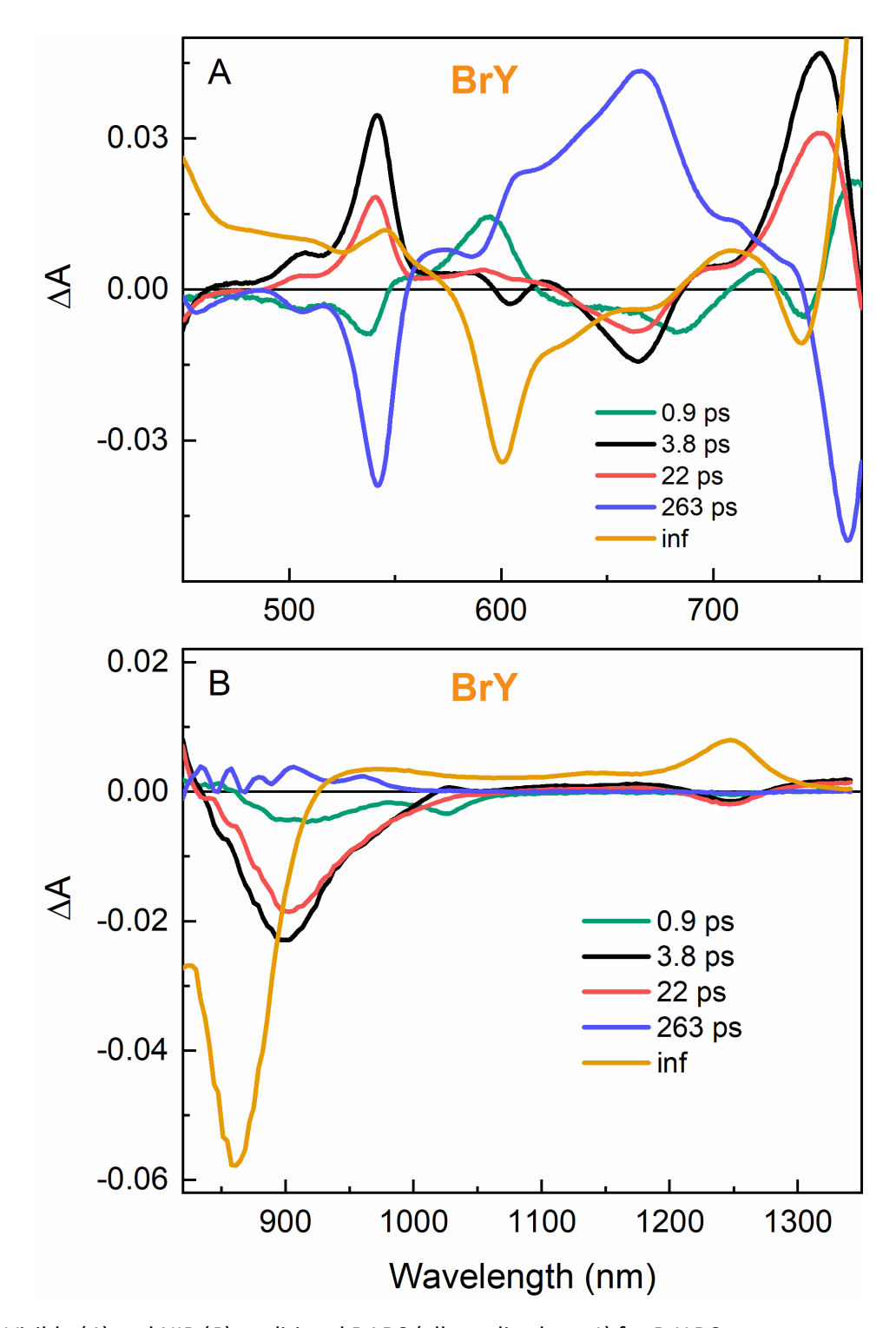
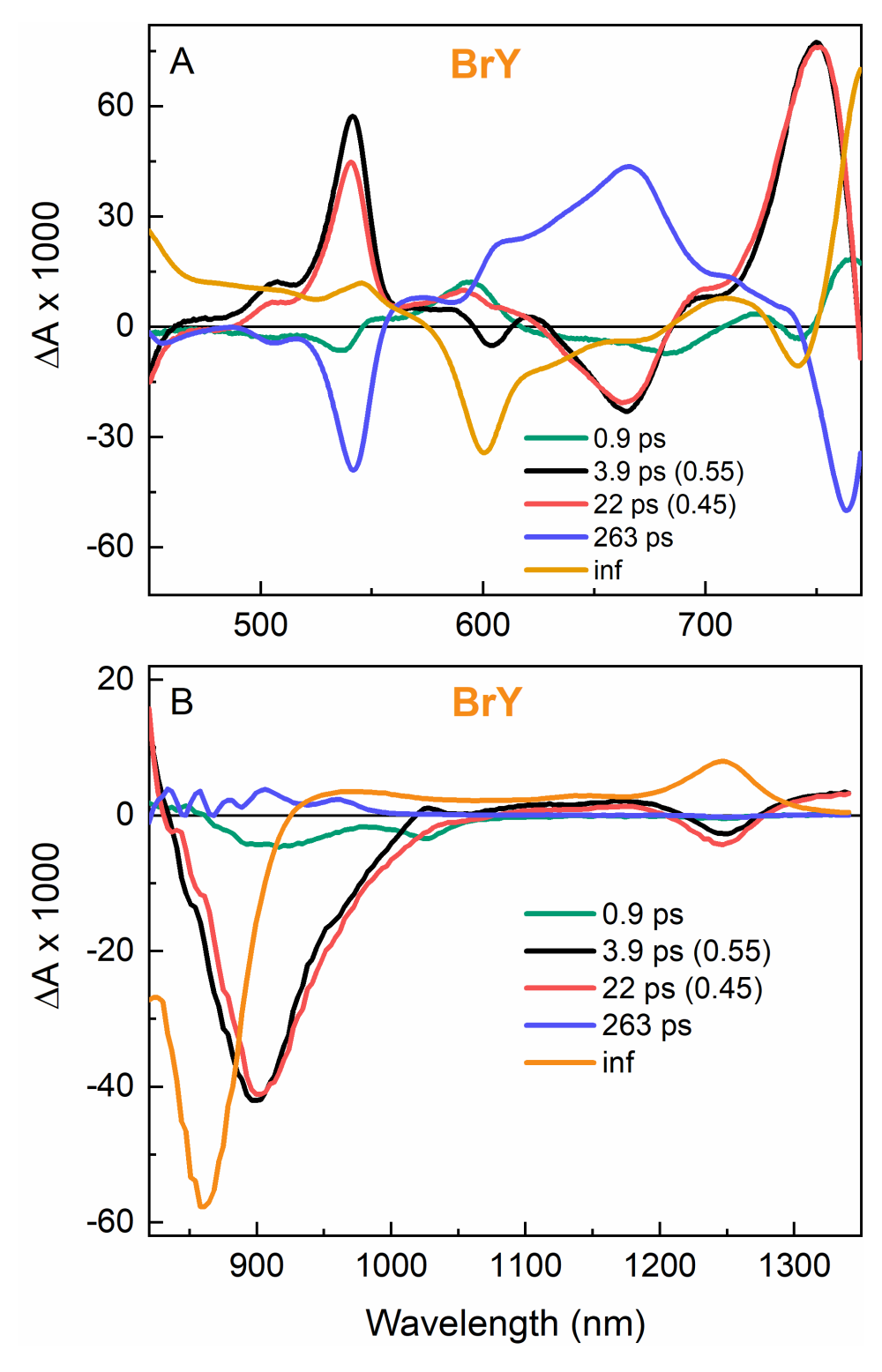


Fig. S48. Visible (A) and NIR (B) traditional DADS (all amplitudes = 1) for BrY RCs.



**Fig. S49.** Visible (A) and NIR (B) for BrY RCs with amplitudes of the  $\sim$ 3 and  $\sim$ 12 ps components set (values in parenthesis) to obtain comparable amplitudes of the two DADS, which are expected to reflect decay of  $P_1^*$  and  $P_2^*$ , respectively. The time constants are similar (but not identical) to those obtained for traditional DADS in Fig. S48 and are the values listed in Table S4.

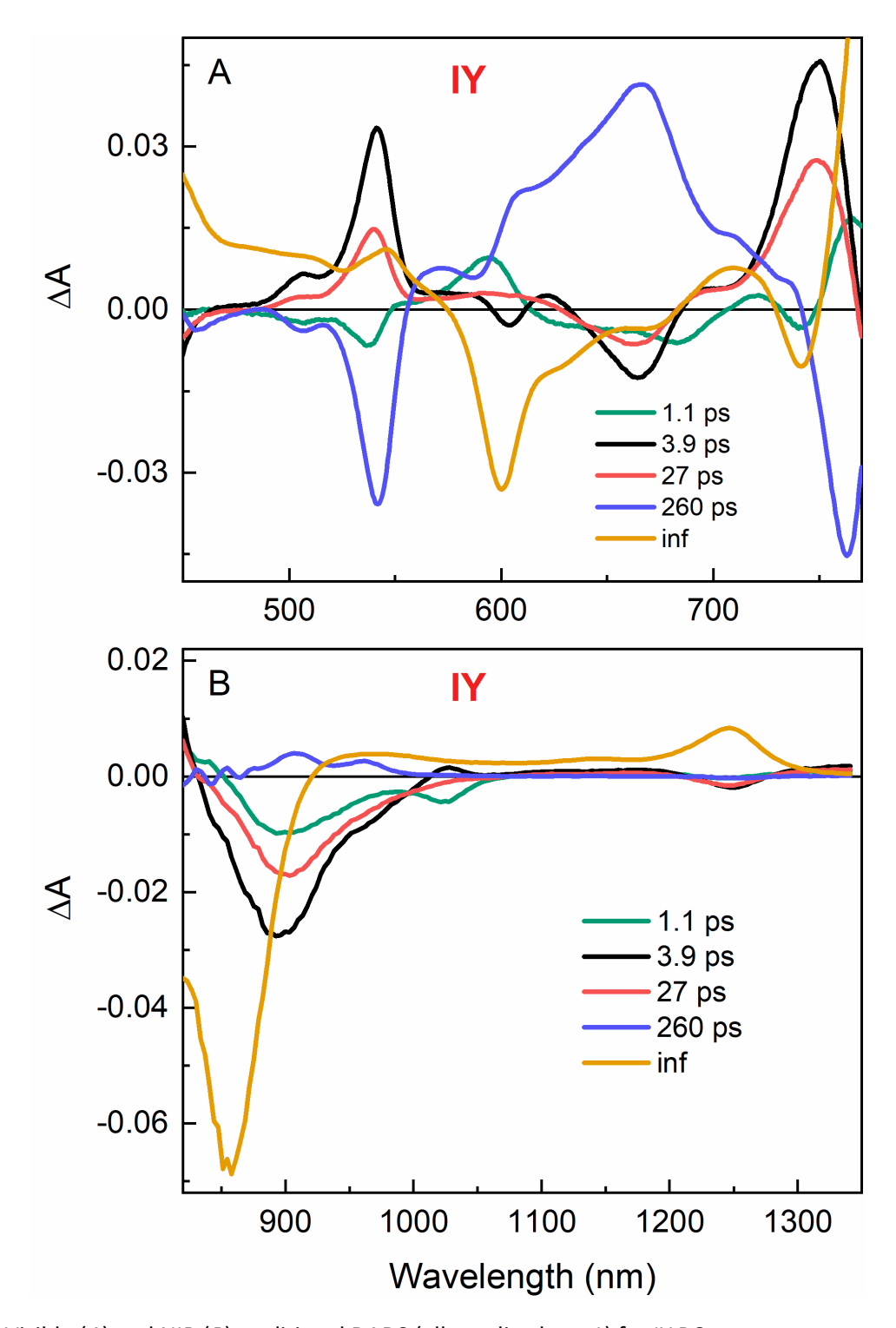
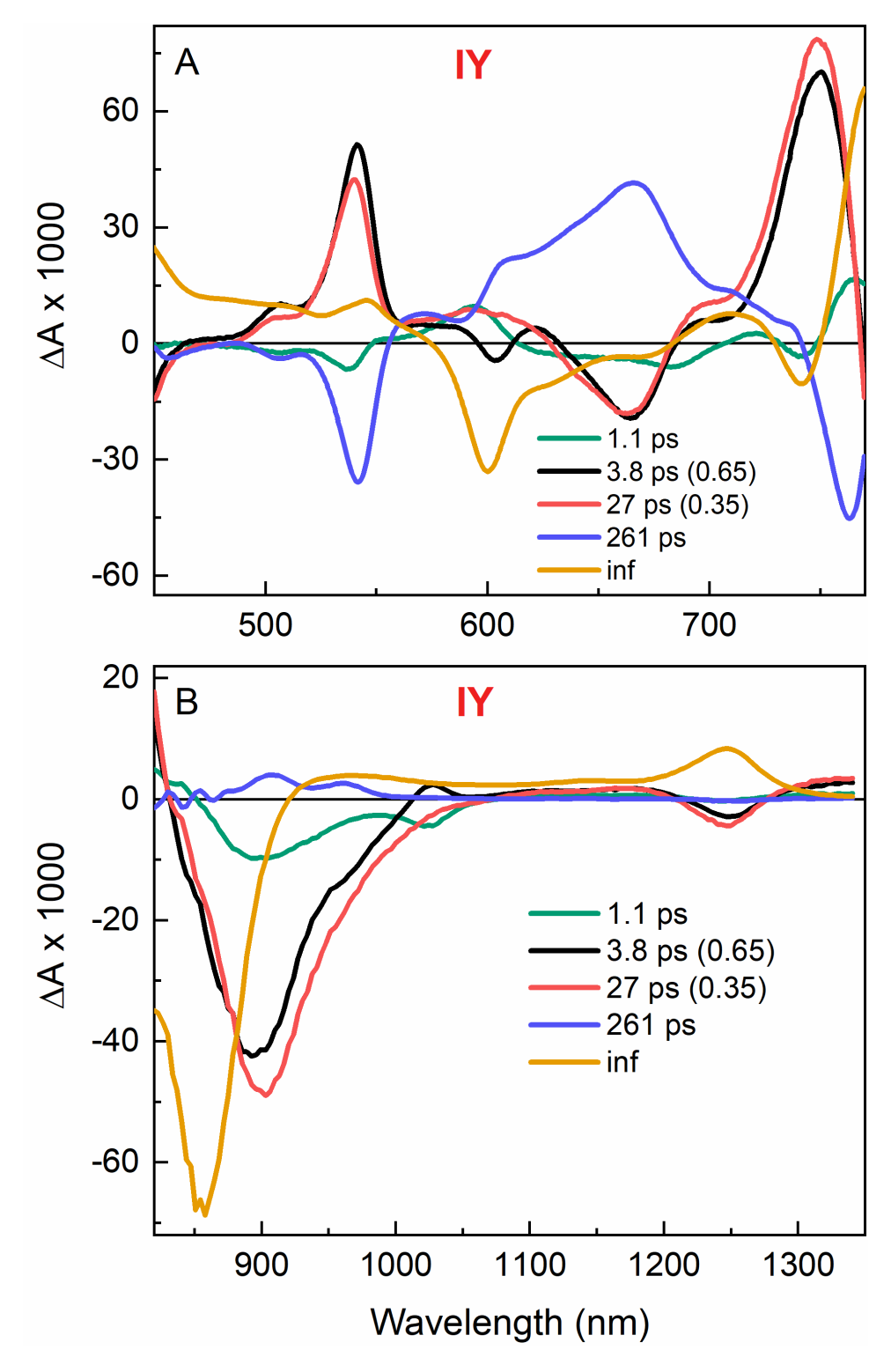


Fig. S50. Visible (A) and NIR (B) traditional DADS (all amplitudes = 1) for IY RCs.



**Fig. S51.** Visible (A) and NIR (B) DADS for IY RCs with amplitudes of the  $\sim$ 3 and  $\sim$ 12 ps components set (values in parenthesis) to obtain comparable amplitudes of the two DADS, which are expected to reflect decay of  $P_1^*$  and  $P_2^*$ , respectively. The time constants are similar (but not identical) to those obtained for traditional DADS in Fig. S50 and are the values listed in Table S4.

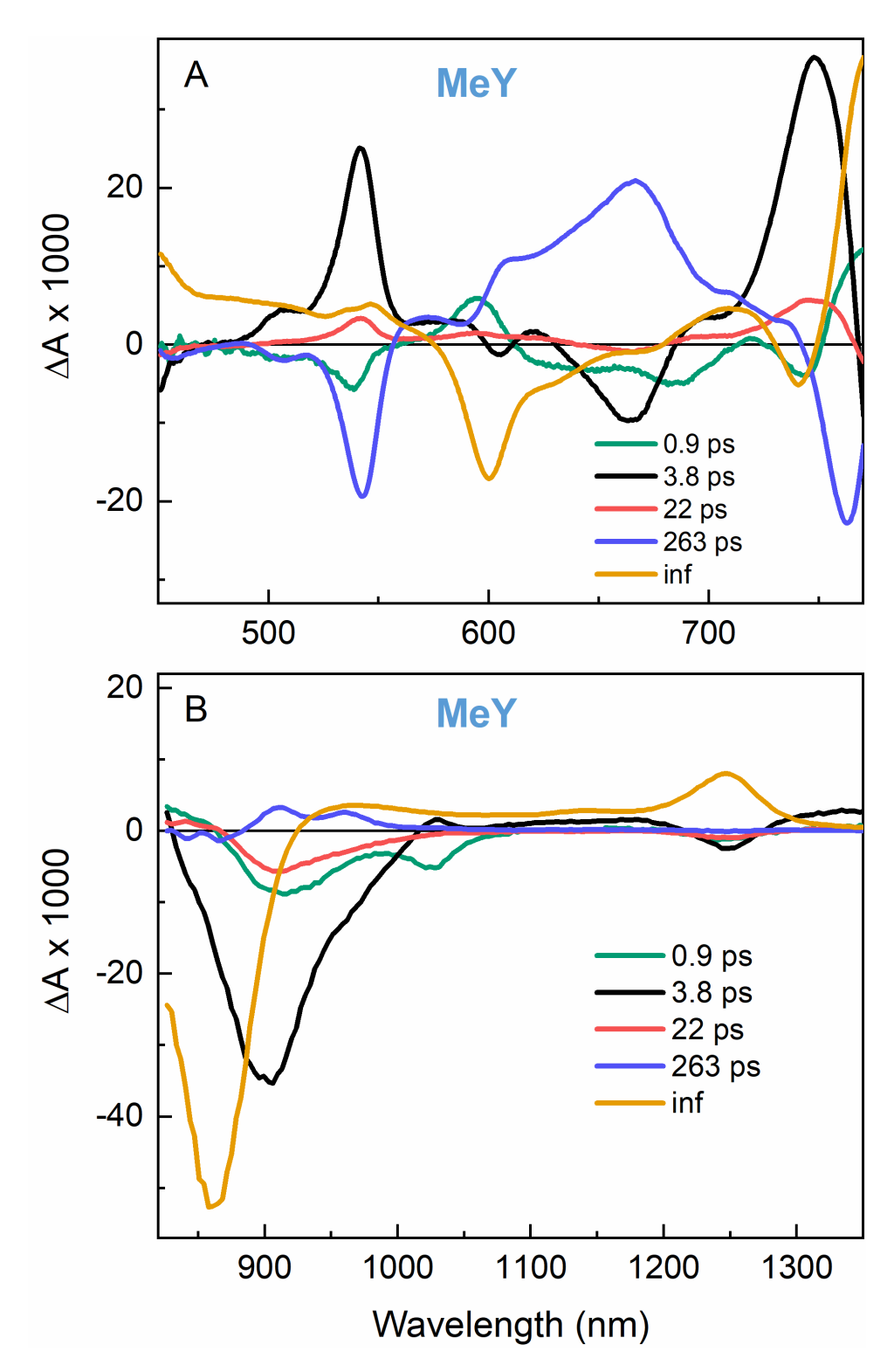
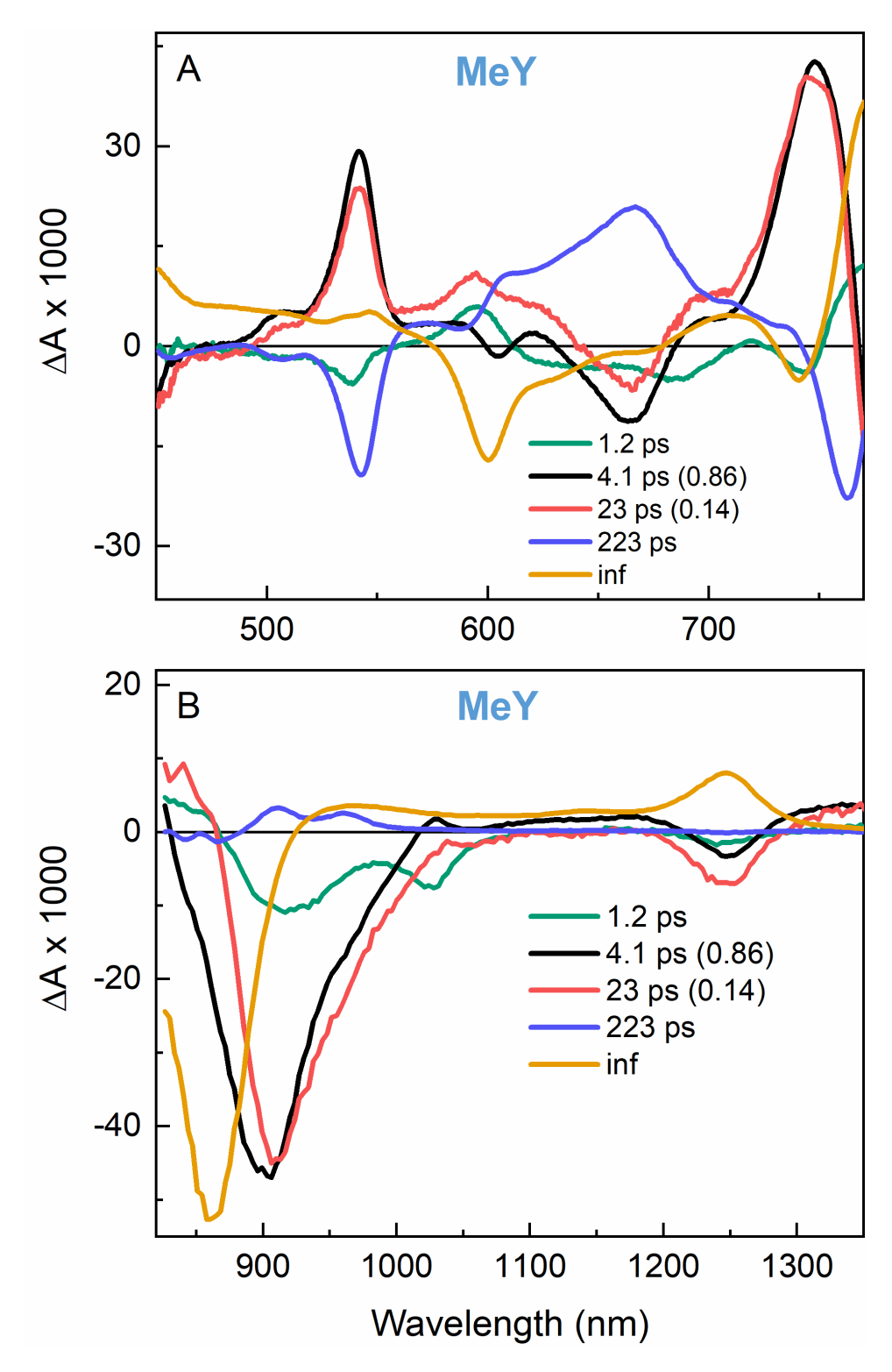
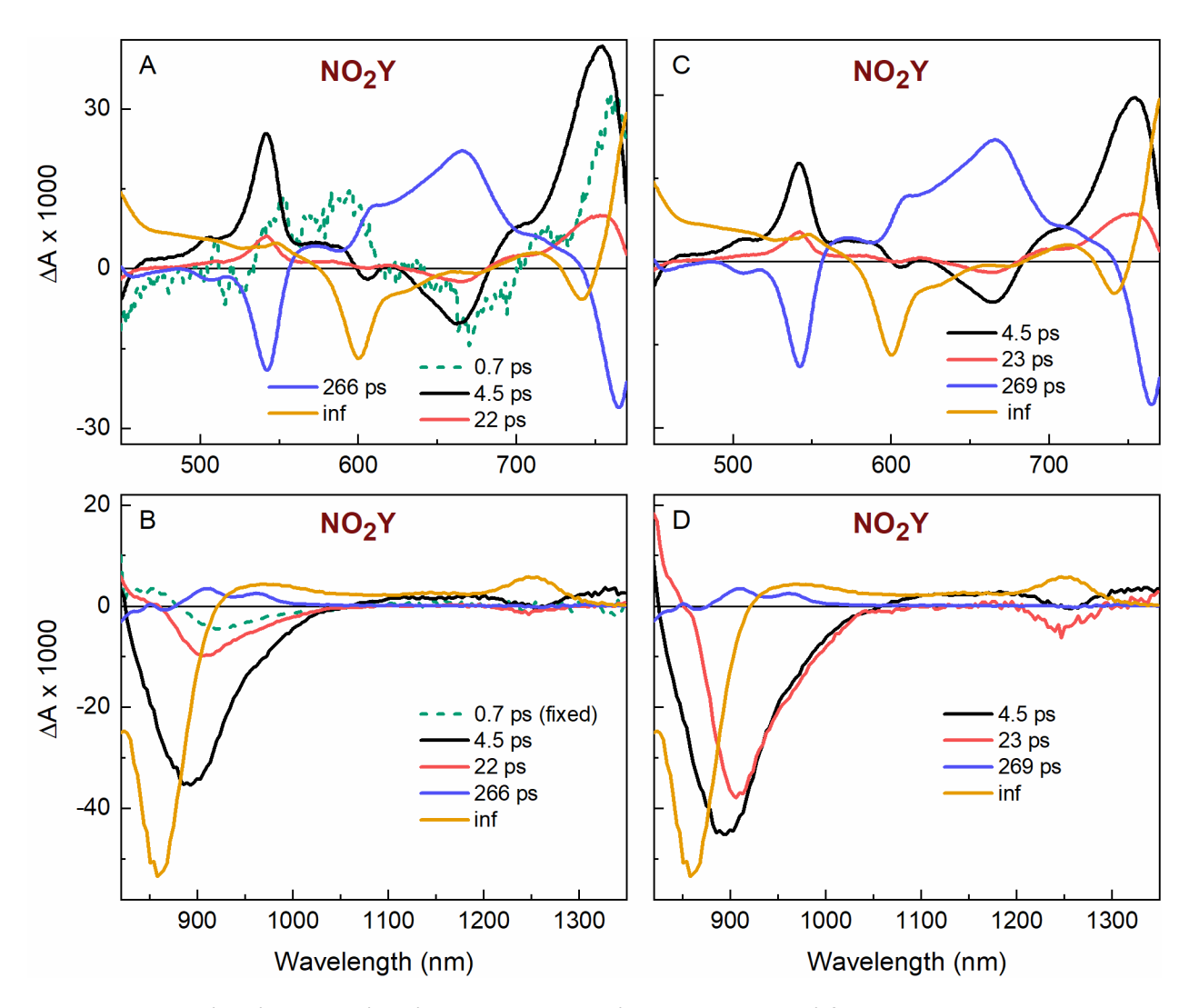


Fig. S52. Visible (A) and NIR (B) traditional DADS (all amplitudes = 1) for MeY RCs.



**Fig. S53.** Visible (A) and NIR (B) DADS for MeY RCs with amplitudes of the  $\sim$ 3 and  $\sim$ 12 ps components set (values in parenthesis) to obtain comparable amplitudes of the two DADS, which are expected to reflect decay of  $P_1^*$  and  $P_2^*$ , respectively. The time constants are similar (but not identical) to those obtained for traditional DADS in Fig. S52 and are the values listed in Table S4.



**Fig. S54.** Visible (A, C) and NIR (B, D) traditional DADS (all amplitudes = 1) for NO<sub>2</sub>Y RCs. For panels A and B, a fast component (with a time constant fixed at 0.7 ps) was included for consistency with the other samples. The 0.7 ps DADS is noisy and suggests either this fast component is not present or there is a much smaller transient population of this component than for the other samples. See Figs. S36–S38. For panels C and D, the 0.7 ps component was not included.

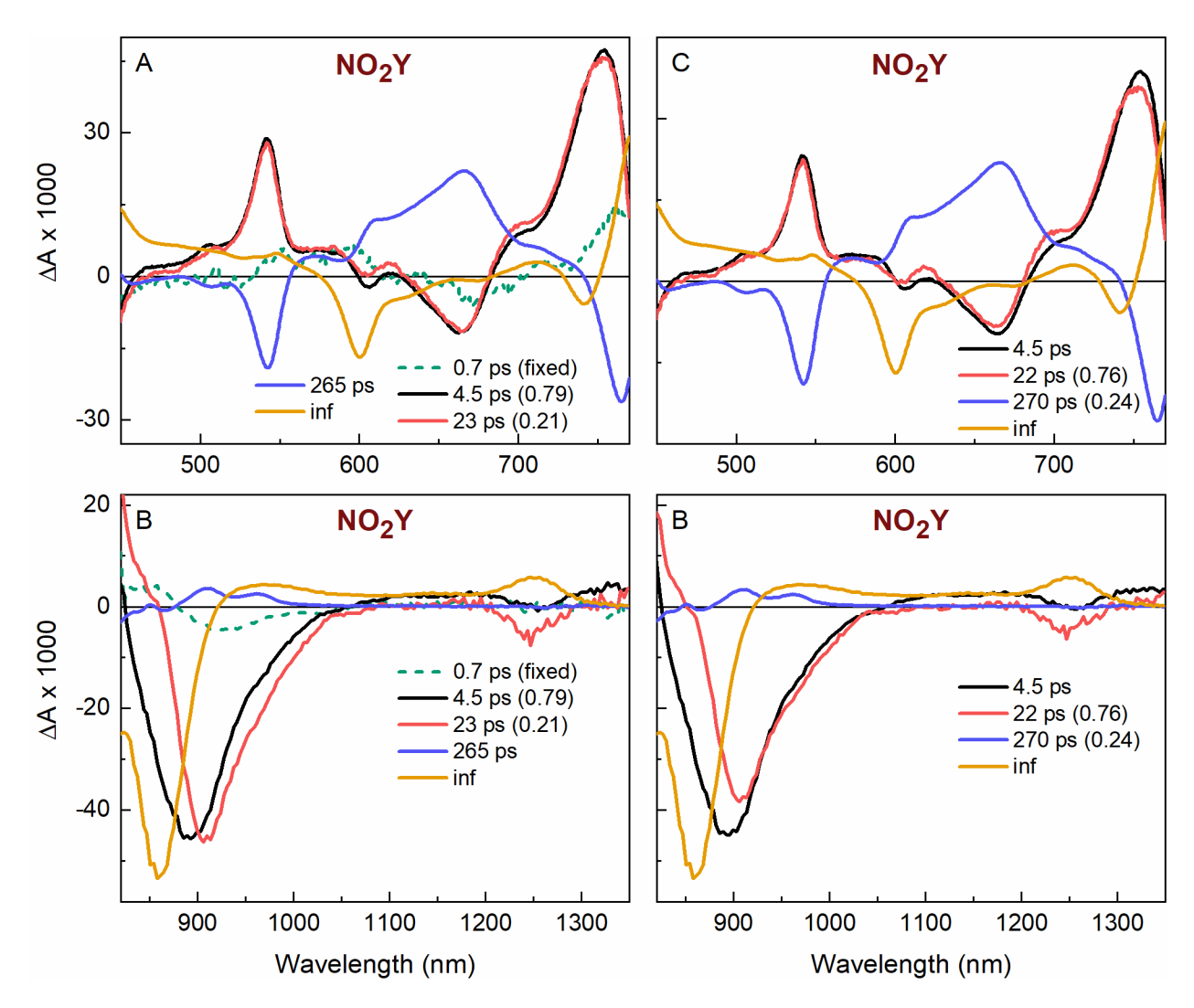


**Fig. S55.** Visible (A, C) and NIR (B, D) DADS for NO<sub>2</sub>Y RCs with amplitudes of the  $\sim$ 3 and  $\sim$ 12 ps components set (values in parenthesis) to obtain comparable amplitudes of the two DADS, which are expected to reflect decay of P<sub>1</sub>\* and P<sub>2</sub>\*, respectively. The time constants are similar (but not identical) to those obtained for traditional DADS in Fig. S54 and are the values listed in Table S4. For panels A and B, a fast component (with a time constant fixed at 0.7 ps) was included for consistency with the other samples. The 0.7 ps DADS is noisy and suggests either this fast component is not present or there is a much smaller transient population for this component than for the other samples. See Figs. S36–S38. For panels C and D, the 0.7 ps component was not included.

## S3.9 Comparison of SADS with specific time constants

Section S3.9 presents SADS analogous to the presention of DADS in Section S3.7. Fig. S56 presents the kinetic models for the SADS. Each subsequent figure in Section S3.9 compares the SADS for a specific state for each of the six samples. The various SADS reflect, progressing from shorter to longer lifetimes  $P^+B_A^-$  (1.5-1.9; Fig. S57),  $P_1^*$  (2.5-4.6 ps; Fig. S58),  $P_2^*$  (20-28 ps; Fig. S59),  $P^+H_A^-$  (220-265 ps; Fig. S60), and  $P^+Q_A^-$  (infinity = no decay; Fig. S61).

Examination of each figure in Section S3.9 shows that the SADS for a specific state has virtually the same characteristics for all six samples, except the 0.7 ps SADS for NO<sub>2</sub>Y RCs is not as readily assigned to P\*B<sub>A</sub><sup>-</sup> as for the other samples. Furthermore, characteristics for a given state are those expected for that state based on the extensive literature on RC photochemistry. The features include, for P\*B<sub>A</sub><sup>-</sup> (Fig. S57), a 1030 nm absorption feature for B<sub>A</sub><sup>-</sup> that has a comparable extinction coefficient to that for P\* at 1250 nm. The analogous NIR anion band is shifted to shorter wavelengths ( $\sim$ 950 nm or lower) for H<sub>A</sub><sup>-</sup> in state P\*H<sub>A</sub><sup>-</sup> (Fig. S60). In the visible region, the B<sub>A</sub> anion absorption is broader and has its peak at somewhat longer wavelength ( $\sim$ 680 nm in Fig. S57) than that for the H<sub>A</sub> anion ( $\sim$ 665 nm in Fig. S60). These differences are, again, in keeping with spectra of BChI vs BPh anions in solution (56, 57) and prior spectra for transient states P\*B<sub>A</sub><sup>-</sup> (and P\* $\beta$ <sub>A</sub><sup>-</sup>, where a BChI replaces H<sub>A</sub>) vs P\*H<sub>A</sub><sup>-</sup> (24, 39, 46–48, 53, 54, 59). Additionally, in the vicinity of 540 nm the spectrum for P\*B<sub>A</sub><sup>-</sup> contains a derivative-like (S-shaped) feature that likely represents an electrochromic shift on the Q<sub>x</sub> absorption of H<sub>A</sub> due to the presence of a hole and an electron on nearby chromophores. This observation is also in keeping with prior work (11, 24).

The SADS for  $P_1^*$  and  $P_2^*$  (Fig. S58 and Fig. S59) for each sample are also generally in excellent agreement with one another, and with expectations. Both show the expected bleaching of the  $Q_X$  (600 nm) and  $Q_Y$  (865 nm) ground state absorption bands of  $P_Y$ , and  $P_Y^*$  stimulated emission is at longer wavelengths than the  $Q_Y$  bleach. The only indication of a minor modeling error perhaps in  $P_1^*$  or  $P_2^*$ 

SADS for some samples is the presence of small features around the 540 nm  $H_A$   $Q_x$  region that are not present in the raw spectra for  $P^*$  at early times. These minor features may reflect, at least in part, the possible presence of a distribution of  $P^*$  populations that we are modeling as only two populations. An additional population could reflect a second two-step population with longer lifetimes than we have modeled here for  $P_1^*$  and  $P^*B_A^-$ , as has been suggested for WT RCs (24) and has been suggested for B-branch ET in a mutant (11). We have also not included potential thermal repopulation of  $P_1^*$  from  $P^*B_A^-$ ,  $P^*B_A^-$  from  $P^*H_A^-$ , or  $P_2^*$  from  $P^*H_A^-$ . (We have also not included competing decay of  $P_1^*$  and  $P_2^*$  by internal conversion to the ground state with the known  $\sim$ 200 ps time constant for RCs in Deriphat (10). Inclusion of that process will not change the shapes of the SADS, but may give a small (5-10%) reduction in the yield of  $P^*H_A^-$  from  $P_2^*$  in the superexchange population.) In short, we used the simplest model with the fewest number of parameters that captures the main features of TA data and conveys the key differences among the six samples.

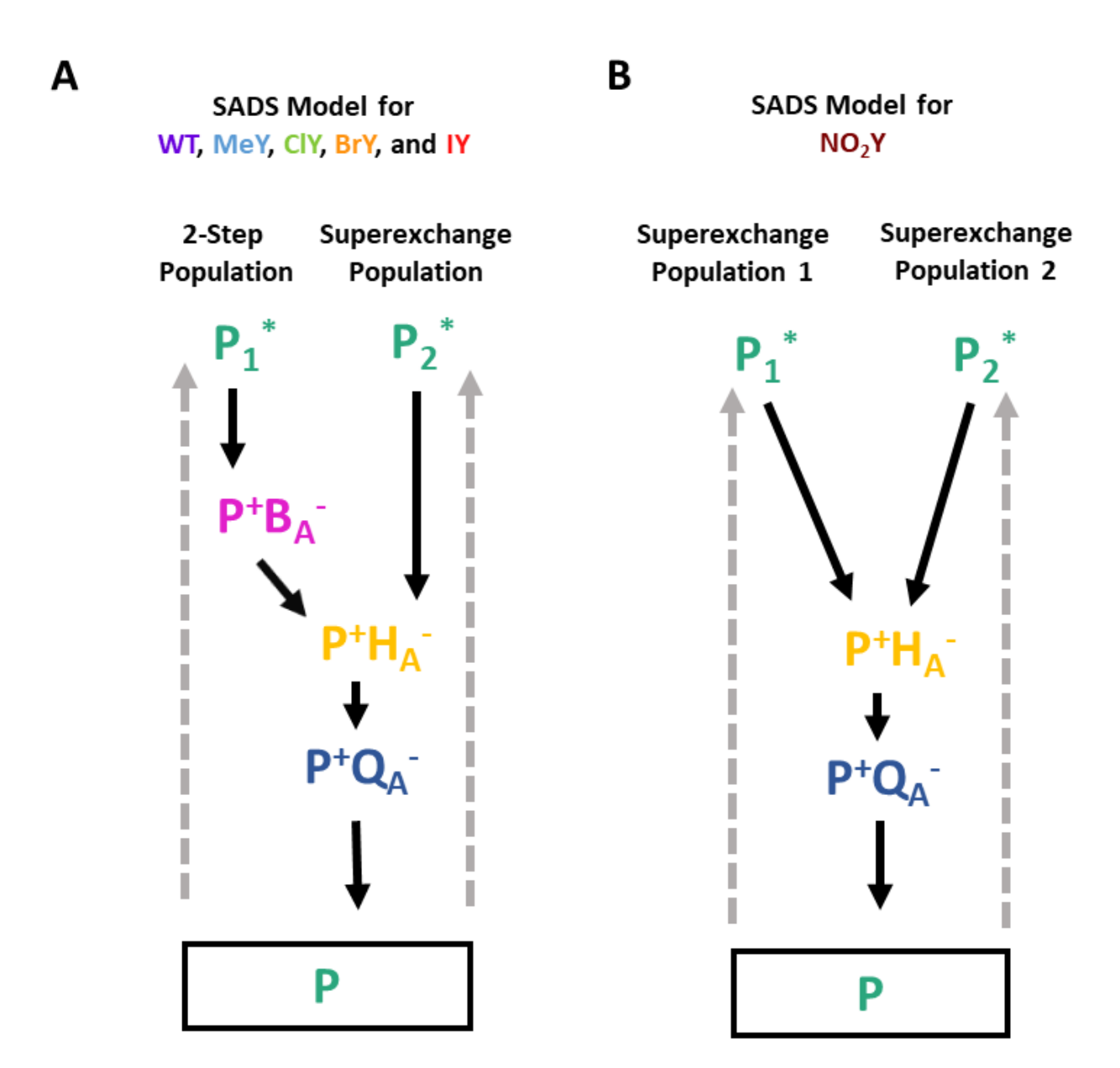


**Fig. S56.** (*A*) Model used for target analysis to produce SADS for all variants except for NO<sub>2</sub>Y RCs. (*B*) Model used for target analysis to produce SADS for NO<sub>2</sub>Y. For both (*A*) and (*B*) an  $\sim$ 0.1 ps component was included to account for flash artifacts (e.g., Raman scattering). Dashed grey arrows indicate light absorption from the ground state of P. P<sup>+</sup>Q<sub>A</sub><sup>-</sup> decay to ground state was modeled with an infinite (large) lifetime as it takes place over a timescale significantly longer than TA experiments ( $\sim$  100 ms). For completeness, SADS (and DADS) were obtained for NO<sub>2</sub>Y RCs if a  $\sim$ 0.7ps fixed component for P<sup>+</sup>B<sub>A</sub><sup>-</sup> decay was modeled; these are shown in appropriate sections of this document.

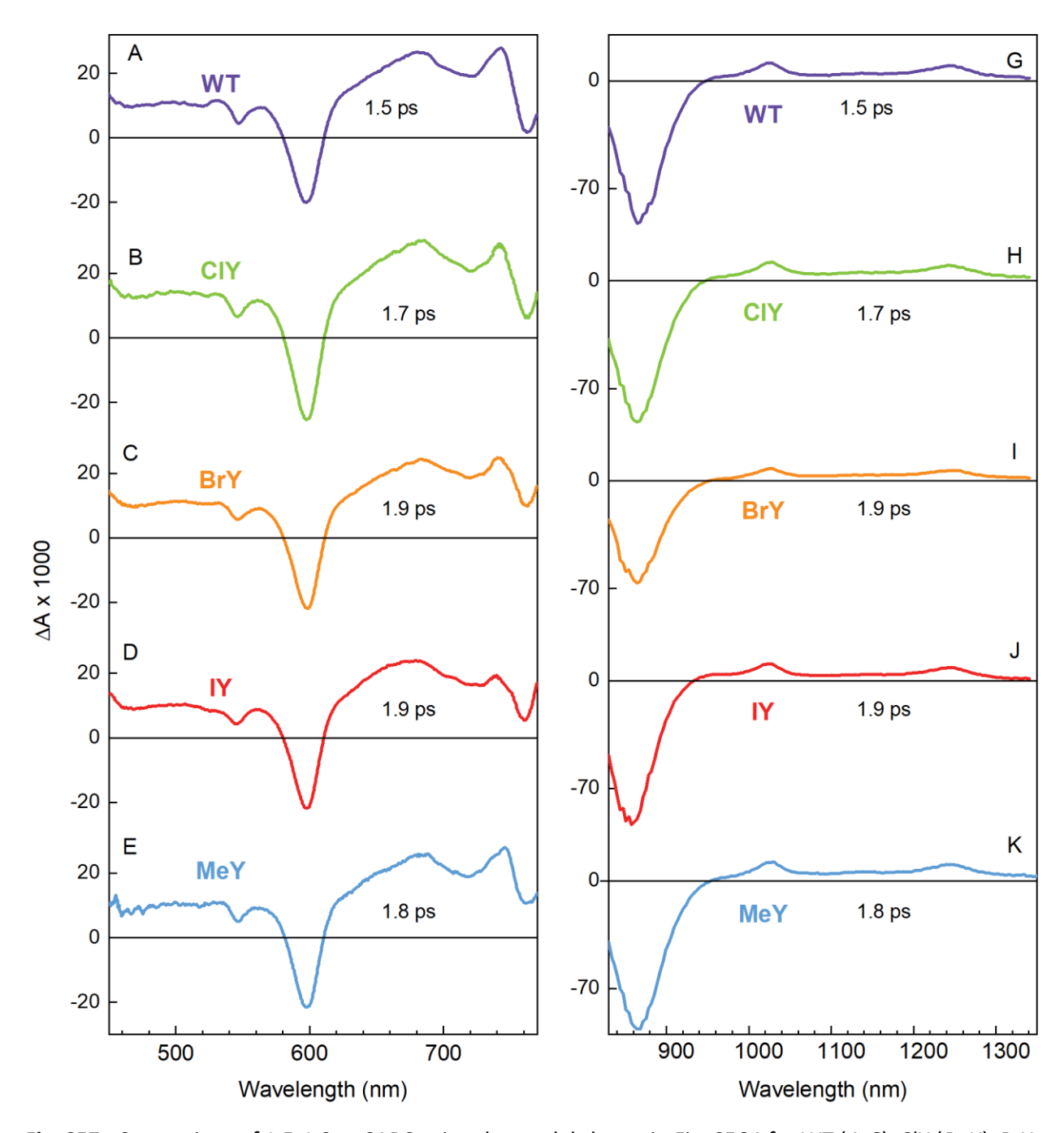


**Fig. S57.** Comparison of 1.5-1.9 ps SADS using the model shown in Fig. S56A for WT (A,G), CIY (B, H), BrY (C, I), IY (D, J), MeY (E, K). For NO $_2$ Y RCs, an  $^-$ 1 ps component is not included in the SADS analysis shown here and in Figs. S58–S61 for the longer-lived components. If a 0.7 ps component is fixed for NO $_2$ Y RCs, the associated SADS (Fig. S72A&B) are noisy and less readily assigned, indicating either no P<sup>+</sup>B<sub>A</sub><sup>-</sup> formation or a much smaller transient population. The time constants of the longer-lived components are similar to those obtained if the 0.7 ps fixed component is not included (Fig. S72C&D).

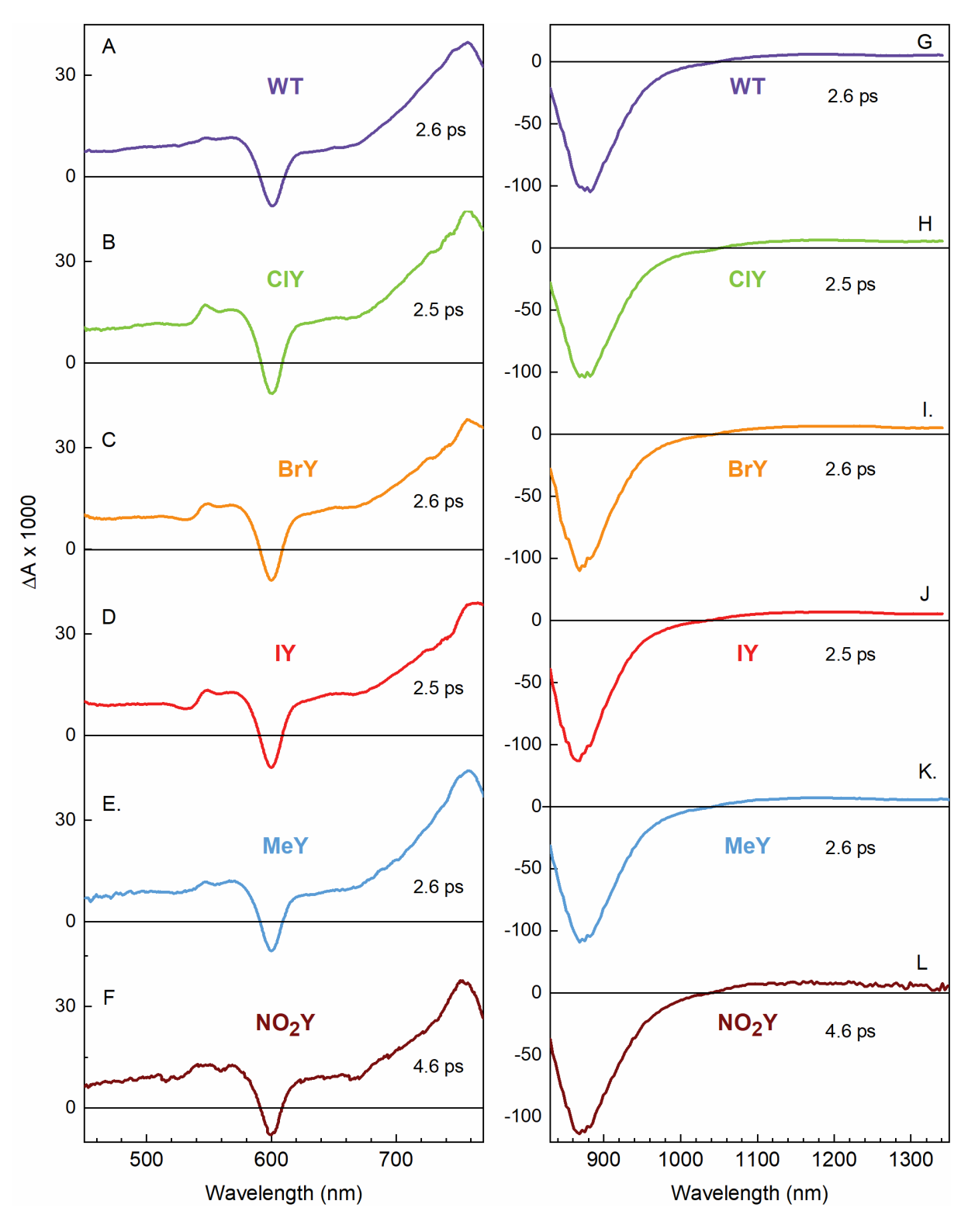


**Fig. S58.** Comparison of 2.5-4.6 ps SADS using the model shown in Fig. S56A for WT (A,G), ClY (B,H), BrY (C,I), IY (D,J), MeY (E,K), and NO<sub>2</sub>Y (F,L) RCs.

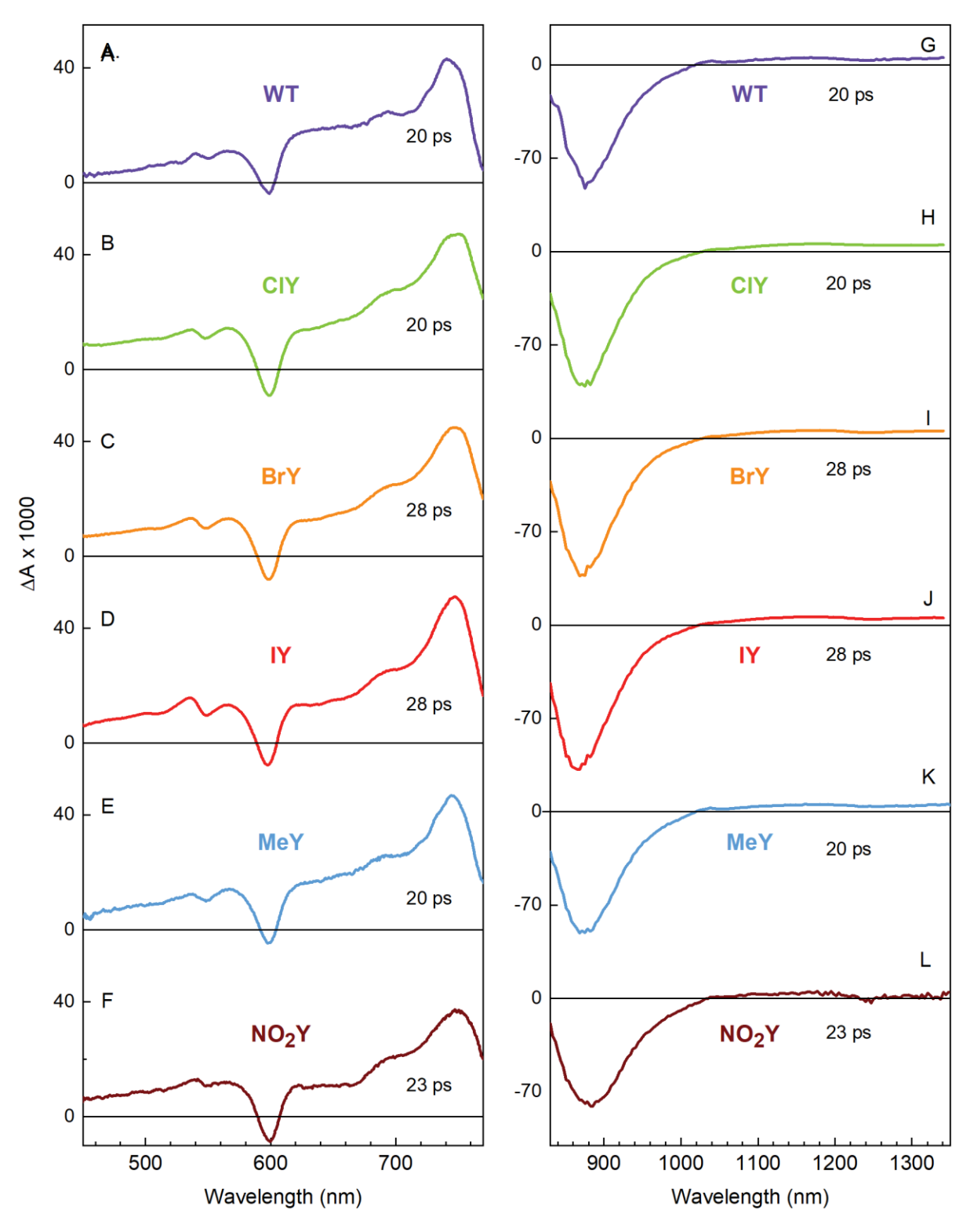


**Fig. S59.** Comparison of 20-28 ps SADS using the model shown in Fig. S56A for WT (A,G), CIY (B, H), BrY (C, I), IY (D, J), MeY (E, K), and NO<sub>2</sub>Y (F, L) RCs.

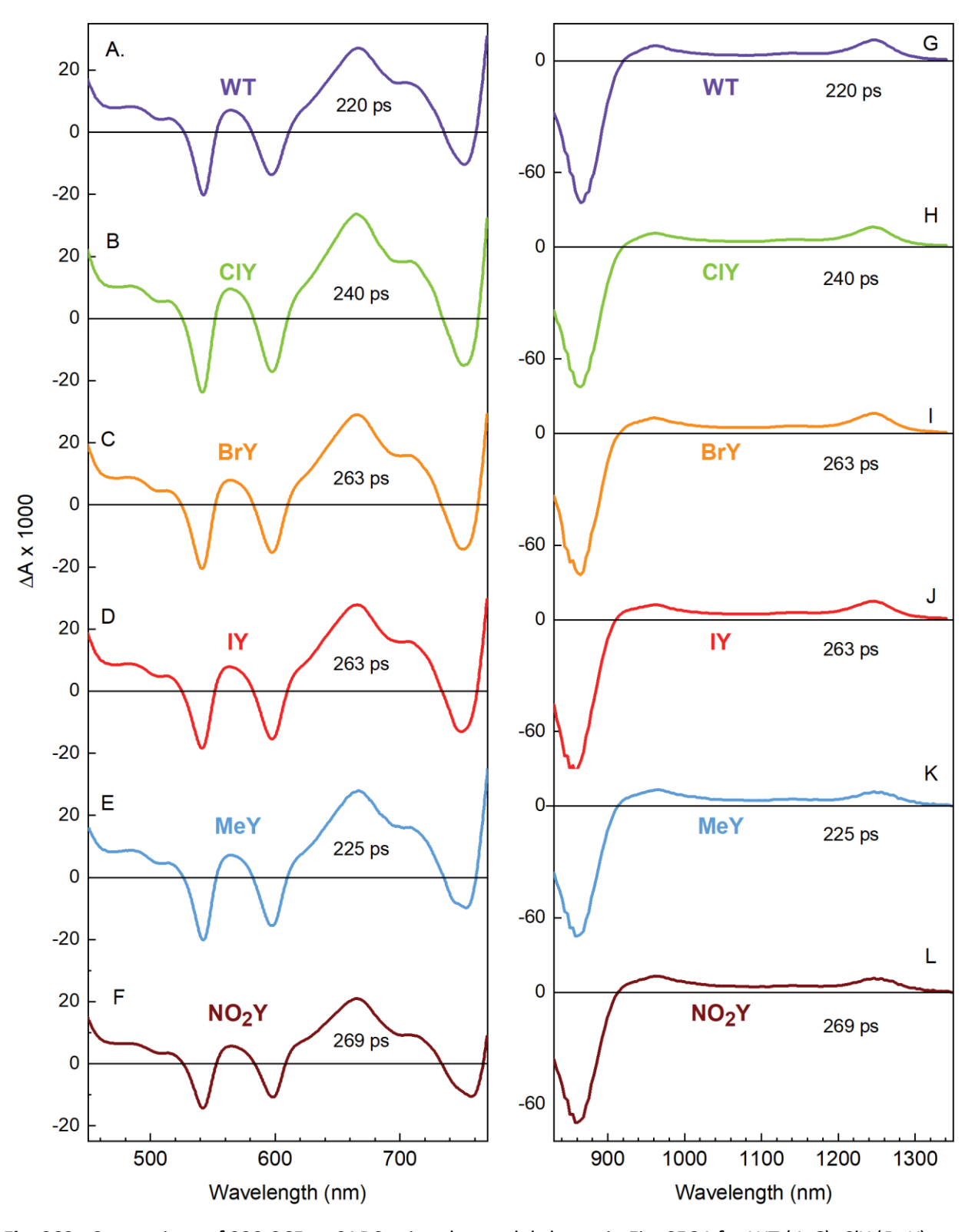


**Fig. S60.** Comparison of 220-265 ps SADS using the model shown in Fig. S56A for WT (A,G), ClY (B,H), BrY (C,I), IY (D,J), MeY (E,K), and NO<sub>2</sub>Y (F,L) RCs.

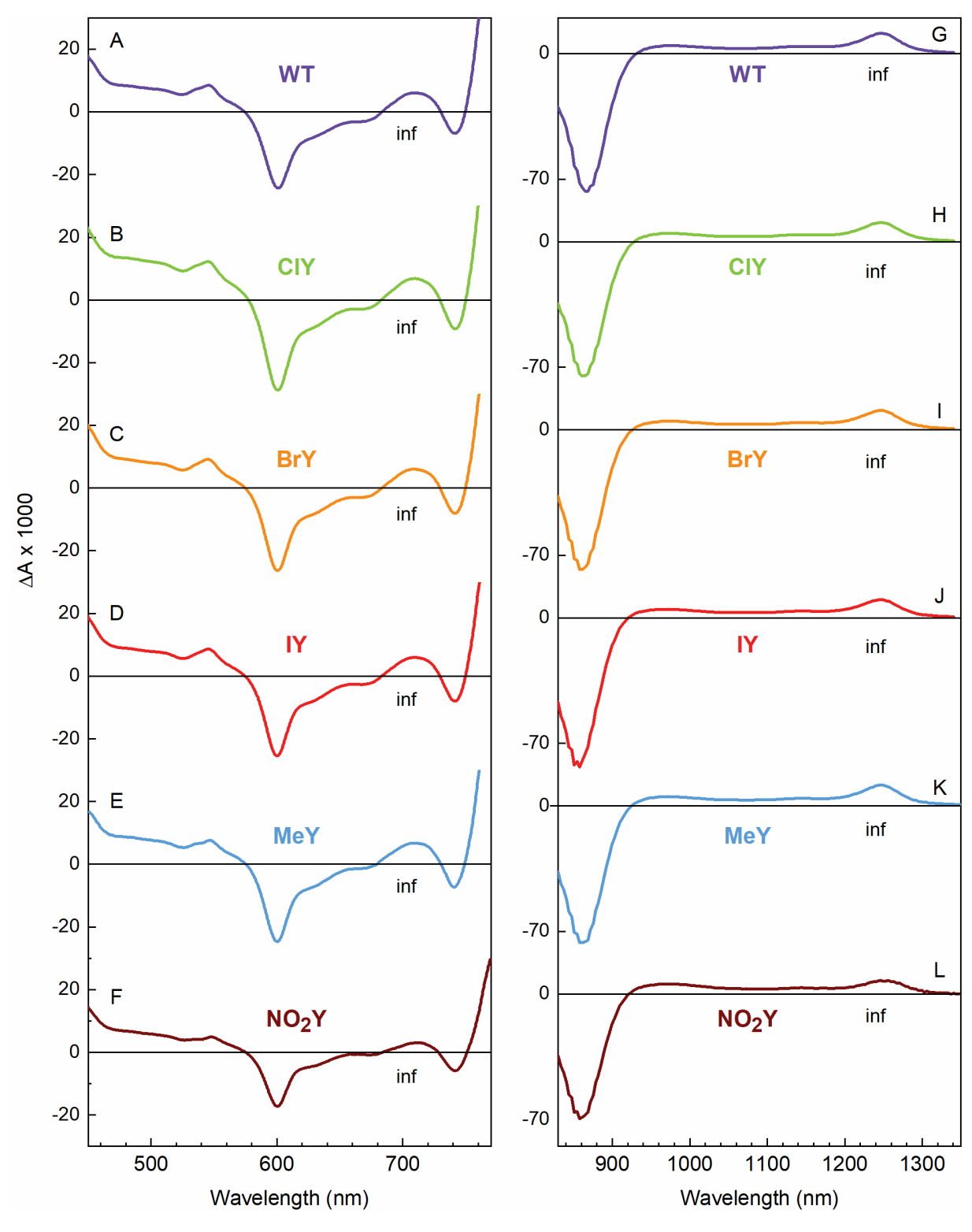


**Fig. S61.** Comparison of infinity (no decay) SADS using the model shown in Fig. S56A for WT (A,G), CIY (B, H), BrY (C, I), IY (D, J), MeY (E, K), and NO<sub>2</sub>Y (E, L) RCs.

## S3.10 SADS summary for each sample

Section S3.10 (Figs. S62–S73) shows the results of the SADS global analysis in a different format than given in Section S3.9. The first of two figures for each sample shows the SADS for all the states —  $P_1^*$ ,  $P_2^*$ ,  $P^+B_A^-$ ,  $P^+H_A^-$  and  $P^+Q_A^-$ —on the same plot. Recall that the SADS are effectively differential extinction coefficient ( $\Delta\varepsilon$ ) spectra. Thus, to relate to the raw data ( $\Delta A$  spectra), the SADS for a given state must be multiplied by the concentration of that state as a function of time ( $\Delta A = \Delta\varepsilon \cdot c \cdot 1$ , for a unity pathlength). Thus, the plot of concentration versus time for each state derived from the SADS global analysis are shown in the second figure of the pair for each sample in Section S3.10 (e.g. Fig. S62 and Fig. S63 for WT RCs). Overall, the quality of the SADS shows that the general model shown in Fig. S56A is appropriate. The differences between samples dervied from the SADS are consistent with the differences obtained from DADS and from fitting of the kinetic profiles at key wavelengths using the appropriate fitting function for each wavelength's kinetic profile. These data are summarized in Table S4 of Section S3.11.

Finally, as noted above concerning the raw TA data and global analysis for the  $NO_2Y$  mutant, there is little direct evidence for  $P^+B_A^-$  formation present in transient spectra. Thus, the data sets for  $NO_2Y$  RCs were modeled using a dual superexchange model in which both  $P_1^*$  (4.6 ps lifetime) and  $P_2^*$  (23 ps lifetime) decay directly to  $P^+H_A^-$  (Fig. S56B). The resulting SADS and concentrations vs time are shown in panels C and D of Fig. S72-S73. When TA data for  $NO_2Y$  is modeled using the two-step model that includes short-lived  $P^+B_A^-$  (e.g., 0.7 ps) in Fig. S56A, aside from the  $\sim$ 0.7 ps lifetime SADS, which gave poor SADS amplitude, all other states are in excellent agreement and gave comparable spectra for these states (panels A and B of Fig. S72 and Fig. S73). To be thorough, it is also important to state the unreasonable DADS for the nominal  $\sim$ 1 ps kinetic component or  $\sim$ 0.7 ps SADS for  $P^+B_A^-$  (see Fig. S72 panels A and B) for  $NO_2Y$  could be attributed to low signal from a lower concentration than in WT due to an increase in the rate of  $P^+B_A^-$  decay. This is not the model emphasized in the main text of this study, as

there is no direct evidence for an increase in the rate of  $P^+B_A^-$  decay to 0.7 ps in  $NO_2Y$ . Also, this model made less sense in the context of other energetic results developed in this work since it is not clear how an increase in  $P^+B_A^-$  energetics relative to WT would make an apparently barrierless reaction increase in the  $P^+B_A^-$  decay rate.

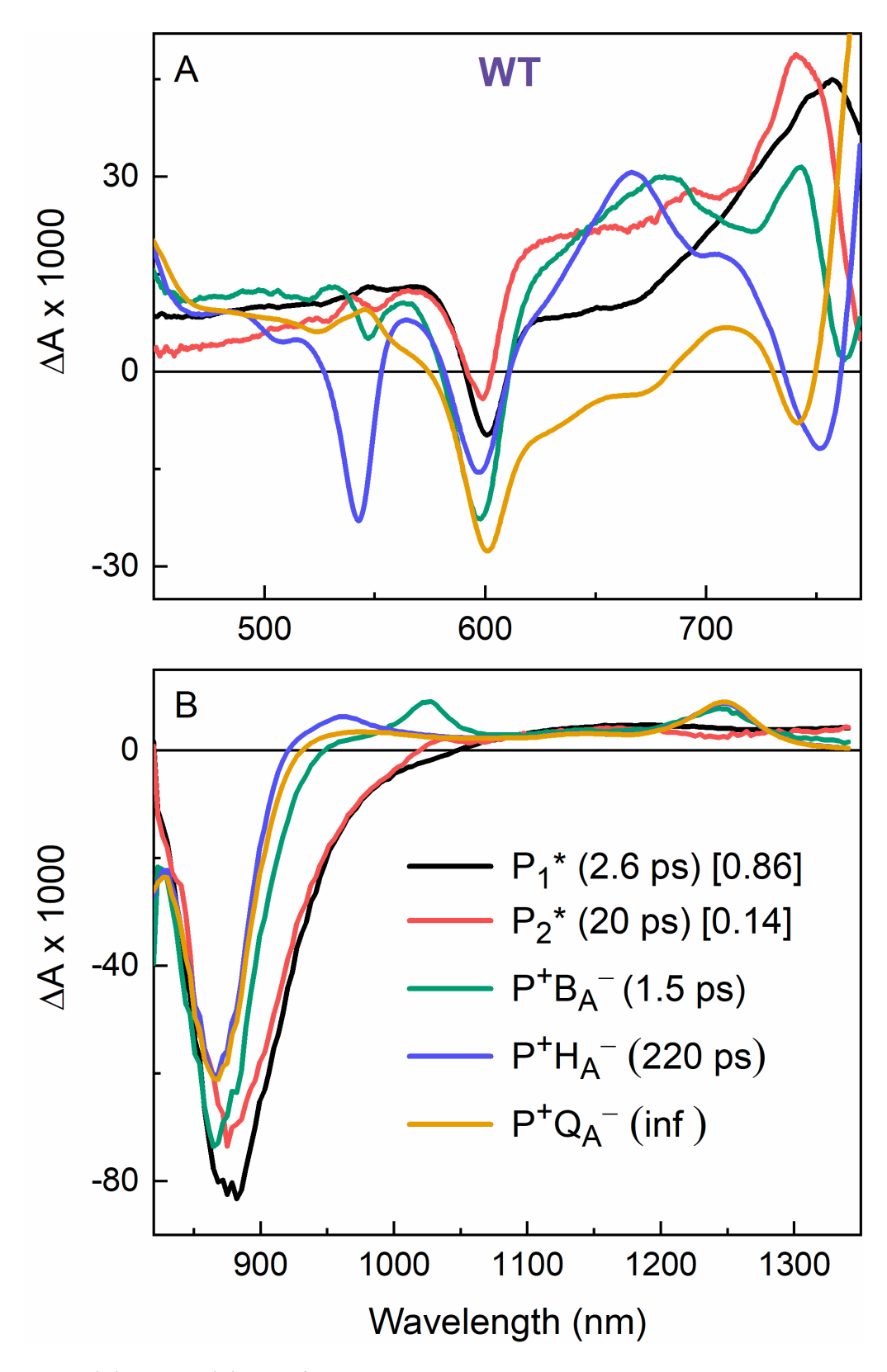


**Fig. S62.** Visible (A) and NIR (B) SADS for WT RCs using the model shown in Fig. S56A. The time constants are shown in parenthesis. The initial relative populations of  $P_1^*$  and  $P_2^*$  are given in square brackets. The associated concentrations vs time are shown in Fig. S63.

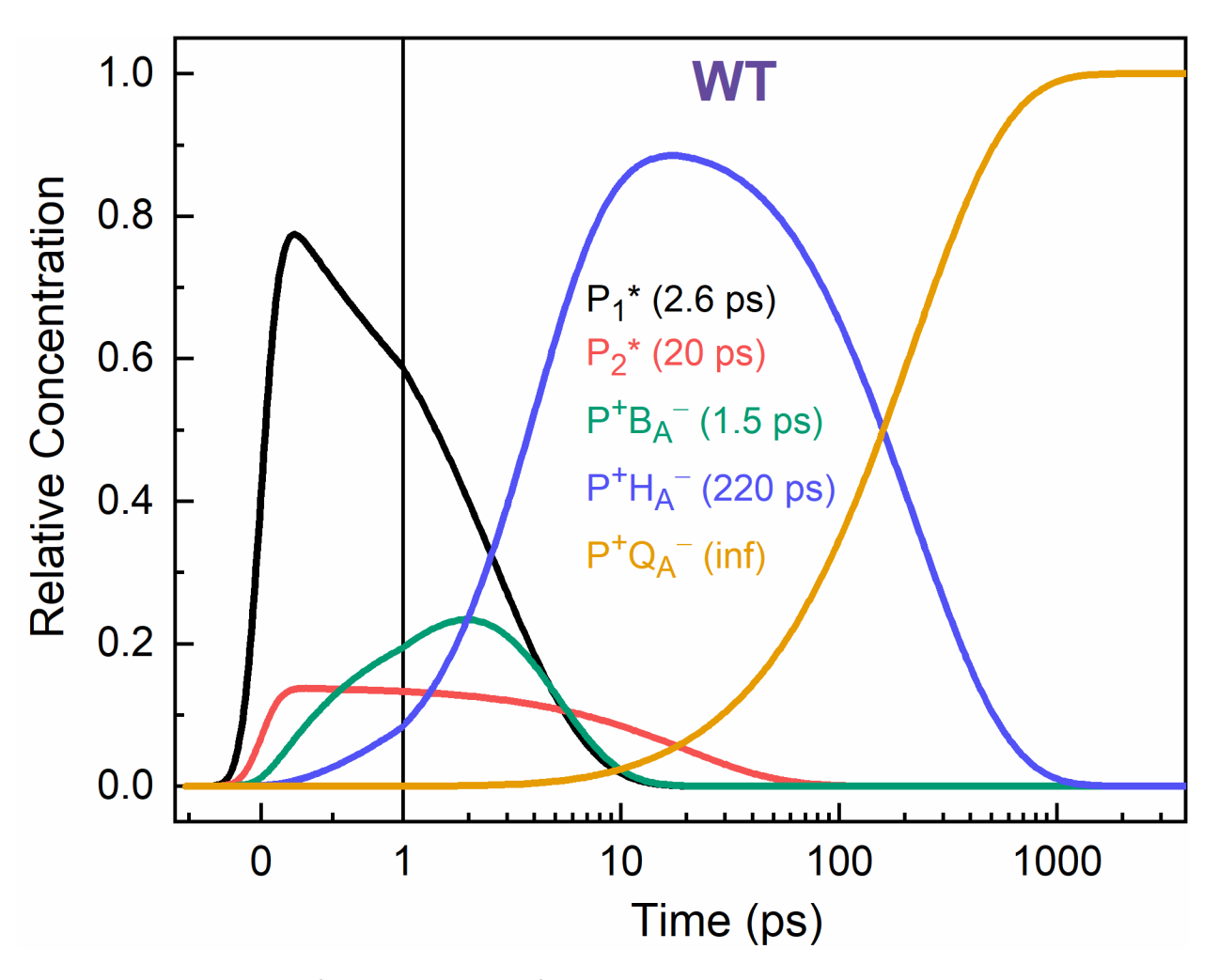


**Fig. S63.** Concentrations of the various states for WT RCs, with times associated with the SADS given in Fig. S62. The time axis is linear up to 1 ps and logarithmic past 1 ps.

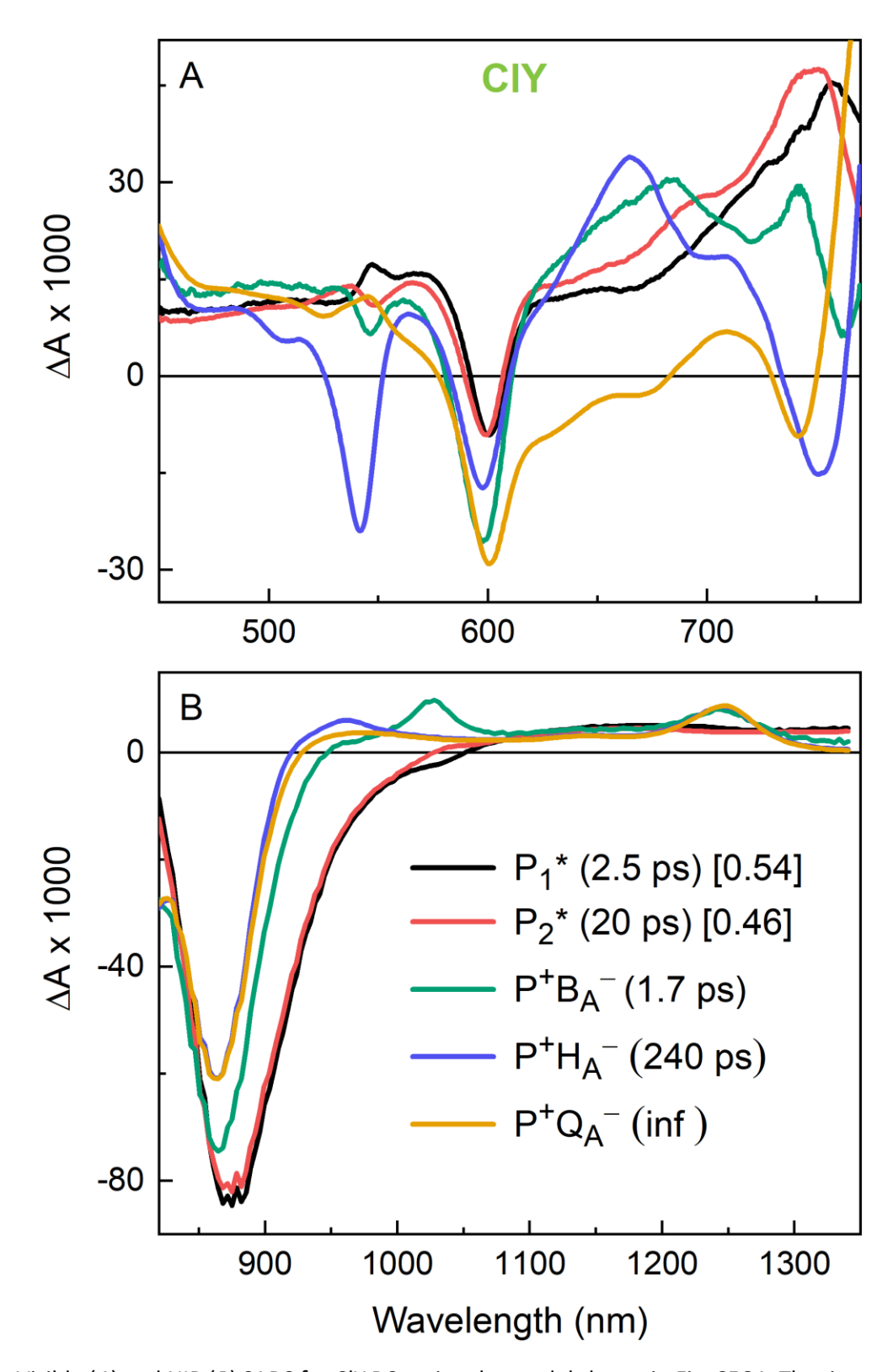


**Fig. S64.** Visible (A) and NIR (B) SADS for CIY RCs using the model shown in Fig. S56A. The time constants are shown in parenthesis. The initial relative populations of  $P_1^*$  and  $P_2^*$  are given in square brackets. The associated concentrations vs time are shown in Fig. S65.

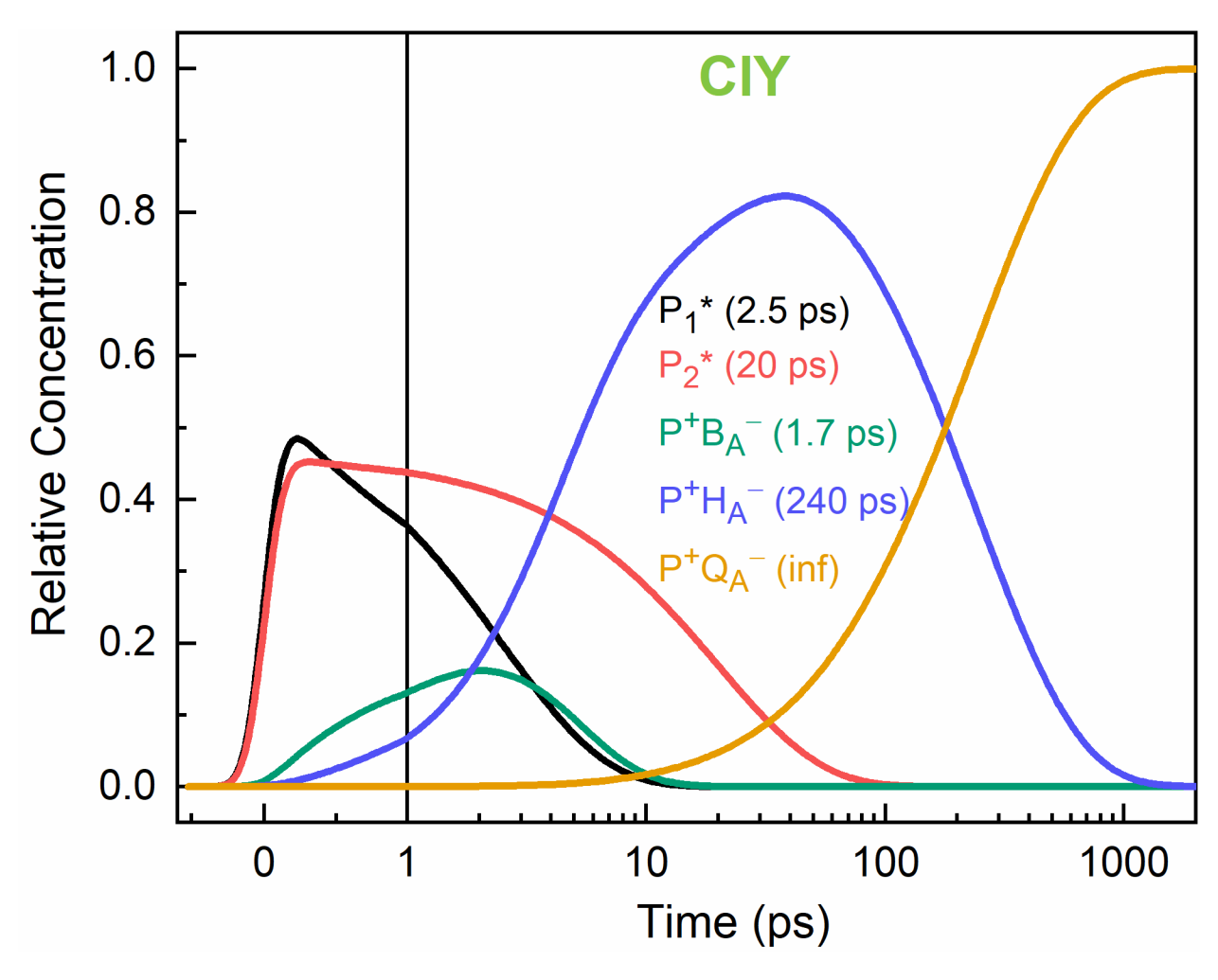


**Fig. S65.** Concentrations of the various states for CIY RCs, with times associated with the SADS given in Fig. S64. The time axis is linear up to 1 ps and logarithmic past 1 ps.

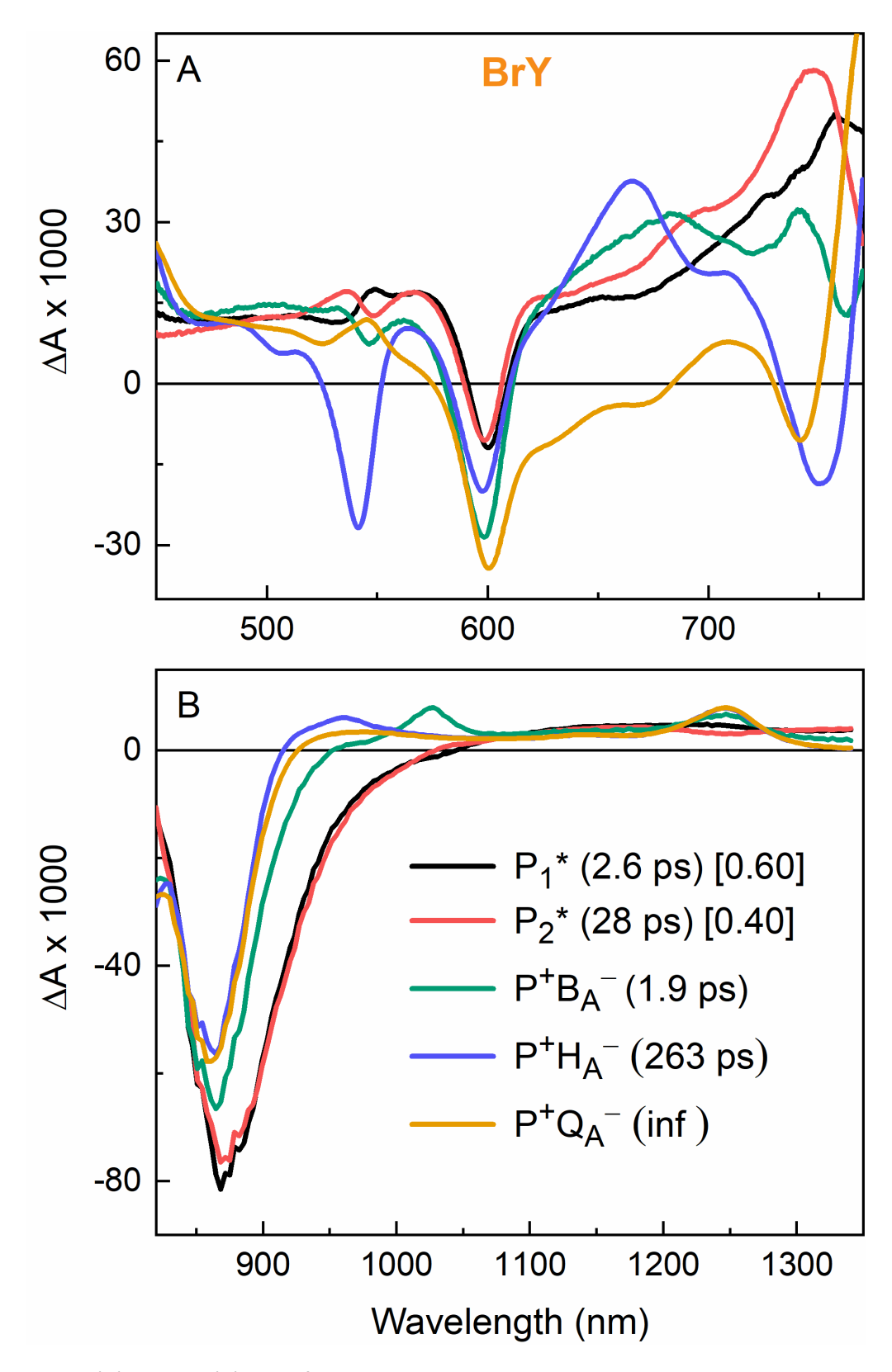


**Fig. S66.** Visible (A) and NIR (B) SADS for BrY RCs using the model shown in Fig. S56A. The time constants are shown in parenthesis. The initial relative populations of  $P_1^*$  and  $P_2^*$  are given in square brackets. The associated concentrations vs time are shown in Fig. S67.

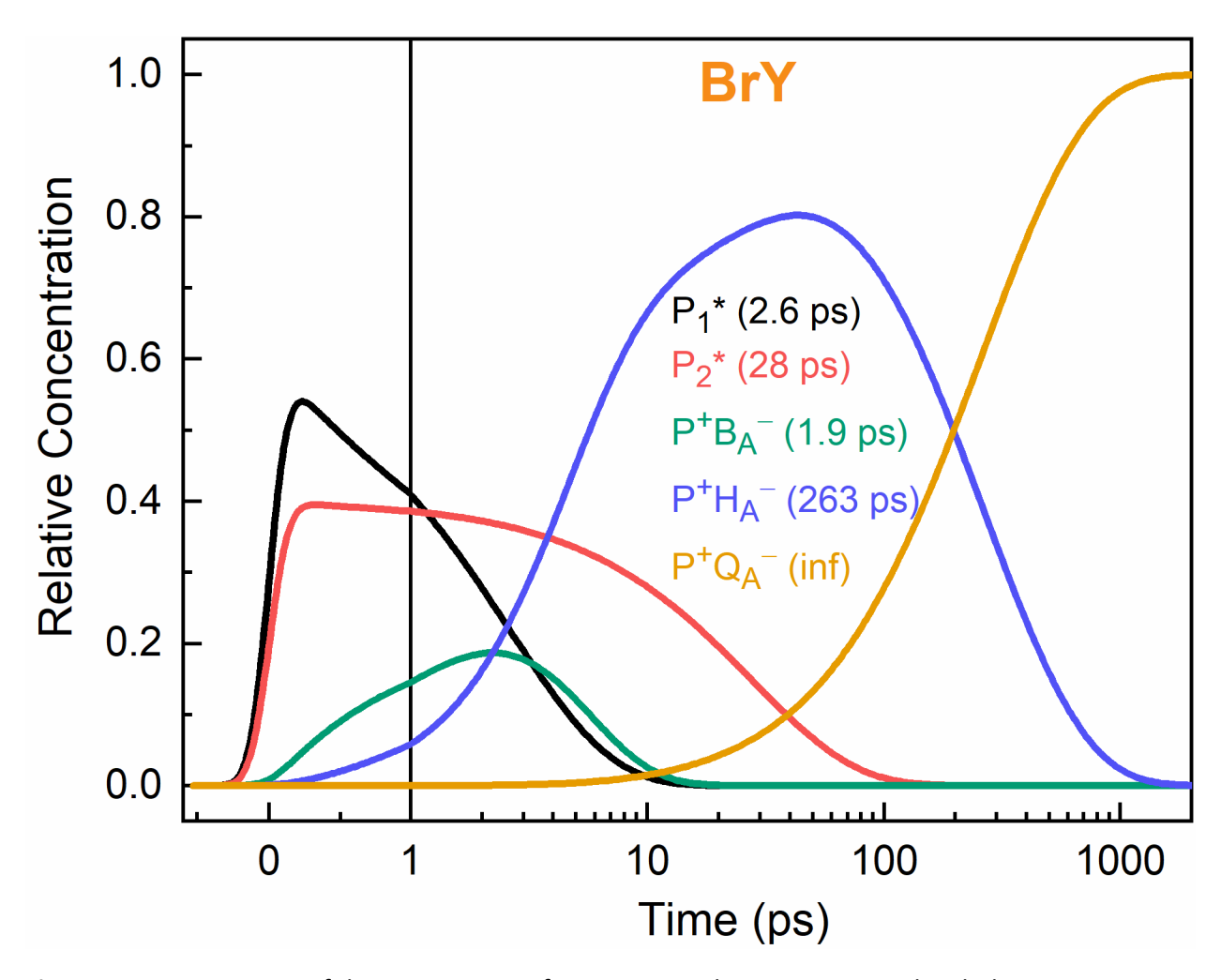


**Fig. S67.** Concentrations of the various states for BrY RCs, with times associated with the SADS given in Fig. S66. The time axis is linear up to 1 ps and logarithmic past 1 ps.

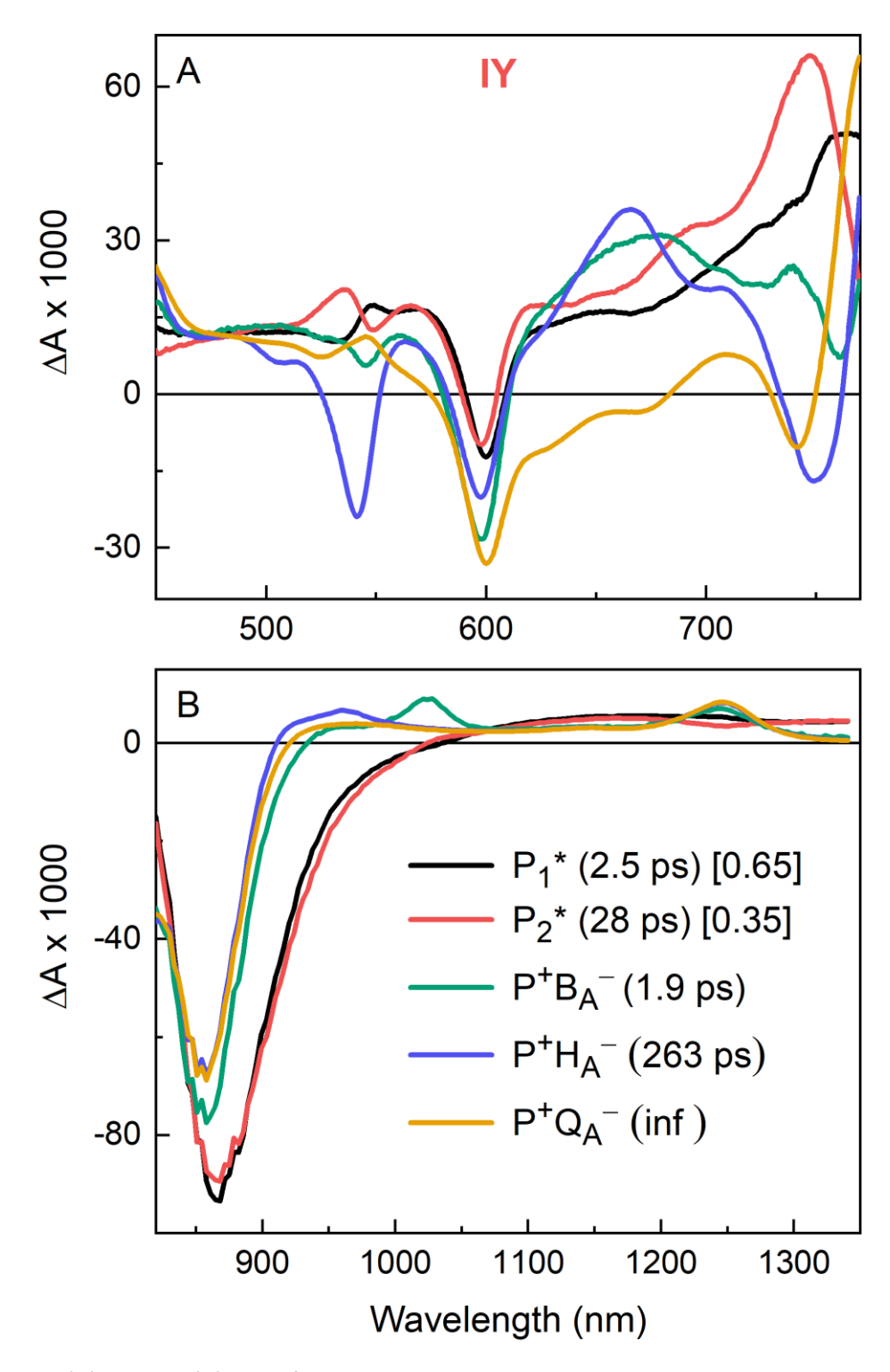


**Fig. S68.** Visible (A) and NIR (B) SADS for IY RCs using the model shown in Fig. S56A. The time constants are shown in parenthesis. The initial relative populations of  $P_1^*$  and  $P_2^*$  are given in square brackets. The associated concentrations vs time are shown in Fig. S69.

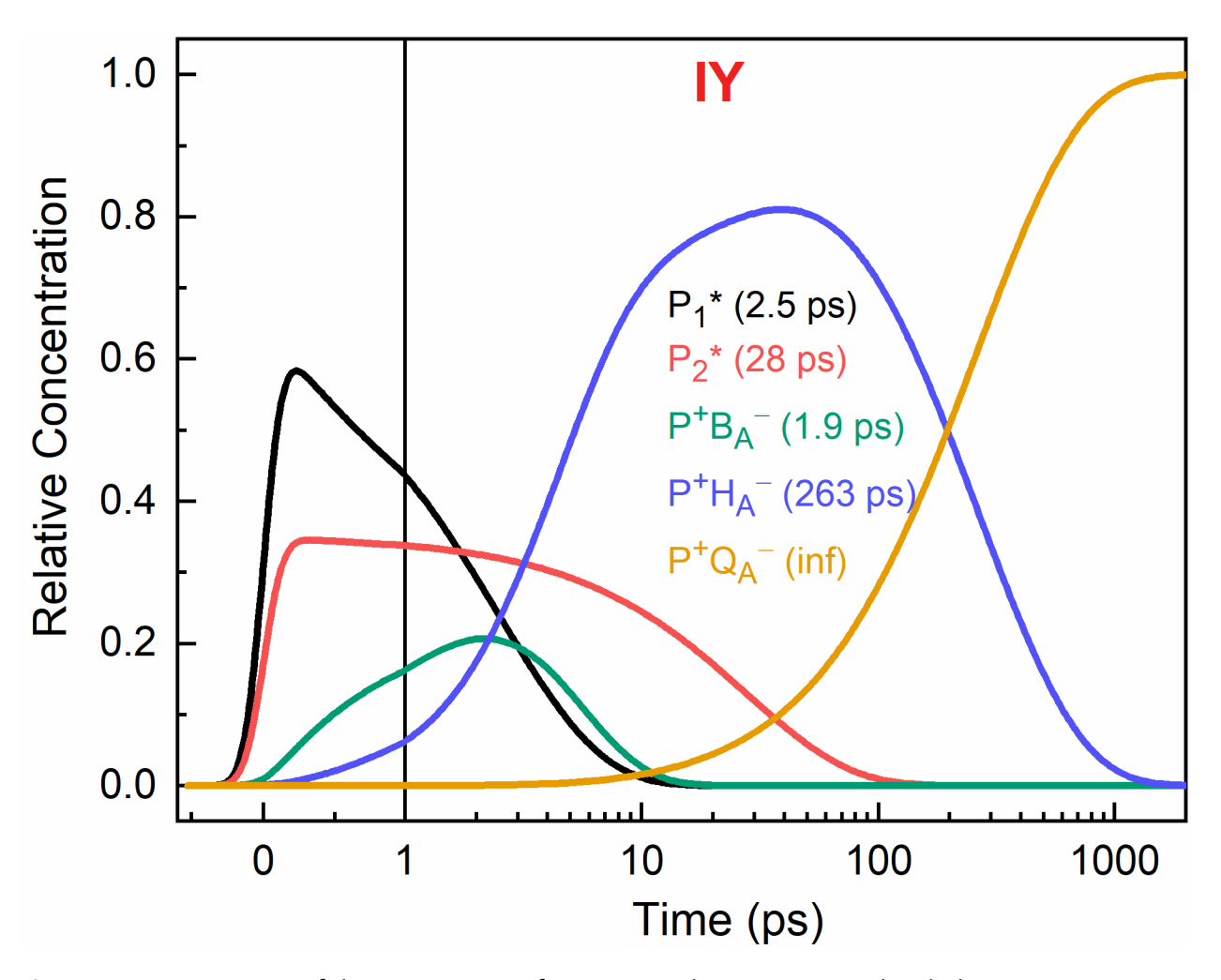


**Fig. S69.** Concentrations of the various states for IY RCs, with time associated with the SADS given in Fig. S68. The time axis is linear up to 1 ps and logarithmic past 1 ps.

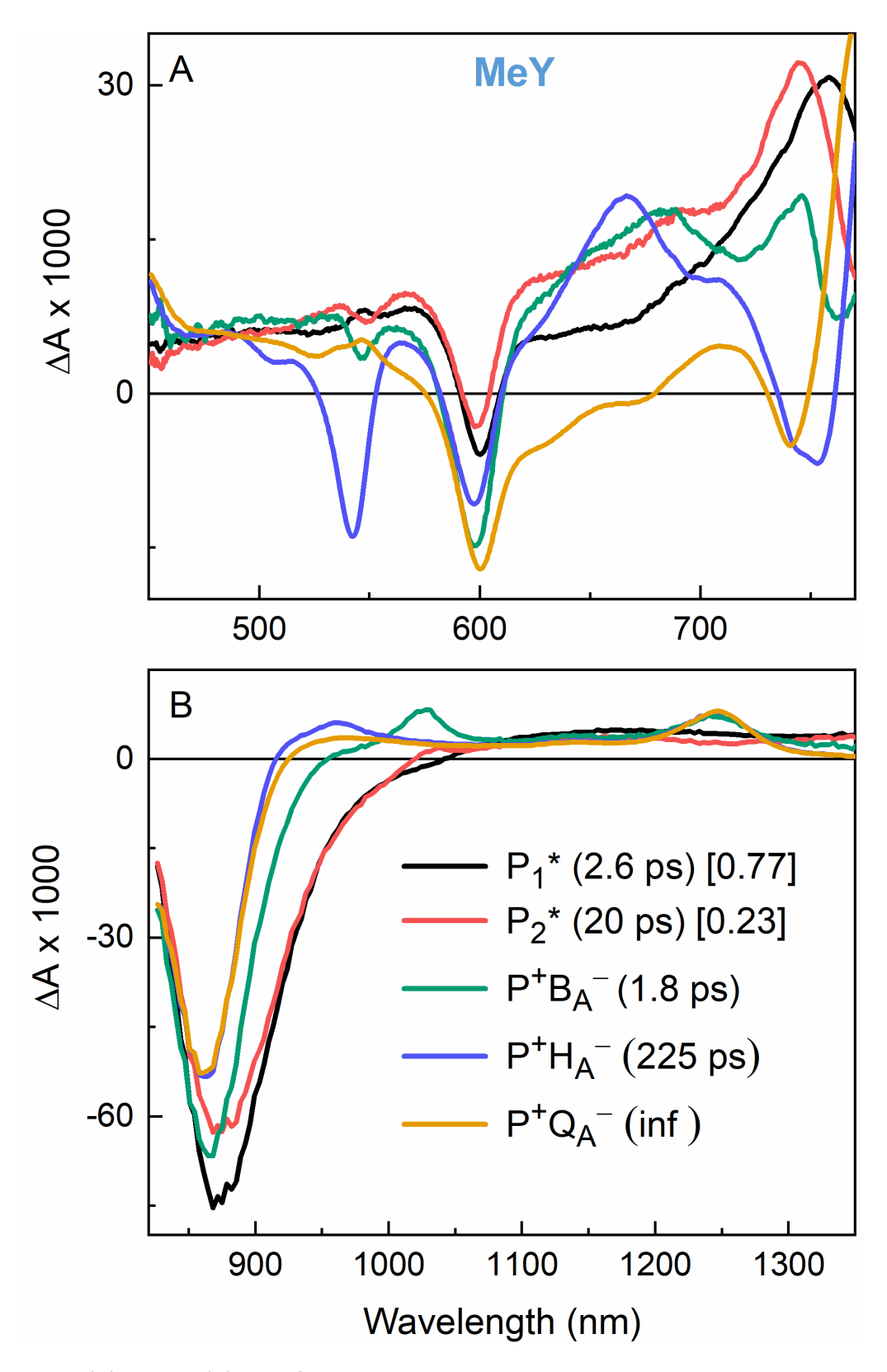


**Fig. S70.** Visible (A) and NIR (B) SADS for MeY RCs using the model shown in Fig. S56A. The time constants are shown in parenthesis. The initial relative populations of  $P_1^*$  and  $P_2^*$  are given in square brackets. The associated concentrations vs time are shown in Fig. S71.

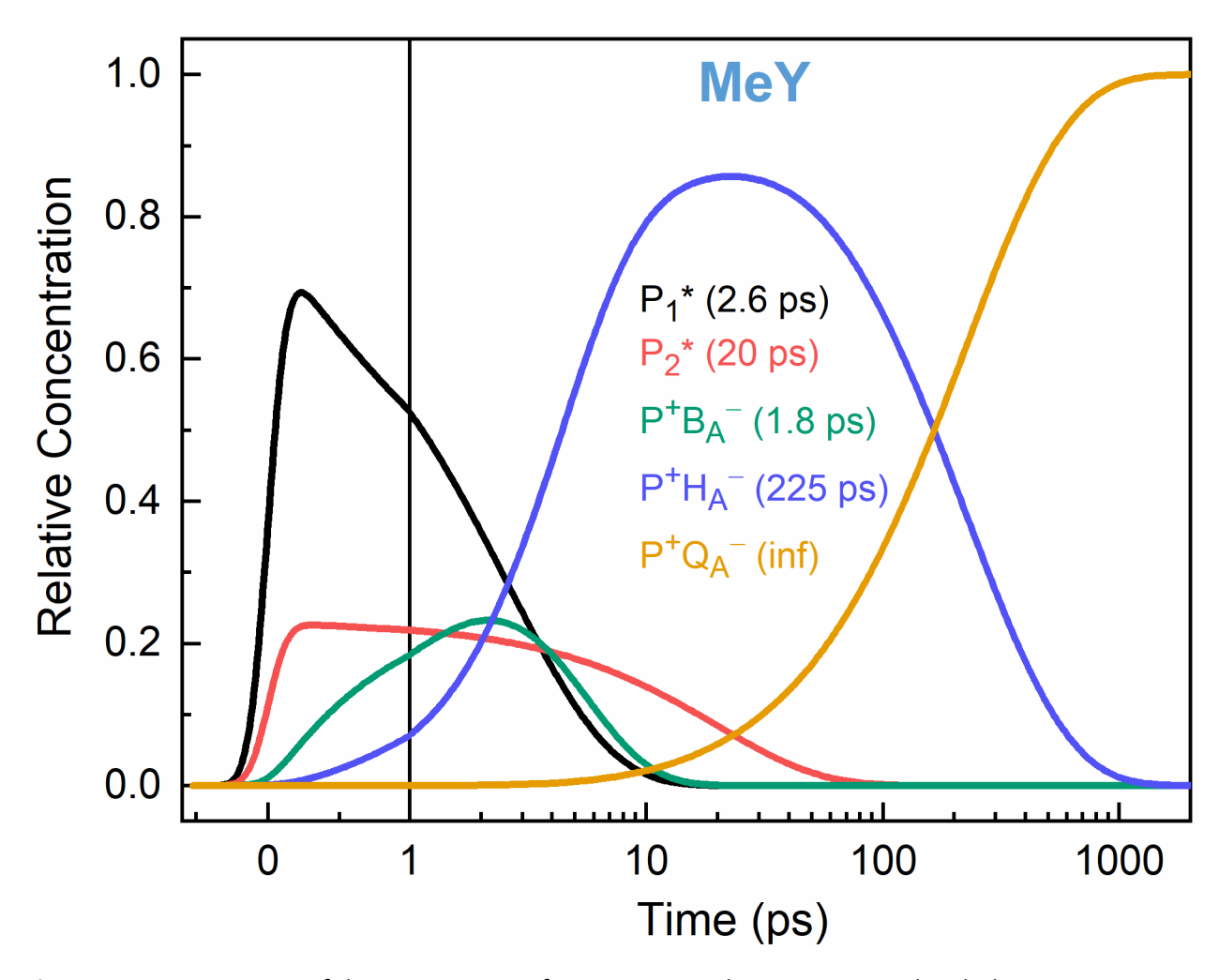


**Fig. S71.** Concentrations of the various states for MeY RCs, with time associated with the SADS given in Fig. S64. The time axis is linear up to 1 ps and logarithmic past 1 ps.

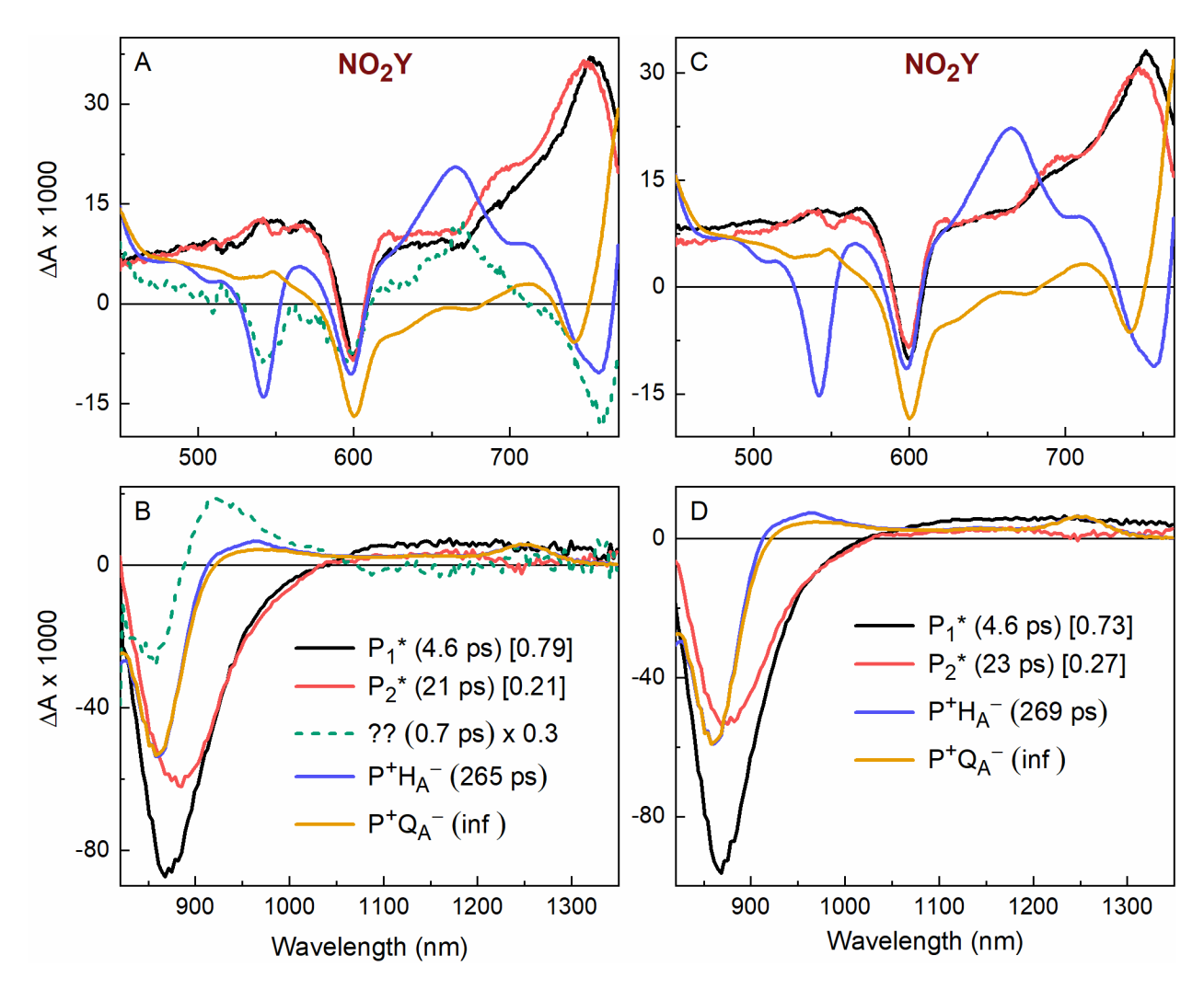


**Fig. S72.** Visible (A, C) and NIR (B, D) SADS for NO<sub>2</sub>Y RCs using the model shown in (A, B) Fig. S56A or (C, D) Fig. S56B. The time constants are shown in parenthesis. The initial relative populations of P<sub>1</sub>\* and P<sub>2</sub>\* are given in square brackets. The associated concentrations vs time are shown in Fig. S73. Note that the 0.7 ps SADS in panels A and B is not a clean spectrum for state P<sup>+</sup>B<sub>A</sub><sup>-</sup> as it is for the other samples, but rather has some features of P<sup>+</sup>H<sub>A</sub><sup>-</sup> plus others. This SADS is noisy and has a very low concentration (see Fig. S73A) which leads to a very large extinction coefficient ( $\Delta \varepsilon = \frac{\Delta A}{\ell \cdot C}$ ) to match the measured  $\Delta A$  spectrum and unlike with other samples, had to be scaled down by a factor of 3 to fit and be visualized with other SADS in the in panels A and B. The 0.7 ps component is absent for the SADS in panels C and D and, thus, in this model (Fig. S56B) both P<sub>1</sub>\* and P<sub>2</sub>\* decay to produce P<sup>+</sup>H<sub>A</sub><sup>-</sup> by a one-step superexchange mechanism.

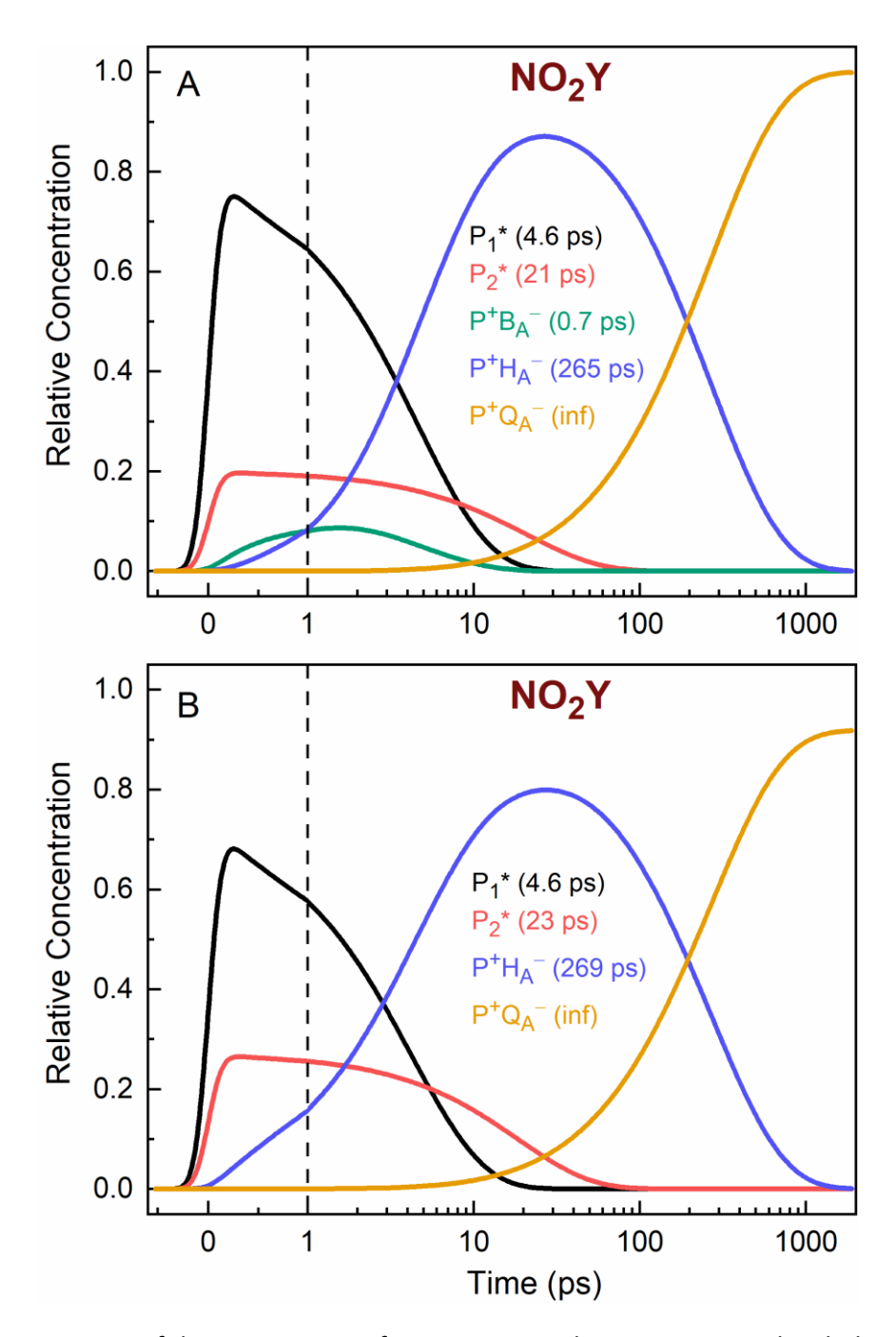


**Fig. S73.** Concentrations of the various states for  $NO_2Y$  RCs, with times associated with the SADS given in (A) Fig. S72A&B, which uses the model shown in Fig. S56A, or (B) Fig. S72C&D, which uses the model shown in Fig. S56B. The time axis is linear up to 1 ps and logarithmic past 1 ps.

### S3.11 Kinetic Analysis Summary Tables

**Table S4.** Summary of kinetic analysis of TA data.<sup>a</sup>

Component	WT	CIY	BrY	IY	MeY	NO <sub>2</sub> Y <sup>g</sup>
	τ (ps)	τ (ps)	τ (ps)	τ (ps)	τ (ps)	τ (ps)
SADS						
$P^{+}B_{A}^{-}$	1.5	1.7	1.9	1.9	1.8	_
P <sub>1</sub> *	2.6 (0.86)	2.5 (0.54)	2.6 (0.60)	2.5 (0.65)	2.6 (0.77)	4.6 (0.73)
P <sub>2</sub> *	20 (0.14)	20 (0.46)	28 (0.40)	28 (0.35)	20 (0.23)	23 (0.27)
$P^{+}H_{L}^{-}$	220	240	263	263	225	269
DADS <sup>b</sup>						
$P^{+}B_{A}^{-}$	<b>1</b> <sup>c</sup>	1.0	0.9	1.1	1.2	_
P <sub>1</sub> *	3.3 (0.87)	4.1 (0.60)	3.9 (0.57)	3.8 (0.65)	4.1 (0.86)	4.5 (0.76)
P <sub>2</sub> *	12 (0.13)	21 (0.40)	22 (0.43)	27 (0.35)	23 (0.14)	22 (0.24)
$P^{+}H_{A}^{-}$	220	240	263	261	223	270
924 nm 3 exp						
P <sub>1</sub> *	2.6 (0.70)	3.1 (0.53)	3.0 (0.52)	2.7 (0.57)	3.3 (0.78)	3.3 (0.68)
P <sub>2</sub> *	7.2 (0.30)	18 (0.47)	20 (0.48)	21 (0.43)	15 (0.22)	17 (0.32)
P* (avg) <sup>d</sup>	4.5	10.1	10.9	10.7	6.0	7.6
P* (2 exp fit) <sup>e</sup>	3.7	7.8	9.4	7.8	4.6	6.6
$P^{+}H_{A}^{-}$	225 <sup>f</sup>	240 <sup>f</sup>	265 <sup>f</sup>	265 <sup>f</sup>	225 <sup>f</sup>	265 <sup>f</sup>
542 nm 3 exp						
P <sub>1</sub> *	4.1 (0.97)	4.1 (0.60)	4.1 (0.59)	3.9 (0.64)	4.5 (0.88)	3.7 (0.62)
P <sub>2</sub> *	14 (0.03)	18 (0.40)	18 (0.41)	20 (0.36)	17 (0.12)	12 (0.38)
P* (avg) <sup>d</sup>	4.5	9.6	9.9	9.6	6.0	7.1
P* (2 exp fit) <sup>e</sup>	4.3	7.0	7.3	6.5	5.1	5.9
$P^{+}H_{L}^{-}$	225	259	293	292	237	293

Time constants are in picoseconds. The values in parenthesis are the relative amplitudes of the two P\* decay components (P<sub>1</sub>\* and P<sub>2</sub>\*). For simplicity in making comparisons, the first column gives the state that is thought to decay with the listed time constant. Rigorously, each kinetic component for DADS reflects all absorbance changes that occur on a particular time scale, which nominally involves the decay of one state and formation of another.

- <sup>b</sup> Values from DADS using fixed relative amplitudes of the P<sub>1</sub>\* and P<sub>2</sub>\* components. Similar time constants are obtained from the traditional DADS in which all amplitudes are set at 1. See Section S3.8.
- <sup>c</sup> The value was fixed in the fit.
- $^{d}$  P\*(avg) is the amplitude-weighted-average lifetime for P<sub>1</sub>\* and P<sub>2</sub>\*.
- The P\* lifetime determined from a 2-exponent fit. This included only one component for the P\* decay (rather than two components for the decay of  $P_1^*$  and  $P_2^*$ ) and one component for the decay of  $P^+H_A^-$  (the lifetime obtained being about the same as that derived from the 3-exponential fit).
- Value fixed at the P+H<sub>A</sub> lifetime obtained from global analysis (DADS and SADS) of the visible region data sets, because this state makes only a small contribution at 924 nm, which is dominated by P\* stimulated emission.
- 9 DADS for NO₂Y did not include an ~1 ps fast component, and SADS were created with the model in Fig. S56B rather than the model in Fig. S56A for the other samples. If a fixed 0.7 ps component is included, the time constants given in Table S5 are obtained, which are like those obtained in the absence of the fast component. The DADS and SADS for all other components are similar with and without the inclusion of the fast component, as shown in the Figures in Sections S3.7-S3.10.

**Table S5.** Kinetic Analysis of NO<sub>2</sub>Y TA data where SADS are created using Fig. S56A and the DADS contain a related fast kinetic component.

Component	NO <sub>2</sub> Y		
	τ (ps)		
SADS			
$P^{+}B_{A}^{-}$	0.7		
P <sub>1</sub> *	4.6 (0.79)		
P <sub>2</sub> *	21 (0.21)		
$P^{+}H_{A}^{-}$	265		
DADS			
$P^{+}B_{A}^{-}$	0.7		
P <sub>1</sub> *	4.5 (0.79)		
P <sub>2</sub> *	23 (0.21)		
$P^{+}H_{A}^{-}$	265		

<sup>&</sup>lt;sup>a</sup> If the P<sup>+</sup>B<sub>A</sub><sup>-</sup> state is present, the P<sup>+</sup>B<sub>A</sub><sup>-</sup> lifetime must be <1 ps to account for the extremely small B<sub>A</sub> anion band appearing at 1030 nm (see Figs. S36–S38). The time constant was fixed at 0.7 ps in the SADS and DADS because a reliable fit value could not be obtained. The time constants for the other components are very close to those obtained if the fast component is not included, which are given in the last column of Table S4 (see Figs. S54-S55, Figs. S72-S73).

# S4 Spectroscopy and P/P<sup>+</sup> Redox Potential Determination

#### S4.1 298 K UV-vis-NIR Absorption and Data Analysis

All room temperature UV-vis-NIR absorption measurements in this study were performed in PerkinElmer Lambda 25 and Lambda 365 spectrometers. To obtain P\* energetics (Fig. S74), spectra were truncated to a region between 10,000 and 14,300 cm $^{-1}$  (700–1000 nm) with RC samples all in Deriphat Dialysis Buffer (10 mM Tris, pH 8.0, 0.05% Deriphat 160C) at room temperature. Since neither  $B_A$  and  $B_B$  nor  $H_A$  and  $H_B$  can be resolved at room temperature, all spectra were fit well to a sum of three pseudo-Voigt functions. The inclusion of an additional pseudo-Voigt band (fits performed in the NIR region with 4 pseudo-Voigt functions) to fit the upper- and lower-exciton bands of P's  $Q_{\gamma}$  transition negligibly affected the performance of the fit and shifted P\* energetics by less than 10 cm $^{-1}$ . This is unsurprising given spectra were obtained at room-temperature and, even for cryo-temperatures (77 K), the upper exciton band makes only a minor contribution to P's absorbance and is resolvable primarily through 2-dimensional electronic spectroscopy data (60). Since electron transfer proceeds primarily through the lower exciton band (60), our fits should determine the relevant P\* energetic changes for electron transfer. All samples were in Deriphat Dialysis Buffer with concentrations such that absorbance at all peak maxima was below 0.5 at 1 cm pathlengths.

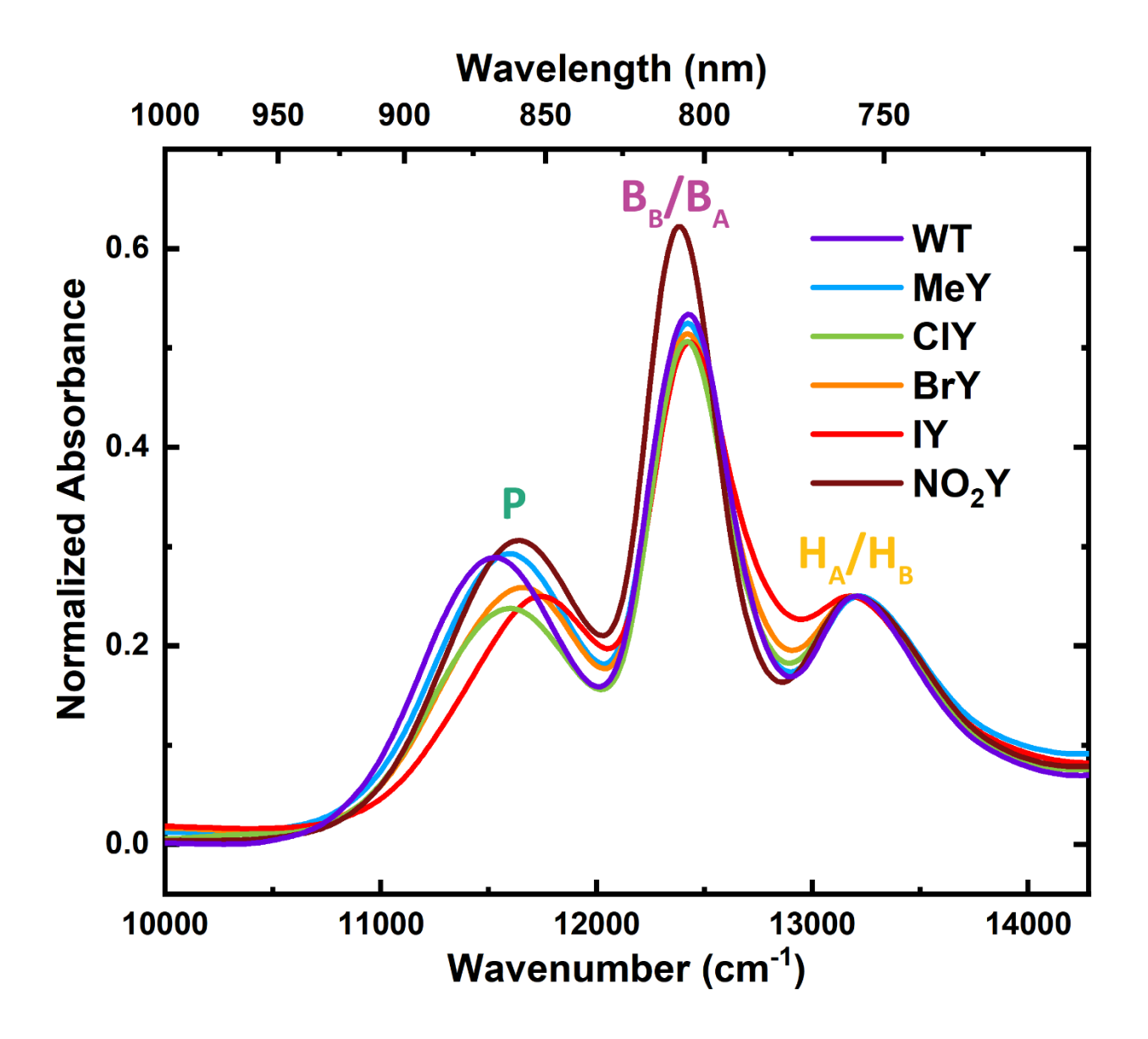


**Fig. S74.** Room temperature absorbance date for all RC variants, where the P  $Q_y$  absorbance band is the peak with lowest energy at  $\sim 11,600~\text{cm}^{-1}$ , the  $B_A/B_B~Q_y$  peak follows at  $\sim 12,400~\text{cm}^{-1}$  and the highest energy  $H_A/H_B~Q_y$  peak occurs at  $\sim 13,200~\text{cm}^{-1}$ . The absorbance spectrum for each RC were normalized at the  $H_A/H_B~Q_y$  absorbance band maximum.

#### S4.2 Redox Titration

Redox titrations were performed with freshly prepared 500 mM potassium ferrocyanide (Allied Chemical) and 500 mM potassium ferricyanide (J.T.Baker Chemical Co.) following literature protocol (9, 61). All protein samples were performed in the same set of titration starting conditions: approx. 800 µL

of 3.1  $\mu$ M of protein sample in Deriphat Dialysis buffer and 1.15  $\mu$ L of 500 mM ferrocyanide (to ensure protein samples were fully reduced). A ferricyanide aliquot was then gradually added to increase the solution potential by 5-10 mV. Titrations began with the addition of 0.58  $\mu$ L 500 mM ferrocyanide oxidant and over 200  $\mu$ L aliquots of oxidant were added towards the end of the titration to reach the necessary potentials required to fully oxidize P. Following each oxidant addition, protein solution was gently mixed with a syringe, the potential (voltage) was measured, and the absorbance at the Q<sub>y</sub> P absorbance maxima (~865 nm) was measured. Electric potentials throughout the titration were measured with a platinum counter electrode and a Ag|AgCl|KCl (saturated) reference electrode loaned to us by Dr. Thomas Cook and Jasper Ainsworth at Stanford University.

## S4.3 Redox Titration Data Analysis

For each data set, RC P absorbance at the Q<sub>Y</sub> P absorbance maxima at ~865 nm (A) was plotted as a function of redox potential (E). To account for changes in concentration, P absorbance was normalized to the Q<sub>Y</sub> H absorbance at 759 nm which does not significantly shift or change intensity upon P oxidation. A modified form of the Nernst Equation can be derived from the Beer-Lambert Law,  $A = \varepsilon \cdot \ell \cdot c$ , and the Nernst Equation,  $E = E^\circ - \frac{RT}{F} \ln{([P^+]/[P])}$ , which is as follows:

$$A = A_0 - \frac{\Delta A_0}{1 + \exp\left[\frac{-(E - E^\circ)}{25.4 \ mV}\right]}$$
 (S1)

Note that at room temperature RT/F is  $\sim$ 25.4 millivolts,  $A_0$  is the initial absorbance at  $\sim$ 865 nm, and  $\Delta A_0$  is the initial difference in absorbance between P and P $^+$ . Data was fit to this modified form of the Nernst Equation. Since we take  $\varepsilon_{P}^+ \approx 0$  at  $\sim$ 865 nm, we can use  $A_0$  and  $\Delta A_0$  to both baseline our data and normalize our initial absorbance to unity such that we can equate absorbance with the fraction of P still reduced. This was done to all measured data. Titrations were performed at least twice on each

sample and for all titrations there was  $\leq$ 3 mV difference in P/P<sup>+</sup> reduction midpoint potential determined,  $E^{\circ}$ .

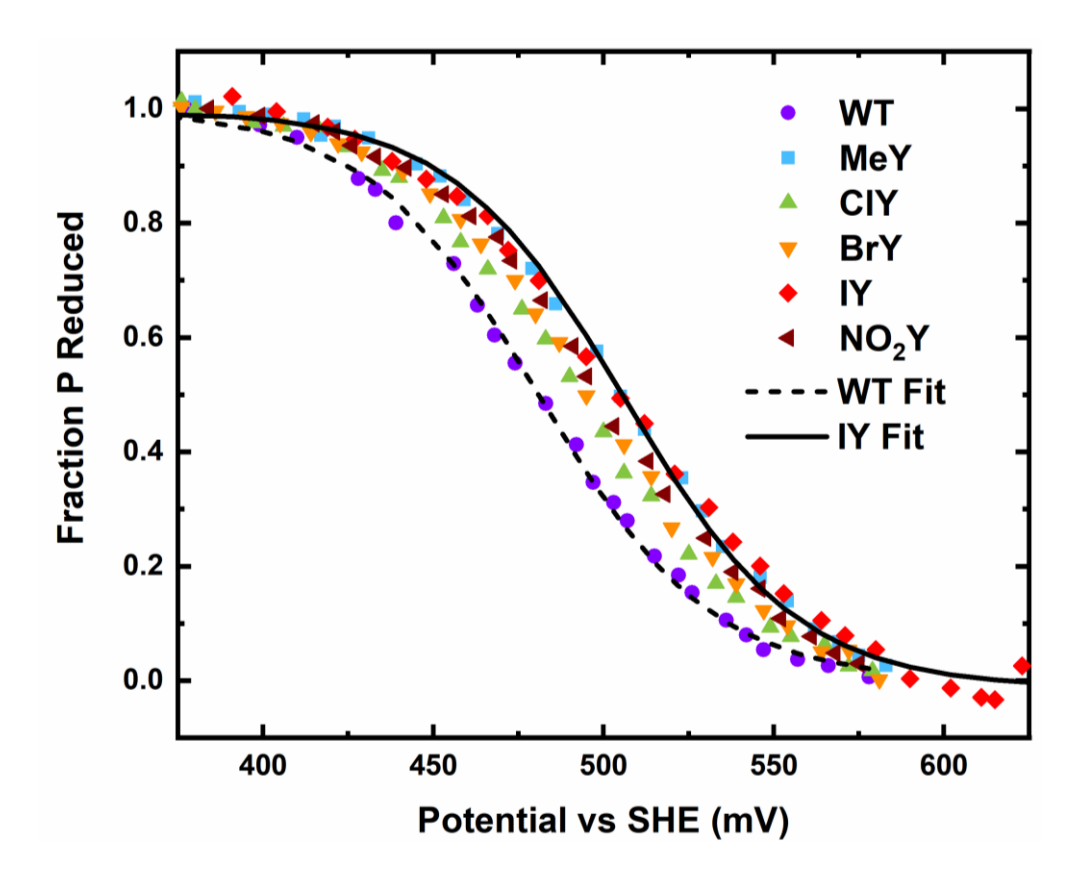


**Fig. S75.** Redox titration curves for all RC samples, where fits for the lowest and highest reduction midpoint potential,  $E^{\circ}$ , are displayed for WT and IY, respectively. The fraction of unoxidized (and still absorbing) P remaining is calculated based on P absorption at the P  $Q_y$  maximum for that sample as described in the text.

Data summarizing absorbance and redox potentials for all variants is given in Fig. S76, leading to estimates for the change in  $\Delta G$  for  $P^* \to P^+$  ( $\Delta \Delta G_2$ ) for M210 variant relative to WT displayed also in Fig. 7 in the main text.

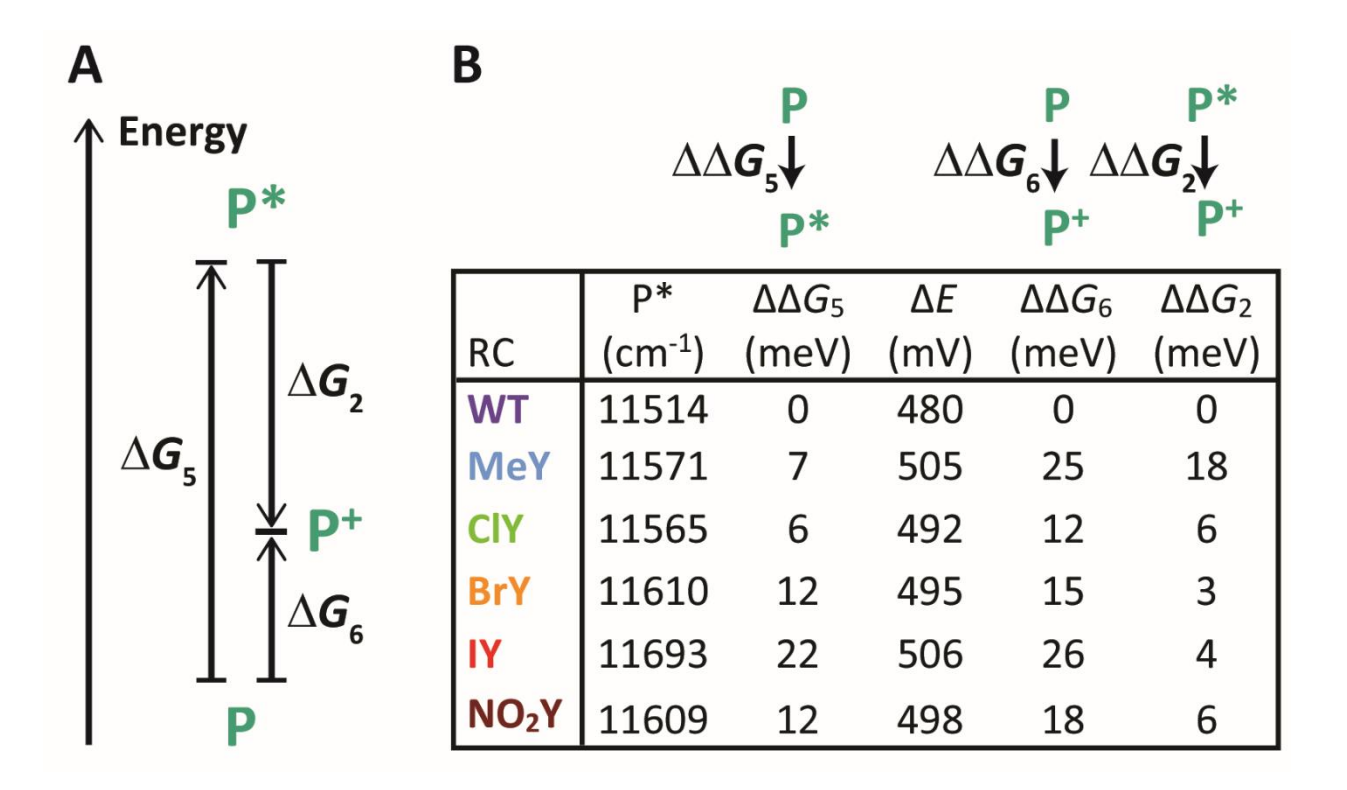


**Fig. S76.** (*A*) Energy diagram depicting the relative relationship between P\*, P\*, and P energy levels, with numbers indicating individual energetic processes. Note this is the energy diagram for P/P\*/P\* alone and not for the charge transfer states (e.g. P\*B<sub>A</sub><sup>-</sup>) seen in primary charge transfer which is described in Fig. 1. Processes were numbered 2, 5, and 6 due to previous energetic process numbering (1–4) in Figs. 6-7 in the main text. Note that the vertical axis is not to scale. (*B*) Energetic values for P\* and Δ*E* are determined from fits to 298 K absorption spectra and to redox titrations, respectively. Here  $\Delta\Delta G_5$  is the shift in P\* free energy from WT,  $\Delta\Delta G_6$  is the shift in ground state P oxidation free energy from WT, and  $\Delta\Delta G_2 = \Delta\Delta G_6 - \Delta\Delta G_5$ . Energetic processes associated with each  $\Delta\Delta G$  are depicted and labeled above each column. All RC redox potentials (Δ*E*) had an error of ± 1 mV when repeated but error on calibration of the Ag|AgCl|KCl (± 5 mV) reference indicates protein midpoint potential conservatively would also have an error of 5 mV and consequently an error of 5 meV in  $\Delta\Delta G_6$ . P\* values all had an instrumental error of ±7 cm<sup>-1</sup> (1 meV) due to spectrometer resolution. Collectively this led to an error of ±5 meV in  $\Delta\Delta G_2$ .

#### S4.4 Energetic Approximations

In the discussion that follows,  $\Delta\Delta G$  will be followed by the reaction it describes in parenthesis,

i.e. the  $\Delta\Delta G$  for  $B_A \to B_A^-$  will be  $\Delta\Delta G$  ( $B_A \to B_A^-$ ).

In Fig. 7 we utilize the following approximation:

$$\Delta \Delta G \left( B_A^* H_A \to B_A^+ H_A^- \right) \approx -\Delta \Delta G \left( B_A \to B_A^- \right) \tag{S2}$$

We do this based on the rationale below:

(1) Based on the assumption that RC tyrosine variation does not affect the energetics of  $H_A$  due to the tyrosine substituent's distance to the  $H_A$  chromophore, we approximate the following:

$$\Delta \Delta G \left( \mathsf{B}_{\mathsf{A}}^* \mathsf{H}_{\mathsf{A}} \to \mathsf{B}_{\mathsf{A}}^+ \mathsf{H}_{\mathsf{A}}^- \right) \approx \Delta \Delta G \left( \mathsf{B}_{\mathsf{A}}^* \to \mathsf{B}_{\mathsf{A}}^+ \right) \tag{S3}$$

(2) The  $\Delta\Delta G$  (B<sub>A</sub>  $\rightarrow$  B<sub>A</sub><sup>+</sup>) can be estimated similarly to how we approximate  $\Delta\Delta G$  (P\*  $\rightarrow$  P\*) from the  $\Delta\Delta G$  (P  $\rightarrow$  P\*) and the  $\Delta\Delta G$  (P  $\rightarrow$  P\*) (Fig. S76). Because the energetics of B<sub>A</sub>\* with respect to B<sub>A</sub> do not change significantly from WT as all B<sub>A</sub> Q<sub>y</sub> absorbance maxima are shifted by 3 nm or less (<4 meV) (Fig. S74), we estimate the following:

$$\Delta \Delta G \left( \mathsf{B}_{\mathsf{A}}^* \to \mathsf{B}_{\mathsf{A}}^+ \right) \approx \Delta \Delta G \left( \mathsf{B}_{\mathsf{A}} \to \mathsf{B}_{\mathsf{A}}^+ \right) \tag{S4}$$

(3) Finally, since the tyrosine perturbations in these variants are largely electrostatic changes to the WT  $B_A$  and P chromophore environments, we assume they will affect the opposite charge transfer process equivalently. This is supported by the minimal change in the  $B_A$   $Q_y$  absorbance maxima. Because the  $Q_y$  band of bacteriochlorins is dominated by the LUMO-HOMO free energy gap (62) and since the  $Q_y$  band of  $B_A$  (and  $B_B$ ) at 800 nm is shifted at most by  $\sim$ 3 nm ( $\sim$ 4 meV) among the mutants, the HOMO and LUMO of  $B_A$  appear to be shifted similarly by the tyrosine variants examined here. This leads us to make the final approximation:

$$\Delta \Delta G (B_A \to B_A^+) \approx -\Delta \Delta G (B_A \to B_A^-)$$
 (S5)

### S4.5 Characterization of Phenolic Dipoles

Based on past simulations performed on WT RCs (63) and previous experiments (9), the interaction between the dipole of the tyrosine hydroxyl and  $B_A$  is an important contributing factor to the protein's stabilization of  $P^+B_A^-$  (63); those simulations were a primary motivation for this work. Previous experiments indicate halogens minimally perturb the electronic properties of aromatic rings even when

directly attached to the  $\pi$ -system being spectroscopically probed (7, 64, 65). In order to get a sense of the effects of substituents on the O-H dipole, we performed density functional theory (DFT) calculations on substituted phenols as tyrosine analogs (2-X-4-methylphenol, where X is the substituent varied. These calculations suggest that the halogen and methyl substituents do not strongly affect the O-H dipole, while a nitro substituent causes a more significant change. Nitro-substituted phenols decrease the O-H dipole moment by 0.3 – 0.7 D relative to an unsubstituted phenol at the 2-position (Table S6). This smaller dipole in NO2Y RCs would presumably destabilize P<sup>+</sup>B<sub>A</sub><sup>-</sup> relative to WT. Within the three halogenated RCs, two populations are present; P\*B<sub>A</sub><sup>-</sup> free energy in one is WT-like and that in the other population is significantly destabilized. It seems likely that the destabilizing population is due to a fraction of RCs where the halogen is oriented towards the Mg<sup>2+</sup> of B<sub>A</sub> based on the correlation in trends of populations observed from resonance Stark spectroscopy and X-ray crystallography (Figs. 2 and 6). That said, studies detailing the consequences of a halogen fixed proximal to the Mg<sup>2+</sup> in bacteriochlorophylls or chlorophylls are not discussed in the literature and to be definitive would require more characterization. Additionally, the orientation of the O-H dipole at M210 is not known and it is possible that halides might alter the dipole orientation normally present in WT RCs and change the P<sup>+</sup>B<sub>A</sub><sup>-</sup> free energy. In the case of MeY RCs, the energetic change was small and mainly affected the oxidation of P\*.

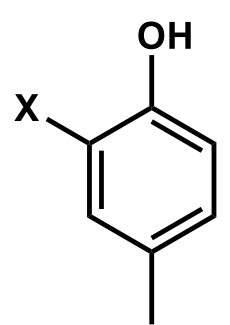


Fig. S77. 2-X-4-methyl phenol used in DFT calculations in Table S6.

**Table S6.** Functional group perturbations of phenol O–H dipoles based on DFT calculations <sup>a</sup>

Functional/ Basis/Pop. Analysis	B3LYP/ 6-31++G(d,p)/MK <sup>b</sup>		B3LYP/ LanL2DZ/MK <sup>b</sup>		B3LYP/LanL2DZ/ Mulliken	
Phenol Substituent <sup>c</sup>	Dipole (D)	$\Delta$ Dipole <sup>d</sup> (D)	Dipole (D)	$\Delta$ Dipole <sup>d</sup> (D)	Dipole (D)	$\Delta$ Dipole <sup>d</sup> (D)
Hydrogen	5.2	0.0	6.0	0.0	4.1	0.0
Methyl	5.0	-0.2	5.7	-0.3	4.1	0.0
Chloro	5.1	-0.1	5.8	-0.2	4.0	-0.1
Bromo <sup>e</sup>	_	_	5.6	-0.3	4.0	-0.1
lodo <sup>e</sup>	_	_	_	_	4.1	-0.0
Nitro	4.6	-0.7	5.2	-0.7	3.8	-0.3

<sup>&</sup>lt;sup>a</sup> All calculations are performed on Gaussian16 using a chloroform polarizable continuum model (dielectric constant = 4.7113) to coarsely approximate a hydrophobic membrane protein interior. For all phenols, geometry was optimized and then a population analysis was performed. All phenol substituents are *ortho* to the hydroxyl to mimic the various tyrosine analogs incorporated in the tyrosine variants.

## **S5 Resonance Stark Effect Spectroscopy**

#### S5.1 Conceptual and Theoretical Framework for Resonance Stark Effect

It has been previously demonstrated that  $B_A^*$  is coupled to a  $B_A^+H_A^-$  charge—transfer state (66–69). Specifically, the width and position of the  $B_A$   $Q_y$  NIR band is slightly tuned by the relative free energies of  $B_A^*$  and  $B_A^+H_A^-$  by virtue of this alternative decay pathway for  $B_A^*$ . By modulating this process with an electric field as is done in Stark Spectroscopy, one can monitor  $B_A^*$ s absorption Stark spectrum and characterize the driving force from  $B_A^*$  to  $B_A^+H_A^-$  via this resonance Stark effect (RSE) (66–69). This driving force measurement allows us to get a rough approximation of how a change in  $B_A^*$ s protein environment from WT would affect other charge transfer processes in which  $B_A$  is involved (see the main

<sup>&</sup>lt;sup>b</sup> Merz-Singh-Kollman (MK) population analysis.

<sup>&</sup>lt;sup>c</sup> Substituents are all at the 2-position (X in Fig. S95).

 $<sup>^</sup>d$  The  $\Delta$  Dipole for each phenol O–H bond is calculated with reference to phenol lacking a substituent at the 2-position (hydrogen) to mimic the change in Tyr O–H bond dipole at M210 between WT and RC variants.

 $<sup>^</sup>e$  Bromine and iodine are not included in the 6-31++G(d,p) basis set and a Merz-Kollman radius is not included for iodine in Gaussian16 to perform a MK population analysis.

text section, *Energetic Characterization*). Because this method is not that well known and quite involved, we present an intuitive picture of the origin(s) of the RSE in the following to complement our previous publications which provide a rigorous framework and the experimental results used to validate it (66–69).

Stark spectroscopy, in its usual form, amounts to the measurement of spectral changes under field perturbation. Classical Stark effects for molecular systems in the condensed phase, as described by Liptay (70), assume that the field only affects spectra through transition energy shifts and transition dipole moment changes between the ground and excited states of molecules (electronic or vibrational), which can be conveniently expanded in a power series of the magnitude of the externally applied field F (= $|\vec{F}|$ ; this is usually written as  $F_{\rm ext}$  but we drop the subscript for simplicity in the below equations). The corresponding difference dipole moment between the ground and excited state of the molecule,  $|\Delta \vec{\mu}|$ , can be extracted through a sum-of-derivative analysis (71). Other parameters, such as the absorption/emission bandshapes and concentrations/yields/populations/equilibrium constants, are assumed to be unaffected by application of the field, and any effects that alters these two sets of parameters are called non-classical Stark effects (72).

In cases where the absorption lineshape is affected by electric field perturbation, such as through significant excited-state lifetime perturbation, the sum-of-derivative analysis is not adequate to describe the new phenomenon and a different formulation is needed. The RSE belongs to this category: the excited state of the molecule of interest,  $B_A^*$  in our case, is coupled to a vibrationally derived continuum of dark charge-transfer states (CT for short,  $B_A^+H_A^-$  in our case), whose energy can be strongly perturbed by an external electric field relative to that of  $B_A^*$  because it is a charge-separated state (Fig. S80). The term "dark" refers to the fact that the direct Franck-Condon transition from the ground-state of  $B_A$  to the CT state is much less probable than  $B_A \to B_A^*$  because significant nuclear reorganization

(large Huang-Rhys factor) is required to accommodate the CT state when generated from the  $B_A$  ground state. Any field perturbation on the CT state can only be indirectly observed from the absorption spectrum of  $B_A$  through its coupling to  $B_A^*$ . Note that the classical Stark effect formulation still applies to  $B_A \rightarrow B_A^*$ , but it is complicated or even overwhelmed by the RSE in the case of higher-order Stark effects  $(4\omega, 6\omega, etc.)$  (66, 67). By analyzing RSE data, the pertinent ET-related parameters associated with  $B_A^* \rightarrow B_A^+H_A^-$  are extracted spectroscopically, offering an orthogonal approach to the traditional ways of analyzing excited-state charge-transfer pathways through kinetic measurements. Since the charge transfer process is expected to be the most sensitive to field perturbation among all possible excited-state decay pathways, Stark spectroscopy can isolate the charge-transfer contribution in a clean manner through the field-on-minus-field-off strategy, regardless of other possible pathways and virtually identical zero-field absorption profiles among variants, as is clearly seen for our variants.

Intuitively, when the excited state of a molecule is coupled to multiple states, the resulting new excited state upon mixture is expected to have a different energy and a shortened lifetime due to the alternative decay pathways. These two aspects manifest themselves through an energy shift and an additional lifetime broadening of the absorption spectrum. If the coupled states can be reasonably treated as a continuum (bath) due to the small vibrational energy spacing for the dominant vibrational mode participating in the nuclear reorganization during the electron transfer process, the Fano theory (73–75) offers an excellent theoretical framework to model the change in absorption lineshape upon excited-state coupling. This is a more illustrative basis for explaining lifetime broadening and the resulting Lorentzian lineshape than the less precise but widely accepted argument of Heisenberg's energy-lifetime uncertainty principle (76). The detailed derivation can be found in Fano's original paper and quantum mechanics textbooks (73, 75, 77), but the process is rather unilluminating, tedious, and full of technical subtleties that obscure the core concepts. Instead, we will now build from a three-state

model (with the excited state only coupled to *one* CT level) and gradually infer physical concepts from increasingly complicated models.

For the three-state model, we should not expect to see a noticeable lifetime change as there is only one state coupled to the excited state, but it can nonetheless motivate the rather formidable formula of the energy shift in the excited state in the Fano theory (*vide infra*). Let us assume the transition energy of the CT state and  $B_A^*$  from  $B_A$  to be  $\bar{\nu}_{CT}$  and  $\bar{\nu}_0$ , respectively. The coupling strength between  $B_A^*$  and the CT state is V. The Hamiltonian can be written as:

$$H = \begin{pmatrix} \bar{\nu}_0 & V \\ V & \bar{\nu}_{CT} \end{pmatrix} \tag{S6}$$

We then expect two resulting transitions from B<sub>A</sub> upon coupling, with new transition energies at:

$$\bar{\nu}_0' = \bar{\nu}_0 + \frac{\bar{\nu}_{CT} - \bar{\nu}_0}{2} \pm \frac{\sqrt{(\bar{\nu}_{CT} - \bar{\nu}_0)^2 + 4V^2}}{2}$$
 (S7)

This is an exact result, but we are specifically interested in the limit where V is much smaller than  $\bar{\nu}_{CT} - \bar{\nu}_0$  (V was determined to be 29–59 cm<sup>-1</sup> while  $\bar{\nu}_{CT} - \bar{\nu}_0$  was estimated to be 140–860 cm<sup>-1</sup> between B<sub>A</sub>\* and B<sub>A</sub><sup>+</sup>H<sub>A</sub><sup>-</sup> in several RC mutants by Treynor *et al.* (69)), thus:

$$\bar{\nu}_0' \approx \bar{\nu}_0 + \frac{\bar{\nu}_{CT} - \bar{\nu}_0}{2} \pm \frac{\bar{\nu}_{CT} - \bar{\nu}_0}{2} \pm \frac{V^2}{|\bar{\nu}_{CT} - \bar{\nu}_0|} = \bar{\nu}_{CT} + \frac{V^2}{\bar{\nu}_{CT} - \bar{\nu}_0} \text{ or } \bar{\nu}_0 + \frac{V^2}{\bar{\nu}_0 - \bar{\nu}_{CT}}$$
(S8)

The transitions are indeed close to  $\bar{v}_{CT}$  and  $\bar{v}_0$  when V is small. This correction from the coupling for each transition energy is proportional to the coupling strength V squared and inversely proportional to the difference in the energy  $|\bar{v}_{CT} - \bar{v}_0|$  between the states before coupling, so the correction is the largest when  $\bar{v}_0 = \bar{v}_{CT}$  (on resonance). Of course, the resonance limit is nonsensical in Equation S8 since the small V assumption breaks down, but we qualitatively reproduce the intuition for state mixing as in molecular orbital theory: the higher/lower energy state becomes even higher/lower in energy upon coupling. If we assign the transitions associated with  $\bar{v}_{CT}$  and  $\bar{v}_0$  as dark and bright, respectively, the

transition dipole moment between  $B_A$  and  $B_A^*$  before coupling will be partitioned between the two new transitions (Equation S8). The one with transition energy closer to  $\bar{\nu}_0$  will receive a larger contribution (brighter) but will still be less intense than the original  $\bar{\nu}_0$  transition.

Now consider the case where the bright excited state is coupled to a continuum of dark states (without upper and lower bounds and with a uniform density of states) with equivalent coupling V for all. From our intuition given by the three-state model, since there are equal numbers of states higher and lower than the excited state  $B_A^*$ ,  $\bar{\nu}_0$  should not be modified upon coupling, so the absorption maximum stays constant ( $\bar{\nu}_0' = \bar{\nu}_0$ ). However, the transition dipole moment from the  $\bar{\nu}_0$  transition will be diluted into the newly formed continuum states upon mixing: those states closest to  $\bar{\nu}_0$  would be the brightest, while further ones would be darker. The contribution of the original excited state is effectively smeared into the resulting continuum states, causing a net broadening of the absorption peak from a delta function to a Lorentzian lineshape (a.k.a. the Breit-Wigner resonance profile), which can be solved with a discretized and equally spaced continuum (77):

$$\sigma(\bar{\nu}) = \frac{v^2}{(\bar{\nu} - \bar{\nu}_0)^2 + V^2 + \left(\frac{\hbar\Gamma}{2}\right)^2}$$
 (S9)

where  $\Gamma$  is the lifetime of the excited state (originally infinite; the intrinsic emission lifetime is similarly due to the excited state coupled to a photon bath) owing to the multiple pathways for irreversible decay provided by the continuum:

$$\Gamma = \frac{2\pi}{\hbar} \frac{V^2}{\Lambda} \tag{S10}$$

which is exactly expected from Fermi's Golden Rule, with  $\Delta$  being the energy spacing of the original continuum before coupling (and the density of state is  $\Delta^{-1}$ ).

A distribution of coupling constants  $V(\bar{\nu})$  between the excited state and different states in the continuum can be accounted for in Fano theory, so we are not constrained to a constant V. The corresponding absorption profile (cf. Equation S9) can be calculated as:

$$\sigma(\bar{\nu}) = \frac{V(\bar{\nu})^2}{[\bar{\nu} - \bar{\nu}_0 - U(\bar{\nu})]^2 + \pi^2 V(\bar{\nu})^4}$$
(S11)

The width of the absorption profile upon coupling is again determined directly by  $\pi V(\bar{v})^2$ , which is equivalent to the contribution from  $\Gamma$  in Equation S9 (cf. Equation S10). The vertical excitation energy shift,  $U(\bar{v})$ , is a slightly more sophisticated version of Equation S8:

$$U(\bar{\nu}) = P \int_{-\infty}^{\infty} \frac{V(\bar{\nu})^2}{\bar{\nu} - \bar{\nu}'} d\bar{\nu}' = H[\pi V(\bar{\nu})^2]$$
 (S12)

which is summed over all contributions from the continuum with energy  $\bar{v}'$  and happens to be coincidental with the Hilbert transformation H of  $\pi V(\bar{v})^2$ . The Cauchy principal part P is defined as follows to tame the improper integral and enforce equal weight for continuum states above and below the original excited state:

$$P \int_{-\infty}^{\infty} \frac{f(x)}{x} dx \equiv \lim_{\varepsilon \to 0^{+}} \left[ \int_{-\infty}^{-\varepsilon} \frac{f(x)}{x} dx + \int_{\varepsilon}^{\infty} \frac{f(x)}{x} dx \right]$$
 (S13)

If  $\pi V(\bar{\nu})^2$  has a symmetric "absorption" lineshape with attenuation at upper and lower limits such as the Gaussian distribution, the corresponding Hilbert transform will be an antisymmetric "dispersion" lineshape. This is not surprising, as  $\bar{\nu}_0$  matching the maximum of  $\pi V(\bar{\nu})^2$ , which is  $\bar{\nu}_{CT}$  as we will see later, would not receive any shift due to symmetry (on resonance, as in the previous case with uniform coupling and density of states), while the peak would be red-shifted or blue-shifted if the  $\pi V(\bar{\nu})^2$  maximum is higher or lower in energy than  $\bar{\nu}_0$ , respectively (Fig. S79). When the  $\pi V(\bar{\nu})^2$  maximum is far away from  $\bar{\nu}_0$ , the absorption is effectively decoupled (off resonance). For the absorption width, the onresonance condition causes the most broadening (Fig. S79 and Fig. S81). This is the basis of the

resonance Stark effect, and why  $\bar{v}_{CT} - \bar{v}_0$  (which can then be converted to driving forces of excited-state ET) can be extracted combined with field perturbation.

In our cases, the coupling distribution  $V(\bar{\nu})$  originates from the vibronic coupling between the vibrational states of  $B_A^*$  and the vibrational continuum of  $B_A^+H_A^-$ . We can therefore evaluate  $V(\bar{\nu})^2$  with the Born-Oppenheimer, Condon, and Einstein (single-vibrational-mode) approximations:

$$V(\bar{\nu})^2 \approx V_0^2 \rho_{FC}(\bar{\nu}) \propto V_0^2 |\langle \varphi_m^{CT} | \varphi_n^e \rangle|^2 \tag{S14}$$

where  $|\varphi\rangle$  are the nuclear wavefunctions. Analytical calculation of the general Franck-Condon factors can be complicated; however, only the ground-state vibrational level (n=0) for the electronic excited state  $B_A^*$  matters since the transition between  $B_A$  and  $B_A^*$  is dominated by the 0-0 transition. The Franck-Condon factors with n=0 between two displaced harmonic oscillators with the same force constants follow a Poisson distribution (Fig. S78):

$$|\langle \varphi_m^{CT} | \varphi_0^e \rangle|^2 = e^{-S} \frac{S^m}{m!} \tag{S15}$$

with the mean at S and the standard deviation at  $\sqrt{S}\,\bar{v}_{mean}$ , where S is the Huang-Rhys factor (determined from the horizontal displacement) between the excited state and the CT manifold, and  $\bar{v}_{mean}$  is the mean vibrational energy spacing of the harmonic oscillators following the Einstein approximation. With small  $\bar{v}_{mean}$ , the Poisson distribution can be taken to the continuous limit and becomes Pekarian:

$$|\langle \varphi_m^{CT} | \varphi_0^e \rangle|^2 \approx e^{-S} \frac{S^m}{\Gamma(m+1)}$$
 (S16)

Since  $\rho_{FC}(\bar{\nu}_0)$  should be maximized at when  $\bar{\nu}_0 = \bar{\nu}_{CT}$  (on resonance), the maximum appears at  $\bar{\nu}_{CT}$  for  $\rho_{FC}(\bar{\nu})$ . In the large S limit, the distribution can be well approximated by a Gaussian distribution, which is convenient for analytical purposes.

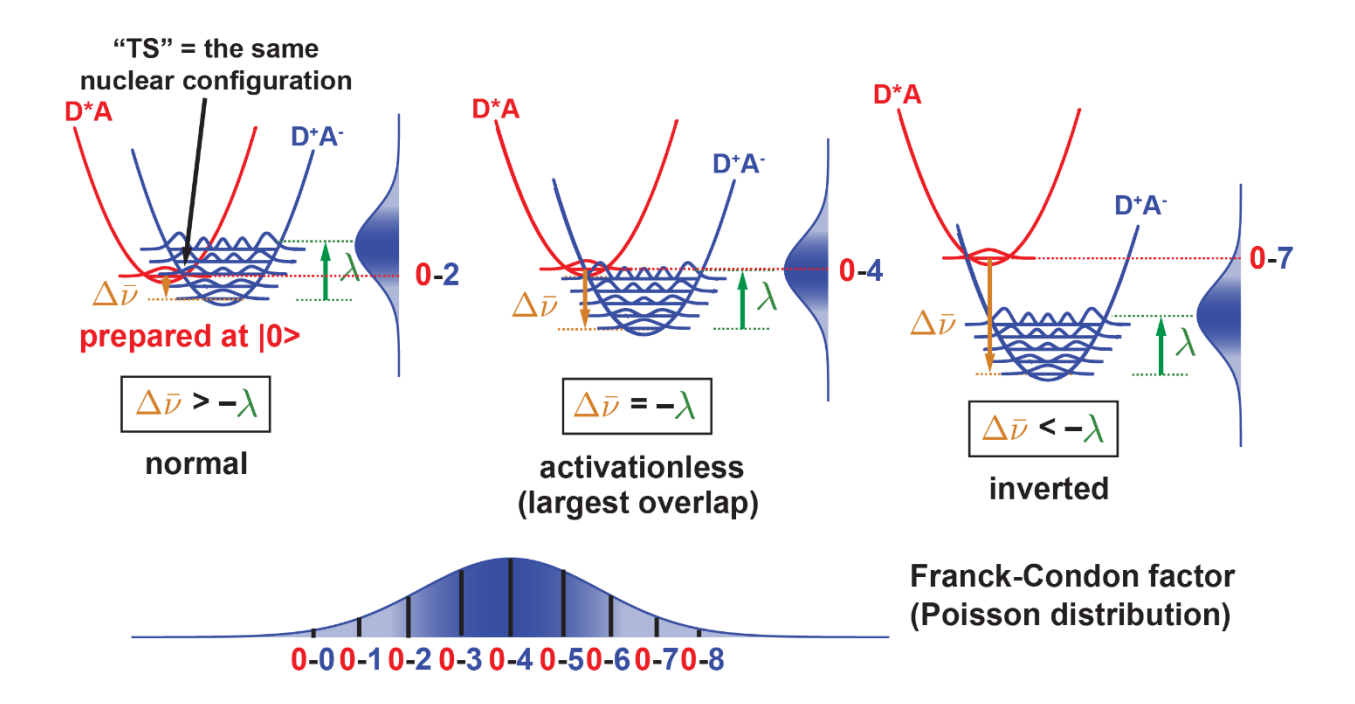
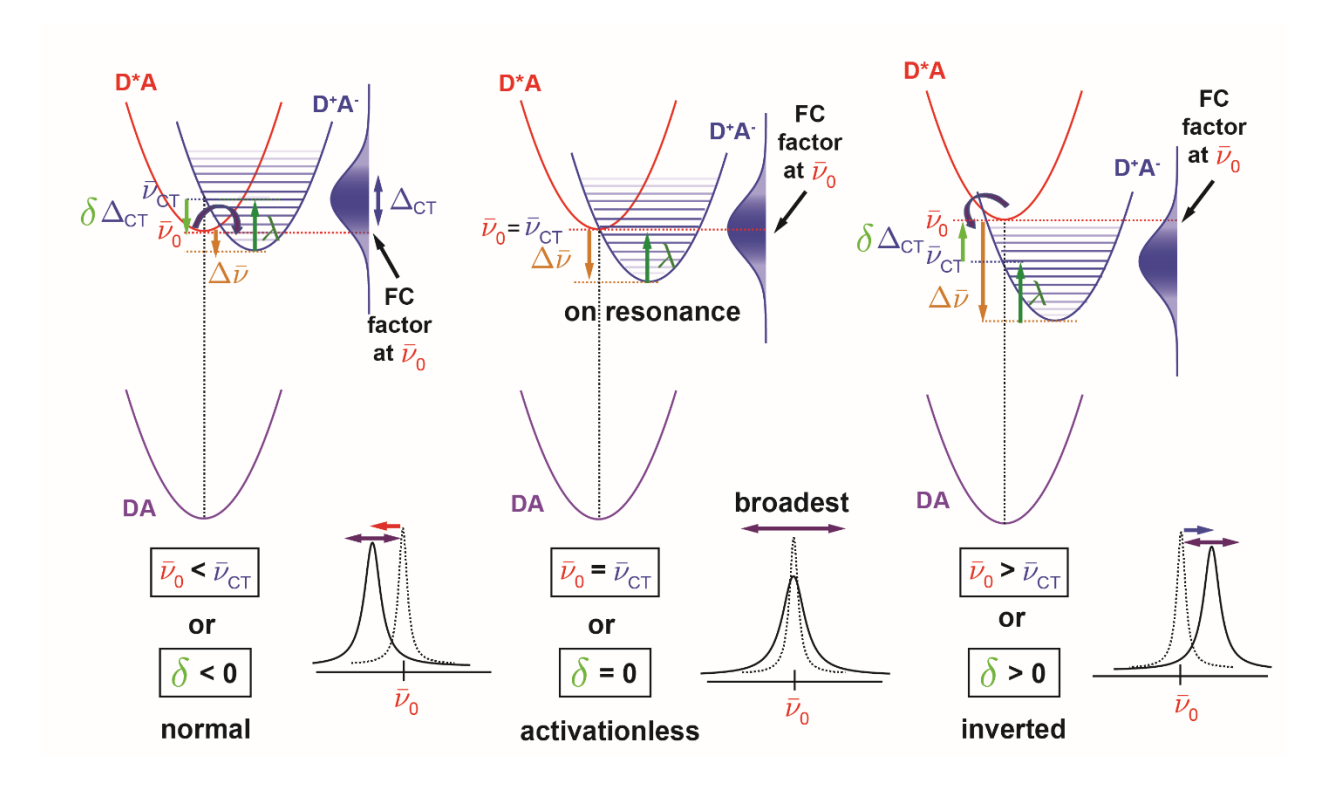


Fig. S78. Diagram depicting the horizonal Franck-Condon factor for the Marcus theory (electron transfer kinetics) and the Franck-Condon factor distribution for the Fano theory (absorption profile influenced by excited-state electron transfer) between the D\*A state ( $B_A*H_A$  for the problem at hand) and the coupled D\*A\* state ( $B_A*H_A$ \*) and its dependence on driving force  $\Delta \bar{\nu}$ , classified with the Marcus regions. The reorganization energy  $\lambda$  is shown as constant across these three regions. The largest horizontal Franck-Condon factor (as energy must be conserved during electron transfer) is realized when the transition state ("TS") coincides with the reactant state, hence the activationless region.

Following this discussion on the Fano theory, we can now deduce the behavior of the lineshape upon coupling within each regime of  $\delta$  (i.e., difference between  $\bar{\nu}_0$  and  $\bar{\nu}_{CT}$ ), as illustrated in Fig. S79.



**Fig. S79.** Diagram depicting the absorption profiles upon excited-state coupling observed as a function of the sign of  $\delta$  (i.e., difference between  $\bar{\nu}_0$  and  $\bar{\nu}_{CT}$ ) according to the Fano theory. The Marcus regions classified based on the sign of  $\delta$  are shown to better relate to the traditional methods for analyzing excited-state electron transfer.  $\Delta_{\text{CT}}$  is the full width at half-maximum (fwhm) of the Franck-Condon distribution shown in Fig. S78. The conversion between the Marcus driving force  $\Delta\bar{\nu}$  and  $\delta$  can be directly read off and written as Equation S23.

Note that the Franck-Condon factor invoked in the Fano theory is a distribution rather than a single value because any vibrational states in the CT manifold can be coupled to the excited state B<sub>A</sub>\*, while the Franck-Condon factors for both the Marcus theory and vertical excitation upon photon absorption (Franck-Condon transition) are subject to energy conservation and mismatch in electronic and nuclear timescales. Specifically, in the Marcus theory, since the transition state with the nuclear configuration(s) that bring the reactant and product state to the *same* energy must be transiently reached, the relevant Franck-Condon factors come from *horizontally* overlapped vibrational wavefunctions and the resulting electron transfer kinetics are determined by the sum over all combinations of vibrational quanta that obey energy conservation (i.e., Franck-Condon-weighted density (FCWD)). For reference and further discussion on these topics see (75) and SI Section S11 of

reference (78). For a Franck-Condon transition for photon excitation, the nuclear motion is too slow to keep up with electronic excitation, so the relevant Franck-Condon factors are from the *vertically* overlapped vibrational wavefunctions. In contrast, Fano theory is not restricted by these notions, as the couplings that accounts for the absorption profile do not depend upon timescales or energy conservation, nor are the corresponding Franck-Condon factors condensed down to a single quantity as in the Marcus rate constant. As a consequence, the RSE offers a powerful and orthogonal spectroscopic approach to study the energetics of excited-state electron transfer. Analyses utilizing the Marcus theory rely on preparing compounds over a range of driving forces to obtain the energetics, under the assumption of constant electronic coupling and reorganization energy across the series. The RSE is *not* based on the Marcus theory, requires no such assumptions, and a single sample is sufficient (69), as field application on an isotropic sample automatically spans a range of  $\delta$  (or driving forces) while leaving other parameters intact. Moreover, it is straightforward to connect the sign of  $\delta$  to the three Marcus regions (Fig. S79):  $\delta$  = 0 (on resonance) is the activationless case, while  $\delta$  > 0 and < 0 corresponds to the inverted and normal region, respectively.  $\delta$  can also be readily converted into the driving force through Equation S23.

When we apply an electric field, we modulate the relative vertical displacement between the maximum of  $\rho_{FC}(\bar{\nu})$  and  $\bar{\nu}_0$  (Fig. S80). In the following we deduce the lowest order Stark lineshape  $\Delta A(2\omega)$  of the RSE for an isotropically distributed and immobilized sample via physical intuition. For example, when  $\delta$  = 0, there are equal populations (with opposite electron transfer directions) in the sample that possess positive and negative  $\delta$  (sharing the same magnitude) upon field application, so there is no net peak shift. However, since driving  $\delta$  away from resonance narrows the absorption band,

we expect a net band narrowing lineshape that looks somewhat like an inverted second derivative lineshape (Fig. S80).

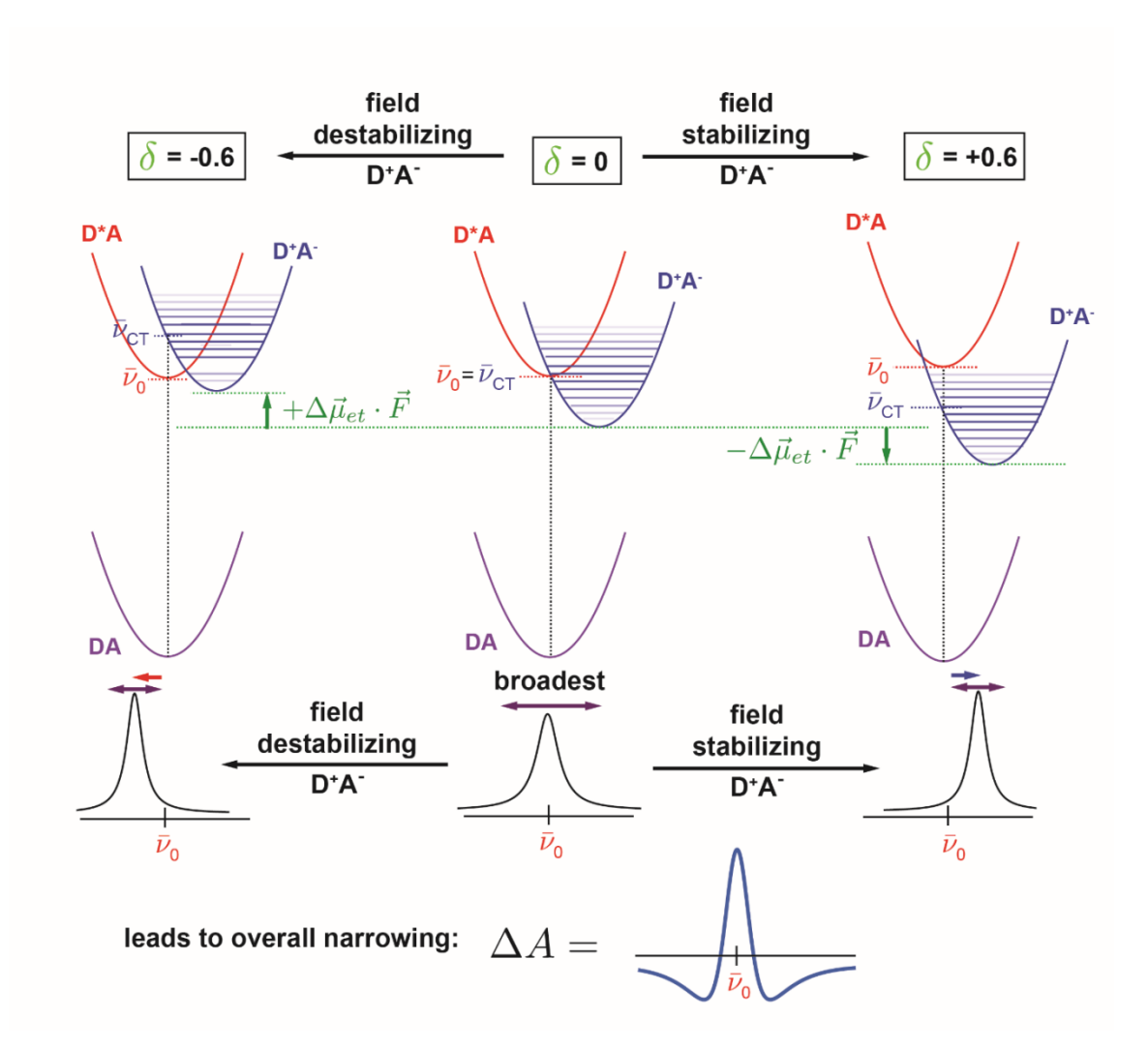


**Fig. S80.** Diagram depicting the consequent lowest order RSE bandshape  $\Delta A(2\omega)$  based on band shift and band broadening/narrowing expected upon field application in the case of  $\delta$  = 0.  $\Delta \mu_{\rm et}$  represents the difference dipole moment associated with  $B_A^*H_A \to B_A^+H_{A^-}$  and F is the externally applied field.

Analogous conclusions can be achieved with other  $\delta$ 's based on the same shifting and broadening principles (Fig. S81). This provides an intuitive basis for why the Stark lineshape from the RSE is sensitive to  $\delta$ . These shapes are rather broad and asymmetric and cannot be explained by the sum-of-derivative analysis. Note that when comparing two types of populations with opposite electron transfer directions, the one with  $\delta$  closer to zero will dominate the effect, as the coupling weakens for larger

difference between  $\bar{v}_0$  and  $\bar{v}_{CT}$ . Along the same line, a sample with larger  $|\delta|$  (e.g., zero driving force or uphill energetics) would experience a smaller RSE, so even if the shapes could be the same for  $\Delta A$  at a specific harmonic of the electric field modulation for two different  $\delta$ 's, the magnitude difference can be a clue for discerning them. The best way to distinguish different  $\delta$ 's is by acquiring  $\Delta A(4\omega)$  and  $\Delta A(6\omega)$ , and these shapes together serve as a good fingerprint for each  $\delta$ . Unfortunately, there is not an analogous way to understand the  $\delta$  dependence of Stark lineshapes at higher harmonics (Fig. 5 in (67)), since they are higher-order and smaller contributions to  $\Delta A$ . Zhou and Boxer (67) have offered an alternative strategy to explain  $\Delta A(4\omega)$  and  $\Delta A(6\omega)$  through a perturbative argument and lineshape analysis, explaining why RSE lineshapes still tend to resemble combinations of 1st and 2nd derivatives even at higher harmonics, as opposed to the expected highly undulating nth-derivative lineshape for  $\Delta A(n\omega)$  based on the classical Stark mechanism (71).

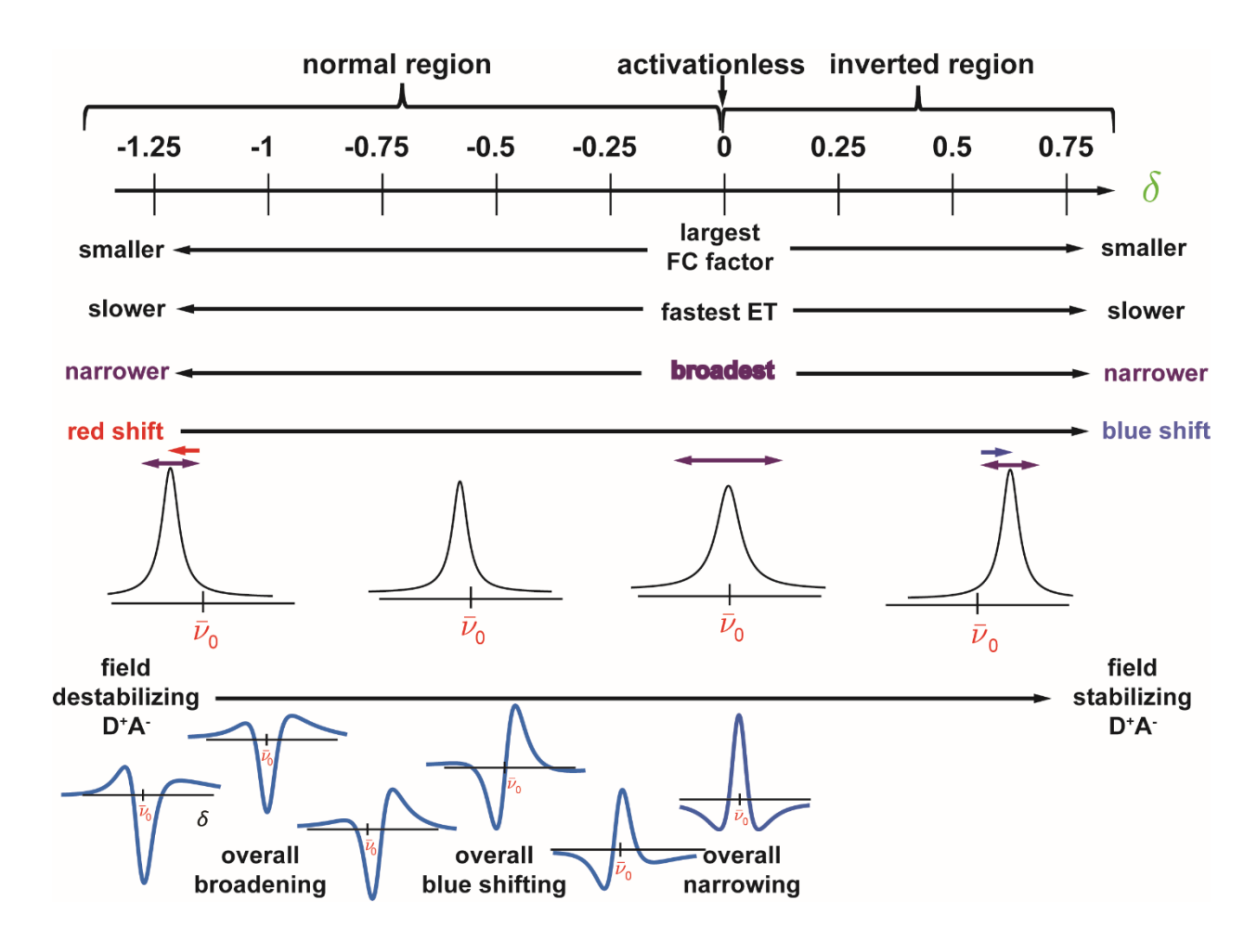


**Fig. S81.** Illustration of the effect on band broadening and band shifts for the NIR  $B_A$  band of RCs with a range of different driving force for  $B_A*H_A \to B^+H_A^-$  (middle) and the resultant lowest-order RSE lineshapes  $\Delta A$  (2ω) one would expect due to field-induced band broadening and band shift (bottom). The effect for the excited-state electron transfer kinetics is also summarized. FC factor refers to the horizontal Franck-Condon factor crucial for the Marcus theory (see text). Note that the conventional classical Stark effect (typically second derivative of absorption) usually dominates the 2ω spectrum due to the change in dipole moment, in this case for  $B_A \to B_A*$ , but this conventional effect involving higher derivatives is overwhelmed by the RSE for 4ω and 6ω spectra.

# S5.2 77K Electronic Stark Spectroscopy Experimental Procedure

All samples were exchanged into a buffer of 50% glycerol, 50% High Deriphat Dialysis Buffer (10 mM Tris, pH 8.0, 0.1% Deriphat) on Amicon Ultra-0.5 mL 50 kDa Centrifugal Filters and then concentrating protein until at  $\sim 1$  mM. Protein samples were then diluted with glycerol until 50% glycerol by volume. Sample concentration was checked with UV-vis-NIR absorption measurements at

the absorbance maxima of the B  $Q_y$  band (~804 nm). Prior to dilution with glycerol the sample is tacky and difficult to pipette but following dilution can be pipetted slowly, but manageably for sample cell loading. Samples were centrifuged in 0.6 mL microcentrifuge tubes (Fisher) for 1-2 hrs to remove all bubbles from the sample. The remainder of the electronic Stark spectroscopy protocol was performed per the protocol of Lin *et al.* (7).  $\chi$  angles between the applied electric field and the polarization of the probe light at 90°, 70°, and 50° were sampled at each applied field strength with an increment of 0.3 kV in root-mean-square voltage  $V_{rms}$  across the sample cell to obtain a complete data set. Main deviations from methods for Lin *et al.* (7) only consisted in detecting the X and Y components of the Stark signal  $\Delta I$  (4 $\omega$ ) and  $\Delta I$  (6 $\omega$ ) at the fourth harmonic (4 $\omega$ ) and sixth harmonic (6 $\omega$ ), respectively, of the applied AC field. The Stark spectra  $\Delta A$  can be constructed according to the following expressions:

$$\Delta A(4\omega) = \frac{8\sqrt{2}}{\ln 10} \frac{\Delta I(4\omega)}{I}$$
 (S17)

$$\Delta A(6\omega) = \frac{32\sqrt{2}}{\ln 10} \frac{\Delta I(6\omega)}{I}$$
 (S18)

where I is the signal directly probed by the diode detector without any pre-processing. Only Stark signals from higher harmonics are analyzed primarily because the Stark signal  $\Delta I$  ( $2\omega$ ) is most contaminated by classical Stark features. When detecting Stark spectra at higher harmonics of the applied field, these features have negligible signals due to the rather low difference dipole between the ground and excited state of the  $B_A$  (and most) chromophore(s) ( $|\Delta\vec{\mu}| \sim 2.4 \, \text{D/f}$ ) (79) compared to the difference dipole of the coupled charge transfer state ( $|\Delta\vec{\mu}_{et}| \equiv |\Delta\vec{\mu}_{B_A^+ H_A^-}| \sim 46 \, \text{D/f}$ ) (69). By obtaining both  $\Delta I$ ( $4\omega$ ) and  $\Delta I$ ( $6\omega$ ) with good signal-to-noise we can simultaneously fit both to obtain the relevant parameters discussed in the following. Since  $\Delta I$ ( $4\omega$ ) and  $\Delta I$ ( $6\omega$ ) have different lineshapes but are fit with the same experimental parameters, fitting both simultaneously allows for more certainty in the data analysis.

## S5.3 Stark Spectroscopy Data Analysis

This section involves the methodology for RSE spectral fitting and rationale behind each choice. All Stark spectra  $\Delta A$  ( $n\omega$ ) shown were scaled to 1 MV/cm field according to its proportionality to field strength to the nth power ( $F^n$ ) at  $\chi=90^\circ$  to facilitate comparison between different samples, regardless of what harmonic field detection was being performed. This field strength scaling is technically not legitimate for RSEs and only suitable for the classical Stark mechanism (71), as the large difference dipole moment  $\Delta\mu_{\rm et}$  associated with  $B_A^*H_A \to B_A^+H_A^-$  leads to much larger contamination from components with higher-order field dependence ( $\Delta A$  (( $\Delta \vec{\mu}_{\rm et} \cdot \vec{F}$ ) $^m$ )  $\equiv \Delta A$  ( $F^m$ )  $\propto F^m$ , m > n) (68):

$$\Delta A(2\omega) = \Delta A(F^2) + \Delta A(F^4) + \frac{15}{16}\Delta A(F^6) + \frac{7}{8}\Delta A(F^8) + \frac{105}{128}\Delta A(F^{10}) + \frac{99}{128}\Delta A(F^{12}) + O(F^{14})$$
 (S19)

$$\Delta A(4\omega) = \Delta A(F^4) + \frac{3}{2}\Delta A(F^6) + \frac{7}{4}\Delta A(F^8) + \frac{15}{8}\Delta A(F^{10}) + \frac{495}{256}\Delta A(F^{12}) + O(F^{14})$$
 (S20)

$$\Delta A(6\omega) = \Delta A(F^6) + 2\Delta A(F^8) + \frac{45}{16}\Delta A(F^{10}) + \frac{55}{16}\Delta A(F^{12}) + O(F^{14})$$
 (S21)

In other words, each  $\Delta A$  ( $n\omega$ ) spectrum cannot be only accounted for with the lowest-order term  $\Delta A$  ( $F^n$ ), especially at higher fields (F > 0.8 MV/cm). We thus label each Stark spectrum with the field strength at which the data were acquired to reflect this caveat. The higher-order contamination also implies the necessity of considering large m in  $\Delta A$  ( $F^n$ ) when fitting the spectra; we truncate our simulations to  $\Delta A$  ( $F^{12}$ ) in this work as shown in Equations S19-S21.

Because of the RSE, data acquired for  $\Delta A$  ( $4\omega$ ) and  $\Delta A$  ( $6\omega$ ) have a very different lineshape and fitting protocol than that used in classical Stark analysis (7, 71, 80). Since the  $Q_y$  band of  $B_A$  largely overlaps with that of  $B_B$ , which experiences a negligible RSE (69, 81), the B chromophore from both branches have to be considered when fitting the absorption spectra. Only  $B_A$ , however, exhibits the RSE and this effect dominates the  $\Delta A$  ( $4\omega$ ) and  $\Delta A$  ( $6\omega$ ) spectra. The following are the parameters involved with the fit, according to the notations in Treynor *et al.* (68, 69). Some are allowed to vary, and some are not according to the following prescription (68, 69).

- $\bar{\nu}_0$  and  $\bar{\nu}_{0B}$ : the position of absorption maxima for B<sub>A</sub> and B<sub>B</sub>, respectively, obtained from the absorption spectra.
- state decay pathways), fixed at 90 and 35 cm<sup>-1</sup>, respectively, to match previous literature protocol (69). While more recent estimations for both the homogeneous and inhomogeneous widths have been determined (60) which vary from those we use,  $\delta$  extracted with these previous values do not significantly vary (see Fig. 5 in ref. (69)) and linear IR spectra can't significantly differentiate the two.
- $\Gamma_{Gauss}$  and  $\Gamma_{Gauss,B}$ : the inhomogeneous (Gaussian) full width at half-maximum (fwhm) for B<sub>A</sub> and B<sub>B</sub>, fixed at 50 and 150 cm<sup>-1</sup>, respectively.
- $A_0$  and  $A_{0B}$ : a scaling factor to account for the absorption intensities of  $B_A$  and  $B_B$ , respectively. If there were no overlap between two bands, these parameters would not be required. The ratio is fixed to allow for a peak height ratio of 2:1 between the  $B_A$  and  $B_B$  band for M210 variants.
- $\Delta_{CT}$ : the fwhm of the Franck-Condon factor (nuclear wavefunction overlap squared) distribution  $\rho_{FC}(\bar{\nu})$  between  $B_A^*$  and  $B_A^+H_A^-$  when approximated with a Gaussian distribution. Technically, this distribution should be Poissonian in the discrete limit (Equation S15) and Pekarian in the continuous limit (Equation S16) with harmonically approximated potential for each species, but the symmetric Gaussian distribution is also representative as the vibrational energy spacing is small. This quantity is fixed at 1000 cm<sup>-1</sup>.
- $\delta$ : effectively represents the difference between the vertical transition energies of  $B_A^+H_A^-(\bar{\nu}_{CT})$  and  $B_A^*(\bar{\nu}_0)$  from  $B_A$ , which is related but not identical to the sought-after driving force,  $\Delta\bar{\nu}$ , associated with  $B_A^*H_A \to B_A^+H_A^-$ . The exact transformations between these energies are

$$\bar{\nu}_{\rm CT} - \bar{\nu}_0 = -\delta \Delta_{\rm CT} \tag{S22}$$

$$\Delta \bar{\nu} = \bar{\nu}_{\rm CT} - \bar{\nu}_0 - \lambda = -\delta \Delta_{\rm CT} - \lambda \tag{S23}$$

where  $\lambda$  is the reorganization energy of  $B_A^*H_A \to B_A^+H_A^-$ , an additional parameter that is required to evaluate  $\Delta \bar{\nu}$  and is estimated to be 1200 cm<sup>-1</sup> (69). We assume that the reorganization energy is largely unperturbed across the variants with different tyrosine substitution.

•  $W_R$ : effectively represents the strength of electronic coupling  $V_0$  between  $B_A^*H_A$  and  $B_A^+H_A^-$ :

$$W_{\rm R} = \frac{V_0^2}{\Delta_{\rm CT}} \tag{S24}$$

•  $\Delta\mu_R$ : effectively represents the difference dipole moment  $\Delta\mu_{et}$  associated with  $B_A^*H_A \to B_A^+H_A^-$ :

$$\Delta\mu_{\rm R} = \frac{\Delta\mu_{\rm et}}{\Delta_{\rm CT}} \tag{S25}$$

•  $\zeta_{\text{et}}$ : the angle between  $\Delta \vec{\mu}_{et}$  and the Q<sub>y</sub> transition dipole moment of B<sub>A</sub>. It is consistently around 45° across mutants according to experiments with  $\chi$  variation (68, 69). Therefore, it is fixed at 45° such that we only have to consider spectra acquired at  $\chi$  = 90°.

In summary, there are six parameters: peak maxima  $\bar{v}_0$  and  $\bar{v}_{0B}$ , peak height of  $B_A$ , reduced driving force  $\delta$ , reduced electronic coupling  $W_R$ , and reduced difference dipole moment  $\Delta\mu_R$ . The last three quantities are all scaled with  $\Delta_{CT}$  due to smaller covariances (larger independence) among these parameters during fitting compared with the more fundamental  $\bar{v}_{CT} - \bar{v}_0$ ,  $V_0$ , and  $\Delta\mu_{et}$  (68). Even though there are six parameters obtained from the data, judged on the basis of the results obtained from a variety of RC mutants (69), changes in resonance Stark spectra between different RCs can be primarily mapped to changes in  $\delta$  or driving force by analysis of the Stark lineshape. This can be rationalized by the fact that interchromophoric distances remain unchanged (Table S3), so we expect the electronic coupling (W<sub>R</sub>) to be the same,  $B_A$  and  $B_B$  peak maxima ( $\bar{v}_0$  and  $\bar{v}_{0B}$ ) and peak height are fairly constant among samples (Fig. S90), and the Stark lineshape is most sensitive to changes in  $\delta$  while  $\Delta\mu_R$  primarily influences signal intensity (along with  $W_R$ ) (68). Our goal is therefore to extract  $\delta$  and convert it to the driving force of  $\Delta\bar{v}$  associated with  $B_A^*H_A \to B_A^*H_A^-$  using Equation S23.

As an easier conceptual starting point, the absorption spectrum of  $B_B$  is modeled by a Lorentzian lineshape convolved with a Gaussian distribution  $b_B(\bar{\nu})$  to simulate the effect of inhomogeneous broadening:

$$A_{\rm B}(\bar{\nu}) = \frac{A_{0B}\Gamma_{0B}}{(\bar{\nu} - \bar{\nu}_{0B})^2 + \Gamma_{0B}^2} * b_{\rm B}(\bar{\nu}) = A_{0B} \operatorname{Im} \left[ \frac{1}{\bar{\nu} - \bar{\nu}_{0B} - i\Gamma_{0B}} \right] * b_{\rm B}(\bar{\nu})$$
 (S26a)

and

$$b_B(\bar{v}) = \frac{\sqrt{8 \ln 2}}{\sqrt{2\pi} \Gamma_{\text{Gauss,B}}} \exp \left[ -4 \ln 2 \left( \frac{\bar{v}}{\Gamma_{\text{Gauss,B}}} \right)^2 \right]$$
 (S26b)

where Im represents the imaginary part of the argument and the asterisk operator denotes convolution. The introduction of complex numbers seems to be an overcomplication at first, but it will turn out to be very useful when simulating the charge transfer effect on  $B_A$  absorption using the Fano theory. It is fortunate that  $Q_y$  bands of  $B_A$  and  $B_B$  are both dominated by the 0-0 transition and can be treated this way, and thus an additional Huang-Rhys factor is not required between  $B_A$  and  $B_A^*$  for simulating  $B_A$ 's absorption band. For the  $B_A$  band, an analogous expression to that developed for the  $B_B$  band (Equations S26a and S26b) can be written and we only need a slight complication from coupling of  $B_A^*$  and  $B_A^*H_{A^-}$ , which is all encoded in a frequency and field dependent function  $W(F, \bar{\nu})$  based on the Fano theory (Equation S11). The Stark effect on  $\bar{\nu}_0$  (and also  $\bar{\nu}_{0B}$ ) is not considered since electron redistribution within the chromophore (i.e., the difference dipole moment in the classical Stark effect) is negligible compared to that associated with long-range electron transfer.

$$A_{\mathbf{A}}(\bar{\nu}) = A_0 \operatorname{Im} \left[ \frac{1}{\bar{\nu} - \bar{\nu}_0 - W(F, \bar{\nu}) - i\Gamma_0} \right] * b_{\mathbf{A}}(\bar{\nu}) = A_0 \operatorname{Im} [\epsilon(\bar{\nu})] * b_{\mathbf{A}}(\bar{\nu})$$
 (S27a)

$$b_{\rm A}(\bar{\nu}) = \frac{\sqrt{8 \ln 2}}{\sqrt{2\pi} \Gamma_{\rm Gauss}} \exp \left[ -4 \ln 2 \left( \frac{\bar{\nu}}{\Gamma_{\rm Gauss}} \right)^2 \right] \tag{S27b}$$

The detail of  $W(F, \bar{\nu})$  will be discussed later. The overall absorption band around 800 nm can be accounted for by the sum of two bands from  $B_A$  and  $B_B$ .

$$A(\bar{\nu}) = A_{\mathcal{A}}(\bar{\nu}) + A_{\mathcal{B}}(\bar{\nu}) \tag{S28}$$

According to the Fano theory (Equation S27a), the absorption of  $B_A$  can be affected by the coupling in two ways: its homogeneous line width can be modified by the imaginary part of  $W(F, \bar{v})$  and its absorption maximum can be shifted by the real part of  $W(F, \bar{v})$  (Fig. S79):

$$W(F,\bar{\nu}) = i\pi |V(F,\bar{\nu})|^2 + P\frac{1}{\pi} \int_{-\infty}^{\infty} \frac{\pi |V(F,\bar{\nu}')|^2}{\bar{\nu} - \bar{\nu}'} d\bar{\nu}' = i\pi |V(F,\bar{\nu})|^2 + H[\pi |V(F,\bar{\nu})|^2]$$
(S29)

in which  $V(F, \bar{v})$  is the field dependent electronic-nuclear coupling between  $B_A^*$  and  $B_A^*H_A^-$  (vide infra), P is the Cauchy principal part of the integral owing to the ill-defined singularity at  $\bar{v}' = \bar{v}$ , and H is the Hilbert transform of a function. In MATLAB, an array x's Hilbert transform can be conveniently implemented by taking the imaginary part of hilbert[x] but note that, similar to other integral transforms (e.g., Fourier transform), a sufficiently wide range of  $\bar{v}'$  (0 – 25000 cm<sup>-1</sup> in our cases) is required to well approximate the integration in Equation S29. Consistent with the past literature, we apply the Condon approximation to  $V(F,\bar{v})$  in order to separate the contributions from the electronic coupling  $V_0$  and vibrational wavefunction overlap (the square of the latter is the Franck-Condon factor  $\rho_{FC}(F,\bar{v})$ ). As mentioned previously, we can approximate  $\rho_{FC}(F,\bar{v})$  at zero field with a Gaussian function:

$$\pi |V(F=0,\bar{\nu})|^2 \approx \pi V_0^2 \rho_{\text{FC,Gaussian}}(\bar{\nu}) = 2\sqrt{\pi \ln 2} \frac{V_0^2}{\Delta_{\text{CT}}} \exp \left[ -4 \ln 2 \left( \frac{\overline{\nu} - \overline{\nu}_{\text{CT}}}{\Delta_{\text{CT}}} \right)^2 \right]$$
 (S30a)

which is dependent on  $\delta$  through  $\bar{\nu}_{CT}$ . A Pekarian function (continuous Poisson) is physically more accurate and exclusively used in this work:

$$\pi |V(F = 0, \bar{\nu})|^{2} \approx \pi V_{0}^{2} \rho_{\text{FC,Pekarian}}(\bar{\nu}) = \frac{s^{-S}}{0.9635} \frac{V_{0}^{2}}{\Lambda_{\text{CT}}} \frac{s^{S + \sqrt{5.57S}\left(\frac{\bar{\nu} - \bar{\nu}_{\text{CT}}}{\Lambda_{\text{CT}}}\right)}}{\Gamma\left[s + 1 + \sqrt{5.57S}\left(\frac{\bar{\nu} - \bar{\nu}_{\text{CT}}}{\Lambda_{\text{CT}}}\right)\right]}$$
(S30b)

where S is 51.035 to match the lineshape from experiments using Equation S27a,  $\Gamma$  is the Gamma function (continuous factorial), 0.9635 is applied to normalize  $\rho_{FC,Pekarian}(\bar{\nu})$  to unity area, and 5.57 arises from the conversion of the standard deviation from fwhm (Equation 41 in Reference (68)). In practice, both functional forms give rise to very similar answers ( $\delta$  differing by 0.02, amounting to 20 cm<sup>-1</sup> in  $\Delta \bar{\nu}$ ) (69), but the Pekarian form consistently affords a better fit (68).

So far, the field effect has been implicit. The only Stark effect is the linear dependence of  $\bar{\nu}_{\rm CT}$  on electric field, corresponding to the field dependence of  $\delta$ :

$$\delta(\vec{F}) = \delta + \Delta \vec{\mu}_{R} \cdot f \vec{F} \tag{S31}$$

In principle, one can plug Equation S31 with a sinusoidally modulated field into either Equation S27a or S27b to simulate the field effect directly and extract each frequency component  $\Delta A_{\rm A}(n\omega)$  through Fourier series of Equation S27a. This approach could be advantageous, as it avoids perturbation expansion in F (Equations S19-S21) and higher-order field effects can be directly included without further approximation. However, because we work with isotropic samples and orientational averaging for terms with different  $F^n$  dependence are not the same, we still have to appeal to a Taylor expansion in F. As explained in (67) and (68), it requires  $\varepsilon(\bar{\nu})$  defined in Equation S27a and wavenumber derivatives of  $W(F=0,\bar{\nu})$ . Since n! appears everywhere due to the Taylor expansion, to simplify expressions derived below we define:

$$W^{(n)}(\bar{\nu}) \equiv \frac{1}{n!} \left[ \frac{d^n}{d\bar{\nu}^n} (W(F=0,\bar{\nu})) \right]$$
 (S32)

The following expressions up to  $F^{12}$  can then be achieved through use of combinatorics:

$$\Delta A(F^2) = A_0 \text{Im} \left\{ \epsilon^2 W^{(2)} + \epsilon^3 \left[ W^{(1)} \right]^2 \right\} \frac{(\Delta \mu_{\text{et}} f F)^2}{15} \left[ 5 + (3 \cos^2 \zeta_{\text{et}} - 1)(3 \cos^2 \chi - 1) \right] * b_{\text{A}}(\bar{\nu})$$
 (S33)

$$\begin{split} \Delta A(F^{10}) &= A_0 \text{Im} \left\{ \epsilon^2 W^{(10)} + \epsilon^3 \left[ \left( W^{(5)} \right)^2 + 2 W^{(1)} W^{(9)} + 2 W^{(2)} W^{(8)} + 2 W^{(3)} W^{(7)} + 2 W^{(4)} W^{(6)} \right] \right. \\ &+ \epsilon^4 \left[ 3 \left( W^{(1)} \right)^2 W^{(8)} + 3 \left( W^{(2)} \right)^2 W^{(6)} + 3 \left( W^{(3)} \right)^2 W^{(4)} + 3 \left( W^{(4)} \right)^2 W^{(2)} \right. \\ &+ 6 W^{(1)} W^{(2)} W^{(7)} + 6 W^{(1)} W^{(3)} W^{(6)} + 6 W^{(1)} W^{(4)} W^{(5)} + 6 W^{(2)} W^{(3)} W^{(5)} \right] \\ &+ \epsilon^5 \left[ 4 \left( W^{(1)} \right)^3 W^{(7)} + 4 \left( W^{(2)} \right)^3 W^{(4)} + 4 \left( W^{(3)} \right)^3 W^{(1)} + 6 \left( W^{(1)} \right)^2 \left( W^{(4)} \right)^2 \right. \\ &+ 6 \left( W^{(2)} \right)^2 \left( W^{(3)} \right)^2 + 12 \left( W^{(1)} \right)^2 W^{(2)} W^{(6)} + 12 \left( W^{(1)} \right)^2 W^{(3)} W^{(5)} \right. \\ &+ 12 \left( W^{(2)} \right)^2 W^{(1)} W^{(5)} + 24 W^{(1)} W^{(2)} W^{(3)} W^{(4)} \right] \\ &+ \epsilon^6 \left[ \left( W^{(2)} \right)^5 + 5 \left( W^{(1)} \right)^4 W^{(6)} + 20 \left( W^{(1)} \right)^3 W^{(2)} W^{(5)} + 20 \left( W^{(1)} \right)^3 W^{(3)} W^{(4)} \right. \\ &+ 20 \left( W^{(2)} \right)^3 W^{(1)} W^{(3)} + 30 \left( W^{(1)} \right)^2 \left( W^{(2)} \right)^2 W^{(4)} + 30 \left( W^{(1)} \right)^2 \left( W^{(3)} \right)^2 W^{(2)} \right] \\ &+ \epsilon^7 \left[ 6 \left( W^{(1)} \right)^5 W^{(5)} + 15 \left( W^{(1)} \right)^4 \left( W^{(3)} \right)^2 + 15 \left( W^{(2)} \right)^4 \left( W^{(1)} \right)^2 \right. \\ &+ 30 \left( W^{(1)} \right)^4 W^{(2)} W^{(4)} + 60 \left( W^{(1)} \right)^3 \left( W^{(2)} \right)^2 W^{(3)} \right. \\ &+ \epsilon^8 \left[ 7 \left( W^{(1)} \right)^6 W^{(4)} + 42 \left( W^{(1)} \right)^5 W^{(2)} W^{(3)} + 35 \left( W^{(1)} \right)^4 \left( W^{(2)} \right)^3 \right] \\ &+ \epsilon^9 \left[ 8 \left( W^{(1)} \right)^7 W^{(3)} + 28 \left( W^{(1)} \right)^6 \left( W^{(2)} \right)^2 \right] + 9 \epsilon^{10} \left( W^{(1)} \right)^8 W^{(2)} + \epsilon^{11} \left( W^{(1)} \right)^{10} \right\} \\ &+ \frac{\left( \Delta \mu_{\text{exf}} F_{\text{F}} \right)^{10}}{143} \left[ 13 + 5 \left( 3 \cos^2 \zeta_{\text{et}} - 1 \right) \left( 3 \cos^2 \chi - 1 \right) \right] * b_A(\tilde{v}) \left( \text{S37} \right) \right] \right. \\ &+ \frac{\left( \Delta \mu_{\text{exf}} F_{\text{F}} \right)^{10}}{143} \left[ 13 + 5 \left( 3 \cos^2 \zeta_{\text{et}} - 1 \right) \left( 3 \cos^2 \chi - 1 \right) \right] * b_A(\tilde{v}) \left( \text{S37} \right) \right. \\ \\ &+ \frac{\left( \Delta \mu_{\text{exf}} F_{\text{F}} \right)^{10}}{143} \left[ 13 + 5 \left( 3 \cos^2 \zeta_{\text{et}} - 1 \right) \left( 3 \cos^2 \chi - 1 \right) \right] * b_A(\tilde{v}) \left( \text{S37} \right) \right] \right] + \delta \left[ \frac{\left( \Delta \mu_{\text{exf}} F_{\text{F}} \right)^{10}}{143} \left[ 13 + 5 \left( 3 \cos^2 \zeta_{\text{et}} - 1 \right) \left( 3 \cos^2 \chi - 1 \right) \right] * b_A(\tilde{v}) \left( \text{S37} \right) \right]$$

$$\begin{split} \Delta A(F^{12}) &= A_0 \text{Im} \left\{ \epsilon^2 W^{(12)} \right. \\ &+ \epsilon^3 \left[ \left( W^{(6)} \right)^2 + 2 W^{(1)} W^{(11)} + 2 W^{(2)} W^{(10)} + 2 W^{(3)} W^{(9)} + 2 W^{(4)} W^{(8)} \right. \\ &+ 2 W^{(5)} W^{(7)} \right] \\ &+ \epsilon^4 \left[ \left( W^{(4)} \right)^3 + 3 \left( W^{(1)} \right)^2 W^{(10)} + 3 \left( W^{(2)} \right)^2 W^{(8)} + 3 \left( W^{(3)} \right)^2 W^{(6)} + 3 \left( W^{(5)} \right)^2 W^{(2)} \right. \\ &+ 6 W^{(1)} W^{(2)} W^{(9)} + 6 W^{(1)} W^{(3)} W^{(8)} + 6 W^{(1)} W^{(4)} W^{(7)} + 6 W^{(1)} W^{(5)} W^{(6)} \right. \\ &+ 6 W^{(2)} W^{(3)} W^{(7)} + 6 W^{(2)} W^{(4)} W^{(6)} + 6 W^{(3)} W^{(4)} W^{(5)} \right] \\ &+ \epsilon^5 \left[ \left( W^{(3)} \right)^4 + 4 \left( W^{(1)} \right)^3 W^{(9)} + 4 \left( W^{(2)} \right)^3 W^{(6)} + 6 \left( W^{(1)} \right)^2 \left( W^{(5)} \right)^2 \right. \\ &+ 6 \left( W^{(2)} \right)^2 W^{(4)} W^{(6)} + 12 \left( W^{(2)} \right)^2 W^{(2)} W^{(8)} + 12 \left( W^{(1)} \right)^2 W^{(3)} W^{(7)} \\ &+ 12 \left( W^{(1)} \right)^2 W^{(4)} W^{(6)} + 12 \left( W^{(2)} \right)^2 W^{(1)} W^{(7)} + 12 \left( W^{(2)} \right)^2 W^{(3)} W^{(5)} \\ &+ 12 \left( W^{(3)} \right)^2 W^{(2)} W^{(6)} + 24 W^{(1)} W^{(2)} W^{(4)} + 12 \left( W^{(4)} \right)^2 W^{(1)} W^{(3)} \\ &+ 24 W^{(1)} W^{(2)} W^{(3)} W^{(6)} + 24 W^{(1)} W^{(2)} W^{(4)} W^{(5)} \right] \\ &+ \epsilon^6 \left[ 5 \left( W^{(1)} \right)^4 W^{(6)} + 5 \left( W^{(2)} \right)^4 W^{(4)} + 10 \left( W^{(2)} \right)^3 W^{(3)} \right)^2 + 20 \left( W^{(1)} \right)^3 W^{(2)} W^{(7)} \\ &+ 20 \left( W^{(1)} \right)^3 W^{(3)} W^{(6)} + 20 \left( W^{(1)} \right)^3 W^{(4)} W^{(5)} + 20 \left( W^{(2)} \right)^3 W^{(1)} W^{(5)} \\ &+ 20 \left( W^{(1)} \right)^3 W^{(3)} W^{(6)} + 20 \left( W^{(1)} \right)^3 W^{(4)} W^{(5)} + 20 \left( W^{(2)} \right)^3 W^{(1)} W^{(5)} \\ &+ 20 \left( W^{(1)} \right)^3 W^{(2)} W^{(2)} + 30 \left( W^{(1)} \right)^2 W^{(2)} W^{(3)} W^{(5)} + 60 \left( W^{(2)} \right)^2 W^{(4)} \\ &+ 30 \left( W^{(1)} \right)^4 W^{(2)} W^{(6)} + 30 \left( W^{(1)} \right)^4 W^{(3)} W^{(5)} + 30 \left( W^{(2)} \right)^4 W^{(1)} W^{(3)} \right. \\ &+ \epsilon^7 \left[ \left( W^{(2)} \right)^6 W^{(6)} + 30 \left( W^{(1)} \right)^4 W^{(3)} W^{(5)} + 30 \left( W^{(2)} \right)^4 W^{(1)} W^{(3)} \right. \\ &+ 60 \left( W^{(1)} \right)^3 W^{(2)} W^{(5)} + 60 \left( W^{(2)} \right)^3 \left( W^{(1)} \right)^2 W^{(4)} + 90 \left( W^{(1)} \right)^2 \left( W^{(2)} \right)^2 \left( W^{(3)} \right)^2 \\ &+ 120 \left( W^{(1)} \right)^3 W^{(2)} W^{(3)} W^{(4)} \right. \\ &+ \epsilon^8 \left[ 7 \left( W^{(1)} \right)^6 W^{(6)} + 21 \left( W^{(2)} \right)^5 \left( W^{(1)} \right)$$

$$+ 42(W^{(1)})^{5}W^{(3)}W^{(4)} + 105(W^{(1)})^{4}(W^{(2)})^{2}W^{(4)} + 105(W^{(1)})^{4}(W^{(3)})^{2}W^{(2)}$$

$$+ 140(W^{(1)})^{3}(W^{(2)})^{3}W^{(3)} \Big]$$

$$+ \epsilon^{9} \Big[ 8(W^{(1)})^{7}W^{(5)} + 28(W^{(1)})^{6}(W^{(3)})^{2} + 56(W^{(1)})^{6}W^{(2)}W^{(4)}$$

$$+ 70(W^{(1)})^{4}(W^{(2)})^{4} + 168(W^{(1)})^{5}(W^{(2)})^{2}W^{(3)} \Big]$$

$$+ \epsilon^{10} \Big[ 9(W^{(1)})^{8}W^{(4)} + 72(W^{(1)})^{7}W^{(2)}W^{(3)} + 84(W^{(1)})^{6}(W^{(2)})^{3} \Big]$$

$$+ \epsilon^{11} \Big[ 10(W^{(1)})^{9}W^{(3)} + 45(W^{(1)})^{8}(W^{(2)})^{2} \Big] + 11\epsilon^{12}(W^{(1)})^{10}W^{(2)} + \epsilon^{13}(W^{(1)})^{12} \Big\}$$

$$\frac{(\Delta\mu_{\rm et}fF)^{12}}{195} \Big[ 15 + 6(3\cos^{2}\zeta_{\rm et} - 1)(3\cos^{2}\chi - 1) \Big] * b_{\rm A}(\bar{\nu})$$
 (S38)

where we suppress most  $\bar{v}$  dependence for clarity. By plugging Equations S33-S38 back into Equations S20 and S21, we finally obtain  $\Delta A(4\omega)$  and  $\Delta A(6\omega)$  for the RSE up to the  $F^{12}$  term. For F close to 1 MV/cm, higher order terms can be appreciable, and this truncation is still unfortunately insufficient; we instead simulate at a lower field and scale the resulting spectra to 1 MV/cm as the overall shapes that determine  $\delta$  remain largely unchanged. In practice, the derivatives of  $W(\bar{v})$  with Gaussian  $\rho_{FC}$  can be analytically calculated and later numerically evaluated (e.g., diff and eval in MATLAB), while the Pekarian counterpart needs to be numerically differentiated with the aid of filters for higher-order derivatives to minimize noise (e.g., gradient and sgolayfilt in MATLAB). The Hilbert transform is only executed after differentiation, utilizing the fact that these two operations are commutative.

The raw data set of A,  $\Delta A(4\omega)$  and  $\Delta A(6\omega)$  acquired for each sample are first scaled such that the maximum absorbance  $Q_V$  band of H is 0.1, and the Stark spectra are scaled to 1 MV/cm to standardize the following fitting procedure. The starting values for the six free parameters (three related to charge transfer and three related to the absorption spectrum) are guessed according to the previously published values (69), and the pre-processed data are *simultaneously* fit to the simulated spectra by varying the free parameters subject to certain bounds using nonlinear least squares algorithm

(lsqcurvefit in MATLAB). If the simulated spectra are calculated at different wavenumber points from those for acquired spectra, spline interpolation is incorporated (interpl with 'spline' option in MATLAB). Since the shapes of the Stark spectra are sensitive to  $\delta$ , while the field dependence is related to  $\Delta\mu_{\rm R}$ , the three reduced parameters  $\delta$ ,  $W_{\rm R}$ , and  $\Delta\mu_{\rm R}$  can be determined independently without mutual interference. Specifically, the intensities of  $\Delta A(4\omega)$  and  $\Delta A(6\omega)$  are roughly proportional to  $W_R \cdot \Delta \mu_R^4$  and  $W_R \cdot \Delta \mu_R^6$ , respectively (68), inferred from second-order perturbation in  $V_0$  and the field dependence. Because the absorption spectrum is about two orders of magnitude more intense than the corresponding  $\Delta A(4\omega)$  and  $\Delta A(6\omega)$ , which share similar orders of magnitude, extra weights on the order of 1 and 100 are given to the absorption spectrum and Stark spectra, respectively, to treat all three spectra equally for residual evaluation. Consideration of the shapes of both  $\Delta A(4\omega)$  and  $\Delta A(6\omega)$ offers a consistency check of the resulting  $\delta$ , since it is possible for two different  $\delta$ 's to share similar shapes for Stark spectra acquired at a certain harmonic but highly unlikely for them to still share similar lineshapes for Stark spectra acquired at a different harmonic (67). Occasionally, when  $\Delta A(6\omega)$  is acquired at too high of a field such that the truncation at  $F^{12}$  order is not accurate, only A and  $\Delta A(4\omega)$ are fit, and the predicted shape of  $\Delta A(6\omega)$  at a lower field is then compared with the experimentally determined  $\Delta A(6\omega)$ . This strategy is valid because the shapes of Stark spectra due to the RSE are mostly sensitive to  $\delta$ , and the field strength difference only slightly affects the scaled magnitudes (at most 10%), but minimally the shapes.

To summarize, we include a flow chart (Fig. S82) to illustrate how the six free parameters determine the absorption and resonance Stark spectra based on the equations listed above. The resulting simulated spectra from the initial guess of free parameters can be subsequently compared to the experimentally obtained data by evaluating the residuals. The data are fit by iteratively updating the free parameter inputs through residual minimization, and the optimal free parameters are achieved and accepted when the residuals cannot be further reduced.

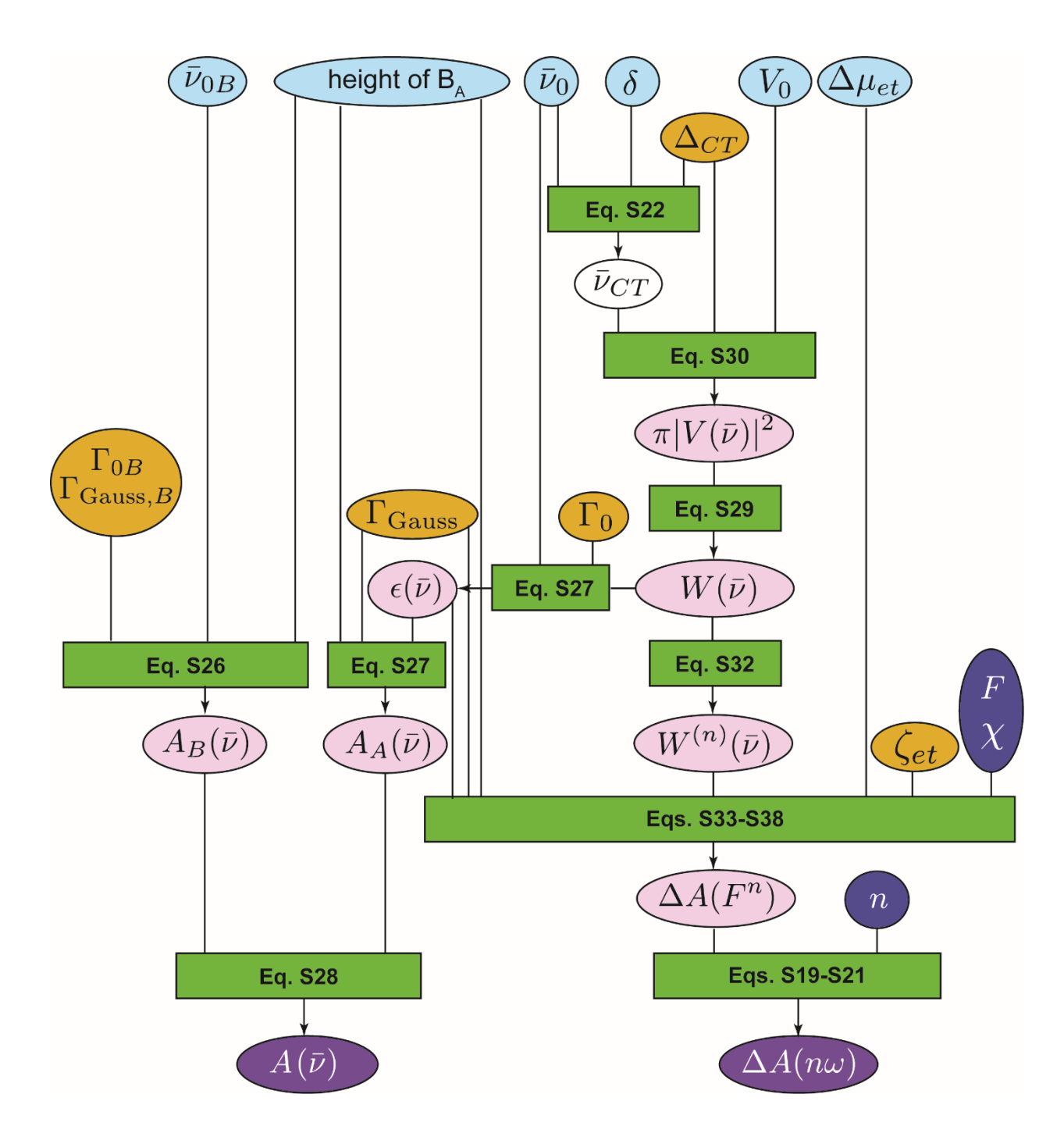


**Fig. S82.** Flowchart diagraming an overview of how the various parameters are incorporated to generate simulated spectra for fitting to experimentally determined resonance Stark ( $\Delta A(n\omega)$ ) and 77 K absorbance spectra ( $A(\bar{\nu})$ ). In light blue are the six free parameters we seek to extract from resonance Stark spectra. In orange are parameters which are fixed for all RC variants. In dark blue are all experimentally controlled parameters (defined and recorded during the experiment). In green are all equations relating the various parameters. In white are the intermediate parameter(s). In pink, all

intermediate functions and in purple are the simulated spectra. Parameters are optimized via a Levenberg–Marquardt minimization feedback loop such that the sum of residuals between simulated spectra and experimentally obtained data is minimized.

### S5.4 Stark Spectra and Simulated Fits of Table

In this section, we detail the analysis of resonance Stark spectra (Fig. 6, Figs. S83–S89) to obtain the key excited-state electron transfer parameters ( $\delta$ , coupling strength  $V_0$ , and electron-transfer distance  $d_{CT} = \Delta \mu_{et}/e$ ; e is the elementary charge). As we are interested in the RSE of the bacteriochlorophyll Q<sub>v</sub> B-band (Fig. S90), only features in 12000-13000 cm<sup>-1</sup> are shown in the subsequent figures. Moreover, we only analyze  $\Delta A(4\omega)$  and  $\Delta A(6\omega)$  because the RSE feature in  $\Delta A(2\omega)$  is largely contaminated by the classical Stark features; for future reference we still summarize the corresponding  $\Delta A(2\omega)$  in Fig. S91. To facilitate comparison, all spectra shown in Figs. S83–S89 are scaled to an absorbance maximum of 0.1 for the bacteriopheophytin (H)  $Q_{\rm V}$  band, and the Stark spectra are all scaled to 1 MV/cm based on the classical behavior  $\Delta A(n\omega) \propto F^n$ . As discussed at the beginning of Section S5.3, however, the actual applied field strength is critical for reproducing each resonance Stark feature due to higher-order contaminations, so it is listed next to each Stark spectrum.  $\Delta A(6\omega)$  spectra were all acquired at higher fields than those acquired for  $\Delta A(4\omega)$  to facilitate a higher signal-to-noise ratio, while both  $\Delta A(4\omega)$  and  $\Delta A(6\omega)$  spectra were simulated with the lower fields at which the  $\Delta A(4\omega)$  spectra are measured due to the truncation error for simulation at higher fields (Equations S19-S21, 14th order and higher terms still contribute non-negligibly at higher fields). The RSE lineshape, however, which determines the sought-after parameter  $\delta$ , is the same when simulated at different field strengths; the intensity differs at most by 10%. Since the intensities of  $\Delta A(4\omega)$  and  $\Delta A(6\omega)$  spectra are proportional to  $V_0^2 d_{\rm CT}^4$  and  $V_0^2 d_{\rm CT}^6$ , the corresponding  $V_0$  and  $d_{\rm CT}$  obtained by simulating at lower fields are still reliable. Note that because we estimate  $d_{CT}$  from  $\Delta \mu_{et}$  and because  $\Delta \mu_{et}$  contains the local field factor f, we include f next to every  $d_{CT}$  to reflect this caveat. This factor accounts for the difference between the applied field and the field experience by the chromophore, is treated as a scalar, and is generally greater

than 1 for electronic chromophores (see SI Section S6 in reference for a more thorough discussion). Nevertheless, f is expected to be constant across all RC mutants and variants (7, 72), so  $fd_{CT}$  can still be compared across them (69) and our entire analysis is relative to WT.

RSEs for wild-type, MeY, and NO<sub>2</sub>Y RCs (Figs. S83–S85) can be well accounted for with one set of parameters ( $\delta$ ,  $V_0$ ,  $fd_{CT}$ , etc.), as was performed previously with conventional mutations (69), indicating the samples do not have multiple distinguishable energetic populations or fractions. We refer to these fits here as "one-fraction fits". The parameters for the WT RC (Fig. S83) are consistent with previously derived values (69). The RSE lineshapes for the MeY RC largely recapitulates those for WT RCs, and the resulting parameters are similar to the WT counterparts (Fig. S84). The methyl group is weakly electron-donating and exhibits a small perturbation even when directly attached to the moieties being probed (7, 64). On the other hand, as a strong electron-withdrawing group, the nitro-modification on the tyrosine at M210 in NO<sub>2</sub>Y RCs causes significant changes to the lineshapes of  $\Delta A(4\omega)$  and  $\Delta A(6\omega)$  (Fig. S85) relative to those seen in WT. These lineshapes are similar to those of Y(M210)W, the most perturbative mutant observed by Treynor *et al.* ( $\delta$  = -0.14) (69) but lineshape analysis (fitting) indicates the introduced nitro-group caused even more perturbation ( $\delta$  = -0.05).

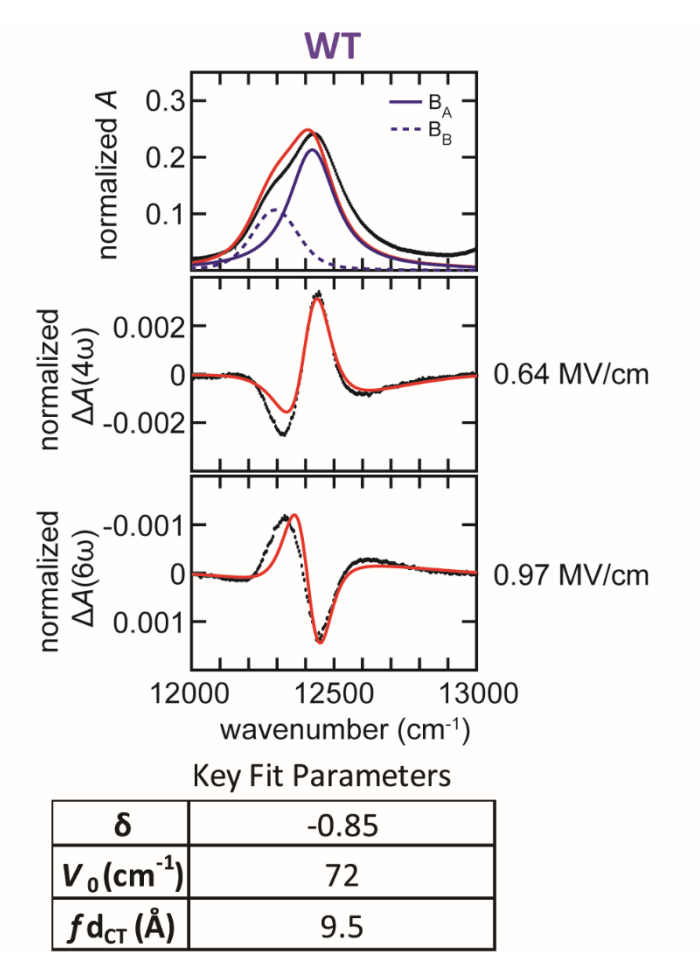


**Fig. S83.** 77 K bacteriochlorophyll ( $B_A$  and  $B_B$ )  $Q_y$  absorption and  $\Delta A(4\omega)$  and  $\Delta A(6\omega)$  Stark spectra for WT RC. All spectra are measured with  $\chi = 90^\circ$  and the applied field strength for each Stark spectrum is shown. Red traces (simulated at 0.64 MV/cm) are one-fraction fits to the data set, with the corresponding key parameters listed at the bottom.

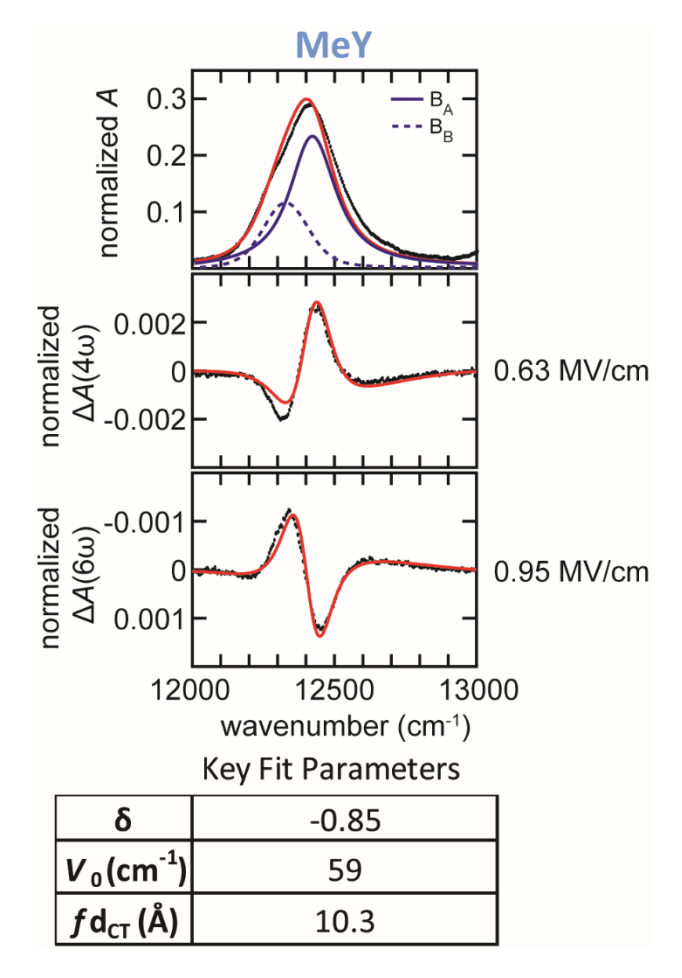


**Fig. S84.** 77 K bacteriochlorophyll ( $B_A$  and  $B_B$ )  $Q_y$  absorption and  $\Delta A(4\omega)$  and  $\Delta A(6\omega)$  Stark spectra for the MeY RC. All spectra are measured with  $\chi = 90^\circ$  and the applied field strength for each Stark spectrum is shown. Red traces (simulated at 0.63 MV/cm) are one-fraction fits to the data set, with the corresponding key parameters listed at the bottom.

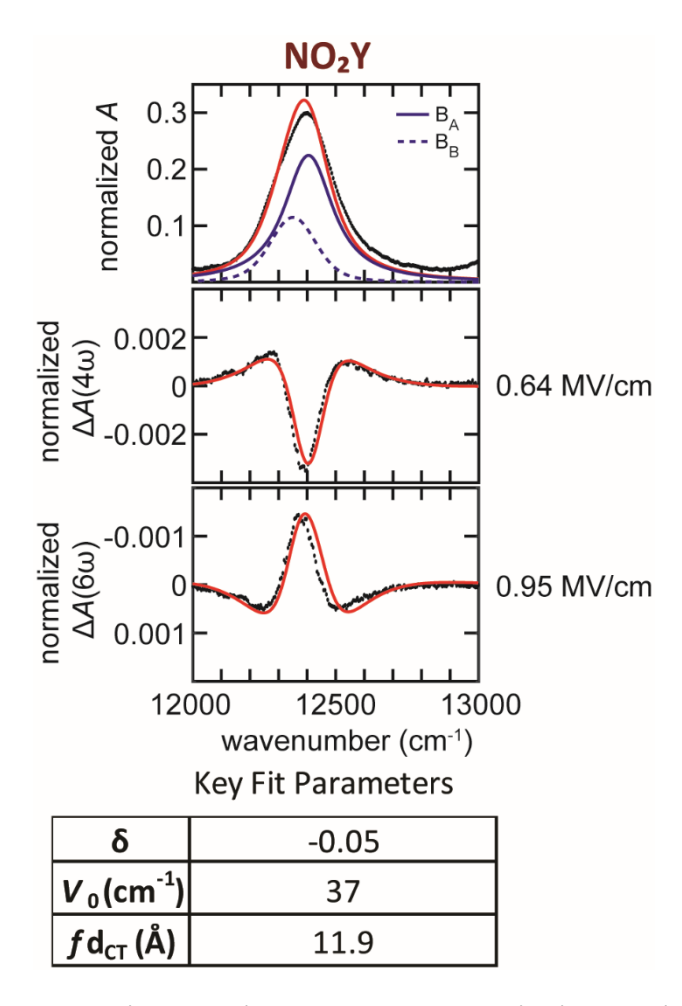


**Fig. S85.** 77 K bacteriochlorophyll ( $B_A$  and  $B_B$ )  $Q_y$  absorption and  $\Delta A(4\omega)$  and  $\Delta A(6\omega)$  Stark spectra for NO<sub>2</sub>Y RC. All spectra are measured with  $\chi = 90^\circ$  and the applied field strength for each Stark spectrum is shown. Red traces (simulated at 0.64 MV/cm) are one-fraction fits to the data set, with the corresponding key parameters listed at the bottom.

The results for the halogenated RCs are more complicated; the CIY RC serves as a representative example and will be discussed in greatest detail (Fig. S86). Without fitting the data, we already observe that the  $\Delta A(4\omega)$  feature for the CIY variant looks nearly canceled and is even less intense than  $\Delta A(6\omega)$ , which is not possible from any one-fraction RSE observed in the previous literature since the magnitude of  $\Delta A(4\omega) \propto \left(\frac{\Delta \mu_{\rm CT} \cdot F}{\Delta_{\rm CT}}\right)^4$  and the magnitude of  $\Delta A(6\omega) \propto \left(\frac{\Delta \mu_{\rm CT} \cdot F}{\Delta_{\rm CT}}\right)^6$ ; under experimentally accessible fields  $\left(\frac{\Delta \mu_{\rm CT} \cdot F}{\Delta_{\rm CT}}\right)^4 > \left(\frac{\Delta \mu_{\rm CT} \cdot F}{\Delta_{\rm CT}}\right)^6$  for RCs (68, 69).  $\Delta A(4\omega)$  and  $\Delta A(6\omega)$  for halotyrosine RCs are consistently less intense than WT, MeY and NO<sub>2</sub>Y, which were well-fit with a single fraction (Figs. S83–S85). To better illustrate the failure of a one-fraction fit, we attempted three fitting schemes: (1) either  $\Delta A(4\omega)$  or (2)

 $\Delta A(6\omega)$  are preferentially fitted or both are (3) simultaneously fitted without bias as was performed on spectra obtained for MeY, NO<sub>2</sub>Y, and WT RCs (Fig. S86). None of the fitting schemes result in satisfactory agreement with simulated spectra for CIY. Moreover, to accommodate the abnormal flip in magnitudes between  $\Delta A(4\omega)$  and  $\Delta A(6\omega)$ , the optimal  $fd_{CT}$  amounts to 7 – 8 Å. This is smaller than the range (9.5 – 13.1 Å) determined for various RC mutants (69). As we see no evidence for a substantial decrease in interchromophore distances upon halogenation (Table S3), this one-fraction fit is likely unphysical. The requirement of at least two fractions is also motivated by the corresponding CIY RC crystal structure (Fig. 2), where two rotamers are observed, with one pointing its chlorine atom towards B<sub>A</sub> and the other away from B<sub>A</sub>. Analysis of Stark spectra are notoriously treacherous when more than one absorption feature overlaps or when two or more fractions are present in the same spectral region due to cancellation of positive and negative features (71), but additional physical inputs from orthogonal methods for deconvolution can help ameliorate the situation (82, 83). In the present case, the crystal structure can be useful. We expect the rotamer with the chlorine atom pointed away from BA to be minimally perturbative (wild-type-like; α fraction) as inferred from the MeY case and halogens being weakly electron-withdrawing when directly attached to the green fluorescent protein chromophore, which has been extensively characterized (7, 64). The corresponding population determined by crystallography is 40% (Fig. 2), which can then be invoked as an initial guess to subtract the wild-typelike fraction (Fig. S83) from the Stark spectra, revealing the second fraction (β fraction). The fact that assuming 40% wild-type-like fraction is enough to generate a self-consistent  $\Delta A(4\omega)$  and  $\Delta A(6\omega)$  for the β fraction with physical ET parameters (Fig. S87B) suggests this is a viable approach. In other words, a bad guess would have resulted in 2 sets of  $\Delta A(4\omega)$  and  $\Delta A(6\omega)$  with inconsistent shapes (i.e., each  $\Delta A(4\omega)/\Delta A(6\omega)$  pair cannot be predicted from the same  $\delta$ ). The fraction ( $\beta$  fraction) which we associate with the protein conformer which places the halogen in close proximity to the magnesium (Fig. 2) curiously results in a significantly more perturbative  $\delta$  that is closer to the NO<sub>2</sub>Y counterpart, which

could suggest some interaction between the halogen and the  $B_A$  magnesium. As a reminder, because only the  $B_A$  chromophore exhibits a RSE (67, 69, 81), both the  $\alpha$  and  $\beta$  fraction resonance Stark spectra are attributed to different energetic fractions of  $B_A$ .

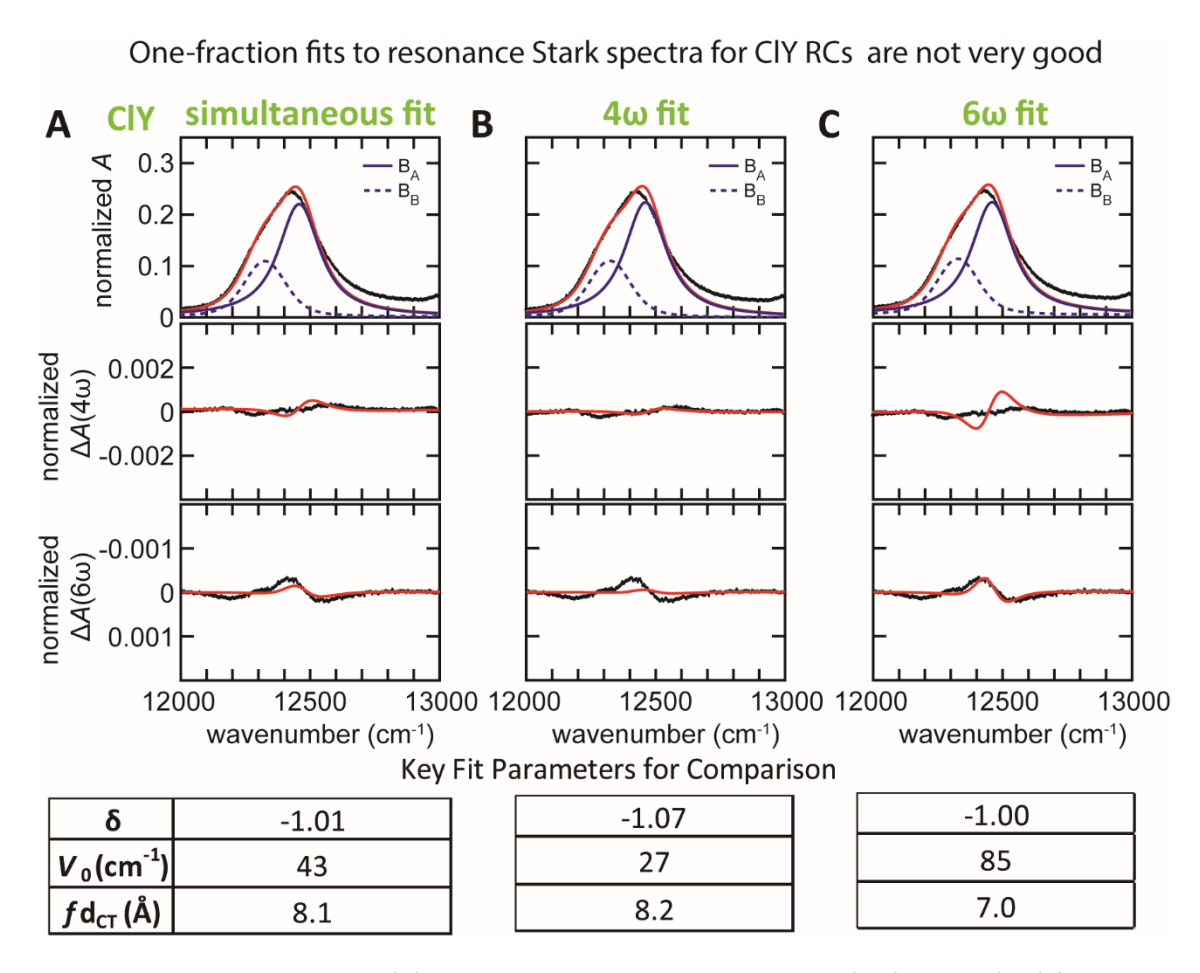


**Fig. S86.** 77 K bacteriochlorophyll (B)  $Q_y$  absorption and Stark spectra  $\Delta A(4\omega)$  and  $\Delta A(6\omega)$  for CIY RCs. All spectra are measured with  $\chi = 90^\circ$ .  $\Delta A(4\omega)$  and  $\Delta A(6\omega)$  were acquired at applied fields of 0.59 MV/cm and 0.88 MV/cm, respectively. Red traces (simulated at 0.59 MV/cm) are one-fraction fits to the data set, with the corresponding key parameters listed at the bottom. (A) Simultaneous one-fraction fit of both  $\Delta A(4\omega)$  and  $\Delta A(6\omega)$  as is done in WT, MeY, and NO<sub>2</sub>Y RC fitting. (B) Simultaneous fit biased towards maximizing agreement with  $\Delta A(4\omega)$ . (C) Simultaneous fit biased towards maximizing agreement with  $\Delta A(6\omega)$ . None show satisfactory results.

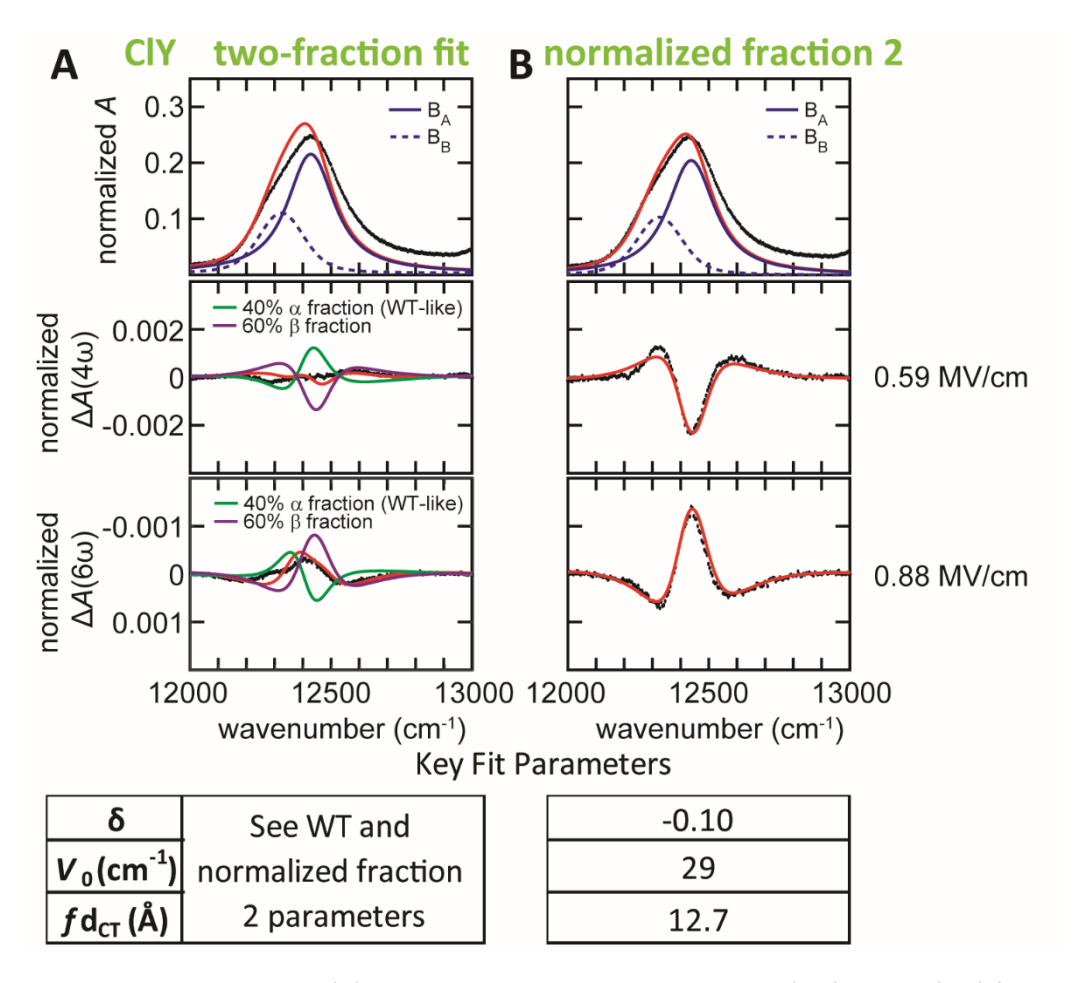


**Fig. S87.** 77 K bacteriochlorophyll (B)  $Q_y$  absorption and Stark spectra  $\Delta A(4\omega)$  and  $\Delta A(6\omega)$  for CIY RCs, the same data set shown in Fig. S86, but now analyzed with two fractions. The α fraction is assumed to be wild-type-like, and with the input of populations from orientations observed by X-ray crystallography (Fig. 2), normalized (population scaled up to 100%) Stark spectra of the β fraction (panel B) are revealed. Red traces (simulated at 0.59 MV/cm) are fits to the data set, with the corresponding key parameters listed at the bottom. Please consult Section S5.4 for more detailed description of the analysis.

As the BrY and IY spectra look similar (Fig. S88 and Fig. S89), we can analyze them together with the same method. First, we attempted one-fraction analysis for both, resulting in satisfactory fits (Fig. S88A and Fig. S89A). However, the extracted  $fd_{CT}$  ( $\sim$  7 Å) are again too small to be physically meaningful. Two orientations are also observed for the BrY and IY crystal structures but with different orientation ratios than that observed for CIY (Fig. 2). Using a similar deconvolution strategy to that used in CIY, the relative proportions for the  $\alpha$  and  $\beta$  fractions are also determined for these two variants, along with the energetics for  $\beta$  fraction (Fig. S88B and Fig. S89B). This time, however, the initial guess of the  $\alpha$  fraction population (50% and 80% for BrY and IY, respectively) is not good enough to unveil the  $\beta$  fraction with

physical electron-transfer parameters (e.g., Stark features being too large), so the minor adjustment in populations shown in the figures was used. The final  $\delta$  for both of the  $\beta$  fraction's is revealed to be -0.05, similar to that observed in CIY RCs, and brings  $\delta$  of the  $\beta$  fraction to be nearly identical to that of the NO<sub>2</sub>Y RC.

We conclude this section by summarizing all parameters for each variant in Table S7. By replacing the critical M210 tyrosine with noncanonical tyrosine analogs, we perturb the energetics of  $B_A^* \to B_A^+ H_A^-$  to a large extent, more so than the most perturbative substitution (Tyr mutated to Trp) observed before (69).

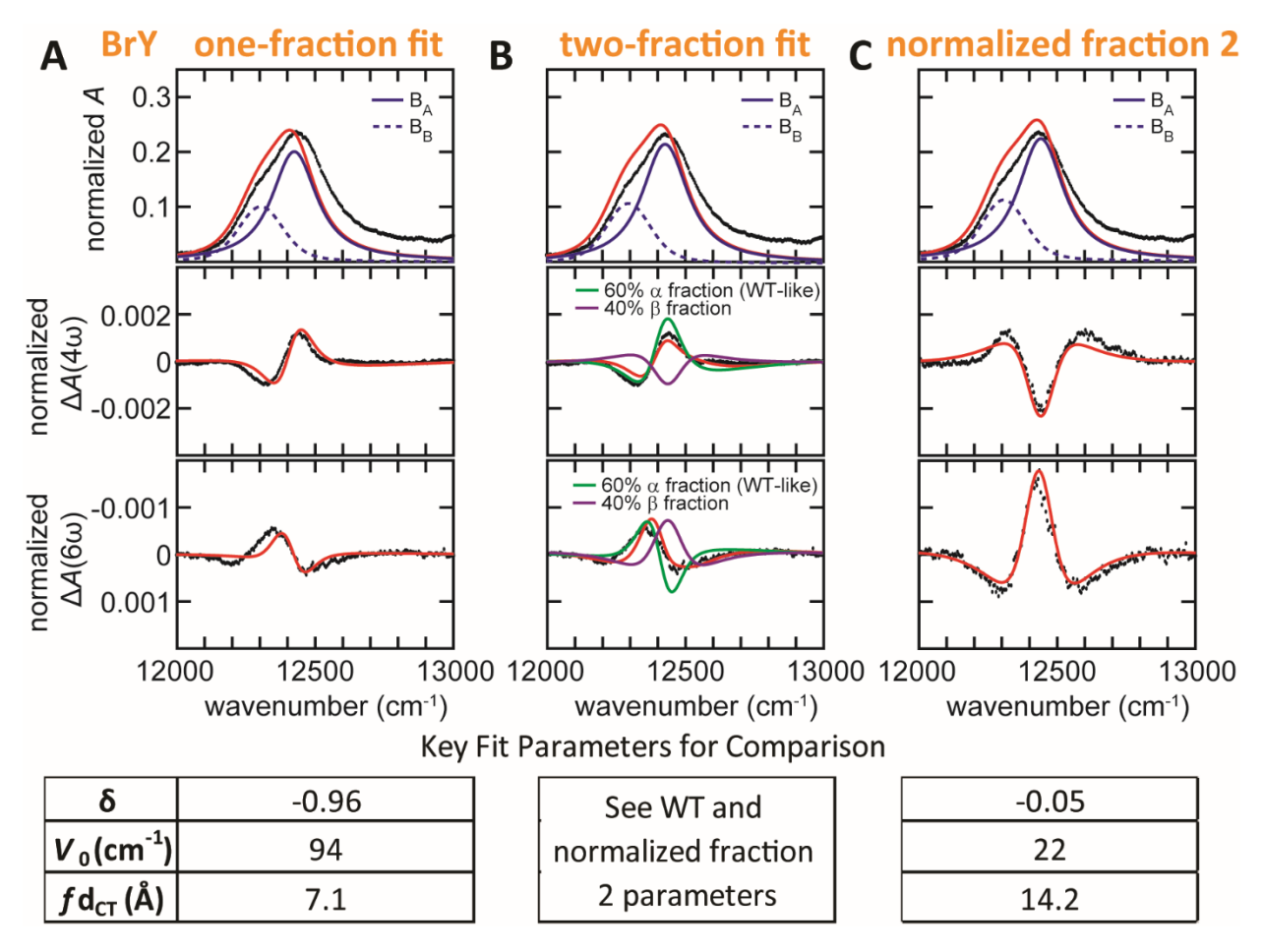


**Fig. S88.** 77 K bacteriochlorophyll (B)  $Q_y$  absorption and Stark spectra  $\Delta A(4\omega)$  and  $\Delta A(6\omega)$  for the BrY RC. All spectra are measured with  $\chi = 90^\circ$ .  $\Delta A(4\omega)$  and  $\Delta A(6\omega)$  was acquired at an applied field of 0.58 MV/cm and 0.87 MV/cm, respectively. Red traces (simulated at 0.58 MV/cm) are fits to the data set, with the corresponding key parameters listed at the bottom. (A) One-fraction fit. (B) Two-fraction fit, with the  $\alpha$  fraction being wild-type like. (C) Normalized (population scaled up to 100%)  $\beta$  fraction.

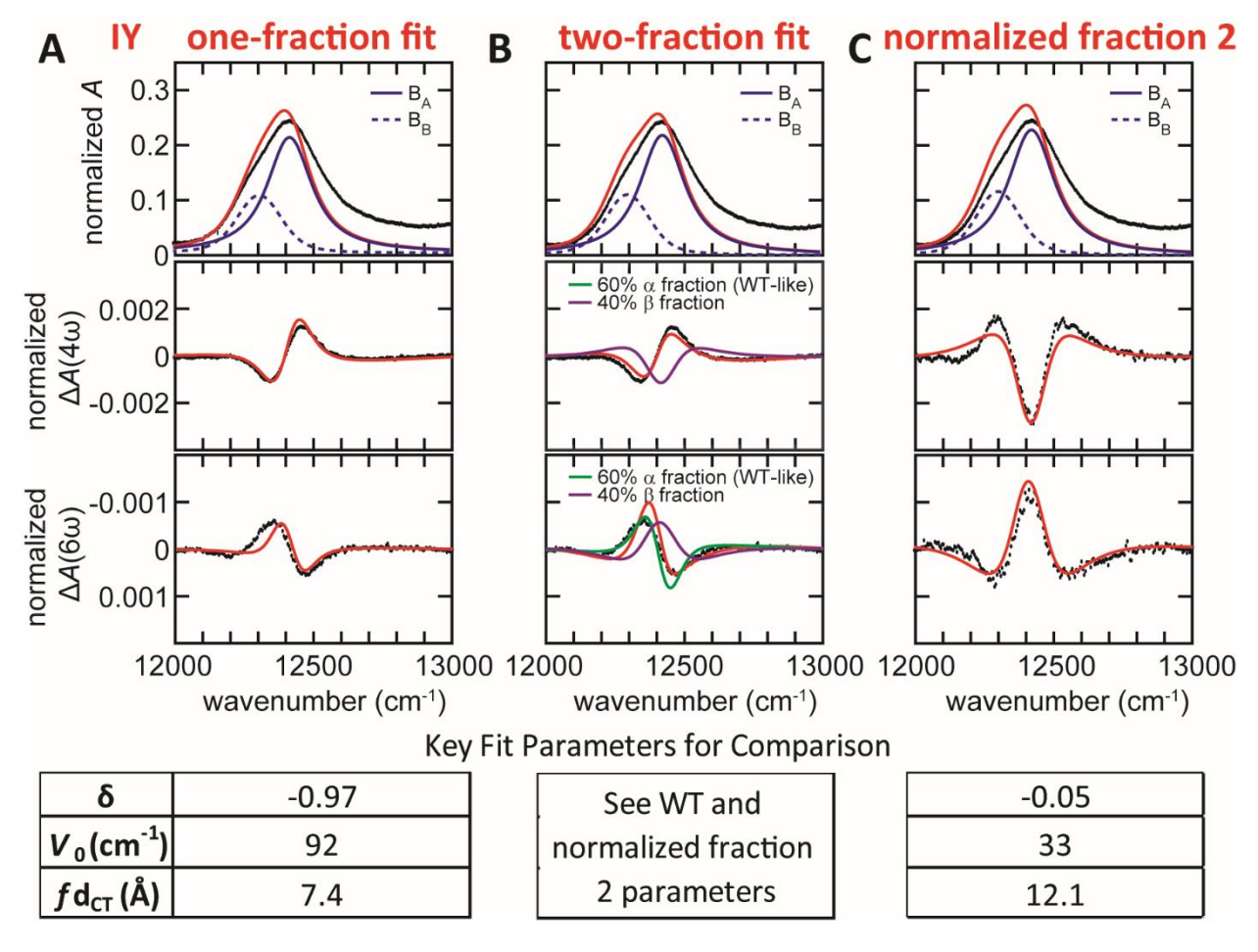


**Fig. S89.** 77 K bacteriochlorophyll (B)  $Q_y$  absorption and Stark spectra  $\Delta A(4\omega)$  and  $\Delta A(6\omega)$  for IY RC. All spectra are measured with  $\chi = 90^\circ$ .  $\Delta A(4\omega)$  and  $\Delta A(6\omega)$  was acquired at an applied field of 0.59 MV/cm and 0.88 MV/cm, respectively. Red traces (simulated at 0.59 MV/cm) are fits to the data set, with the corresponding key parameters listed at the bottom. (A) One-fraction fit. (B) Two-fraction fit, with the α fraction being wild-type like. (C) Normalized (population scaled up to 100%) β fraction.

Fit	B <sub>A</sub> peak position (cm <sup>-1</sup> )	B <sub>A</sub> peak height	B <sub>B</sub> peak position (cm <sup>-1</sup> )	δ	<i>V</i> <sub>0</sub> (cm <sup>-1</sup> )	fd <sub>CT</sub> (Å)
WT	12430	0.215	12295	-0.85	72	9.5
MeY	12425	0.232	12325	-0.85	59	10.3
NO <sub>2</sub> Y	12405	0.231	12350	-0.05	37	11.9
CIY	12460	0.218	12320	-1.01	43	8.1
CIY 4ω	12465	0.221	12320	-1.07	27	8.2
CIY 6ω	12470	0.222	12320	-1.00	85	7.0
<b>CIY</b> α Fraction	12430	0.215	12295	-0.85	72	9.5
CIY β Fraction	12435	0.206	12325	-0.10	29	12.7
BrY	12435	0.200	12325	-0.96	94	7.1
<b>BrY</b> α <b>Fraction</b>	12430	0.215	12295	-0.85	72	9.5
BrY β Fraction	12440	0.223	12305	-0.05	22	14.2
IY	12430	0.213	12310	-0.97	92	7.4
IY α Fraction	12430	0.215	12295	-0.85	72	9.5
IY β Fraction	12420	0.230	12295	-0.05	33	12.1

**Table S7.** Table summarizing free parameters from fits to resonance Stark data from Figs. S83–S85. Entries annotated with "α fraction" or "β fraction" are derived from two-fraction fits, while the rest are from one-fraction fits; the detailed fitting schemes can be found in Figs. S83–S85. Grayed in boxes were fits that were ultimately rejected due to a combination of less adequate agreement of simulated fit with resonance Stark data and due to unphysically short distances of charge transfer from  $B_A$  to  $H_A$  given crystallographic coordinates and previous resonance Stark data in the literature (69). Note that the  $B_A$  peak position is minimally perturbed across these RC variants (Fig. S90) but the driving force of  $B_A*H_A \rightarrow B^+H_A^-$  (or  $\delta$ ) are dramatically modulated, which can only be extracted by resonance Stark effect spectroscopy. Note that  $V_0$  is also significantly perturbed across all variants, but a similarly large range in  $V_0$  is seen previously for other RC mutants (69). The parameters  $V_0$  and  $\delta$  are independent, however, and differently affect the spectra:  $V_0$  influences primarily the intensity of the signal in resonant Stark spectra, not the line shape. Large changes in  $V_0$  do not significantly influence the  $\delta$  extracted from a given set of spectra (68).

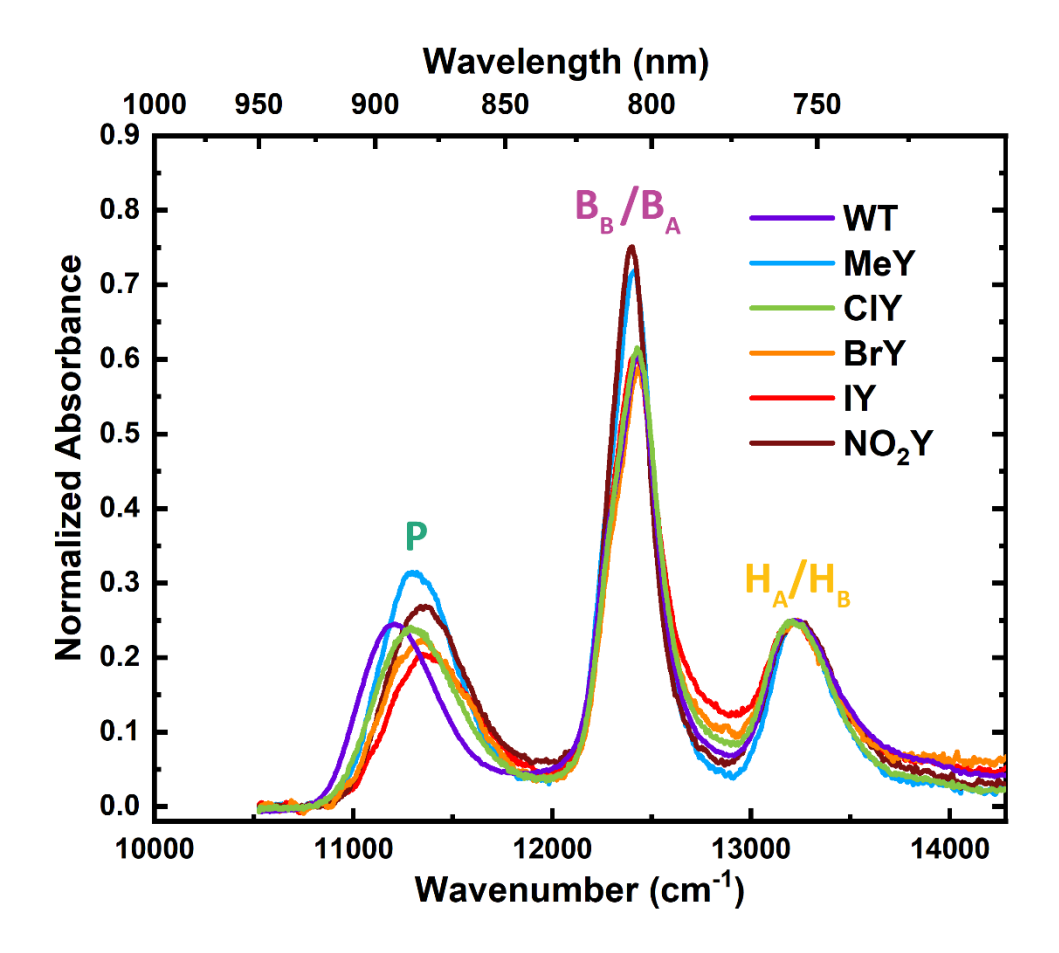


**Fig. S90.** 77K NIR absorption data for all RC variants normalized at the H<sub>A</sub>/H<sub>B</sub> Q<sub>y</sub> absorbance band maximum for each variant (~13,220 cm<sup>-1</sup>). RC variants display similar temperature dependence to WT, e.g.  $\Delta\Delta G_5$  in Fig. S76B at room temperature is similar to  $\Delta\Delta G_5$  at 77K.

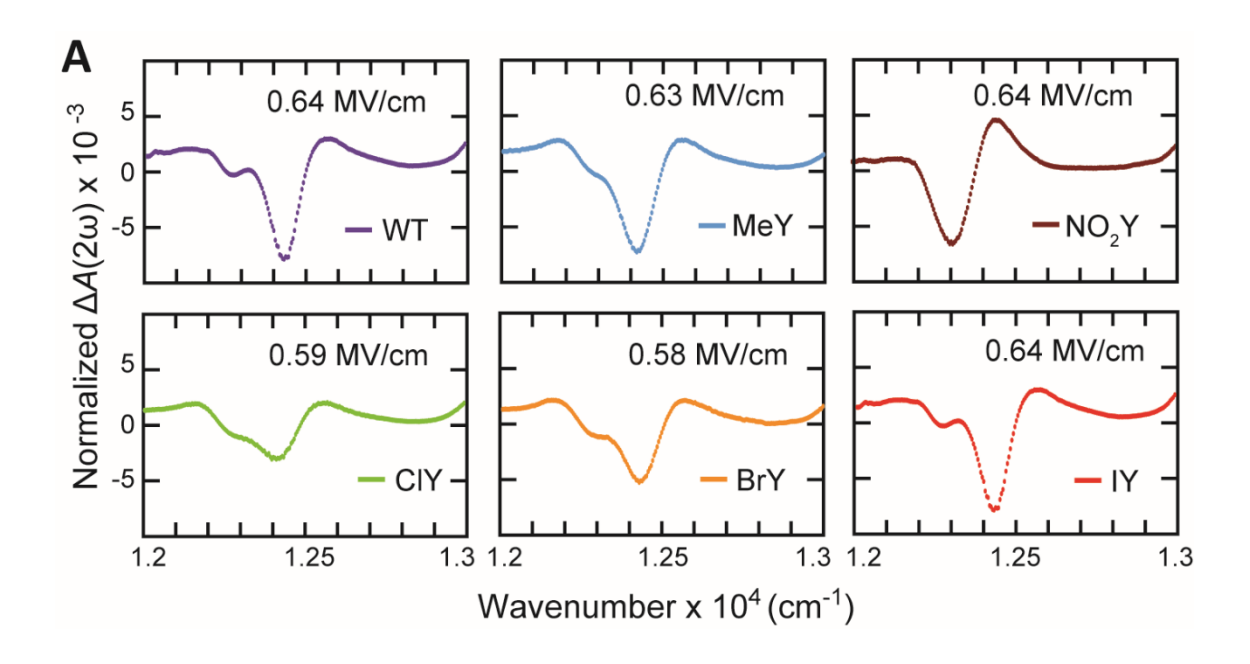


**Fig. S91.**  $\Delta A(2\omega)$  Stark spectra for WT and RC variants for the B band. The applied field is written above each Stark spectrum, and the corresponding absorption spectra A are shown in Fig. S83–Fig. **S89**. Since  $\Delta A(2\omega)$  is contaminated by the presence of classical Stark features, its analysis is beyond the scope of the work.  $\Delta A(2\omega)$  spectra are only presented here for completeness.

### S5.5 Stark Spectra of P

While a resonance Stark effect has been observed for  $B_A$ , P's Stark spectra show no evidence for this effect. Higher order Stark spectra of P ( $\Delta A(4\omega)$  and  $\Delta A(6\omega)$ ) contain largely the same information as that displayed at  $\Delta A(2\omega)$  as predicted with by the classical Stark analysis. The large magnitude of  $|\Delta \vec{\mu}|$  has been ascribed to a much stronger coupling within the bacteriochlorophyll special pair (coupling between  $P^*$  and  $P_A^+P_B^-$ ) than is present in the coupling between  $B_A^*$  and  $B_A^+H_A^-$  ( $\sim 50$  cm<sup>-1</sup>). The lineshape and intensity in Stark data of P are very sensitive to a change in  $P^*$ 's charge transfer character. If RC variants have altered the excited state character of P in WT significantly (84, 85), then Stark data for P should show a significant change in lineshape and intensity, but they do not. RC mutants characterized in the past which alter the charge-transfer character of  $P^*$  such as the heterodimer mutants, P' and P' and P' and P' and P' in the stark effects (41). The P' in the shapes and intensities for P' of WT and MeY are like WT (see Fig. S92 caption), indicating that

charge-transfer character of P\* has not changed significantly. The  $\Delta A(2\omega)$  spectra for BrY and IY RCs have a blue shoulder at  $\sim 1.16 \times 10^4$  cm<sup>-1</sup>, possibly a reflection of the presence of two fractions (similar to the two orientations observed for crystallography and two fractions in B<sub>A</sub> resonance Stark in halotyrosine RCs). Both fractions can be fit, however, with the same set of electrooptic parameters and both fractions have  $|\Delta \vec{\mu}|$  (i.e., a P\* charge-transfer character) similar to WT (see Fig. S93 caption).

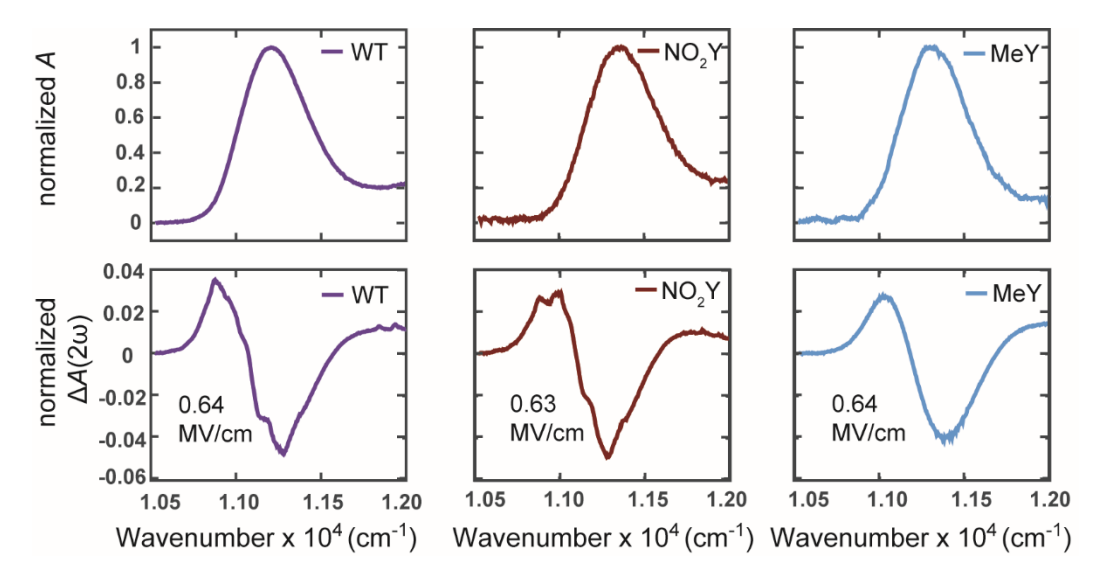


**Fig. 92.** 77K Absorbance spectra are depicted above the corresponding  $\Delta A(2\omega)$  Stark spectra for WT and RC variants for the  $Q_y$  band of P. The applied field is written below each Stark spectrum. The strong similarity in the  $\Delta A(2\omega)$  spectra between MeY, NO<sub>2</sub>Y, and WT is indicative of similar P\* charge transfer character. When fit, the  $|\Delta \vec{\mu}|$  for P was 5.8 D, 7.0 D, and 4.8 D for WT, NO<sub>2</sub>Y, and MeY respectively. These are relatively small changes given the 8.1 Å center-to-center distance between special pair bacteriochlorophylls and the corresponding 41.8 D dipole estimated for the P<sub>A</sub><sup>+</sup>P<sub>B</sub><sup>-</sup> state. Both WT and NO<sub>2</sub>Y Stark spectra were acquired with a Xe arc lamp which has emission spikes at 1.08, 1.11, 1.12, and 1.13 x 10<sup>4</sup> cm<sup>-1</sup> that are not completely removed. All other spectra were acquired with a more stable halogen light source.

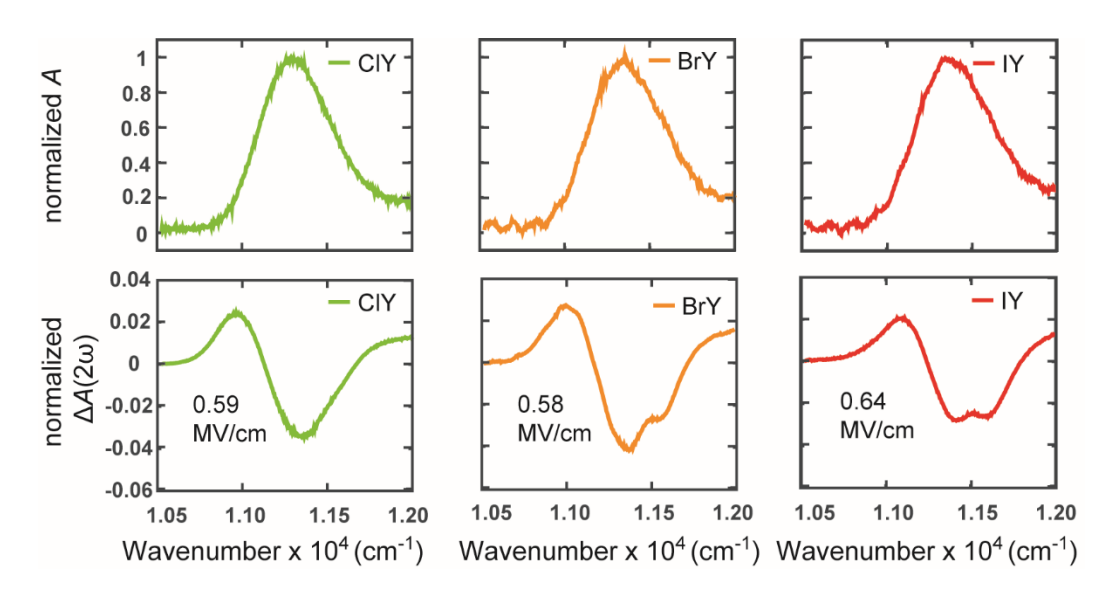


**Fig. S93.** 77K Absorbance spectra are depicted above the corresponding  $\Delta A(2\omega)$  Stark spectra for WT and RC variants for the P band. The applied field is written below each Stark spectrum. For halotyrosine RC variants, the Stark spectra seems to indicate there is inhomogeneity in the P-band such that there are two fractions present (similar to the two orientations observed for crystallography and two fractions in B<sub>A</sub> resonance Stark in halotyrosine RCs). When BrY and IY are fit utilizing two bands, the same set of electrooptic parameters for both bands is sufficient to reproduce the BrY and IY P  $\Delta A(2\omega)$  Stark spectra, indicating the two bands have similar charge-transfer character. When fit, the  $|\Delta \vec{\mu}|$  for P was 5.4 D, 6.2 D, and 4.0 D for CIY, BrY, and IY respectively, similar again to WT RC where  $|\Delta \vec{\mu}| = 5.8$  D. These are relatively small changes given the 8.1 Å center-to-center distance between special pair bacteriochlorophylls and the corresponding 41.8 D dipole estimated for the  $P_A^+P_B^-$  state.

#### S6 References

- 1. J. B. Weaver, S. G. Boxer, Genetic Code Expansion in Rhodobacter sphaeroides to Incorporate Noncanonical Amino Acids into Photosynthetic Reaction Centers. *ACS Synth. Biol.* **7**, 1618–1628 (2018).
- 2. H. S. Jang, *et al.*, Efficient Site-Specific Prokaryotic and Eukaryotic Incorporation of Halotyrosine Amino Acids into Proteins. *ACS Chem. Biol.* **15**, 562–574 (2020).
- 3. S. Herring, et al., The amino-terminal domain of pyrrolysyl-tRNA synthetase is dispensable in vitro but required for in vivo activity. FEBS Letters **581**, 3197–3203 (2007).
- 4. A. E. Owens, K. T. Grasso, C. A. Ziegler, R. Fasan, Two-Tier Screening Platform for Directed Evolution of Aminoacyl–tRNA Synthetases with Enhanced Stop Codon Suppression Efficiency. *ChemBioChem* **18**, 1109–1116 (2017).
- 5. J. J. Porter, *et al.*, Genetically Encoded Protein Tyrosine Nitration in Mammalian Cells. *ACS Chem. Biol.* **14**, 1328–1336 (2019).
- 6. D. Jun, R. G. Saer, J. D. Madden, J. T. Beatty, Use of new strains of Rhodobacter sphaeroides and a modified simple culture medium to increase yield and facilitate purification of the reaction centre. *Photosynth. Res.* **120**, 197–205 (2014).
- 7. C.-Y. Lin, M. G. Romei, L. M. Oltrogge, I. I. Mathews, S. G. Boxer, Unified Model for Photophysical and Electro-Optical Properties of Green Fluorescent Proteins. *J. Am. Chem. Soc.* **141**, 15250–15265 (2019).
- 8. R. G. Saer, *et al.*, Role of Rhodobacter sphaeroides photosynthetic reaction center residue M214 in the composition, absorbance properties, and conformations of H(A) and B(A) cofactors. *Biochemistry* **52**, 2206–17 (2013).
- 9. M. Saggu, et al., Putative hydrogen bond to tyrosine M208 in photosynthetic reaction centers from Rhodobacter capsulatus significantly slows primary charge separation. J. Phys. Chem. B 118, 6721–32 (2014).
- 10. J. I. Chuang, S. G. Boxer, D. Holten, C. Kirmaier, High Yield of M-Side Electron Transfer in Mutants of Rhodobacter capsulatus Reaction Centers Lacking the L-Side Bacteriopheophytin. *Biochemistry* **45**, 3845–3851 (2006).
- 11. P. D. Laible, *et al.*, Switching sides—Reengineered primary charge separation in the bacterial photosynthetic reaction center. *PNAS* **117**, 865–871 (2020).
- 12. K. A. Gray, J. W. Farchaus, J. Breton, D. Oesterhelt, Initial characterization of site-directed mutants of tyrosine M210 in the reaction centre of Rhodobacter sphaeroides. *The EMBO Journal* **9**, 2051–2070 (1990).

- 13. S. C. Straley, W. W. Parson, D. C. Mauzerall, R. K. Clayton, Pigment content and molar extinction coefficients of photochemical reaction centers from Rhodopseudomonas spheroides. *Biochimica et Biophysica Acta (BBA) Bioenergetics* **305**, 597–609 (1973).
- 14. Use of the Stanford Synchrotron Radiation Lightsource, SLAC National Accelerator Laboratory, is supported by the U.S. Department of Energy, Office of Science, Office of Basic Energy Sciences under Contract No. DE-ACO2-76SF00515. The SSRL Structural Molecular Biology Program is supported by the DOE Office of Biological and Environmental Research, and by the National Institutes of Health, National Institute of General Medical Sciences (including P41GM103393). The contents of this publication are solely the responsibility of the authors and do not necessarily represent the official views of NIGMS or NIH.
- 15. S. Russi, *et al.*, Inducing phase changes in crystals of macromolecules: Status and perspectives for controlled crystal dehydration. *Journal of Structural Biology* **175**, 236–243 (2011).
- 16. J. Sanchez-Weatherby, *et al.*, Improving diffraction by humidity control: a novel device compatible with X-ray beamlines. *Acta Cryst. D* **65**, 1237–1246 (2009).
- 17. W. Kabsch, XDS. Acta Cryst D 66, 125–132 (2010).
- 18. A. Vagin, A. Teplyakov, *MOLREP*: an Automated Program for Molecular Replacement. *J Appl Crystallogr* **30**, 1022–1025 (1997).
- 19. P. Emsley, K. Cowtan, *Coot*: model-building tools for molecular graphics. *Acta Cryst.* **60**, 2126–2132 (2004).
- 20. G. N. Murshudov, A. A. Vagin, E. J. Dodson, Refinement of Macromolecular Structures by the Maximum-Likelihood Method. *Acta Cryst. D* **53**, 240–255 (1997).
- 21. K. M. Faries, et al., Optimizing multi-step B-side charge separation in photosynthetic reaction centers from Rhodobacter capsulatus. *Biochimica et Biophysica Acta (BBA) Bioenergetics* **1857**, 150–159 (2016).
- 22. N. W. Woodbury, M. Becker, D. Middendorf, W. W. Parson, Picosecond kinetics of the initial photochemical electron-transfer reaction in bacterial photosynthetic reaction centers. *Biochemistry* **24**, 7516–7521 (1985).
- 23. C. Kirmaier, P. Laible, E. Hindin, D. Hanson, D. Holten, Detergent effects on primary charge separation in wild-type and mutant Rhodobacter capsulatus reaction centers. *Chemical Physics* **294**, 305–318 (2003).
- 24. J. Zhu, I. H. M. van Stokkum, L. Paparelli, M. R. Jones, M. L. Groot, Early Bacteriopheophytin Reduction in Charge Separation in Reaction Centers of Rhodobacter sphaeroides. *Biophysical Journal* **104**, 2493–2502 (2013).
- 25. M. Bixon, J. Jortner, M. E. Michel-Beyerle, A kinetic analysis of the primary charge separation in bacterial photosynthesis. Energy gaps and static heterogeneity. *Chemical Physics* **197**, 389–404 (1995).

- 26. G. Hartwich, H. Lossau, M. E. Michel-Beyerle, A. Ogrodnik, Nonexponential Fluorescence Decay in Reaction Centers of *Rhodobacter sphaeroides* Reflecting Dispersive Charge Separation up to 1 ns. *J. Phys. Chem. B* **102**, 3815–3820 (1998).
- 27. B. Carter, S. G. Boxer, D. Holten, C. Kirmaier, Photochemistry of a Bacterial Photosynthetic Reaction Center Missing the Initial Bacteriochlorophyll Electron Acceptor. *J. Phys. Chem. B* **116**, 9971–9982 (2012).
- 28. L. M. P. Beekman, *et al.*, Primary Electron Transfer in Membrane-Bound Reaction Centers with Mutations at the M210 Position. *J. Phys. Chem.* **100**, 7256–7268 (1996).
- 29. M. Du, *et al.*, Femtosecond spontaneous-emission studies of reaction centers from photosynthetic bacteria. *PNAS* **89**, 8517–8521 (1992).
- 30. C. Kirmaier, D. Holten, Evidence that a distribution of bacterial reaction centers underlies the temperature and detection-wavelength dependence of the rates of the primary electron-transfer reactions. *PNAS* **87**, 3552–3556 (1990).
- 31. P. D. Laible, S. R. Greenfield, M. R. Wasielewski, D. K. Hanson, R. M. Pearlstein, Antenna Excited State Decay Kinetics Establish Primary Electron Transfer in Reaction Centers as Heterogeneous †. *Biochemistry* **36**, 8677–8685 (1997).
- 32. J. M. Peloquin, S. Lin, A. K. W. Taguchi, N. W. Woodbury, Excitation Wavelength Dependence of Bacterial Reaction Center Photochemistry. 1. Ground State and Excited State Evolution. *J. Phys. Chem.* **99**, 1349–1356 (1995).
- 33. H. Wang, *et al.*, Protein Dynamics Control the Kinetics of Initial Electron Transfer in Photosynthesis. *Science* **316**, 747–750 (2007).
- 34. A. R. Holzwarth, M. G. Müller, Energetics and Kinetics of Radical Pairs in Reaction Centers from *Rhodobacter sphaeroides*. A Femtosecond Transient Absorption Study <sup>†, ‡</sup>. *Biochemistry* **35**, 11820–11831 (1996).
- 35. P. Hamm, et al., Subpicosecond emission studies of bacterial reaction centers. *Biochimica et Biophysica Acta (BBA) Bioenergetics* **1142**, 99–105 (1993).
- 36. M. G. Müller, K. Griebenow, A. R. Holzwarth, Primary processes in isolated bacterial reaction centers from Rhodobacter sphaeroides studied by picosecond fluorescence kinetics. *Chemical Physics Letters* **199**, 465–469 (1992).
- 37. M. H. Vos, *et al.*, Direct observation of vibrational coherence in bacterial reaction centers using femtosecond absorption spectroscopy. *PNAS* **88**, 8885–8889 (1991).
- 38. V. Nagarajan, W. W. Parson, D. Davis, C. C. Schenck, Kinetics and Free Energy Gaps of Electron-Transfer Reactions in Rhodobacter sphaeroides Reaction Centers. *Biochemistry* **32**, 12324–12336 (1993).

- 39. K. M. Faries, *et al.*, Consequences of saturation mutagenesis of the protein ligand to the B-side monomeric bacteriochlorophyll in reaction centers from Rhodobacter capsulatus. *Photosynth. Res.* **141**, 273–290 (2019).
- 40. A. Warshel, Role of the chlorophyll dimer in bacterial photosynthesis. *PNAS* **77**, 3105–3109 (1980).
- 41. L. J. Moore, H. Zhou, S. G. Boxer, Excited-State Electronic Asymmetry of the Special Pair in Photosynthetic Reaction Center Mutants: Absorption and Stark Spectroscopy †. *Biochemistry* **38**, 11949–11960 (1999).
- 42. S. L. Hammes, L. Mazzola, S. G. Boxer, D. F. Gaul, C. C. Schenck, Stark spectroscopy of the Rhodobacter sphaeroides reaction center heterodimer mutant. *PNAS* **87**, 5682–5686 (1990).
- 43. S. G. Boxer, R. A. Goldstein, D. J. Lockhart, T. R. Middendorf, L. Takiff, Excited states, electron-transfer reactions, and intermediates in bacterial photosynthetic reaction centers. *J. Phys. Chem.* **93**, 8280–8294 (1989).
- 44. N. W. Woodbury, *et al.*, Relationship between thermodynamics and mechanism during photoinduced charge separation in reaction centers from Rhodobacter sphaeroides. *Biochemistry* **33**, 8101–8112 (1994).
- 45. K. Gibasiewicz, et al., Analysis of the temperature-dependence of P+HA- charge recombination in the Rhodobacter sphaeroides reaction center suggests nanosecond temperature-independent protein relaxation. *Phys. Chem. Chem. Phys.* **15**, 16321 (2013).
- 46. J. Pan, et al., The Protein Environment of the Bacteriopheophytin Anion Modulates Charge Separation and Charge Recombination in Bacterial Reaction Centers. J. Phys. Chem. B 117, 7179–7189 (2013).
- 47. L. Laporte, L. M. McDowell, C. Kirmaier, C. C. Schenck, D. Holten, Insights into the factors controlling the rates of the deactivation processes that compete with charge separation in photosynthetic reaction centers. *Chemical Physics* **176**, 615–629 (1993).
- 48. J. Pan, R. Saer, S. Lin, J. T. Beatty, N. W. Woodbury, Electron Transfer in Bacterial Reaction Centers with the Photoactive Bacteriopheophytin Replaced by a Bacteriochlorophyll through Coordinating Ligand Substitution. *Biochemistry* **55**, 4909–18 (2016).
- 49. C.-K. Tang, J. Williams, A. Taguchi, J. Allen, N. Woodbury, P + H A Charge Recombination Reaction Rate Constant in *Rhodobacter sphaeroides* Reaction Centers Is Independent of the P/P + Midpoint Potentia. *Biochemistry* **38**, 8794–8799 (1999).
- 50. K. Gibasiewicz, et al., Mechanism of Recombination of the P<sup>+</sup> H<sub>A</sub><sup>-</sup> Radical Pair in Mutant Rhodobacter sphaeroides Reaction Centers with Modified Free Energy Gaps Between P<sup>+</sup>B<sub>A</sub><sup>-</sup> and P<sup>+</sup>H<sub>A</sub><sup>-</sup>. J. Phys. Chem. B **115**, 13037–13050 (2011).
- 51. A. Ogrodnik, W. Keupp, M. Volk, G. Aumeier, M. E. Michel-Beyerle, Inhomogeneity of Radical Pair Energies in Photosynthetic Reaction Centers Revealed by Differences in Recombination Dynamics

- of P+HA- When Detected in Delayed Emission and in Absorption. *J. Phys. Chem.* **98**, 3432–3439 (1994).
- 52. Z. Guo, N. W. Woodbury, J. Pan, S. Lin, Protein Dielectric Environment Modulates the Electron-Transfer Pathway in Photosynthetic Reaction Centers. *Biophysical Journal* **103**, 1979–1988 (2012).
- 53. W. Zinth, J. Wachtveitl, The First Picoseconds in Bacterial Photosynthesis Ultrafast Electron Transfer for the Efficient Conversion of Light Energy. *ChemPhysChem.* **6**, 871–880 (2005).
- 54. Y. Kakitani, A. Hou, Y. Miyasako, Y. Koyama, H. Nagae, Rates of the initial two steps of electron transfer in reaction centers from Rhodobacter sphaeroides as determined by singular-value decomposition followed by global fitting. *Chemical Physics Letters* **492**, 142–149 (2010).
- 55. A. G. Yakovlev, A. Ya. Shkuropatov, V. A. Shuvalov, Nuclear Wave Packet Motion between P\* and P\* B<sub>A</sub>- Potential Surfaces with a Subsequent Electron Transfer to H<sub>A</sub> in Bacterial Reaction Centers at 90 K. Electron Transfer Pathway. *Biochemistry* **41**, 14019–14027 (2002).
- 56. J. Fajer, D. C. Borg, A. Forman, D. Dolphin, R. H. Felton, Anion Radical of Bacteriochlorophyll. *Proceedings of the National Academy of Sciences* **95**, 2739–2741 (1973).
- 57. J. Fajer, D. C. Brune, M. S. Davis, A. Forman, L. D. Spaulding, Primary Charge Separation in Bacterial Photosynthesis: Oxidized Chlorophylls and Reduced Pheophytin. *Proceedings of the National Academy of Sciences* **72**, 4956–4960 (1975).
- 58. B. Carter, S. G. Boxer, D. Holten, C. Kirmaier, Trapping the P+B(L)- initial intermediate state of charge separation in photosynthetic reaction centers from Rhodobacter capsulatus. *Biochemistry* **48**, 2571–3 (2009).
- 59. K. M. Faries, et al., Manipulating the Energetics and Rates of Electron Transfer in *Rhodobacter* capsulatus Reaction Centers with Asymmetric Pigment Content. *J. Phys. Chem. B* **121**, 6989–7004 (2017).
- 60. A. Niedringhaus, *et al.*, Primary processes in the bacterial reaction center probed by two-dimensional electronic spectroscopy. *PNAS* **115**, 3563–3568 (2018).
- 61. J. C. Williams, *et al.*, Effects of mutations near the bacteriochlorophylls in reaction centers from *Rhodobacter sphaeroides*. *Biochemistry* **31**, 11029–11037 (1992).
- 62. M. Gouterman, "Optical Spectra and Electronic Structure of Porphyrins and Related Rings" in *The Porphyrins*, (Academic Press, 1978), pp. 1–165.
- 63. R. Alden, W. Parson, Z. Chu, A. Warshel, Orientation of the OH Dipole of Tyrosine (M)210 and Its Effect on Electrostatic Energies in Photosynthetic Bacterial Reaction Centers. *J Phys. Chem.* **100**, 16761–16770 (1996).
- 64. M. G. Romei, C.-Y. Lin, I. I. Mathews, S. G. Boxer, Electrostatic control of photoisomerization pathways in proteins. *Science* **367**, 76–79 (2020).

- 65. Corwin. Hansch, A. Leo, R. W. Taft, A survey of Hammett substituent constants and resonance and field parameters. *Chem. Rev.* **91**, 165–195 (1991).
- 66. H. Zhou, S. G. Boxer, Probing Excited-State Electron Transfer by Resonance Stark Spectroscopy. 1. Experimental Results for Photosynthetic Reaction Centers. *J. Phys. Chem. B* **102**, 9139–9147 (1998).
- 67. H. Zhou, S. G. Boxer, Probing Excited-State Electron Transfer by Resonance Stark Spectroscopy. 2. Theory and Application. *J. Phys. Chem. B* **102**, 9148–9160 (1998).
- 68. T. P. Treynor, S. G. Boxer, Probing Excited-State Electron Transfer by Resonance Stark Spectroscopy: 3. Theoretical Foundations and Practical Applications. *J. Phys. Chem. B* **108**, 13513–13522 (2004).
- 69. T. P. Treynor, C. Yoshina-Ishii, S. G. Boxer, Probing Excited-State Electron Transfer by Resonance Stark Spectroscopy: 4. Mutations near  $B_L$  in Photosynthetic Reaction Centers Perturb Multiple Factors that Affect  $B_L^* \rightarrow B_L^+ H_L^-$ . J. Phys. Chem. B **108**, 13523–13535 (2004).
- 70. W. Liptay, Electrochromism and Solvatochromism. Angew. Chem. Int. Ed. Engl. 8, 177–188 (1969).
- 71. G. U. Bublitz, S. G. Boxer, Stark Spectroscopy: Applications in Chemistry, Biology, and Materials Science. *Annu. Rev. Phys. Chem.* **48**, 213–242 (1997).
- 72. S. G. Boxer, Stark Realities. J. Phys. Chem. B 113, 2972–2983 (2009).
- 73. U. Fano, Effects of Configuration Interaction on Intensities and Phase Shifts. *Phys. Rev.* **124**, 1866–1878 (1961).
- 74. C. Cohen-Tannoudji, J. Dupont-Roc, G. Grynberg, Atom-Photon Interactions: Basic Processes and Applications. Atom-Photon Interactions: Basic Processes and Applications, by Claude Cohen-Tannoudji, Jacques Dupont-Roc, Gilbert Grynberg, pp. 678. ISBN 0-471-29336-9. Wiley-VCH, March 1998. (1998) (December 25, 2020).
- 75. A. Nitzan, Chemical Dynamics in Condensed Phases, 1st Ed. (Oxford University Press, 2006).
- 76. D. J. Griffiths, Introduction to quantum mechanics, 1st Ed. (Prentice Hall, 1995).
- 77. C. Cohen-Tannoudji, B. Diu, F. Laloë, Quantum mechanics, 1st Ed. (Wiley, 1977).
- 78. C.-Y. Lin, J. Both, K. Do, S. G. Boxer, Mechanism and bottlenecks in strand photodissociation of split green fluorescent proteins (GFPs). *PNAS* **114**, E2146–E2155 (2017).
- 79. D. J. Lockhart, S. G. Boxer, Stark effect spectroscopy of Rhodobacter sphaeroides and Rhodopseudomonas viridis reaction centers. *PNAS* **85**, 107–111 (1988).
- 80. W. Liptay, "Dipole Moments and Polarizabilities of Molecules in Excited Electronic States" in *Excited States*, (Elsevier, 1974), pp. 129–229.

- P. Kanchanawong, *The application of non-classical stark effects to study charge transfer reactions* (Stanford University, 2007).
- 82. D. W. Pierce, S. G. Boxer, Stark effect spectroscopy of tryptophan. *Biophysical Journal* **68**, 1583–1591 (1995).
- 83. L. N. Silverman, D. B. Spry, S. G. Boxer, M. D. Fayer, Charge Transfer in Photoacids Observed by Stark Spectroscopy. *J. Phys. Chem. A* **112**, 10244–10249 (2008).
- 84. F. Ma, *et al.*, Dynamic Stark Effect in Two-Dimensional Spectroscopy Revealing Modulation of Ultrafast Charge Separation in Bacterial Reaction Centers by an Inherent Electric Field. *J. Phys. Chem. Lett.* **12**, 5526–5533 (2021).
- 85. F. Ma, E. Romero, M. R. Jones, V. I. Novoderezhkin, R. van Grondelle, Both electronic and vibrational coherences are involved in primary electron transfer in bacterial reaction center. *Nat Commun* **10**, 933 (2019).